

9410562

DYNAMICAL CHARACTERISTICS OF THE WAKE OF A SQUARE CYLINDER AT LOW AND HIGH REYNOLDS NUMBERS

by
Arun Kumar Saha

TH
ME/1999/P
Sa19d



DEPARTMENT OF MECHANICAL ENGINEERING
Indian Institute of Technology, Kanpur

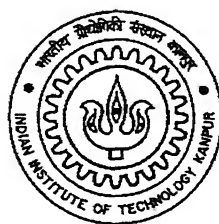
FEBRUARY, 1999

DYNAMICAL CHARACTERISTICS OF THE WAKE OF A SQUARE CYLINDER AT LOW AND HIGH REYNOLDS NUMBERS

A Thesis Submitted
In Partial Fulfilment of the Requirements
for the Degree of
Doctor of Philosophy

by

Arun Kumar Saha



to the
**DEPARTMENT OF MECHANICAL ENGINEERING
INDIAN INSTITUTE OF TECHNOLOGY KANPUR
INDIA**

February, 1999

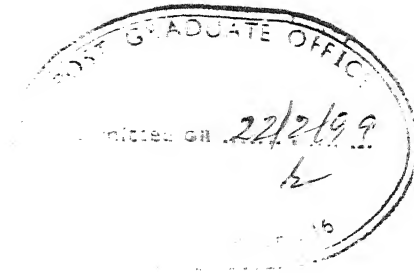
23 JUL 1999/ME
CENTRAL LIBRARY
I. I. T., KANPUR

Acc. No. A 128608

TH
ME/1999/P
Sajid



A128608



Certificate

It is certified that the work contained in the thesis entitled **Dynamical Characteristics of the Wake of a Square Cylinder at Low And High Reynolds Numbers** by Arun Kumar Saha, has been carried out under our supervision and that this work has not been submitted elsewhere for a degree.

Gautam Biswas
Gautam Biswas

Department of Mechanical Engineering
IIT Kanpur

K. Muralidhar
K. Muralidhar

Department of Mechanical Engineering
IIT Kanpur

February, 1999

To

my mother,

father Late Ramani Mohan Saha
and
uncle Late Nagendra Mohan Saha

Abstract

The wake of a square cylinder is exceedingly complex, being characterized by a series of transitions with increasing Reynolds number (Re). The flow regime evolves from a steady two-dimensional state to three-dimensional fully developed turbulent flow. The critical Reynolds numbers of transition lead to major changes in the flow structures. The fact that the points of separation are fixed for a square cylinder leads to significant differences with the corresponding flow field in the wake of a circular cylinder.

The wake of a square cylinder undergoes the first transition from a steady two-dimensional state to become unsteady at a Reynolds number of 45. This transition, called Hopf bifurcation reveals a clear vortex shedding phenomenon. The second transition is the initiation of three-dimensionality of the near-wake at a Reynolds number of 180. The evolution to three-dimensional flow is characterized by different modes of vortex shedding. These modes, labelled A and B reveal distinct spanwise wavelengths, being three times the cylinder size for Mode-A and the cylinder size itself for Mode-B. The Mode-A shedding pattern is accompanied by intermittent low frequency irregularity, called *vortex dislocation* arising from frequency discontinuity in the spanwise direction and phase variations within the shed vortices. With further increase in Reynolds number, additional transitions that follow are: (1) the large scale evolution of the separated shear layer and the consequent development of fine grained turbulence in it and (2) the boundary layer on the cylinder surface itself becoming turbulent.

The present study is concerned with the wake of a square cylinder at low and high Reynolds numbers. The flow regime considered for analysis is $40 \leq Re \leq 21400$. The flow field has been explored numerically as well as through experiments. Both two- and three-dimensional computations have been reported. The Marker-And-Cell (MAC) algorithm has been employed to solve the unsteady incompressible Navier-Stokes equations. To preserve adequate accuracy higher order spatial as well as temporal discretization have been utilized. The code has been

validated against the published results in the open literature and grid independence study has been studied extensively for each problem. The focus of the research is directed towards the structure of the near-wake of the cylinder ($x < 10$). Hotwire experiments at low as well as high Reynolds numbers have been carried out to assess the accuracy of the numerical solution and highlight additional factors that can influence the wake structure.

Low Reynolds number wake ($Re \leq 800$):

Topics studied here include (a) time domain analysis for the route to chaos (Guzmán and Amon, 1996) (b) spatial domain analysis for transition to three-dimensionality (Williamson, 1996), (c) similarity between low Reynolds number instantaneous flow and phase-averaged turbulent flow, (d) comparison of two- and three-dimensional models at transitional Reynolds number and (e) the effect of upstream shear on the force coefficients as well as the wake structures. Results obtained in the present study show the temporal evolution to follow a quasi-periodic route (via frequency locking) to chaos. This route is clearly brought out through qualitative indicators such as the Poincaré map and quantitative indicators such as the Lyapunov exponent. In the spatial domain, the vortex shedding modes are seen to follow $2D \rightarrow A^* (\equiv A + \text{dislocation}) \rightarrow B$, with vortex dislocation being associated with A^* . Important results to emerge from the present study are the following: (1) The change in the flow pattern in the wake barely affects the Strouhal number and the time-averaged forces acting on the cylinder though the respective force fluctuations are sensitive to the transitions; (2) Two-dimensional models consistently overpredict the force fluctuations while three-dimensional models are quite realistic; (3) The instantaneous velocity field has a considerable similarity to phase-averaged high Reynolds number flow field; (4) The differences between the two- and three-dimensional simulation can be adequately explained through the mechanisms of vortex stretching and additional diffusion inherently present in all three-dimensional flows and (5) The kinetic energy budget of the oscillatory components reveal that the convection due to mean motion, the production term and the pressure fluctuations play a vital role for the energy exchange between the mean and the fluctuating motion while the dissipation and diffusion terms are uniformly negligible.

High Reynolds number wake ($Re \geq 8000$):

Numerical calculations have been carried out in three-dimensions with a high order upwind scheme and without any explicit turbulence model. Parallel calculations have also been carried out using RANS in two-dimensions. Three types of turbulence models, namely Standard $k-\epsilon$, Kato-Launder and RNG $k-\epsilon$ have been used in the present study. The overall conclusions to emerge are: (a) turbulence model based on RANS are generally satisfactory for predicting

time-averaged quantities, and show good agreement with published experiments and Large Eddy Simulation. Specifically, the Kato-Launder model is seen to perform the best mainly due to a correct turbulence production in the stagnation region of the square cylinder. Despite the assumption of two-dimensionality the notion of eddy viscosity adequately compensates for diffusion in the third dimension. Experience with three-dimensional model-free computation shows that acceptable results can be obtained at least upto a Reynolds number of 21400, since the flow field shows a good match with experiments. This investigation further shows that the discretization scheme can account for the forward energy cascading mechanism of fully turbulent flow and thus produce good overall results. While the turbulence modeling approach can shed light on phase-averaged flow properties, the model-free calculation determines the instantaneous flow field. Thus it has been possible to assess the relative importance of the coherent (periodic) and incoherent (random) contributions to the velocity fluctuations. Results show the incoherent part to be small in the near-wake, growing preferentially in the regions of high shear and being uniformly dominant in the far-wake.

Hotwire experiments:

Experiments have been carried out at both low and high Reynolds numbers using an \times -wire hotwire probe. Quantities measured are profiles of the time-averaged and rms values of two components of velocity, the cross correlation $(\overline{u'v'})$, Strouhal number and the drag coefficient. All experiments pertain to a low upstream turbulence level. Measurements show an acceptable match with numerical predictions as well as the data reported in the literature. Peculiar discrepancies have been noticed at $x=1.5$ (just outside the base region). These have been attributed to differences in the geometrical factors between theory and experiments and unexpectedly, the role of inlet turbulence in the approach flow. Dedicated experiments involving high turbulence level in the approach flow have been carried out in the present work. These experiments indeed show a movement in the data points and a better overall match between the present work and the published literature.

Acknowledgements

How insufficient are the words to express my sincere gratitude, regards and thanks to my supervisors Prof. G. Biswas and Prof. K. Muralidhar for their excellent guidance, invaluable suggestions and generous help! They not only introduced me to the exciting field of research, but also helped in the successful completion of the thesis through their constant cooperation and encouragement. Their confidence in my capabilities has been the source of great inspiration to explore the problems with new ideas.

I am grateful to Dr. V. Eswaran for his invaluable suggestions and encouragement during my thesis and course work. I am also thankful to Dr. P. K. Panigrahi and Dr. S. Sarkar for their help and suggestions extended on different occasions.

My special thanks to Mr. Sambhunath Sharma for the fabrication of my experimental setup and the other timely helps.

I would like to thank to all my friends in Fluid Mechanics Laboratory, especially Dr. Atul Verma, Mr. Premananda Bera, Mr. S. Senthana, Mr. R. Vasudevan, Mr. P. P. Mukherjee, Mr. Amit Kumar, Ms Tanuja and Ms Meena for their sincere cooperation. I am grateful to Dr. Debasish Mishra and Mr. Atul Srivastava for their pleasant company in the Laboratory.

I don't have enough words to acknowledge Munni for her constant encouragement and cooperation.

I am thankful to all my friends especially Indrada, Susantada, Joydebda, Nilu, Pavitrada, Goutam, Subhojit and Pradipta for making my stay at IIT Kanpur enjoyable and pleasant. It is a pleasure to recall the homely ambiance provided to me by Mr. P.K.Paul, Mr. Gautam Pohit and their families.

I would like to thank Mr. Apurva Prakash for helping me in solving the graphics problem. The academic discussion with Dr. P. K. Maji is gratefully acknowledged.

Last but not the least, the silent support, good wishes and blessings of my parents and other family members have been the source of my inspiration throughout my research work.

Arun Kumar Saha

Contents

Certificate	iii
Dedication	v
Abstract	vii
Acknowledgements	xi
Contents	xiii
List of Figures	xix
List of Tables	xxvii
Nomenclature	xxix
1 Introduction	1
1.1 Flow Past a Square Cylinder	2
1.2 Numerical and Experimental Approaches	3
1.3 Objectives of the Present Work	5
1.4 Thesis Organization	7
2 Review of Literature	9
2.1 Review of Bluff Body Flows	10

2.1.1	Flow past a square cylinder	10
2.1.2	Comparison of square and circular cylinders	12
2.1.3	Flow past a circular cylinder	13
2.1.4	Flow past other bluff body geometries	17
2.1.5	Study of transition and chaos	19
2.1.6	Important experimental studies	22
2.2	Sensitivity of the Wake to External Factors	25
2.3	A Review on Turbulence Modeling	26
2.3.1	Various approaches of modeling turbulent flows	27
2.4	Summary	30
3	Description of Numerical Techniques	33
3.1	Review of Available Numerical Methods	34
3.1.1	Resolution of pressure-velocity coupling	35
3.1.2	Upwind versus central differencing	37
3.1.3	Higher order difference schemes	38
3.2	Incompressible Unsteady Navier-Stokes Equations	39
3.3	Reynolds-averaged Navier-Stokes Equations	41
3.3.1	Phase-averaged flow equations	42
3.3.2	k - ϵ family of turbulence models	42
3.4	Method of Solution	45
3.4.1	Grid system	46
3.4.2	Numerical stability	48
3.5	Computational Issues	48
4	Apparatus and Instrumentation	51
4.1	Apparatus	51
4.2	Review of Instrumentation	55

4.2.1	Imaging techniques	55
4.2.2	Intrusive methods	57
4.3	Hotwire Anemometry	58
4.3.1	Convective principles governing the operation of a hotwire . . .	59
4.3.2	Review of correlations for heat transfer from thin wires	61
4.3.3	Calibration methodology	62
4.3.4	Isothermal calibration of hotwire	63
4.3.5	Explicit non-real time signal analysis	64
4.4	Measurement of Drag and Vortex Shedding Frequency	68
4.5	List of Instruments	69
4.6	Uncertainty Analysis	72
5	Results and Discussion	73
5.1	Transition and Chaos in a Two-Dimensional Wake	74
5.1.1	Analysis of data	77
5.1.2	Qualitative characterization of the wake dynamics	79
5.1.2.1	Power spectra	79
5.1.2.2	Autocorrelation functions	84
5.1.2.3	Time-delay phase-space representation	86
5.1.2.4	Poincaré section	88
5.1.3	Analysis of chaos through quantitative parameters	91
5.1.3.1	Lyapunov exponents	91
5.1.3.2	Fractal dimension	92
5.1.4	Instantaneous flow field	96
5.1.5	Influence of grid size on the chaotic flow	96
5.1.6	Closure	99
5.2	Three-Dimensional Study of Low Reynolds Number Flow	100
5.2.1	Instantaneous flow field	107

5.2.2	Time-averaged integral parameters	128
5.2.3	Rms values of force fluctuations	129
5.2.4	Effect of three-dimensionality on the instantaneous forces	130
5.2.5	Time-averaged flow field	130
5.2.6	Comparison with a circular cylinder	139
5.2.7	Closure	142
5.3	Vortex Structures and Kinetic Energy Budget in Two-Dimensional Flow	144
5.3.1	Wake dynamics at a low Reynolds number	146
5.3.2	Profiles of time-averaged flow field and stresses	148
5.3.3	Instantaneous flow field	153
5.3.4	Time-averaged flow fluctuations	159
5.3.5	Analysis of the kinetic-energy equation of velocity fluctuations .	161
5.3.6	Closure	168
5.4	Comparison of Two- and Three-dimensional Models in Low Reynolds Number Transitional Flow	169
5.4.1	Time traces of selected flow properties	170
5.4.2	Evaluation of vorticity and pressure fields	174
5.4.3	Time-averaged flow field	179
5.4.4	Closure	191
5.5	Influence of Inlet Shear on the Structure of Wake	192
5.5.1	Wake details	193
5.5.2	Closure	201
5.6	Numerical Study of the Partially Enclosed Turbulent Unsteady Wake us- ing RANS	202
5.6.1	Engineering parameters	205
5.6.2	Comparison with experiments	211
5.6.3	Contours of instantaneous quantities	214
5.6.4	Contours of time-averaged stresses	223

5.6.5	Closure	223
5.7	Model-free Computation of High Reynolds Number Turbulent Flow . .	225
5.7.1	Integral parameters	226
5.7.2	Time-averaged flow field	230
5.7.3	Time-averaged turbulence statistics	233
5.7.4	Phase-averaged flow field	235
5.7.5	Closure	252
5.8	Experimental Study at Low and High Reynolds Numbers	253
5.8.1	Low Reynolds number measurements	256
5.8.2	High Reynolds number measurements	261
5.8.3	Effect of inlet turbulence on the wake	267
5.8.4	Spectra	270
5.8.5	Closure	273
6	Conclusions and Scope for Future Work	275
6.1	Conclusions	275
6.2	Scope for Future Work	278
	References	281

List of Figures

1.1	Three different instabilities for a circular cylinder.	2
1.2	Difference between square and circular cylinders.	4
1.3	Flow model past a square cylinder.	6
3.1	Staggered grid arrangement.	47
3.2	Typical nonuniform grid.	47
4.1	Test cells for (a) low (cross-section: 10 cm×5 cm) and (b) high (cross-section: 40 cm×40 cm) Reynolds numbers.	52
4.2	Photographs: (a) small test cell (b) instruments and (c) large test cell.	53
4.3	Crosswire probe and velocity components.	65
5.1.1	Schematic diagram of transition scenario in the wake of a square cylinder.	78
5.1.2	Transverse velocity signals at (a) Re=210 (b) Re=218 (c) Re=300 (d) Re=325 and (e) Re=600.	80
5.1.3	Transverse velocity spectra at (a) Re=210 (b) Re=218 (c) Re=300 (d) Re=325 and (e) Re=600.	82
5.1.4	Variation of the fundamental frequency ratio (f_2/f_1) as function of Reynolds number.	83
5.1.5	Autocorrelation function $A(T)$ of the transverse velocity components: (a) Re=210 (b) Re=325 and (c) Re=600.	85
5.1.6	Three-dimensional time-delay representation of the transverse velocity component: (a) Re=210 (b) Re=218 (c) Re=325 and (d) Re=600. . .	87

5.1.7	Poincaré section of the transverse velocity component: (a) Re=210 (b) Re=218 (c) Re=300 (d) Re=325 and (e) Re=600.	90
5.1.8	Temporal variation of the largest Lyapunov Exponent (λ).	93
5.1.9	Logarithmic plot of the rescaled range $R(\theta)/S(\theta)$ vs θ	95
5.1.10	Instantaneous vorticity contours at different Reynolds numbers: (a) Re=40 (b) Re=210 (c) Re=218 (d) Re=325 and (e) Re=600.	97
5.1.11	Power spectrum for a Reynolds number of 600 at grid size of 436×208 ; inset : grid size of 218×104	98
5.2.1	Time traces of the spanwise component of velocity: (a) Re=150 and 175 and (b) Re=325.	105
5.2.2	Vorticity contours at a Reynolds number of 175: (a) spanwise vorticity and (b) transverse (secondary) vorticity.	106
5.2.3	Iso-surfaces at a Reynolds number of 175 with regular shedding mode (Mode-A): (a) spanwise vorticity ($\omega_z = \pm 0.25$) (b) pressure ($p=0.8$) (c) streamwise (secondary) vorticity ($\omega_x = \pm 0.05$) and (d) transverse (secondary) vorticity ($\omega_y = \pm 0.05$).	109
5.2.4	Vorticity contours and iso-surfaces at a Reynolds number of 250: (a) spanwise vorticity contours (b) transverse (secondary) vorticity contours (c) iso-surfaces of primary vortices ($\omega_z = \pm 0.25$) and (d) iso-surfaces of secondary vortices ($\omega_x = \pm 0.05$).	112
5.2.5	Vorticity contours at a Reynolds number of 175 when vortex dislocation coexist with regular shedding: (a) spanwise vorticity at mid-span ($z=3.0$) (b) transverse (secondary) vorticity (c) spanwise vorticity at $z=1.5$ and (d) spanwise vorticity at $z=4.5$	115
5.2.6	Iso-surfaces at a Reynolds number of 175 when vortex dislocation coexist with regular shedding mode called Mode-A*: (a) spanwise vorticity ($\omega_z = \pm 0.25$) (b) streamwise (secondary vortices) ($\omega_x = \pm 0.05$) and (c) pressure ($p=0.8$).	117
5.2.7	Temporal evolution of vortex dislocation at various time: (a) $t=510.11$ (b) 541.99 (c) 553.81 (d) 561.59 and (e) 572.23.	119
5.2.8	Drag coefficient signal showing the different instances of the vortex dislocation shown in Figure 5.2.7.	120
5.2.9	Time traces of transverse velocity at two different Reynolds numbers.	121
5.2.10	Spectra at two Reynolds numbers corresponding to time-traces shown in earlier figure (Figure 5.2.9).	121

5.2.11	Time traces in the near- as well as far-wake at a Reynolds number of 175.	122
5.2.12	Temporal variations of drag and lift coefficients at various Reynolds numbers: (a) $Re=150$ (b) $Re=175$ and (c) $Re=290$	124
5.2.13	Streamwise variation of spanwise vorticity with Reynolds numbers. .	126
5.2.14	Streamwise variation of streamwise vorticity with Reynolds numbers.	126
5.2.15	Streamwise variation of transverse vorticity with Reynolds numbers.	127
5.2.16	Variation of Strouhal number and drag coefficient with Reynolds number.	128
5.2.17	Variation of force coefficients at various spanwise locations at a Reynolds number 325: (a) lift coefficient and (b) drag coefficient.	131
5.2.18	Variation of time-averaged streamwise velocity for various Reynolds numbers at different locations: (a) $x=0$ (b) 1.0 and (c) 4.0.	133
5.2.19	Variation of time-averaged transverse velocity for various Reynolds numbers at different locations: (a) $x=0$ (b) 1.0 and (c) 4.0.	135
5.2.20	Variation of the streamwise velocity fluctuation for different Reynolds numbers at different locations: (a) $x=0$ (b) 1.0 (c) 6.0 and (d) 14.0. .	138
5.2.21	Streamwise variations of (a) streamwise time-averaged velocity and (b) streamwise velocity fluctuations at various Reynolds numbers.	140
5.3.1	Trajectory of vortex peaks. The vortex moves parallel to the wake centreline in the far-wake.	147
5.3.2	Variation of streamwise location of vortex peaks with time.	148
5.3.3	Downstream decay of peak vorticity.	149
5.3.4	Time-averaged profiles of streamwise velocity component at different x -locations.	150
5.3.5	Time-averaged profiles of transverse velocity component at different x -locations.	150
5.3.6	Time-averaged profiles of streamwise normal stress component at different x -locations.	151
5.3.7	Time-averaged profiles of transverse normal stress component at different x -locations.	152
5.3.8	Time-averaged profiles of shear stress at different x -locations.	152
5.3.9	(a) Instantaneous vorticity contours and (b) Schematic of threading process.	154

5.3.10	Contours for instantaneous streamwise normal stress.	155
5.3.11	Contours for instantaneous transverse normal stress.	155
5.3.12	Contours for instantaneous shear stress: (a) present computation, (b) Cantwell and Coles (1983) (c) Lyn <i>et al.</i> (1995).	157
5.3.13	Contours for time-averaged streamwise normal stress.	158
5.3.14	Contours for time-averaged transverse normal stress.	159
5.3.15	Contours for time-averaged shear stress: (a) present computation and (b) Cantwell and Coles (1983).	160
5.3.16	Contours of the production of kinetic energy of fluctuating velocities.	164
5.3.17	Contours of the diffusion of kinetic energy of fluctuating velocities.	165
5.3.18	Contours of the dissipation of kinetic energy of fluctuating velocities.	165
5.3.19	Transverse variation of different terms of kinetic energy equation at (a) $x=1.0$ and (b) 3.0	166
5.3.20	Streamwise variation of different terms of kinetic energy equation at $y=0$	167
5.4.1	Comparison of time evolution of (a) lift and (b) drag coefficients obtained by two- and three-dimensional simulation.	171
5.4.2	Evolution of spanwise velocity at locations $x=2.4$ and 13.7	173
5.4.3	Time-averaged vorticity contours for (a) two-dimensional and (b) three-dimensional simulation.	175
5.4.4	Instantaneous vorticity contours for (a) two-dimensional and (b) three-dimensional simulation.	177
5.4.5	Instantaneous pressure contours for (a) two-dimensional and (b) three-dimensional simulation.	178
5.4.6	Comparison of time-averaged profiles: (a) streamwise velocity and (b) transverse velocity at various locations and (c) centreline recovery of streamwise velocity.	181
5.4.7	Comparison of time-averaged profiles of (a) streamwise normal stress (b) transverse normal stress and (c) shear stress.	183
5.4.8	Transverse variation of $\frac{\partial \bar{u}}{\partial y}$, $\frac{\partial^2 \bar{u}}{\partial y^2}$ and $\overline{u'^2}$ at a location $x=4.0$	184

5.4.9	Comparison of streamwise variations of velocity fluctuations along the wake centreline: (a) streamwise component and (b) transverse component.	187
5.4.10	Comparison of spatial distribution of streamwise fluctuations $(\overline{u'^2})$: (a) two-dimensional and (b) three-dimensional simulation.	188
5.4.11	Comparison of spatial distribution of transverse fluctuations $(\overline{v'^2})$: (a) two-dimensional and (b) three-dimensional simulation.	189
5.4.12	Comparison of spatial distribution of shear stress $(\overline{u'v'})$: (a) two-dimensional and (b) three-dimensional simulation.	190
5.5.1	Instantaneous (a) streamlines (b) vorticity contours and (c) pressure contours for a Reynolds number of 500 with $K=0.0$	194
5.5.2	Instantaneous (a) streamlines and (b) vorticity contours for a Reynolds number of 500 with $K=0.2$	195
5.5.3	Power spectra and time series of lift and drag coefficients for a Reynolds number of 1000 with (a) $K=0$ (b) $K=0.1$ and (c) $K=0.2$	200
5.6.1	Time evolution of lift coefficient: (a) standard $k-\epsilon$ (b) KaLa and (c) RNG $k-\epsilon$	208
5.6.2	Streamwise variation of (a) peak vorticity and (b) decay rate of peak vorticity.	209
5.6.3	Time-averaged streamwise velocity profiles at (a) $x=0$ (b) 1.0 and (c) 5.0.	210
5.6.4	Time-averaged transverse velocity profiles at (a) $x=0$ and (b) 5.0.	212
5.6.5	Time-averaged streamwise velocity recovery along the centreline ($y=0$).	213
5.6.6	Streamwise variation of total time-averaged kinetic energy along the centreline ($y=0$).	213
5.6.7	Instantaneous vorticity contours: (a) standard $k-\epsilon$ (b) KaLa and (c) RNG $k-\epsilon$	215
5.6.8	Instantaneous turbulent kinetic energy contours: (a) standard $k-\epsilon$ (b) KaLa and (c) RNG $k-\epsilon$	217
5.6.9	Instantaneous turbulent dissipation contours: (a) standard $k-\epsilon$ (b) KaLa and (c) RNG $k-\epsilon$	219
5.6.10	Contours of the time-averaged streamwise normal stress: (a) standard $k-\epsilon$ (b) KaLa and (c) RNG $k-\epsilon$	220

5.6.11	Contours of the time-averaged transverse normal stress: (a) standard $k-\epsilon$ (b) KaLa and (c) RNG $k-\epsilon$	221
5.6.12	Contours of the time-averaged shear stress: (a) standard $k-\epsilon$ (b) KaLa and (c) RNG $k-\epsilon$	222
5.7.1	Time-averaged profiles of (a) streamwise velocity at $x=1.5$ (b) transverse velocity at $x=1.5$ and (c) shear stress at $x=1.0$	229
5.7.2	Iso-surfaces of spanwise vorticity ($\omega_z=\pm 0.5$): (a) Run 2 and (b) Run 4.	231
5.7.3	Iso-surfaces of streamwise vorticity ($\omega_x=\pm 0.5$): (a) Run 2 and (b) Run 4.	232
5.7.4	Comparison of the time-averaged flow: (a) streamwise and (b) transverse velocity at locations $x=0.0, 1.0, 1.5$ and 4.0 and (c) centreline recovery of streamwise velocity.	235
5.7.5	Comparison of time-averaged fluctuations at locations $x=0.0, 1.0, 1.5$ and 4.0 : (a) streamwise normal stress (b) transverse normal stress and (c) shear stress.	237
5.7.6	Spectra at different axial locations: (a) streamwise velocity and (b) transverse velocity.	238
5.7.7	Spectrum of lift coefficient.	239
5.7.8	Two different phases for phase-averaging.	240
5.7.9	Contours of (a) phase-averaged spanwise vorticity (b) instantaneous spanwise vorticity (c) phase-averaged pressure at phase-I and (d) phase-averaged vorticity at phase-II.	243
5.7.10	Contours of phase-averaged stresses due to periodic fluctuations at phase-I for the horizontal mid-span ($z=3.0$): (a) streamwise normal stress (b) transverse normal stress and (c) shear stress.	245
5.7.11	Contours of phase-averaged (a) streamwise normal stress (b) transverse normal stress (c) shear stress and (d) pressure fluctuations due to random components at phase-I for the horizontal mid-span ($z=3.0$).	248
5.7.12	Comparison of streamwise variation of maximum (a) streamwise normal stress (b) transverse normal stress and (c) shear stress at phase-I.	251
5.8.1	Comparison of measured Strouhal number with published data	256
5.8.2	Comparison of measured drag with published data	257
5.8.3	Measured time-averaged streamwise velocity profiles: (a) $Re=200$ and (b) $Re=390$	258

5.8.4	Measured time-averaged transverse velocity profiles: (a) Re=200 and (b) Re=390	259
5.8.5	Measured time-averaged streamwise velocity fluctuations: (a) Re=200 and (b) Re=390	260
5.8.6	Measured time-averaged shear stress: (a) Re=200 and (b) Re=390 .	260
5.8.7	Comparison of measured time-averaged streamwise velocity profiles: (a) Re=8700 and (b) Re=17625	261
5.8.8	Comparison of measured time-averaged transverse velocity profiles: (a) Re=8700 and (b) Re=17625	262
5.8.9	Comparison of measured time-averaged profiles of streamwise velocity fluctuations: (a) Re=8700 and (b) Re=17625	263
5.8.10	Comparison of measured time-averaged profiles of transverse velocity fluctuations: (a) Re=8700 and (b) Re=17625	264
5.8.11	Comparison of measured time-averaged profiles of turbulent shear stress: (a) Re=8700 and (b) Re=17625	265
5.8.12	Comparison of recovery of measured time-averaged streamwise velocity along the wake centreline: (a) Re=8700 and (b) Re=17625	266
5.8.13	Effect of upstream turbulence on time-averaged profiles of (a) streamwise velocity (b) transverse velocity and (c) streamwise velocity fluctuations at $x=1.5$ for a Reynolds number of 12000	268
5.8.14	Effect of upstream turbulence on time-averaged profiles of (a) streamwise velocity (b) transverse velocity and (c) streamwise velocity fluctuations at $x=2.5$ for a Reynolds number of 12000	269
5.8.15	u -spectra at various streamwise locations	271
5.8.16	v -spectra at various streamwise locations	272

List of Tables

3.1	Constants for the k - ϵ family of turbulent models	44
5.1.1	Grid Independence Test	75
5.1.2	Comparison of Drag and Strouhal Number of the Present Study with Published Results	76
5.2.1	Grid Independence Test	101
5.2.2	Comparison of present results with published data	101
5.2.3	Code validation at a high Reynolds number	102
5.2.4	Rms values of lift and drag coefficients	129
5.3.1	Decay Rate of Peak Vortices	149
5.4.1	Comparison of Lift & Drag Coefficient and Strouhal Number	172
5.5.1	Variation of vortex strength with distance in the downstream behind the obstacle. $Re=500$, $K=0.0$	193
5.5.2	Effect of shear on the Strouhal number, mean and rms values of drag coefficient and rms values of lift coefficient	196
5.6.1	Strouhal number and time-averaged drag and coefficients	205
5.7.1	Comparison of model-free computations with experiments and LES .	227

Nomenclature

A	Length of the cylinder, m
Ar	Projected area of the cylinder (=A.B), m ²
B	Obstacle width, m
C_D	Drag coefficient, $\mathcal{D}/(\frac{1}{2}\rho u_{av}^2 Ar)$
C_L	Lift coefficient, $\mathcal{L}/(\frac{1}{2}\rho u_{av}^2 Ar)$
C'_D	rms value of drag coefficient
C'_L	rms value of lift coefficient
d	Fractal dimension
\mathcal{D}	Drag force on the square cylinder, $\sum_1 \tilde{P} \delta y \delta z - \sum_2 \tilde{P} \delta y \delta z$, N
f	Frequency of vortex shedding, Hz
G	Transverse velocity gradient
H	Width of the flow domain
Hr	Hurst's exponent
\mathcal{L}	Lift force on the square cylinder, $\sum_3 \tilde{P} \delta x \delta z - \sum_4 \tilde{P} \delta x \delta z$, N
k	Turbulent kinetic energy due to random fluctuations of velocities, (m/s) ²
K	Shear parameter
m,n	Reconstruction and embedding dimensions in fractal analysis
p	Static pressure, N/m ² or dimensionless ¹
\tilde{p}	Periodic component of pressure fluctuation
p'	Total (periodic+random) pressure fluctuation
p''	Random component of pressure fluctuation
\tilde{P}	Pressure distribution on the surface of the square cylinder
r_0	Relaxation factor in MAC algorithm
$R(\theta)$	Range defined between the maximum and minimum accumulated influx in fractal analysis
Re	Reynolds number, $\rho u_{av} B / \mu$
S	Strouhal number, fB/u_{av}
$S(\theta)$	Standard deviation of the modified scale in the calculation of fractal dimension

¹All lengths are nondimensionalized by cylinder width B

All velocities are nondimensionalized by inlet average velocity u_{av}

All pressures are nondimensionalized by ρu_{av}^2

t	Time, sec
t_s	Sampling time
u, v, w	Streamwise, transverse and spanwise components of velocity, normalized by u_{av}
$\tilde{u}, \tilde{v}, \tilde{w}$	Periodic components of velocity
u', v', w'	Three components of total velocity fluctuations (periodic+random)
u'', v'', w''	Three components of velocity fluctuations due to random components
$\bar{u}, \bar{v}, \bar{w}$	Time-averaged three components of velocity
u_c	Convective velocity at the outflow plane
$\tilde{u}\tilde{u}$	Instantaneous streamwise normal stress due to periodic component of velocity fluctuations
$\tilde{v}\tilde{v}$	Instantaneous transverse normal stress due to periodic component of velocity fluctuations
$\tilde{u}\tilde{v}$	Instantaneous shear stress due to periodic component of velocity fluctuations
$\overline{\tilde{u}\tilde{u}}$	Time-averaged streamwise normal stress due to periodic component of velocity fluctuations
$\overline{\tilde{v}\tilde{v}}$	Time-averaged transverse normal stress due to periodic component of velocity fluctuations
$\overline{\tilde{u}\tilde{v}}$	Time-averaged shear stress due to periodic component of velocity fluctuations
$\overline{u'u'}$	Time-averaged streamwise normal stress due to (periodic+random) velocity fluctuations
$\overline{v'v'}$	Time-averaged transverse normal stress due to (periodic+random) velocity fluctuations
$\overline{u'v'}$	Time-averaged shear stress due to (periodic+random) velocity fluctuations
$u''u''$	Instantaneous streamwise normal stress due to random velocity fluctuations
$v''v''$	Instantaneous transverse normal stress due to random velocity fluctuations
$u''v''$	Instantaneous shear stress due to random velocity fluctuations
x, y, z	Streamwise, transverse and spanwise coordinates
$X(t, \theta)$	Accumulated influx in fractal analysis

Subscripts

av	Average
D	Drag
L	Lift
p	Peak value
1,2	Forward and rear sides of the cylinder
3,4	Top and bottom sides of the cylinder

Greek symbols

ϵ	Dissipation of turbulent kinetic energy, m^2/s^3
ϵ_{ijk}	Alternating tensor
λ_z	Spanwise wavelength of secondary vortices, m
μ	Dynamic viscosity of the fluid, Pa.sec
ν	Kinematic viscosity of fluid, m^2/s
ν_t	Eddy viscosity, m^2/s
ρ	Density of the fluid, kg/m^3
τ	Delay time, sec
ω_i	Instantaneous vorticity, $\epsilon_{ijk} \frac{\partial u_k}{\partial x_j}$
$\overline{\omega_i}$	Time-averaged vorticity
ω_i'	Total component of vorticity fluctuation

Chapter 1

Introduction

Fluid flow past bluff bodies in general, and square and circular cylinders in particular, are topics of considerable complexity. For example, the wake of a circular cylinder is known to undergo a series of transitions with increasing Reynolds number. Starting from a steady attached state, the flow becomes unsteady with separation at a Reynolds number of 45. The complexity of the unsteady flow increases with the Reynolds number. The flow becomes three-dimensional beyond a Reynolds number of 180. The flow is apparently chaotic around a Reynolds number of 500 and possibly turbulent at a Reynolds number of 1000. At the transitional Reynolds number (leading to three dimensionality), two distinct modes of vortex shedding have been observed. These are characterized by the spanwise wavelengths of the streamwise (secondary) vortices. The initial modes at the transitional Reynolds number are Mode-A (a wavelength of three-cylinder diameters) and Mode-B (which occurs at the later part of the transitional regime and has a wavelength of one-cylinder diameter). Mode-A also includes an intermittent low frequency irregularity in the vorticity field, called *vortex dislocation*. The wake of a circular cylinder increasingly embodies complex physics; more complexities are encountered at higher Reynolds number. Three different instabilities arise owing to those of the boundary layer, the separated shear layer and the Kármán vortex street. The Kármán vortex street is formed as a result of Hopf bifurcation which takes place at a Reynolds number as low as 45. The second subsequent instability takes place at a much later stage and is thought to be at a Reynolds number around 1000. The third instability is about the transition of boundary layer from laminar to turbulent and occurs at a very high Reynolds number. Figure 1.1 shows a schematic of the three instabilities in the wake. As a result, three distinct flow

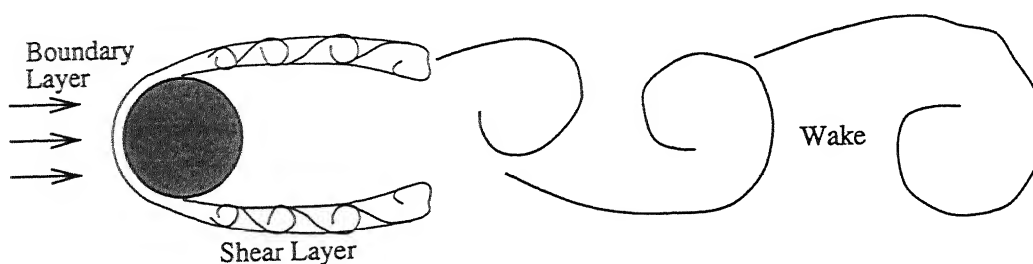


Figure 1.1: Three different instabilities for a circular cylinder.

fields interact among themselves and culminate in a complex flow structure.

An important application where the knowledge of unsteady wakes is required is in flow-induced vibration. Three possibilities arise, namely: (i) flow past a rigid body where the flow is self sustained and oscillates at a dominant frequency creating an alternate array of Kármán vortices, (ii) flow past a freely suspended body where the vortex shedding frequency locks into the oscillation of the body caused by the flow, and (iii) flow past a vibrating body in which the flow oscillates at the forcing frequency. The flow past a bluff body is of direct relevance to the design of off-shore structures, heat exchanger components and wherever flow induced vibration is important. The analysis of flow past a bluff body placed in the non-uniform stream is somewhat more complex. There exists a wide range of applications for such flows as well. The approaching flow of a curved river against the bridge pier is one such example. Submarines, ships, passenger aircraft, automobiles and missiles are examples where the object is in motion through a stationary fluid medium. High-rise buildings, chimneys and tube banks in heat exchangers are examples where the fluid is in motion. In each class, the wake of the bluff object predominantly determines the performance of the individual devices. Recent applications such as the detection of unobserved objects through signature analysis and the migration and dispersion of pollutants have intensified the need to understand the wake dynamics.

1.1 Flow Past a Square Cylinder

The flow past a square cylinder resembles flow past a circular cylinder as far as the instabilities are concerned. But the separation mechanism and the consequent dependence of the shedding frequency and the aerodynamic forces on the Reynolds number differ significantly. Unlike the circular cylinder, the separation points in the case of square

cylinder are fixed and are either at the leading corners or at the corners of both the leading and trailing edges when there is reattachment. As a result, the aerodynamic forces and the frequency of vortex shedding assume asymptotic values after a particular Reynolds number. The circular cylinder shows continuous variation of these quantities with Reynolds number. This is because the point of separation moves to and fro depending on the surface quality of the cylinder, the Reynolds number and the upstream conditions. Figure 1.2 shows a schematic comparison of the flows past square and circular cylinders.

1.2 Numerical and Experimental Approaches

The two- and three-dimensional vortical instabilities in wakes have been the subject of interest to engineers and the scientists for many years. Although the problem of an unseparated wake behind a splitter plate or symmetric airfoil is amenable to analytical studies, for example stability analysis, a three-dimensional bluff body poses a greater analytical challenge. The wake of a nominally two-dimensional object is itself a complex flow field. Approaches to analyze this problem have been principally numerical and experimental.

In the past, the numerical simulation of the flow past bluff bodies has been carried out by solving the Navier-Stokes equations through the stream function-vorticity approach. But solutions of two-dimensional Navier-Stokes equations or stream function-vorticity equations are restricted to very low Reynolds numbers since the flow often becomes three-dimensional (even at as low a Reynolds number as 180 for a circular cylinder). Therefore, two-dimensional calculations at higher Reynolds numbers are questionable. Turbulent flow past a bluff object involves a wide range of length as well as time scales. The Direct Numerical Simulation (DNS) at very high Reynolds number can be carried out by solving the full Navier-Stokes equation using very fine grids. These grids can resolve all the length scales appearing in the flow field. In such a simulation, a very small time step is used for resolving the smallest scale associated with the flow. DNS is primarily limited by the computational resources. To resolve all the scales of motion, one requires a number of grid points $N \sim L/\eta$, where L is the dimension of the computational domain and η is the smallest scale of motion, namely the Kolmogorov length scale. The ratio L/η is proportional to $Re^{\frac{3}{4}}$ and the total number of grid points required by DNS in three-dimensions is $N \sim Re^{\frac{9}{4}}$. For this reason, DNS has largely been limited to simple geometries at low Reynolds numbers.

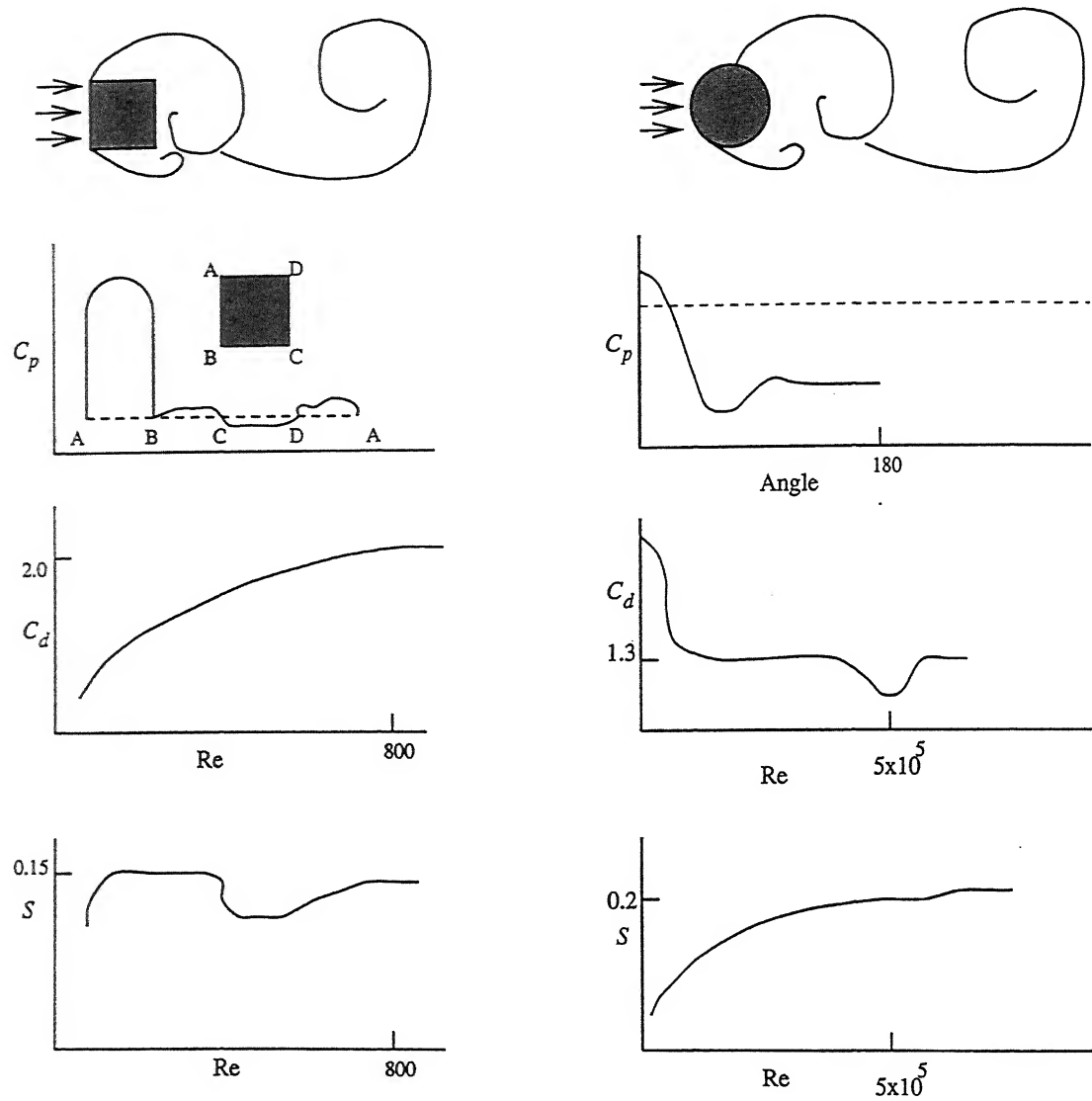


Figure 1.2: Difference between square and circular cylinders.

The alternatives to DNS are the Reynolds-averaged Navier-Stokes Equations (RANS) and the Large Eddy Simulation. RANS contains empirical parameters and hence lacks generality. The model constants for RANS are usually set using the values, determined through a few simple experiments and thus cannot be truly universal. Furthermore, laminar-turbulent transition is exceedingly difficult to predict using the RANS approach, and requires the addition of significant hand-waiving in the form of intermittency functions. However, as far as integral quantities and engineering parameters, such as aerodynamic forces are concerned, the RANS approach is known to work satisfactorily.

The Large Eddy Simulation (LES) is an intermediate approach between DNS and RANS. In LES, the contribution of the large scales, *i.e.*, the energy carrying structures to momentum and energy transfer is computed exactly, and only the contribution of the smallest scales of turbulence is modeled. However, LES also requires fairly fine meshes even though it can be used at a much higher Reynolds number than DNS. Computation of bluff body flows using LES is also expensive.

The experimental investigation of bluff body flows is a formidable task as the flow has recirculation zones, especially in the region of vortex formation. Applicability of any experimental technique depends on the flow domain of interest and the nature of the flow at that particular region. For example, the hotwire anemometer cannot be used in the base region where a negative velocity is encountered, unless a special technique is adopted (example, flying hotwire anemometry). Different methods have been used to measure velocity in bluff body wakes. Among these, hotwire anemometry (HWA), Laser Doppler Velocimetry (LDV) and Particle Image Velocimetry (PIV) are the most common.

1.3 Objectives of the Present Work

The flow configuration considered in the present study is prescribed flow past a cylinder of square cross-section. Figure 1.3 shows the flow model in the present work. In all the cases, the cylinder is long, in the sense that the geometry is nominally two-dimensional. Except for the cylinders with a circular cross-section, the knowledge of unsteady flow around other bluff objects is quite limited. A square cylinder has important applications in practice and at the same time, displays unexpected complexities in the wake structure. The objective of the present thesis is to contribute in fundamental terms to the understanding of wake

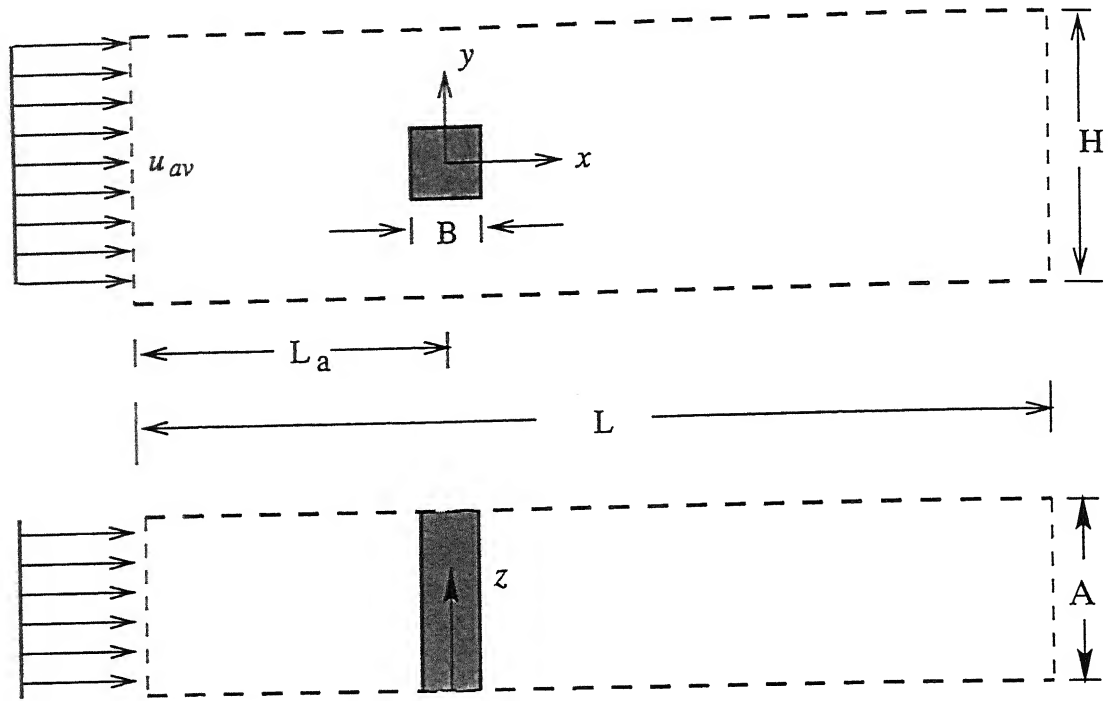


Figure 1.3: Flow model past a square cylinder.

dynamics of a square cylinder.

The present study is concerned with the wake of a square cylinder at both low and high Reynolds numbers. The flow regime considered for the analysis is $40 \leq Re \leq 21400$. The flow field has been explored numerically as well as through experiments. In the numerical study, both two- and three-dimensional computations have been reported. The Marker-And-Cell (MAC) algorithm has been employed to solve the unsteady incompressible Navier-Stokes equations. To preserve adequate accuracy higher order spatial as well as temporal discretization have been utilized. The code has been validated against the published results in the open literature and grid independence study has been carried out extensively for each problem. The focus of the research is directed towards the structure of the near-wake of the cylinder ($x < 10$). Hotwire experiments at low as well as high Reynolds numbers have been carried out to assess the accuracy of the numerical solution and to highlight the additional factors that can influence the wake structure.

Numerical calculations have been carried out in three-dimensions with a higher order scheme and without any explicit turbulence model. Simultaneously, calculations have also been carried out using RANS in two-dimensions. Three turbulence models,

namely standard k - ϵ , Kato-Launder and RNG k - ϵ have been used in the present study to examine their utility for wake predictions.

Experiments have been carried out at both low and high Reynolds numbers using an \times -wire hotwire probe. Quantities measured are profiles of the time-averaged and rms values of two components of velocity, the cross correlation $(\overline{u'v'})$, Strouhal number and the drag coefficient.

Major topics studied in the present thesis include *(a) time domain analysis for the route to chaos, (b) spatial domain analysis for transition to three-dimensionality, (c) similarity between the low Reynolds number instantaneous flow and the phase-averaged turbulent flow, (d) comparison of two- and three-dimensional models at the transitional Reynolds number, (e) the effect of upstream shear on the force coefficients as well as the wake structure, (f) two-dimensional RANS calculation at high Reynolds number turbulent flow, (g) relationship between the coherent and incoherent or random components of velocity and pressure fluctuations at a higher Reynolds number and their relative magnitudes and (h) experimental validation.*

1.4 Thesis Organization

Subsequent chapters of the present thesis have been organized in the following manner.

Chapter-2 reviews the literature related to the different aspects of the flow past a square cylinder, circular cylinder and other bluff bodies. The details of the numerical techniques, governing equations and the different boundary conditions including the grid system used have been presented in Chapter-3. The experimental setups and the associated instrumentation have been discussed in Chapter-4. Chapter-5 deals with the results of the present research and the related discussion. The chapter is divided into eight sections, each with a specific objective. Chapter-6 summarizes major conclusions of the present thesis and scope for future work.

Chapter 2

Review of Literature

The literature pertaining to flow past a square cylinder is reviewed below. A review of the earlier investigations related to the different aspects of the bluff body flows over a range of Reynolds numbers has also been presented. The range includes low to high Reynolds numbers including turbulent flow. A brief review on the modeling aspects of turbulent flow has also been undertaken to examine the performance of various turbulence models for complex geometries.

Flow past bluff bodies has been studied extensively in the past. Depending on the objectives of the work, the numerical approach in some cases has been found to be more appropriate compared to experiments. Numerical calculations invariably produce a large volume of information and permit parametric studies to be carried out at a low cost. In contrast, to understand oblique shedding, long cylinders are required to avoid the effect of end conditions. The complicated nature of the wake in such an application can be analyzed only when the length-to-diameter ratio is high. Such situations can be studied effectively through experiments. Bluff body wakes fall in the category of applications that are characterized by unexpected phenomena. At such instances, one is forced to employ both numerical and experimental approaches to develop a full understanding of the recorded observation.

2.1 Review of Bluff Body Flows

2.1.1 Flow past a square cylinder

Flow past a square cylinder shows the following behaviour with increasing Reynolds number. In the Reynolds number range of 2 - 8, the flow is unseparated and symmetric above and below the cylinder with respect to the axis aligned with the flow. Once the Reynolds number exceeds a certain threshold limit, separation at the leading edge is evident. This is followed by reattachment over the sides of the cylinder and a separation once again at the trailing edges. In the Reynolds number range of 10 - 45, a pair symmetric attached vortices are formed behind the cylinder. The envelop of these vortices has the shape of a bubble. The flow is globally steady, though time dependent behaviour can be revealed within the bubble. The instability of the separation bubble is likely to grow with increasing Reynolds number. At a higher Reynolds number, Hopf bifurcation takes place and the flow becomes unsteady. Once the vortices become unstable, they tend to be shed downstream from the top and bottom halves of the cylinder. A criss-cross flowfield is thus established due to the alternating character of the shedding mode.

Many researchers have determined experimentally and numerically the Reynolds number at which the flow becomes oscillatory to be 40 - 45. Kelkar and Patankar (1992) have performed linear stability analysis to find the critical Reynolds number at which flow becomes unsteady and the effect of unsteadiness on the heat transfer rate from the square cylinder. The two-dimensional linear stability analysis of steady flow has been carried out by computing the evolution of two-dimensional perturbations and the critical Reynolds number is determined from the growth rate of these perturbations. The study shows the critical Reynolds number to be 53 and the predicted Strouhal number matches well with the experiments.

Davis and Moore (1982) have reported two-dimensional numerical simulation of flow past a rectangular cylinder for the Reynolds numbers in the range of 100 to 2800. The simulation was carried out in an infinite medium by applying free stream condition on the transverse boundaries. A third order upwind differencing for convection terms was used with Leith type of temporal differencing. The effects of upstream velocity profile, angle of attack and aspect ratio of the rectangular cylinder have been studied in detail. Their results show that the lift and drag coefficients and Strouhal number

depend strongly on the Reynolds number. The computed Strouhal numbers compare well with those of experiments for a Reynolds number below 1000. For a square cross-section, a small Reynolds number ($Re \leq 100$) led to a low Strouhal number. The Strouhal number subsequently increased with the increase in Reynolds number to a certain value. Further increase in Reynolds number resulted in the decrease in Strouhal number, finally yielding an asymptotic value. Within the range of Reynolds number considered, the drag coefficient continuously increased with Reynolds number. Davis *et al.* (1984) have carried out both numerical and experimental study of flow past a rectangular cylinder in a confined geometry. This study has highlighted the effect of blockage due to a transverse boundary on the mean flow parameters such as the lift and drag coefficients and Strouhal number. Qualitative comparisons of the experiments and the numerical results were also accomplished in this study through flow visualization. These were found in to be in good agreement. Through numerical results, the authors were able to show the generation of wall vortices at higher blockage. These vortices were also shed downstream along with the Kármán vortices.

Mukhopadhyay *et al.* (1992) have reported a numerical study of flow past a square cylinder in a channel. The range of Reynolds number considered here is 60 - 800. The Strouhal number was seen to increase with the increase in blockage. The strength of the vortices of the the flow were damped in the downstream due to the blockage effect.

Tamura and Kuwahara (1990) have computed two- as well as three-dimensional flow past a square cylinder for varying aspect ratios. The aspect ratio is the spanwise length divided by the size of the square cylinder. The authors used third order spatial discretization for the convective terms without using any model for the subgrid scales. The Reynolds number considered in the study was 10^5 . Periodic boundary conditions were employed in the spanwise direction. The aerodynamic parameters of the cylinder such as lift, drag and Strouhal number were determined through the computation of the two- and three-dimensional flows. The study showed significant differences between the two sets of results. Their investigation revealed that three-dimensional structures emerged due to vortex instability and these structures have an appreciable effect on the aerodynamic behaviour. The computational results show that the three-dimensional structures decrease the time-averaged drag and the rms values of the lift and hence with the long-length periodicity one can get results closer to the experimental value.

Suzuki and Suzuki (1994) have carried out a computational as well as experimental

study of flow in a channel with a built-in square rod at a Reynolds number of 150. Their computed results reveal that the momentum transfer is enhanced due to the apparent shear stress resulting from the non-zero value of the cross-correlation. This was confirmed by the hotwire measurements. The quick recovery of velocity field could be attributed to this nonzero value at some positions in the wake. The criss-cross motion of the Kármán vortex has been explained in terms of the interaction between the Kármán vortex street and the disturbed wall shear layer. The wavering motion of the separated vorticity layers on both sides of the rod and the periodic formation of an isolated vortex island from the lifted tip of the wall vorticity layer have also been discussed. This vortex island has been found to play an important role not only for the occurrence of the criss-cross motion of the Kármán vortex but also for the generation of the non zero value of the cross-correlation term.

2.1.2 Comparison of square and circular cylinders

The primary difference between the flow past a circular and a square cylinders is that in the former case there is no definite point of separation on the surface of the body. In the latter, the leading corners are the two points where flow separates. In the case of a circular cylinder the point of separation depends on the Reynolds number but the point of separation in the case of a square cylinder is independent of the Reynolds number. The variation of the drag coefficient in the case of a circular cylinder is continuous with Reynolds number, while the square cylinder has an asymptotic behaviour after a certain value. Similarly the Strouhal number shows continuous and asymptotic trends for the circular and square cylinders respectively. This difference in the behaviour of the two bluff objects are due to the differences in their points of separation.

In an comparative study of the circular and square cylinders, Franke *et al.* (1990) have considered laminar flow past both the cylinders. The Reynolds number chosen for the circular cylinder was upto 5000 and for a square cylinder, upto 300. The third order QUICK scheme was used to discretize the convective terms and SIMPLEC methodology to solve the two-dimensional Navier-stokes equations. No turbulence model was adopted in this study. The Strouhal number and the time-averaged drag coefficient were the basis of their comparison with the published experimental and numerical results. Satisfactory results were reported for Reynolds number upto 1000 for the circular cylinder and upto

300 for the square cylinder. The disagreement at higher Reynolds numbers was attributed to the influence stochastic fluctuations. In the case of a square cylinder, a large discrepancy was seen in the distribution concerning variation of Strouhal number as a function of Reynolds number. As expected, the sharpness of the cylinder corners in the experiments and the numerical treatment of these corners considerably influenced the shedding frequency.

Tamura *et al.* (1990) have computed the flow behind a circular and a square cylinder by solving the two- and three-dimensional Navier-Stokes equations. The authors have used a third order upwind scheme for a Reynolds number range of $20 - 10^6$. Their findings show that the flow structures in the near-wake of the cylinder have a significant effect on the determination of the drag and lift forces. The difference between the aerodynamic forces computed by two- and three-dimensional simulations at higher Reynolds number is due to the secondary vortices created in the two-dimensional computation.

2.1.3 Flow past a circular cylinder

The survey of the literature shows that a large number of investigations on the flow past a circular cylinder have been accomplished in the past. It is beneficial to review the wake of the circular cylinder and then look for the similarities between the wakes of circular and square geometries.

Perry *et al.* (1982) have demonstrated the presence of vortex shedding behind a circular cylinder at a Reynolds number of 100 with the help of a flow visualization technique. They have explained the penetration of the fluid into the closed cavity just behind the cylinder. Their results show structural similarity between a laminar wake and a phase-averaged turbulent wake.

At a relatively higher Reynolds number the separated shear layer becomes unstable and shows a mixing-layer type of behaviour. Thus at higher Reynolds numbers, the flow becomes complex due to the presence of three simultaneous instabilities, namely the boundary layer instability (over the surface of the cylinder), separated shear layer instability (generation of mixing layer type of vortices) and the primary vortex (or Kármán vortex) instability. Three different mechanisms interact among themselves and produce a complex flow structure. The applicability of the two-dimensional calculation in predicting

such complex behaviour is clearly doubtful. Shear layer vortices at a Reynolds number of 350 can be expected, but vortices below a Reynolds number of 1000 have not been reported.

Braza *et al.* (1986) have numerically studied flow past a circular cylinder. The Reynolds numbers used in their study were 100, 200 and 1000. The Strouhal number, the lift and the drag coefficients matched well with experiments. The authors also studied the interaction of the unsteady pressure and velocity fields and found a phase relation between them. Their investigation revealed that the strongly rotational viscous region, the convection of the eddies and the inviscid flow determine this interaction. Analysis of structures of varying scales and their interactions during fully developed vortex shedding showed the following: The secondary eddies in the near-wake appearing at Reynolds numbers greater than 200 have a significant presence even at a Reynolds number of 1000. Pairs of them merge and form the main eddies along the path of Kármán vortices, whereas a secondary eddy merges with an already existing one. The analysis shows that all such interactions appear once in a period and the global periodic flow is not greatly influenced by these phenomena.

Braza *et al.* (1990) have attempted a two-dimensional direct numerical simulation (DNS) for Reynolds numbers in the range of 2000 - 10000. Apart from the vortex shedding phenomenon, it has been shown that the transition waves develop in the separated shear layers and lead to mixing layer eddies. The ratio of the computed transition wave frequency to the Strouhal number is in good agreement with experimental results. The instability leading towards the mixing layer eddies has been proven to be of two-dimensional origin and successfully predicted by the two-dimensional form of Navier-Stokes equations.

Behr *et al.* (1995) have investigated the effect of blockage for a circular cylinder at a Reynolds number of 100. Their results show that on decreasing the blockage from 5.5 to 1.6%, the Strouhal number, the drag coefficient and the rms lift coefficient decrease by 5, 6 and 6% respectively.

The two-dimensionality of the vortex shedding is present in the range of Reynolds number between 45 and 180. Most of the recent developments on the flow past bluff bodies, especially the flow past a circular cylinder have been discussed elaborately in the review papers of Roshko (1993) and Williamson (1996c). This particular range of Reynolds number is also susceptible to end conditions. The latest discovery which can

be thought of as one of the major reasons for three-dimensionality in nominally two-dimensional geometry at low Reynolds numbers is the vortex dislocation (Williamson, 1989, 1992). Other phenomena which trigger three-dimensionality include oblique shedding, phase expansions and phase shocks (Miller and Williamson 1994; Monkewitz *et al.*, 1996) and cellular shedding (König *et al.*, 1990, 1992). It is now well understood that the end boundary conditions (at the ends along the span of a cylinder) are very important in controlling the wake pattern across the complete span (Williamson, 1988a, 1989; Eisenlohr and Eckelmann, 1989; Hammache and Gharib, 1989, 1991). They indeed dictate the pattern of vortex shedding as oblique or parallel to the cylinder axis in the laminar regime.

Once the Reynolds number exceeds 180, the overall shedding pattern becomes complex. Together with the spanwise primary vortices (Kármán vortices), the secondary vortices start getting generated in the streamwise direction. In the range of Reynolds number between 160 and 240, the secondary vortices are found with a wavelength of several cylinder diameters and is designated as Mode-A. Another type of the secondary vortices are also found which have a wavelength of about one cylinder diameter and this mode is termed as Mode-B.

The transition of the wakes behind bluff objects as characterized by the secondary vortices with a dominant spanwise wavelength, have been the subject of many recent experimental and numerical investigations. Two different modes of instability involved in the wake transition show up with vortex loops (Mode-A) and the streamwise vortex pairs (Mode-B). This has been demonstrated and documented by Williamson (1988b, 1992). The author has observed experimentally that the spanwise length scale for Mode-A is around 3-4 diameters of the cylinder and Mode-B instability has a length scale of approximately 1-1.5 diameters. Henderson (1996) has proved the existence of these two modes through their numerical study using Floquet stability analysis. They have shown that the Mode-A occurs through subcritical bifurcation whereas Mode-B is brought about by supercritical bifurcation with no frequency shift near the threshold. In another work by Henderson and Barkley (1996), the three-dimensionality has been demonstrated as the cause of the secondary instability. The critical Reynolds number for this instability has been found to be 188.5 while Mode-A has a spanwise wavelength of 4 diameters. The recent developments in the low Reynolds number experiments (Williamson, 1992, 1996a, 1996b) indicate that the discontinuity in the Strouhal-Reynolds number curve in the case

of a circular cylinder is due to the presence of large scale low frequency structures during Mode-A instability. This combined mode is called Mode-A*. Williamson (1992) has shown that wake behind a circular cylinder at a Reynolds number of about 200 reveals the formation of the intermittent low frequency large scale structures. This structure was generated intentionally in the experiments with the help of a disc of small thickness mounted over the cylinder. The presence of the disc created a frequency discontinuity across the span of the cylinder. The presence of large scale intermittent low frequency velocity irregularities were also reported by Roshko (1954) and later by Bloor (1964). Hama (1957) confirmed the formation of the secondary vortices. In an experimental study, Gerrard (1978) has called the secondary vortices as *finger of dye*. Wu *et al.* (1994) have reported an experimental study using particle image velocimetry (PIV) and investigated the near wake structures quantitatively through velocity and transverse vorticity (ω_y) distribution over a range of Reynolds numbers between 50 and 180.

Williamson (1988a) has shown the existence of a discontinuity in the Strouhal-Reynolds number relationship for the laminar vortex shedding from a circular cylinder. The underlying physical mechanism was found to be caused by a change in the mode of oblique shedding. But with parallel shedding (with the manipulation of end conditions) the resulting Strouhal-Reynolds number curve was seen to be completely continuous. This data agreed well with the oblique-shedding data when transformed by $S_0 = S_\theta / \cos\theta$ (where S_θ is the Strouhal number corresponding with the oblique-shedding angle θ). It was proved that this relationship also agreed well with the data from a completely different experimental facility. It was thus concluded that the Strouhal-Reynolds number curve was universal.

König *et al.* (1992) have reported based on flow-visualization that end effects give rise to cells of different frequencies appearing simultaneously across the span of a circular cylinder in the laminar Reynolds number range of 40 - 160. The smoke-wire technique was used to obtain a visual image of the wake in the end region of the cylinder. Their findings reveal that each cell is associated with a different angle between the vortex axis and the cylinder. They have confirmed that the discontinuities in the Reynolds-Strouhal number relationship are due to the movement of the cell boundaries across the span of the cylinder as a function of Reynolds number.

Mittal and Balachandar (1995b) have performed a direct numerical simulation past a circular cylinder. Their observations reveal that the streamwise structures are formed

due to the stretching of core vorticity along with the stretching of small scale streamwise vorticity already present outside the core. The observed hairpin vortex plays a central role in transferring vorticity out of the core. The authors remark that the hairpin structures are associated with a spanwise subharmonic mode and thus exhibit a period-doubling mechanism.

Zhang *et al.* (1995) have reported from experiments as well as numerical calculations that the spanwise vortices evolve naturally even without any external source. These authors have also shown the formation of three-dimensional shedding modes. They have observed four physically different instabilities. Out of these, one is a vortex adhesion mode and the other three are near-wake instabilities, associated with three different spanwise wavelengths of approximately 1, 2 and 4 diameters.

The wake of a circular cylinder has been investigated by Brede *et al.* (1996) for Reynolds numbers between 160 and 500 by means of particle image velocimetry. They have measured for the first time, the cross-stream velocity fields for two classes of secondary vortices (Mode-A and Mode-B). Their results show that the circulation associated with the Mode-A secondary vortices in this plane is approximately twice the circulation of the Mode-B secondary vortices. The spanwise wavelength of the secondary vortices is four to five cylinder diameters for Mode-A and one diameter for the Mode-B. Mode-A makes an appearance under certain conditions in the interval of $160 < Re < 240$ and Mode-B at Reynolds numbers above 240. Modes-A and -B could be identified as topologically different vortex structures in this work.

It should be remarked that the wake of the square cylinder has not been studied as closely as the circular cylinder. Predominant research on square cylinder has focussed on engineering quantities such as forces. The present work aims at understanding the wake of a square cylinder over a wide range of Reynolds numbers, with a view towards establishing a connection with the circular cylinder geometry.

2.1.4 Flow past other bluff body geometries

The flow past bodies other than the circular and square cylinder have also been the subject of interest to many researchers. Kiya and Matsumura (1988) have performed experiments on flow past a flat plate at normal incidence. They have described the characteristics of

the random incoherent fluctuations in the near-wake. They have found that the shear stress associated with the incoherent fluctuations has contributions mainly from those components whose frequencies are around half of the vortex shedding frequency. Tafti and Vanka (1991) have performed a two-dimensional computational study of flow over a blunt plate placed along the flow direction. The Reynolds numbers considered are 150, 250, 300 and 1000. Their study reveals that the first three Reynolds numbers lead to a steady wake and their computed reattachment lengths match well with experimental data. For a Reynolds number of 1000, the flow field is observed to be unsteady with the formation of spanwise vortices in the separated shear layer. These vortices were found to coalesce to form larger vortices which were then shed periodically beyond the reattachment length. The authors were able to capture the dynamics of vortex shedding even with a two-dimensional model though the flow can be expected to be three-dimensional at this high Reynolds number. Time dependent features such as vortex shedding frequencies and vortex convection velocities were seen to be in good agreement with the experiments. The most interesting phenomenon presented in this study is the generation of positive surface velocities within the separation bubble at a Reynolds number of 1000. This is attributed to the unsteady entrainment of the irrotational fluid by the vortices in the separated shear layer.

Mittal and Balachandar (1995a) have carried out a two- and three-dimensional computational study of flow past bluff objects, circular and elliptic in cross-section. Fourier Chebychev spectral collocation methodology was used in this work. The Reynolds number chosen was 525 for both geometries. When the flow is physically three-dimensional, the two-dimensional simulation was seen to give inaccurate aerodynamic behaviour. The three-dimensional model gave results very close to the experiments. Higher in-plane Reynolds stresses was the main cause for over-prediction of drag in the two-dimensional simulation. The recirculation length was seen to be smaller in two-dimensions compared to three-dimensions and correspondingly the effect of Reynolds stresses on the surface pressure was higher in two-dimensions. Large secondary vortices were observed in the mean flow pattern of the two-dimensional simulation whereas the secondary vortices formed in three-dimensions were smaller in size. The drop in peak to valley level of the lift coefficient was found to be primarily due to the excursion of Kármán vortices about their mean position in the wake. It was found that these vortices were seen to come closer to the cylinder surface and thereby inducing a larger pressure fluctuations on the surface and this resulted in a larger amplitude of lift fluctuations.

Najjar and Vanka (1995) have performed a two-dimensional numerical study of flow past a normal flat plate over a Reynolds numbers range of 80 - 1000. Higher order spatial (fifth order upwind bias for convective terms and fourth order for diffusive terms) and temporal (second order Adams-Bashforth) discretization were used. At lower Reynolds numbers (~ 100), the Kármán vortices were seen to travel parallel to the centreline and the drag fluctuated sinusoidally. However, at Reynolds numbers 500 and 1000, complex interactions were seen in the far-wake and two distinct interaction periods could be identified. In one period the vortices travelled in the usual manner but in the second period the vortices paired and crossed over the centerline. These interactions were confirmed via the instantaneous snapshots of the flow field and the low frequency modulation of the velocity time trace.

Heist and Gouldin (1997) have experimentally studied turbulent flow past a triangular cylinder mounted on a wall at a Reynolds number of 2.8×10^4 . The authors have used LDV in a gravity driven water tunnel in their experiments. The importance of the pressure transport term at the high speed edge of the shear layer was proved through energy balance. The relationships and details of energy balance with the shapes of spectra have been established from the experiments.

Majumdar and Amon (1997) have carried out a direct numerical simulation for a transitional Reynolds number of 400 in a communicating channel geometry. Their results show that an oscillatory momentum transport mechanism is established, which in turn can be related to various terms of the kinetic energy equation, the oscillatory shear stress and the transitional eddy viscosity.

2.1.5 Study of transition and chaos

Fluid flow past a square cylinder has been the subject of fundamental research because of the intricate mechanisms in the wake that result in a variety of unexpected phenomena. Examples are wake unsteadiness even at low Reynolds numbers, detachment of the free shear layer and the consequent shedding of vortices, generation of harmonics, three-dimensionality in nominally two-dimensional geometries, onset of chaos and the transition to turbulence. This by itself is a sequence of transitions, each being identified with a critical Reynolds number and an associated flow topology. The theoretical determination of the critical Reynolds numbers via a numerical model when the wake approaches a chaotic

state forms the topic of the present discussion.

At a low Reynolds number (10 - 45), a steady separated pattern is observed. The flow field becomes periodic as the Reynolds number crosses a critical value with a Hopf bifurcation. The transition to chaotic state through different routes is brought about if the control parameter, the Reynolds number, in the present investigation is increased in steps. The routes and the respective critical Reynolds number may differ due to several factors such as inflow conditions, end conditions and confinement effects.

A nonlinear dynamical system can go to a chaotic state through three distinct routes. These involve period doubling of the frequencies (Feigenbaum, 1980), the Ruelle-Takens-Newhouse route through quasi-periodicity (Ruelle and Takens, 1971) and intermittency (Manneville and Pomeau, 1980). These routes have been identified in the context of lumped systems. Their appearance in continuous systems and the generalization to spatially distributed chaotic fields have been investigated by various researchers. Vittori and Blondeaux (1993) have reported a quasi-periodic route to chaos in their numerical study of two-dimensional oscillatory flow around a circular cylinder. They have found that the system gets phase-locked before it becomes chaotic.

In the quasi-periodic route, the dynamical system initially at steady state becomes unstable as the control parameter crosses a particular threshold limit. The nonlinearity of the system generally increases as a result of an increase in control parameter. For example, an increase in the Reynolds number diminishes diffusion and dissipation mechanisms, resulting in greater prominence of the nonlinear acceleration terms. As a consequence of instability, the dynamical behaviour approaches a limit cycle caused by a Hopf bifurcation. With further increase in the control parameter, additional Hopf bifurcations take place and the system moves to the state of double (and occasionally triple) frequencies. Over a range of the control parameter, the three frequencies co-exist in a ratio, dependent on the control parameter. Over a second range of this parameter, the frequency ratio is a constant; this phenomenon is referred as frequency-locking. When the control parameter is further raised, the system enters a chaotic state. Guzmán and Amon (1996) have shown a quasi-periodic and frequency-locking route to chaos in two- as well as three-dimensional converging-diverging channels. They have reported that a two-dimensional simulation of a self sustained oscillatory flow experiences three successive supercritical Hopf bifurcations as the Reynolds number is increased. The first Hopf bifurcation takes place at $130 < Re_c < 135$. The flow becomes chaotic with the increase in the Reynolds

number from 150 to 500 through T^2 torus \rightarrow phase-locking $\rightarrow T^3$ torus scenario. However, in a three-dimensional calculation the flow was seen to reach a quasi-periodic self-sustained oscillatory state at a Reynolds number of 226 following two superficial Hopf bifurcations.

Gollub and Benson (1980) have demonstrated experimentally the different routes to chaos in Rayleigh-Benard (R-B) convective flows by varying the aspect ratio, Prandtl number and the mean flow corresponding to the number of rolls. They have shown that the convective field becomes chaotic via quasi-periodicity and the phase-locking route. They also found broad-spectrum flows preceded in Rayleigh number by quasi-periodicity and phase-locking, by quasi-periodic two- and three-frequency flows, by a succession of subharmonic period-doubling bifurcations, and by intermittent noise. Mukutmoni and Yang (1993) have numerically determined the route to chaos for R-B convection in a small aspect ratio enclosure to be of the period-doubling type. Their results showed dependence of the transitions on boundary conditions. The above result was obtained with symmetry conditions without which the route seemed to be of the quasi-periodic form. The authors also found that the period doubling route to chaos can be realized only if the oscillating velocity and temperature field preserve the four-fold symmetry of the mean-flow on the horizontal plane.

Karniadakis and Triantafyllou (1992) have reported dynamics of a three-dimensional flow and transition to turbulence in the wake of a circular cylinder. They have found that the system undergoes a rapid transition to a chaotic three-dimensional state at a Reynolds number of 500 starting from a laminar two-dimensional state at a Reynolds number of 200. The corresponding route followed by the system to the chaotic state was seen to be of the period-doubling type. In the work of Pulliam and Vastano (1993), the transition to chaos of an open unforced two-dimensional flow past an airfoil has been documented. The salient findings of their study are that the system undergoes a period-doubling bifurcation to chaos as the Reynolds number is increased from 800 to 1600. Windows of periodic behaviour are seen to exist in the chaotic regime past a Reynolds number of 1600. The chaotic attractor behaviour has been characterized by estimating the Lyapunov exponent and the fractal dimension. The authors have also demonstrated that the observed chaos was not numerically generated. The effects of mesh resolution, artificial dissipation and the order of temporal accuracy of the numerical method have been systematically studied. The authors thus have explained the physical mechanism underlying the route to chaos.

2.1.6 Important experimental studies

Experiments are useful in validating numerical calculations on one hand, and explaining unexpected observations on the other. Thus, they complement to computational research, particularly in the context of complex flow configurations. Extensive experiments have been reported for the study of wake of a circular cylinder. Selected experiments are also available for a square cylinder.

Okajima (1982) has conducted an experimental study of flow past a rectangular cylinder in a Reynolds number range of $70 - 2 \times 10^4$ and the width-to-height ratio of 2 and 3. With a change in the width-to-height ratio, the flow pattern changed abruptly with a discontinuity in Strouhal number. Experiments were performed in a water as well as in a wind tunnel using hotfilm and hotwire anemometry respectively. The experimental results compared well with his numerical simulation. The Strouhal number dependence for both square and rectangular cylinders on the Reynolds number was clearly brought out.

In the wake of a bluff-body flow, the time-varying component $\phi(x_i, t)$ (for example, velocity and pressure) may be written as the combination of global mean component $\bar{\phi}(x_i)$, a periodic component $\tilde{\phi}(x_i, t)$ and a random component $\phi''(x_i, t)$ (Hussain, 1983). The above statement can be expressed in the form

$$\phi(x_i, t) = \bar{\phi}(x_i) + \tilde{\phi}(x_i, t) + \phi''(x_i, t) = \bar{\phi}(x_i) + \phi'(x_i, t) = \langle \phi \rangle(x_i, t) + \phi''(x_i, t) \quad (2.1)$$

where $\phi''(x_i, t)$ refers to turbulent flow alone whereas $\bar{\phi}(x_i)$ and $\tilde{\phi}(x_i, t)$ are common for both laminar and turbulent flows. Due to this random fluctuations, the instantaneous flow can be studied as the phase-averaged field. This filters out the random fluctuations and the flow field looks coherent over a larger spatial domain. The phase-averaged fields can be generated with the help of a reference signal which is less noisy in the presence of random components. Generally, the reference signals are pressure on the cylinder surface or the component of velocity at a location that records a comparatively clean signal. The measurement of phase-averaged flow fields have been reported by various authors.

In the experimental investigation of transport process, Cantwell and Coles (1983) have studied the near-wake of a circular cylinder at a Reynolds number of 140000. A flying-hotwire technique was used to measure phase-averaged quantities in a wind tunnel. The phase-averaged (namely periodic) as well as the random components have been shown

to have comparable amplitudes. A considerable emphasis has been placed on the topology of the unsteady mean flow. This emerges as a pattern of centres and saddles in a frame of reference moving with the eddies. The kinematics of the vortex formation process has been described through the critical point theory. The important conclusion of the work is that the turbulence production is concentrated near the saddles. Entrainment of the fluid into the wake is also found to be closely associated with the formation and location of the saddles.

Durão *et al.* (1988) have reported laser-Doppler measurements of the velocity characteristics for turbulent flow around a square cylinder mounted in a water channel for a Reynolds number of 14000. The study involved spectral analysis and digital filtering of the LDV data obtained behind the cylinder. The authors could separate and quantify the turbulent and periodic, non-turbulent motions of the wake flow. They showed that near the zone of highest velocity oscillations, the energy associated with the turbulent fluctuations is about 40% of the total energy.

Zhou and Antonia (1993) carried out experimental study of turbulent flow in a wind-tunnel at a Reynolds number of 5600. Turbulent vortices in the wake of a circular cylinder have been detected by a method which includes vorticity and circulation criteria. They have found out that the vorticity and circumferential velocity distributions which correspond to these detections are exponential in shape, similar to those for an Oseen vortex. The conditionally-averaged streamwise velocity distribution through the vortex centre has a maximum at the centre, implying a vortex convection velocity greater than the local mean velocity. They have also reported that the measured mean velocity and the Reynolds stresses match well with that of the Oseen vortex model. Results have also been reported for the streamwise variations of the vorticity concentration, circulation and the size of the vortices.

In the experiments of Lyn and Rodi (1994), the turbulent shear layer and the associated recirculation region (on the sidewall) due to the flow separation from forward corner of a square cylinder have been studied with one-component Laser-Doppler velocimetry in a water-tunnel at a Reynolds number of 21400. The authors have studied the relationship in phase and amplitude between intensities and gradients of the phase-averaged velocity. They have also investigated the self-similarity of the phase-averaged profiles in the shear layer as well as the streamwise growth of the shear layer. Though phase-averaged velocity profiles collapse well in similarity co-ordinates they found that normalized turbu-

lence intensities exhibit systematic deviations. The shear layer growth was seen to depart markedly from a linear trend of the unforced plane mixing layer. The possible cause for some of these deviations was associated with the effect of recirculation.

Lyn *et al.* (1995) have reported an LDV study of turbulent flow past a square cylinder with emphasis on the ensemble-averaged characteristics of the flow behaviour. The Reynolds number considered in their study was 21400. The experiments were carried out in a closed and constant head water tunnel. Data analysis was carried out using the triple-decomposition approach of the variables (Equation 2.1). Their results showed a relationship to exist between the flow topology and the turbulence distribution. Vorticity saddles and streamlines saddles could be clearly distinguished. A distinction could be seen between the flow in the base region and the near-wake. Differences in the length and velocity scales, and celerity of the vortices of flows between a circular and a square cylinder have also been compared. Lyn *et al.* (1995) have discussed the topology of turbulent flow with respect to peak vorticity (ω_p), streamline centre (for closed streamlines), saddles (intersection of streamlines) and the turbulent kinetic energy.

Ensemble-averaged characteristics of the turbulent near-wake around two identical square cylinders placed side-by-side have been studied by Kolar *et al.* (1997) in a water-tunnel at a Reynolds number of 23100. They have used the two-component laser-Doppler velocimetry for their measurements. They have reported a case with a gap/diameter ratio of 2 for which the resulting individual vortex streets are coupled so as to give a symmetric flow about the line midway between the two cylinders. The results of the two-cylinder and the one-cylinder data have been compared. The differences between the flow structures on the side towards the centreline (inner structure) and the structures on the free-stream side (outer structure) have been studied. The circulation associated with the inner structure was seen to decrease drastically with the downstream direction. This is in contrast with the outer structure which shows a decay rate similar to the single cylinder. The authors have highlighted the vortex structure motion and the relevant length and time scales. The differences in momentum and vorticity transport across the flow centreline have been demonstrated. The invariant of the local velocity gradient have been related to the critical points (centres and saddles) and turbulence statistics.

2.2 Sensitivity of the Wake to External Factors

The majority of research reported above employs uniform upstream conditions. The sensitivity of the observed phenomena in the wake to upstream non-uniformities is definitely a pertinent issue. Nonuniformities in the approach flow are common to both in engineering application as well as in nature. The shear generated due the nonuniform velocity profile may be in a direction axial to the bluff object, or may be transverse to it. Transverse shear is seen in flow past a bridge pier in a curved river. Uniform shear is a regular upstream condition in flow past horizontal pipelines just above the ground level due to the formation of boundary layers. A second type of nonuniformity can arise due to turbulent fluctuations. The inlet turbulent fluctuations, having different intensity and length scales can influence the aerodynamic characteristics such as vortex shedding frequency, drag and lift coefficient and their rms values.

Lee (1975) has carried out the measurements in a wind tunnel for a square cylinder at a Reynolds number of 1.76×10^5 at different angles of incidence. Surface pressures were measured with the help of pressure taps mounted on the cylinder surface. The turbulence intensity and the length scales were varied between 0.5-12.5% and 0.063-0.155 (as a fraction of the cylinder size) respectively along with the incidence angle between $0-45^\circ$. The results show the following: (i) With the increase in intensity of turbulence in the flow normal to the prism the drag coefficient decreases (ii) Increase in turbulent intensity cause the vortex formation region to move downstream (iii) The pressure energy is reduced by a factor of 5 when turbulence intensity of the incident flow is increased from 0.5 to 12.5 percent (iv) The drag coefficient decreases initially with the incident angle upto a value of 15° and then starts to increase and (v) The Strouhal number is shown to increase to a maximum at the angle at which the mean drag is minimum. The experiments of Huot *et al.* (1986) shows the effect of turbulence intensity and length scales on the mean and the fluctuating pressure field. Measurements of cross-spectra at different points on the same cross-section, have shown how the fluctuating surface pressure field downwind of separation has a narrowband component at the Strouhal frequency that is sensitive to the turbulence. They have also revealed how a broadband component is generated by the recirculating flow that is insensitive to the upwind turbulence.

The frequency of vortex shedding from a circular cylinder in a uniform shear flow and the flow patterns around it have been experimentally investigated by Kiya *et al.*

(1980). The Reynolds number based on the cylinder diameter and the approach velocity at its center is between 35 and 1500. The shear parameter is defined as the transverse velocity gradient and is varied between 0 and 0.25. The critical Reynolds number beyond which vortex shedding occurs has been found to be higher and increases linearly with the increase in shear parameter (>0.06). Vortex shedding is seen to disappear for sufficiently large shear parameters in the Reynolds-number range 43 - 220. However, the Strouhal number increases with the increase in the shear parameter beyond 0.1 for a Reynolds number range of 100 - 1000. Kwon *et al.* (1992) have carried out extensive laboratory experiments in a water tunnel for a uniform-shear flow approaching a circular cylinder. Their study was aimed at deducing the dependence of Strouhal number on Reynolds number for a wide range of shear parameters. They have reported their results for a range of Reynolds number of 600 - 1600 using an flow visualization in conjunction with image processing technique. Their findings show that the drag coefficient decreases with increasing Reynolds number and the shear parameter. Ayukawa *et al.* (1993) have demonstrated numerically the effect of shear rate on the flow around a square cylinder in a uniform shear flow at a Reynolds number of 4000. The flow has been modeled to be the superposition of potential flow (a system of vortex filaments representing approximately the square cylinder) and the shear layer originating from separation at the corners of the cylinder. Their findings reveal that the effect of shear rate on the Strouhal number and the force acting on the cylinder are small. However, the flow pattern is affected by the shear rate. At high shear rate, von Kármán vortex street is seen to break down with the flow pattern far downstream tending to be similar at any instant.

2.3 A Review on Turbulence Modeling

Newtonian fluid flow is now understood to be fully represented by the Navier-Stokes equations. Numerical solution of Navier-Stokes equations is thus a successful modeling tool for laminar and turbulent flows. If turbulent flow is computed using the same grid and time step as in laminar flow, the solutions will not reveal the existence of the small scale eddies. Hence, the transport of turbulent kinetic energy from the larger to the smaller eddies will not be addressed. Nevertheless, the Navier-Stokes equations can be solved on a fine enough grid with an exceptionally accurate discretization method so that both fine scale and large scale aspects of turbulence can be calculated. This approach

is termed as the *Direct Numerical Simulation* (DNS) of turbulence (Kim *et al.*, 1987; Rai and Moin, 1991). DNS has been a very successful tool over the past ten years for the study of transitional and turbulent flow physics. It has however a severe limitation. In order to resolve all scales of motion, one requires a very large number of nodes. A typical DNS may require nearly 40×10^6 grid points for a Reynolds number of 2500 and the computational time is of the order of 700 hours on a 150 Mflops machine. The DNS approach to turbulence modeling is a subject matter of research.

2.3.1 Various approaches of modeling turbulent flows

Practical computations of turbulent flows adopt strategies different from DNS. The turbulence motion is random in nature and so it is conjectured that it can be described by statistical tools. For analysis, it may be convenient to decompose the instantaneous velocity of the fluid into a time-averaged and a fluctuating component and look for the solutions of time-averaged velocities¹. The effect of the fluctuating components on the mean motion can be modeled using empirical relations obtained from experiments. The Navier-Stokes equations together with the equation of mass conservation form a closed system of equations. However, if the equations are averaged to focus on the mean velocity component and pressure, the system possesses more unknowns than the number of equations. The splitting of instantaneous velocity into a time-averaged and a fluctuating part is called *Reynolds decomposition*. The system of equations obtained on averaging (*Reynolds-averaged Navier-Stokes*) cannot be closed unless additional relations are supplied from experiments to correlate the fluctuating components with the mean motion. This difficulty is termed as the *closure problem*.

The averaging of the governing equations can be done in various ways (Hinze, 1987). Time averaging is suitable when the mean flow is stationary or slowly changing with time. Phase averaging is basically a statistical concept which is more meaningful for unsteady mean flows. A third alternative is space averaging which is used in a technique known as the *Large Eddy Simulation* (LES). LES is an emerging area of turbulence research (Schumann, 1975; Moin and Kim, 1982; Tafti and Vanka, 1991; Piomelli, 1993; Ghosal *et al.*, 1995). In LES, large scale motions are calculated from DNS and subgrid scale motions

¹ u_i, u_j used in algebraic expressions in this subsection are dimensional velocities.

are modeled. The subgrid scale contribution contains all length scales smaller than the grid interval.

The time-averaged equations of motion are similar to the Navier-Stokes equations except that they have additional terms containing the contribution of the fluctuating components of velocities to the mean flow dynamics. These terms are identical for the time-averaged and the phase-averaged equations. The contributions of the fluctuating components have an effect similar to viscous stresses and are called Reynolds stresses. Space averaging produces a few additional terms besides the Reynolds stress components. To address the closure problem, Reynolds stresses have to be expressed in a physically meaningful manner in terms of the mean velocity field. Such a relationship is called a *turbulence modeling*.

Most of the widely used turbulence models are based upon the eddy viscosity concept of Boussinesq (Rodi and Spalding, 1970; Launder and Spalding, 1974; Kato and Launder, 1993; Yakhot and Orszag, 1986 and Yakhot *et al.*, 1992). The influence of turbulence on the mean flow is that it absorbs kinetic energy from the mean flow and increases the rate of transport of mass, momentum and energy normal to the streamlines of the flow. The second effect is similar to that of viscosity in laminar flows. The Boussinesq approximation utilizes this analogy and assumes that Reynolds stresses can be represented by an *eddy-viscosity* and the relevant velocity gradients. This concept guides in expressing the turbulent shear stress as

$$-\overline{\rho u'_i u'_j} = \mu_t \left(\frac{\partial \bar{u}_i}{\partial x_j} + \frac{\partial \bar{u}_j}{\partial x_i} \right) - \frac{2}{3} \rho k \delta_{i,j} \quad (2.2)$$

where μ_t is eddy viscosity, k is the turbulent kinetic energy and $\delta_{i,j}$ is the Kronecker delta function. All eddy-viscosity models assume the correctness of this relationship and differ only in their method for estimating μ_t . The eddy viscosity models are indeed useful for engineering applications, although they have been criticized for assuming the turbulent eddy action to be isotropic.

Two-dimensional calculations are not appropriate for bluff body wakes at high Reynolds numbers since the flow is three-dimensional beyond a Reynolds number of 180 (Williamson, 1988b). The flow is chaotic and possibly turbulent at a Reynolds number of 400. Flows above a Reynolds number of 400 require to be computed by solving the three-dimensional unsteady Navier-Stokes equations using very fine grids. To economize the computation, engineering applications for higher Reynolds numbers are being presently

computed in two-dimensions using various eddy viscosity models of turbulence. In such simulations, energetic interactions with respect to the third component of velocity are effectively set to zero. Hence, the occurrence of shedding and the prediction of the nuances of shedding depend significantly on the turbulence model used and the details of the numerical technique.

Okajima *et al.* (1992) have carried out a detailed study for rectangular cylinders with round and square leading edges while the trailing edge is square in all the cases. The authors have simulated flows over a range of Reynolds numbers ($1 \times 10^3 - 7 \times 10^3$) using the standard $k-\epsilon$ model. Though some aspects of bluff body aerodynamics were captured, they found significant differences between the experiments and the numerical predictions. Franke and Rodi (1993) have shown that the occurrence of shedding past a square cylinder and its characteristics depend on the turbulence model used. They have also reported that the physically meaningful predictions are modulated by the details of the numerical technique itself. Hadid *et al.* (1992) have reported turbulent simulation past a square cylinder using two different approaches, namely the standard $k-\epsilon$ model and an anisotropic $k-\epsilon$ model. The anisotropic $k-\epsilon$ model was found to resolve the anisotropy of the Reynolds stresses and predict the mean energy distribution closer to the experiments vis-a-vis the standard $k-\epsilon$ model. Rodi (1993) has reviewed calculations performed on vortex shedding past long cylinders of various shapes at high Reynolds numbers using different $k-\epsilon$ models, the Reynolds Stress Equations (RSE) model and the Large Eddy Simulation (LES). The RSE model and the LES simulation have emerged superior in his reviews. Bosch and Rodi (1996) have reported experimental as well as numerical results for the flow past a square cylinder at a Reynolds number of 22000 placed at various distances from the adjacent wall. Their experimental observation reveals that vortex shedding and the consequent unsteadiness in the flow field are suppressed when the cylinder is placed very close to the wall. This has been successfully simulated by two different turbulence models, though the predictive procedure handles a two-dimensional flow field. Having analyzed a wide range of models and numerical techniques, Rodi *et al.* (1997) conclude that the square cylinder flow is difficult to simulate because the inflow is laminar and transition takes place in the separated shear layer on the sides of the cylinder. The simulation is sensitive to small changes in various factors related to the modeling strategy and the computational algorithm. This conclusion is quite consistent with the properties of transitional flows which are generally known to be sensitive to small perturbations.

2.4 Summary

Flow past a bluff body has been studied extensively in the past but continues to be a topic of serious research. However, many important aspects of this flow have remained unexplored. The main difference between the flow past a circular and a square cylinder is that the former does not have any fixed points of separation as in the case of the latter which have the points of separation at the leading edges. Many investigations on the circular cylinder are available in open literature. The square cylinder albeit being an important topic of research, has not been studied with as much rigour.

The mechanism of the transition to unsteady from a steady flow for a square cylinder has been well discussed in the literature. The corresponding range of critical Reynolds numbers has also been documented. The effect of Reynolds number on the aerodynamic forces on the square cylinder have been numerically established. Similarly the dependence of Strouhal number on Reynolds number has also been discussed in the the literature. The flow behaviour at the high Reynolds number turbulent flow has been studied with respect to the triple decomposition of the flow variables. The effect of inlet turbulence on the flow past a square cylinder, especially on the aerodynamic forces have also been reported in the literature. The effect of transverse shear on the the aerodynamic forces on the square cylinder has been discussed.

The transitional behaviour and the phenomenon from a two-dimensional to three-dimensional flow have been studied for the circular cylinder. However, there is no study related to the transitional behaviours (spatial as well temporal) for the flow past a square cylinder. The transitional behaviour has not been well understood due to the susceptibility of such flows to various factors affecting the transition phenomenon. As a result, there is very little understanding of this important aspect of flow behaviour. Similarly, the transition and route to chaos are not known for the flow past a square cylinder. The effect of inlet shear on the wake structure of the square cylinder has also not been studied in detail. The role of the random components in a turbulent flow and its relationship with the large scale structures are not well understood. The generation mechanism of the random components which are otherwise believed to be universal in nature seem to depend on the large scale structures. Lastly, the reliability of the two-dimensional computations for the three-dimensional flows has not been critically evaluated for the flow past bluff objects. The discrepancy of the two paradigms has been demonstrated with respect

to the aerodynamic forces but the reasons of the differences in wake structure and the corresponding pressure field have not been studied so far.

The advent of the high speed computers have made it easier to tackle the complex problem numerically as well as experimentally. Experimentally, the data acquisition system permits handling a large volume of data and getting detailed information has not remained difficult. Similarly, direct numerical simulation is also likely to be possible for complex problems due to the rapid evolution of the powerful computers. The physics of a particular problem and the new findings can be strengthened by conducting both numerical and experimental study. Once the numerical calculation is validated, one can achieve a greater understanding about the unknown aspects of the problem.

The present study aims at addressing *heretofore* unknown aspects of the flow past a square cylinder. Both numerical and experimental approaches have been adopted to accomplish the objectives of the investigation. The experimental study is based on hotwire anemometry whereas the numerical study involves a finite difference based simulation tool. The Reynolds number considered in the present study ranges from a very low value of 40 to a high value of 21400.

Chapter 3

Description of Numerical Techniques

Fluid flow can be modeled using the principle of conservation of mass and Newton's second law of motion. These laws can be developed in the form of the partial differential equations along with the suitable boundary conditions. It is well known that these partial differential equations are nonlinear and do not admit analytical solutions even for problems of modest complexity. A numerical approach is a practical alternative for analyzing flow problems.

A proper description of the flow field including accuracy is feasible when the solution can resolve all the length and temporal scales associated with it. The solution of the Navier-Stokes equations is comparatively easier for low Reynolds number laminar flows due to its larger length and time scales. With increasing Reynolds numbers, the spatial and temporal scales become smaller and obtaining a meaningful solution becomes more difficult.

Extensive investigations have been carried out in the recent decades for developing numerical schemes to solve the incompressible Navier-Stokes equations in regular and multi-dimensional complex geometries. The main difficulty with incompressible flow simulation is the absence of an obvious equation for pressure. Specifically, the nature of coupling of the pressure and the velocity variables is implicit in nature. When the flow is treated as incompressible, pressure does not have the usual thermodynamical meaning. Here it has a relative value which adjusts itself instantaneously in such a way that the condition of zero divergence is satisfied at all computational cells. This behavior is related to the fact that the speed of sound becomes infinite in an incompressible fluid. As

a consequence, the pressure field cannot be calculated by an explicit time-advancement procedure. Instead it requires at least a partially implicit determination which is able to take into account the coupling between the pressure and the velocity field, subject to the boundary conditions. This aspect is the most distinctive feature of the primitive variable formulation of the incompressible Navier-Stokes equations.

The difficulties associated with the determination of pressure has led to the methods that eliminate pressure from the governing equations. In two dimensions, the elimination of pressure by cross differentiation of the two momentum equations leads to the vorticity transport equation. This equation when combined with the definition of stream function forms the basis of the well known stream function-vorticity method. However, this approach becomes less attractive when a three-dimensional flow is computed because of the absence of a single scalar stream function in three-dimensions. A primitive variable formulation involving velocity and pressure is often preferred for solving the Navier-Stokes equations since it is directly extendable to three-dimensional geometries. Such a formulation also allows boundary conditions to be applied in a straightforward manner.

3.1 Review of Available Numerical Methods

Finite difference, finite volume, finite element and spectral methods are some of the popular numerical methods. Both finite volume and finite element methods belong to the class of weighted residual methods (Fletcher, 1988). However, in implementation, finite volume discretizations closely resembles finite difference methods.

The finite difference method converts the differential equation into an algebraic (difference) equation centered around a node of a grid. Thus it provides a pointwise approximation to the partial differential equation. Derivatives in the governing partial differential equations are replaced by equivalent finite difference expressions which involve the values of the dependent variable at discrete grid points of the domain. The finite difference method is easy to implement. The major advantage of the finite difference method is that higher order spatial discretization of low order derivatives is handled easily and therefore can be used for complex flows in a regular geometry with less computational effort.

Traditionally, finite volume methods have demanded the use of a body fitted mesh. These meshes are formed from a cuboid of elements which can be stretched to fit any surface provided the topological structure of the mesh is prescribed. Consequently, with the original finite volume schemes certain complex geometries can be meshed easily while others require coordinate transformation.

The finite element method starts with a piecewise approximation to the dependent variables. Various methods of this class exist, all requiring an integral representation of the partial differential equation to be constructed. The classical finite element method for structural mechanics are based on variational principles. But for many engineering problems, particularly in fluid flow, more general approaches, such as the method of weighted residuals are used. The primary advantage of this method is its ability to handle a complex geometry. The limitation of the finite element method is that it cannot handle the convective terms in a systematic manner at higher Reynolds numbers.

The spectral method can be viewed as a high order weighted residual method (Canuto *et al.*, 1986 and Gottlieb and Orszag, 1977). Unlike the finite element method, the trial functions of the spectral method are globally specified over the full physical domain. Such global functions can be constructed only for a regular geometry and when the solution is known to be smooth. The basic idea of a spectral method is to express the dependent variables in the form of a truncated expansion of orthogonal eigen functions of the Sturm-Liouville problem. The coefficients of this expansion are determined using either a Galerkin or a collocation formulation. The spectral method is known for achieving high accuracy. For an equivalent number of grid points, spectral methods provide excellent accuracy compared to either finite volume or finite element methods. However, the spectral method has its own limitations. The main weakness of the spectral method compared to the finite difference and the finite element approaches is its inflexibility in adapting to irregular computational domains. For the method to be applicable, the solution of the physical problem needs to be smooth and the physical domain, regular.

3.1.1 Resolution of pressure-velocity coupling

Research effort has been directed at two- as well as three-dimensional problems that can be computed following a primitive variable approach without encountering non-physical wiggles in pressure distribution. One of the suggestions has been to employ a different

grid for each of the dependent variables. Harlow and Welch (1965) have used a staggered grid for the dependent variables in their well known **MAC** (Marker and Cell) method. The MAC method is one of the earliest and is widely used for solving the incompressible Navier-Stokes equations. Here, the solution for velocities is obtained in two steps. In the first step, the provisional values of velocity components are computed explicitly using advection, diffusion and pressure gradients of the earlier time step. This explicitly advanced provisional velocity field may not ensure mass balance at the level of the local grid. In the second step, pressure and velocity components are corrected through the solution of a Poisson equation for pressure in such a way that mass balance is enforced. The equation for pressure correction (denoted by '^') can be obtained by relating the provisional velocities (denoted by '*') and pressures at the previous time step with the corrected ones with the help of the dimensionless momentum and continuity equations as:

$$\delta t \left(\frac{\partial^2 \hat{p}}{\partial x_i^2} \right) = \frac{\partial u_i^*}{\partial x_i} - \frac{\partial u_i}{\partial x_i} \quad (3.1)$$

On discretization and putting $\frac{\partial u_i}{\partial x_i} = 0$, the above equation will take the following form:

$$\begin{aligned} & \left[\frac{u_{i,j,k}^{*n+1} - u_{i-1,j,k}^{*n+1}}{\delta x} + \frac{v_{i,j,k}^{*n+1} - v_{i,j-1,k}^{*n+1}}{\delta y} + \frac{w_{i,j,k}^{*n+1} - w_{i,j,k-1}^{*n+1}}{\delta z} \right] \\ &= \delta t \left[\frac{\hat{p}_{i+1,j,k} - 2\hat{p}_{i,j,k} + \hat{p}_{i-1,j,k}}{(\delta x)^2} + \frac{\hat{p}_{i,j+1,k} - 2\hat{p}_{i,j,k} + \hat{p}_{i,j-1,k}}{(\delta y)^2} \right. \\ & \quad \left. + \frac{\hat{p}_{i,j,k+1} - 2\hat{p}_{i,j,k} + \hat{p}_{i,j,k-1}}{(\delta z)^2} \right] \quad (3.2) \end{aligned}$$

If the pressure corrections in the neighbouring cells are neglected, one can get an algebraic equation for pressure. This is discussed in Section 3.4. A related technique developed by Chorin (1967) involves a simultaneous iteration on pressure and velocity components. Vieceilli (1971) has shown that the two methods as applied to the MAC method are equivalent. The original version of the MAC method has been modified by Harlow and Amsden (1970) and Nichols and Hirt (1971). Hirt and Cook (1972) have applied this method for free surface flows. The MAC method has been used by many researchers to determine flows in complex geometry. For example, Braza *et al.* (1986, 1990) have computed the unsteady wake behind a circular cylinder. Mukhopadhyay *et al.* (1993) have obtained the periodic wake behind a rectangular obstacle. In fact, the MAC method has been successfully used even to simulate highly unsteady turbulent flows (Robichaux *et al.*, 1992). It has been experienced that the MAC method is efficient in the studies of temporal flow development. It has stability restrictions on the time step which slow

down the calculations when steady state results are desired. However, this method is well suited for the unsteady flows having smaller time scales.

3.1.2 Upwind versus central differencing

A major difficulty in the numerical modeling of flow equations is in discretizing the convective term. A good scheme should possess the following properties: accuracy, stability, boundedness and algorithmic simplicity. These requirements are often in opposition with one another. Stability and boundedness require that the scheme has diffusive smoothing, whereas this leads to loss of accuracy.

It is now well known that the even order central differencing of the convective terms suffers from dispersive errors or spurious oscillations unless very fine grids are used to limit the cell Peclet number below a value of 2. If the cell Peclet number exceeds a value of 2, the transportive property is violated and the solution becomes unstable as a result of nonphysical oscillations. On the other hand odd order upwind differencing causes severe false diffusion. The presence of false diffusion can be shown with the following example: Consider the model Burgers' equation

$$\frac{\partial \zeta}{\partial t} + u \frac{\partial \zeta}{\partial x} = \nu \frac{\partial^2 \zeta}{\partial x^2} \quad (3.3)$$

where ν is a diffusion coefficient. If the convective part of the above equation is discretized with an upwind scheme and the final difference equation is brought back to the PDE with the help of Taylor series expansion one will be astonished to see the equation as

$$\frac{\partial \zeta}{\partial t} + u \frac{\partial \zeta}{\partial x} = \nu \frac{\partial^2 \zeta}{\partial x^2} + \nu_e \frac{\partial^2 \zeta}{\partial x^2} \quad (3.4)$$

Here the artificial viscosity $\nu_e = (1/2)u(\delta x)(1 - u(\delta t)/\delta x)$ is always positive. It is zero if the convective term is discretized using central differencing scheme. But the accuracy of the upwind schemes can be improved with the help of higher order schemes. These can also reduce the level of numerical diffusion significantly and at the same time satisfy the transportive property. In a given grid system having a cell Peclet number less than 2, central differencing automatically satisfies the transportive property yet avoids false diffusion.

3.1.3 Higher order difference schemes

Many researchers have conducted scientific computations using the finite difference method with higher order spatial as well as temporal discretization. Kim and Moin (1985) have developed a fractional step method in which the governing equations are solved by time-splitting. This method decomposes the operators of the governing equations using physical as well as mathematical arguments. For example, in Navier-Stokes equations, one can interpret the role of pressure in the momentum equations as an operator which projects an arbitrary vector field into a divergence-free vector field. The above statement can be put in the mathematical form as follows:

$$\begin{aligned} \text{Step 1 : } u_i^* &= F(u_i^n, u_i^*, \text{Re}) & \text{and} \\ \text{Step 2 : } u_i^{n+1} &= E(p^{n+1}) & \text{with } D(u_i^{n+1}) = 0 \end{aligned}$$

where F is a function derived from the Navier-Stokes equations and E and D are gradient and divergence operators respectively. The quantity in the governing PDE crucial for maintaining accuracy is the nonlinear acceleration derivative, $\partial(u_j u_i)/\partial x_j$, called the convective term. Rai and Moin (1991) have used higher order discretization for this term for computing high Reynolds number flows without the help of any model to account for the unresolved scales. In high Reynolds number flows, the function of the small scales is to drain energy from the larger scales. The reverse is also possible in rapidly developing flows. But it has been seen that the wakes, mixing layers and the jets involve very less back-scatter, *i.e.*, energy transfer from small scale to large scale. If this small back-scatter is neglected then most of the turbulent flow can be simulated with the higher order spatial and temporal discretization because of the inherent dissipation involved with the upwind discretization of the convective terms. One great advantage of this method of solution of higher Reynolds number flow is that it demands less computing resources compared to conventional turbulence modeling and has the potential to give good results. Many researchers have chosen this particular strategy to solve higher Reynolds number flow in various geometries. Rai and Moin (1991) have solved channel flow by this approach for a Reynolds number of 7500 and got a good comparison with experiments as well as spectral simulation. In a related work, Najjar and Vanka (1995) have successfully studied the flow past a flat plate at normal incidence in the Reynolds number range of 250 - 1000 using fifth order spatial discretization of the convective terms and second order temporal discretization.

3.2 Incompressible Unsteady Navier-Stokes Equations

The wake of a square cylinder is invariably unsteady. It has been taken to be incompressible for the present study due to the range of Reynolds numbers considered, namely $40 < \text{Re} < 22000$. The governing equations are presented in this section. In all the governing equations, velocities have been nondimensionalized with the average velocity u_{av} at the inflow plane, all lengths with the obstacle width B , and pressure with ρu_{av}^2 .

Governing equations

The equations of continuity and momentum may be expressed in the dimensionless form as

$$\frac{\partial u_i}{\partial x_i} = 0 \quad (3.5)$$

$$\frac{\partial u_i}{\partial t} + \frac{\partial (u_j u_i)}{\partial x_j} = -\frac{\partial p}{\partial x_i} + \frac{1}{\text{Re}} \frac{\partial^2 u_i}{\partial x_j^2} \quad (3.6)$$

Einstein summation notation has been used for the divergence term (Equation 3.5) and the nonlinear derivative (Equation 3.6).

Initial and boundary conditions

The calculations are started with initial conditions for all the variables over the entire physical domain. Different initial conditions were tried in the present work but all of them led to the same asymptotic dynamic flow field. A majority of the initial conditions correspond to either a uniform ($u=\text{constant}$, $v=w=0$) or fully developed ($u=u(y, z)$, $v=w=0$) velocity field. A constant pressure initial condition of unity has been employed in the present work.

The boundary conditions for the present studies are:

- Confining boundaries: The boundary conditions for the confining boundaries are being discussed separately for the two- and three-dimensional cases:

Two-dimensional Computations: Two different boundary conditions have been used;

(i) $u=v=0$; (no-slip condition) (ii) $\frac{\partial u}{\partial y}=v=0$; (free-slip condition).

Three-dimensional Computations: Only free-slip boundary conditions have been used, (for example, the boundary conditions at the transverse confining boundaries ($\pm H/2$) are $\frac{\partial u}{\partial y}=v=\frac{\partial w}{\partial y}=0$ and the boundary conditions at the spanwise confining boundaries ($z=0$ and A) are $\frac{\partial u}{\partial z}=\frac{\partial v}{\partial z}=w=0$).

The blockage ratio employed in the present work, being in the range 10-12.5% was quite small. Accordingly the flow dynamics in the wake was found to be insensitive to the side wall conditions.

- Inflow plane: The inflow plane has also been modeled separately for two- and three-dimensional computations.

Two-dimensional Computations: $u=u(y)$ ($u(y)$ will assume the appropriate functional form corresponding to the inlet being (i) uniform (ii) fully developed and (iii) uniform transverse shear), $v=0$.

Three-dimensional Computations: $u=u(y, z)$ (for the present study $u(y, z)=1.0$ has been employed), $v=w=0$.

The uniform velocity inflow condition is well-suited when the data needs to be compared with wind or water tunnel experiments. The fully developed boundary condition has two advantages: (1) boundary-layers that form on the confining channel walls in developing flow need not be resolved and (2) when the obstacle is removed the flow is fully developed everywhere thus ascertaining that the disturbances are related to the cylinder alone. Sheared velocity profiles are commonly used to assess the sensitivity of the wake profiles to external factors that may be encountered in applications.

- Exit: There is no unique prescription for the outflow conditions. The idea is to have specifications that would not affect the flow in the upstream. To this end, the following boundary conditions proposed by Orlanski (1976) has been used:

$$\frac{\partial u_i}{\partial t} + u_c \frac{\partial u_i}{\partial x} = 0$$

where u_c , the convective velocity is the celerity of vortices leaving the outflow plane.

A constant value of $u_c=0.6-0.8$ has been used in all calculations reported in the

present thesis. It has been found that the instantaneous flow is undisturbed by the different values of the u_c within the specified range.

- Obstacle: No-slip boundary conditions ($u=v=w=0$) are used for the velocities on the obstacle surface.

No pressure boundary conditions have been used in the present thesis as the staggered grid which eliminates the pressure node on the boundaries has been used.

3.3 Reynolds-averaged Navier-Stokes Equations

At high Reynolds numbers, three-dimensional random turbulent fluctuations of velocity and pressure are superimposed on the unsteady periodic motion of the wake. The random motion represents small scales of turbulence and can be described by a stochastic model. Thus, in the wake of a bluff-body, the time varying component $\phi(x_i, t)$ (for example, velocity and pressure) may be expressed as a combination of a global mean component $\bar{\phi}(x_i)$, a periodic component $\tilde{\phi}(x_i, t)$ and a random component $\phi''(x_i, t)$ (Hussain, 1983). This can be expressed mathematically as

$$\phi(x_i, t) = \bar{\phi}(x_i) + \tilde{\phi}(x_i, t) + \phi''(x_i, t) = \bar{\phi}(x_i) + \phi'(x_i, t) = \langle \phi \rangle(x_i, t) + \phi''(x_i, t) \quad (3.7)$$

where $\langle \phi \rangle(x_i, t)$ refers to a phase-averaged quantity. Based on this idea, one can adopt the following viewpoint (Bosch and Rodi, 1996): The Reynolds-averaged Navier-Stokes equations determine the phase-averaged velocity and pressure (quantities inside ' $\langle \rangle$ ' in Equation 3.7). The eddy viscosity arising from the Boussinesq approximation can now be associated with the random fluctuations (quantities marked by '' in Equation 3.7). The eddy viscosity in turn can be determined by the transport equations: one for the turbulent energy level k and one for the rate of energy dissipation ϵ . This scheme has come to be called the k - ϵ family of models.

There are various high Reynolds number versions of the k - ϵ model to determine the eddy viscosity and the Reynolds stress tensor $\langle u_i'' u_j'' \rangle$. All these models relate eddy viscosity $\langle \nu_t \rangle$ to turbulent kinetic energy $\langle k \rangle$ and the rate of dissipation $\langle \epsilon \rangle$. Once the eddy viscosity is determined, the stress tensor $\langle u_i'' u_j'' \rangle$ is evaluated from Boussinesq's hypothesis as:

$$\langle u_i'' u_j'' \rangle = \langle \nu_t \rangle \left(\frac{\partial \langle u_i \rangle}{\partial x_j} + \frac{\partial \langle u_j \rangle}{\partial x_i} \right) - \frac{2}{3} \langle k \rangle \delta_{ij} \quad (3.8)$$

3.3.1 Phase-averaged flow equations

At high Reynolds numbers, the wake of a square cylinder can be visualized as the superposition of the three-dimensional (3D) turbulent fluctuations over a two-dimensional (2D) flow field. This can also be viewed as a three-dimensional unsteady periodic flow field. An instantaneous quantity ϕ can, therefore, be described by the summation of the phase-averaged value and the stochastic fluctuation as expressed in Equation 3.7. Assuming incompressible flow, the phase-averaged continuity and momentum equations can be derived to be (Bosch and Rodi (1996))

$$\frac{\partial \langle u_i \rangle}{\partial x_i} = 0 \quad (3.9)$$

$$\frac{\partial \langle u_i \rangle}{\partial t} + \frac{\partial [\langle u_j \rangle \langle u_i \rangle]}{\partial x_j} = \frac{1}{\rho} \frac{\partial \langle p \rangle}{\partial x_i} + \frac{\partial}{\partial x_j} \left[\nu \frac{\partial \langle u_i \rangle}{\partial x_j} - \langle u_i'' u_j'' \rangle \right] \quad (3.10)$$

To enforce the closure, the Reynolds stress tensor $\langle u_i'' u_j'' \rangle$ in the momentum equations is to be suitably modeled. A rational route that facilitates computation is to use Equation 3.8 along with a k - ϵ model for eddy viscosity.

3.3.2 k - ϵ family of turbulence models

Two-equation models are among the most popular turbulence models for scientific and engineering calculations. In these models, two separate transport equations are solved to determine the length and velocity scales of turbulence. By doing so, the necessity to specify the length scale in an adhoc manner as in the case of mixing layer model is avoided. One of the most widely used two-equation models is the k - ϵ model (Launder and Spalding, 1974). The two separate transport equations in this model are equations for turbulent kinetic energy, k and the turbulent dissipation rate, ϵ . The length and time scales are calculated using the turbulent kinetic energy and the turbulent dissipation rate and the turbulent or eddy viscosity is obtained as a function of these two turbulent quantities. The turbulent kinetic energy k and the turbulent dissipation rate ϵ are obtained by solving the modeled transport equations.

In the present thesis, three high Reynolds number versions of the two-equations model have been used to determine the Reynolds stress tensor $\langle u_i'' u_j'' \rangle$. All three models

use the eddy-viscosity concept to relate the eddy viscosity $\langle \nu_t \rangle$ to turbulent kinetic energy $\langle k \rangle$ and the rate of dissipation $\langle \epsilon \rangle$. The three models used are standard k - ϵ (Launder and Spalding, 1974), Kato-Launder modified k - ϵ (Kato and Launder, 1993) (hereafter referred as KaLa) and RNG k - ϵ (Yakhot and Orszag, 1986; Yakhot *et al.*, 1992). In the standard k - ϵ model, the transport equations for $\langle k \rangle$ and $\langle \epsilon \rangle$ are

$$\frac{\partial \langle k \rangle}{\partial t} + \frac{\partial [\langle u_i \rangle \langle k \rangle]}{\partial x_i} = \frac{\partial}{\partial x_i} \left[\frac{\langle \nu_t \rangle \langle k \rangle}{\sigma_k} \frac{\partial}{\partial x_i} \right] + P_k - \langle \epsilon \rangle \quad (3.11)$$

$$\frac{\partial \langle \epsilon \rangle}{\partial t} + \frac{\partial [\langle u_i \rangle \langle \epsilon \rangle]}{\partial x_i} = \frac{\partial}{\partial x_i} \left[\frac{\langle \nu_t \rangle \langle \epsilon \rangle}{\sigma_\epsilon} \frac{\partial}{\partial x_i} \right] + C_{\epsilon 1} P_k \frac{\langle \epsilon \rangle}{\langle k \rangle} - C_{\epsilon 2} \frac{\langle \epsilon \rangle^2}{\langle k \rangle} \quad (3.12)$$

where the production term is

$$P_k = C_\mu \langle \epsilon \rangle S^2, \quad S = \frac{\langle k \rangle}{\langle \epsilon \rangle} \sqrt{\frac{1}{2} \left[\frac{\partial \langle u_i \rangle}{\partial x_j} + \frac{\partial \langle u_j \rangle}{\partial x_i} \right]^2} \quad (3.13)$$

The KaLa model is similar to the standard k - ϵ , except that the turbulence production term in Equation 3.13 is replaced by

$$P_k = C_\mu \langle \epsilon \rangle S \Omega, \quad \Omega = \frac{\langle k \rangle}{\langle \epsilon \rangle} \sqrt{\frac{1}{2} \left[\frac{\partial \langle u_i \rangle}{\partial x_j} - \frac{\partial \langle u_j \rangle}{\partial x_i} \right]^2} \quad (3.14)$$

The quantity Ω is related to the average rotation of a fluid element. In simple shear flow situations, S and Ω are equal. However, in stagnation flows, $\Omega=0$ and $S>0$. This leads to the desired reduction of the production of kinetic energy. This has an important effect of lowering eddy viscosity around the cylinder and permitting vortices to be shed from it.

In RNG k - ϵ model, P_k is given by Equation 3.13 and Equation 3.12 is augmented on the right hand side by an extra strain-rate term R , given by

$$R = - \frac{C_\mu \eta^3 (1 - \eta/\eta_0) \langle \epsilon \rangle^2}{(1 + \beta_0 \eta^3) \langle k \rangle} \quad (3.15)$$

where, the quantity η is given by

$$\eta = \frac{\langle k \rangle}{\langle \epsilon \rangle} \left[\left(\frac{\partial \langle u_i \rangle}{\partial x_j} + \frac{\partial \langle u_j \rangle}{\partial x_i} \right) \frac{\partial \langle u_i \rangle}{\partial x_j} \right]^{\frac{1}{2}} \quad (3.16)$$

The eddy viscosity $\langle \nu_t \rangle$ for the standard k - ϵ and KaLa models is determined from the expression

$$\langle \nu_t \rangle = \rho C_\mu \frac{\langle k \rangle^2}{\langle \epsilon \rangle} \quad (3.17)$$

Table 3.1: Constants for the k - ϵ family of turbulent models

Models	C_μ	$C_{\epsilon 1}$	$C_{\epsilon 2}$	σ_k	σ_ϵ	β_0	η_0
standard k - ϵ and KaLa model	0.09	1.44	1.92	1.0	1.3	-	-
RNG k - ϵ model	0.0845	1.42	1.68	0.7179	0.7179	0.012	4.38

For the RNG k - ϵ , the eddy viscosity expression is

$$\langle \nu_t \rangle = \nu \left[1 + \left(\frac{C_\mu}{\nu} \right)^{\frac{1}{2}} \frac{\langle k \rangle}{\langle \epsilon \rangle^{\frac{1}{2}}} \right]^2 \quad (3.18)$$

The empirical model constants for each of the models appearing in Equations 3.11-3.18 are given in Table-3.1

The numerical solution of the k - ϵ equations requires initial and boundary conditions to be prescribed for k and ϵ . Uniform average axial and vanishing transverse velocity have been used as the initial conditions. The corresponding initial conditions for k and ϵ have been set equal to the respective inflow values. The boundary conditions have been applied as follows. The turbulence intensity ($I = \sqrt{\langle u_i'^2 \rangle} / u_{av}$) is prescribed at the inlet to be 10%. For all the computations, the eddy viscosity is specified as $\langle \nu_t \rangle / \nu = 10$ at the inflow plane (Bosch and Rodi, 1996). The value of $\langle \epsilon \rangle$ is specified using Equation 3.17 or 3.18. The wall function treatment has been used at all the solid boundaries for the standard k - ϵ and the KaLa models. During the wall function treatment, the first set of grid points from the wall were seen to fall in the range of $10 \leq y^+ \leq 30$. In contrast, no such treatment has been adopted for the RNG k - ϵ model. The RNG k - ϵ model has been tested on finer grid sizes in order to see the effect of avoiding the wall function treatment. It was found that the time-averaged drag coefficient changed by less than 1.5% for the finest grid used, justifying that the wall function treatment is not necessary for RNG k - ϵ model. At the outlet, the convective boundary condition due to Orlanski (1976) has been used. This condition may be stated as

$$\frac{\partial f}{\partial t} + u_c \frac{\partial f}{\partial x} = 0$$

where, f can take the values of u_i , k and ϵ , the convective velocity u_c being the streamwise celerity of the vortices leaving the outflow plane.

3.4 Method of Solution

Distinct problems taken up for numerical simulation are:

1. Low Reynolds number, two- and three-dimensional unsteady flow ($40 \leq Re \leq 800$)
2. High Reynolds number, two-dimensional turbulent flow with RANS ($Re=21400$)
3. High Reynolds number, three-dimensional turbulent model-free computation ($Re=21400$)

The governing differential equations in each case have been solved on a staggered grid by using a modified version of the MAC algorithm of Harlow and Welch (1965) (also see Hoffman and Benocci, 1994). The important factor in the choice of the spatial differencing strategy is the formal order of accuracy. The order of accuracy has to be balanced against the global conservation properties of the numerical scheme. The order of accuracy relates the accuracy of the solution whereas the conservative property improves the stability of the scheme.

The Adams-Bashforth scheme having second order accuracy in time has been used for time advancement. Diffusion terms have been approximated by second order central difference. The pressure gradient terms have been discretized using backward differencing. The nonlinear acceleration terms for the three problems referred above have been approximated by:

1. Second order central difference for low Reynolds number flow calculation.
2. Hybrid upwinding difference providing 15% weightage to upwinding in a space-central scheme to eliminate the oscillations associated with the central differencing for the two-dimensional RANS calculation.
3. Third order upwind difference by Kawamura *et al.* (1986) for two- as well as three-dimensional low and high Reynolds number calculations. This particular scheme takes care of the dissipative effect of the small scales by the proper drainage of the energy from the large scale to the small scale through its inherent in-built diffusion.

When the flow is incompressible, pressure and velocity are to be solved simultaneously, since the pressure field has to be compatible with the continuity equation. This has been implemented by a two-step procedure, consisting of (a) a predictor step using current values of pressure (p^n) that is fully explicit, and (b) a corrector step in which the correction to velocity and pressure are obtained by ensuring compatibility with the continuity equation. An explicit second order in time, Adams-Bashforth differencing scheme has been used for the time advancement of the convection and diffusion terms for each case. The complete numerical algorithm is summarized below.

The momentum equation is written using as a space operator, G containing the convection and diffusion terms as

$$\frac{\partial u_i}{\partial t} = G(u_i, u_j) - \frac{\partial p}{\partial x_i} \quad (3.19)$$

Thus the predictor step for the time advancement takes the form

$$\frac{u_i^* - u_i^n}{\delta t} = \frac{3}{2}G(u_i, u_j)^n - \frac{1}{2}G(u_i, u_j)^{n-1} - \frac{\partial p^n}{\partial x_i} \quad (3.20)$$

This is followed by the corrector step

$$\hat{p} = -r_0 \frac{\partial u_i^*}{\partial x_i} / \left[2\delta t \left\{ \frac{1}{(\delta x)^2} + \frac{1}{(\delta y)^2} \right\} \right] \quad (3.21)$$

The final solution for velocity and pressure are given as

$$p^{n+1} \leftarrow p^n + \hat{p} \quad (3.22)$$

$$u_i^{n+1} \leftarrow u_i^* + \frac{\delta t}{\delta x_i} \hat{p} \quad (3.23)$$

The corrector step is solved by point-wise Gauss-Seidel iterations with r_0 as an over-relaxation factor to accelerate the pressure correction process. A typical value of r_0 used in all the simulations is 1.8.

3.4.1 Grid system

The computational domain is divided into a set of rectangular cells and a staggered grid arrangement is used such that the velocity components are defined at the center of the

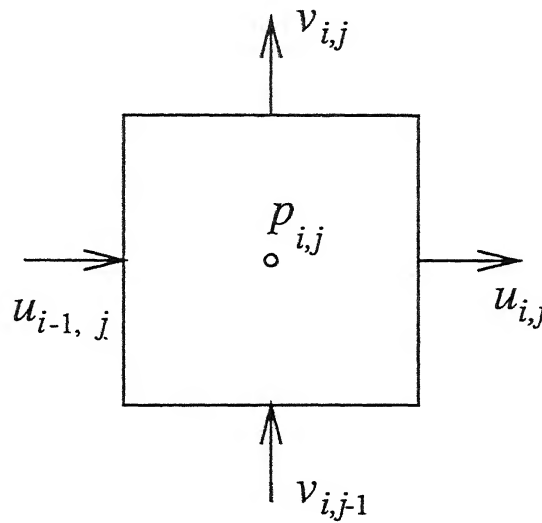


Figure 3.1: Staggered grid arrangement.

cell faces to which they are normal (Figure 3.1). The pressure is defined at the center of the cell. In such an arrangement, pressure difference between two adjacent cells is the driving force for the velocity component located between the interface of these cells. The pressure field will accept a reasonable pressure distribution only for a correct velocity field. Another important advantage of such a grid system is that transport rates across the faces of the control volumes can be computed without explicit interpolation of velocity components.

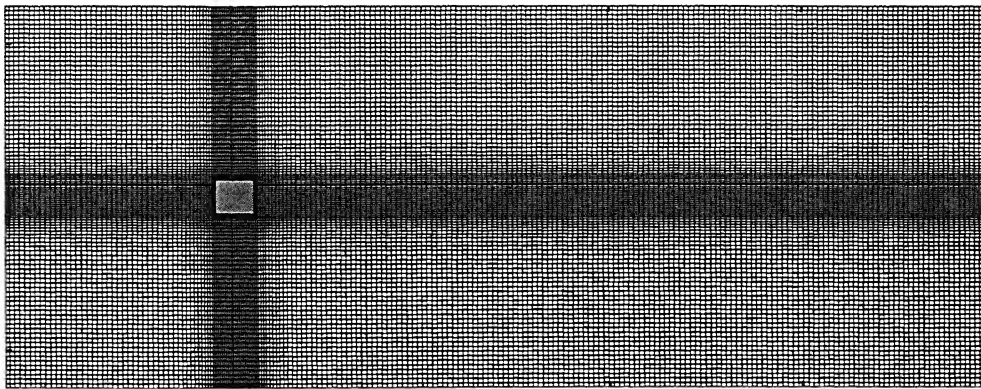


Figure 3.2: Typical nonuniform grid.

Two-dimensional simulations have been carried out on both uniform as well as nonuniform grids. However, all the three-dimensional simulations have been reported

for grids that are nonuniform on the horizontal plane (x - y plane). In three-dimensional simulation, uniform grids have been deployed in the spanwise direction. The grids are clustered near the obstacle and stretched by a specified percentage increase away from the surface of the cylinder. One such grid on the two-dimensional plane is illustrated in Figure 3.2. Grid independence study has been discussed in Chapter-5 for each configuration studied.

3.4.2 Numerical stability

For accuracy, the mesh size must be chosen small enough to resolve the expected spatial variations in all the dependent variables. Once a mesh has been chosen, the conditions on the time step necessary to prevent numerical instabilities are determined from the combination of Courant-Friedrichs-Lewy (CFL) condition and the restriction on the grid Fourier number. According to the CFL condition, the distance the fluid travels in one time increment must be less than one space increment. This leads to a constraint on the time step in the form

$$\delta t < \left\{ \frac{\delta x}{|u|}, \frac{\delta y}{|v|}, \frac{\delta z}{|w|} \right\} \quad (3.24)$$

When the viscous diffusion terms are important, the condition necessary to ensure stability is dictated by the restriction on the grid Fourier number, and can be shown to be

$$\delta t < \frac{\text{Re}}{2} \left\{ \frac{(\delta x)^2 (\delta y)^2 (\delta z)^2}{(\delta x)^2 + (\delta y)^2 + (\delta z)^2} \right\} \quad (3.25)$$

The final time step for each time advancement is the minimum of the values obtained from Equations (3.24) and (3.25).

3.5 Computational Issues

The flow past a square cylinder is primarily unsteady in nature. The time step is restricted by two different factors. One is based on the numerical stability and the other is the physical time scale involved with the flow. Therefore, all the computations were run for a long time to have adequate signal length to compute the flow statistics. This enabled

the analysis of both the time-averaged and phase-averaged quantities. The total time for which any computation was carried out was dictated by the requirement of the problem of interest. For example, to get phase-averaged and random components of turbulent flow, the computations took about two months of CPU time on a 233MHz and 192MB RAM DEC-ALPHA machine for a Reynolds number of 21400 and grid size of $240 \times 130 \times 32$. The CPU time per time step depends on many different factors, namely dimensionality of the problem, Reynolds number, grid size and time step. The typical CPU times per time step for two-dimensional and three-dimensional computation for a Reynolds number of 400 with a nondimensional time step of 0.008 are 0.7 and 7 minutes respectively on a 233MHz and 192MB RAM DEC-ALPHA machine. Similarly the time taken for the high Reynolds number ($Re=21400$) three-dimensional computation for a grid mesh of $240 \times 130 \times 32$ is about 10 minutes on a SUN ULTRA 300MHz and 1GB RAM machine¹.

The code employed in the present work was validated against the results cited in the literature. The parameter used for comparison are the time-averaged values of drag and lift coefficients, their fluctuations and the Strouhal number. For a grid independent solution, the differences between the numerical predictions and the experiments were found to be small. The code validation exercise has been taken up separately for each problem and is discussed in Chapter-5.

¹The compute servers used for the present study were of different makes, namely SUN and DEC-ALPHA, 125 and 233MHz. The relative speeds of these machines may be taken as 3:1:2, though the fastest machine, namely SUN only had limited availability.

Chapter 4

Apparatus and Instrumentation

Experiments at low and high Reynolds numbers have been reported in the present study. The respective experiments were carried out in two different setups. These are described below.

4.1 Apparatus

CENTRAL LIBRARY
I. I. T., KANPUR
A 128608

Two different test cells have been constructed in this study to simulate flow past a square cylinder under laboratory conditions. One has been used to study the wake of the square cylinder at low Reynolds numbers and the other at high Reynolds number turbulent conditions. The test cells have been designed to achieve the required flow and temperature conditions with minimum power consumption and at the smallest possible cost. The two important design parameters of the test cells are the cross-sectional area and length. The aim of the design was to produce the required flow pattern within the test section that is undisturbed by unwanted external factors. Figure 4.1 shows three-dimensional views of the two test cells. Figure 4.2 shows the respective photographs along with instruments. The important components of the test cells are: (i) Entrance cone containing honeycomb and filter (ii) Development section (iii) Measurement section (iv) Passive protection section (v) Blower including speed control and (vi) Traversing mechanism.

The function of the honeycomb is to straighten the flow by damping the transverse components of velocity, and to reduce the turbulence level by suppressing the turbulence

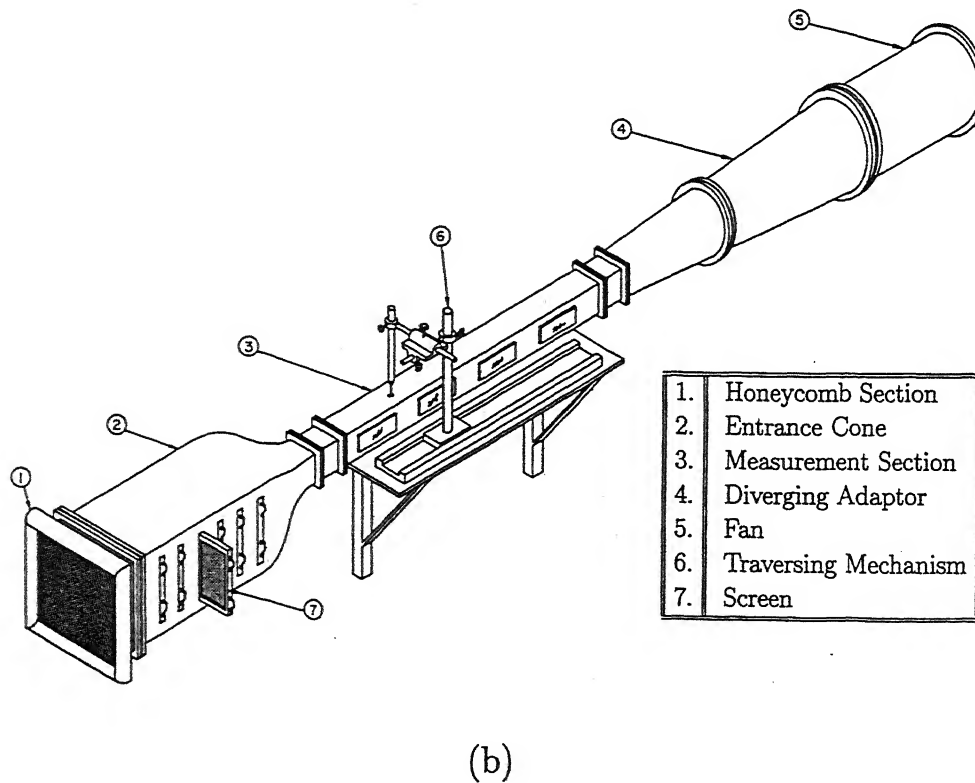
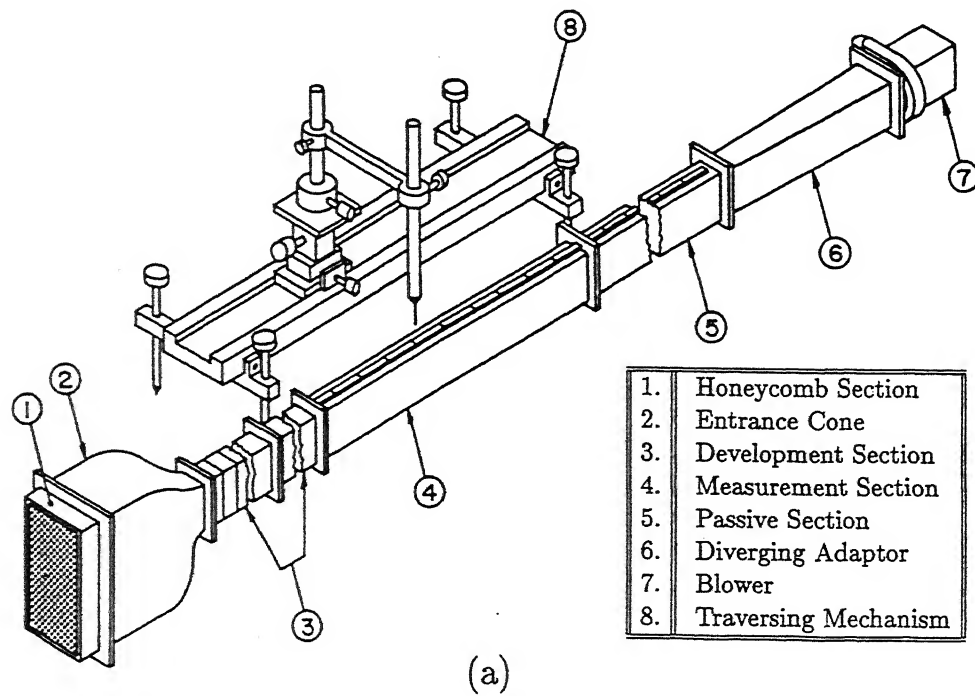
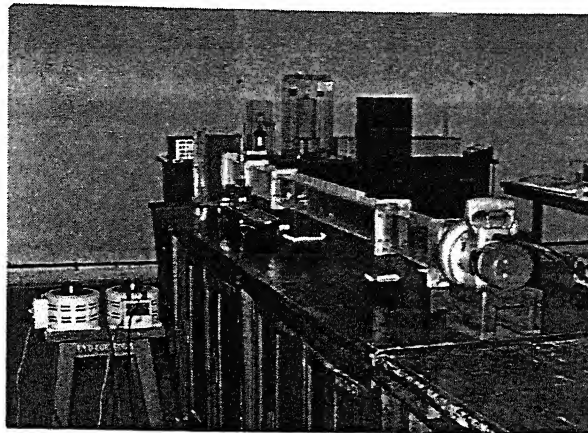
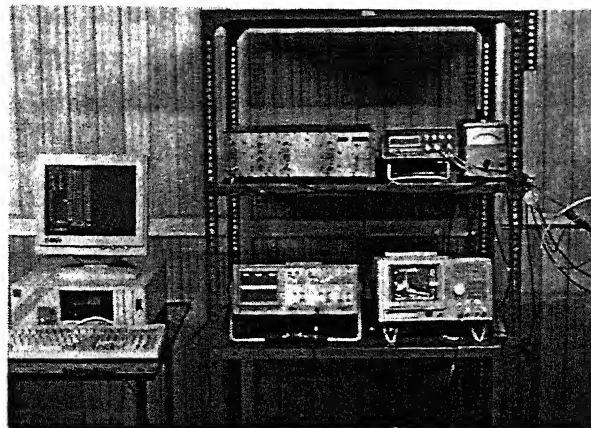


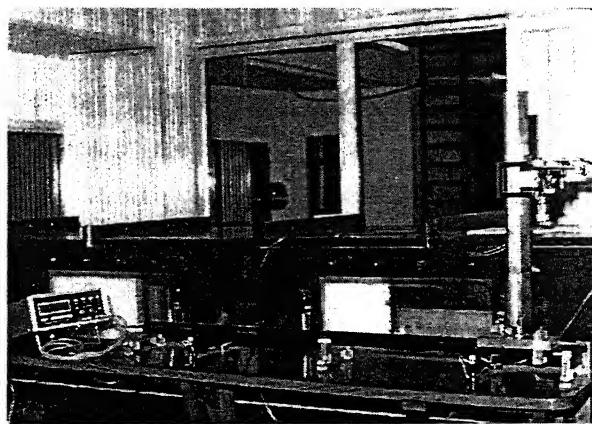
Figure 4.1: Test cells for (a) low (cross-section: 10 cm×5 cm) and (b) high (cross-section: 40 cm×40 cm) Reynolds numbers.



(a)



(b)



(c)

Figure 4.2: Photographs: (a) small test cell (b) instruments and (c) large test cell.

scales that are larger than the size of a honeycomb cell. The filters are used to suppress the small disturbances generated at the outlet tips of the honeycomb. The entrance cone has two parts, namely the settling chamber and contraction cone upstream of the working section. It reduces the spatial irregularities considerably in the velocity distribution and helps in the decay of turbulence intensity present in the upstream by proper stretching of the smaller vortices. The flow development section is used to manipulate the flow condition ahead of the measurement section.

The measurement section for the smaller test cell (Figure 4.1(a)) has a cross-section of 10 cm \times 5 cm and a length of 60 cm. The cross-section of the larger test cell (Figure 4.1(b)) is 40 cm \times 40 cm and an active test section of 3 m. Each wind tunnel has been provided with a narrow slot on the top of the measurement section to incorporate the hotwire probes. Proper care has been taken to ensure minimal disturbance caused by these slots. The measurement section of the larger test cell has a divergence angle of 4° to account for the boundary layer growth. Measurements showed that the pressure across the test sections was fairly constant.

A long passive section has been included with each test cell after the measurement section. The specific purpose of this section is to protect the measurement section from disturbances originating from the blower. This also helps in increasing the overall resistance of the test cell, thus producing stable low velocities.

The flow in both the test cells has been achieved through the use of the suction side of appropriate blowers. For the smaller test cell, velocity was changed with the help of a voltage stabilizer and a variac. The velocity variation during an experiment running for a duration of three hours was within $\pm 0.5\%$. However, the speed control of the larger test cell was achieved properly through an electronically controlled speed regulator having a maximum variation of ± 1 RPM. The corresponding velocity variation was found to be within $\pm 0.05\%$. The maximum turbulence level for undisturbed conditions were 0.3% and 0.01% for the small and the large test cells respectively. The velocity profiles were uniform to within 4% and 0.5% over 90% of the cross section of the inflow sections of the smaller and big test cell respectively. Flow parallelism in the large test cell was particularly better than 95% due to very thin boundary layers.

An important accessory during measurements is the traversing mechanism. The traversing mechanism as used in the present experiments was designed to have three

orthogonal manually-controlled movements. The accuracy of the transverse motions was ± 0.1 mm, through a vernier arrangement, and ± 0.5 mm for movement in the streamwise direction.

4.2 Review of Instrumentation

Experimental research in fluid mechanics has produced a great deal of innovation. Consequently a great number of methods, instruments and techniques are presently available. Most of these methods and instruments have been developed for measuring velocities in flows that are either laminar or assumed to be laminar. In fact only a few are suitable for making measurements in turbulent flows.

The major problems in measuring any complex turbulent flow are caused by the fact that turbulence is a random three-dimensional flow field. The wide range of frequency components makes it very difficult for a measuring instrument to satisfy the basic requirement that the recordings must be as free from amplitude attenuation and distortion of phase. This continues to be a challenge in present-day experiments in turbulent flows.

Broad classification of the various techniques and instruments available shows two major groups, namely (i) Imaging techniques and (ii) Intrusive methods. These are briefly reviewed below.

4.2.1 Imaging techniques

In this group, a tracer is introduced into the fluid to make the flow visible to a detecting apparatus outside the flow field. The most important advantage of this method is that a mechanical probe disturbing the flow can be avoided and the measurement is thus non-intrusive. Rapid changes occurring in turbulent flows with time and space require highly resolved measurement through instantaneous recordings. Application of photographic methods in measurement of turbulent flows is confronted with the difficulties of taking snaps at very short intervals. The three-dimensionality of the turbulent motions makes the interpretation of these recordings very difficult. Use of advanced signal processing and three-dimensional reconstruction algorithms will improve the efficiency of interpretation

techniques but the volume of data to be recorded is large. Simultaneous measurement of various flow properties is another difficulty associated with imaging techniques. One such technique in wide use is Particle Image Velocimetry (PIV).

Particle Image Velocimetry (PIV) measures the motion of small, marked regions of a fluid by observing the locations of the images of the markers at two or more times. This method returns to the fundamental definition of velocity and estimates the local velocity u_i from

$$u_i(x_i, t) = \frac{\Delta x_i(x_i, t)}{\Delta t}$$

where Δx_i is the displacement of a marker, located at x_i at time t , over a short interval Δt separating observations of the marker images. As this technique involves recording of flow frames at different times, it demands a good image capturing and processing unit. The light source generally used is pulsed laser. Like LDV, this technique also require seeding to illuminate the flow with proper tracer particles. The advantages of this technique are (i) the instantaneous information of the whole flow field is possible (ii) the use of Fourier transform based postprocessing helps the data reduction to be rapid. On the other hand the limitations are (i) it cannot be used where tracer-injection is not possible and (ii) the frequency response is not high enough for turbulent flow.

Recent developments in digital image processing have made it possible to measure an instantaneous vector distribution in three-dimensional space. Several researchers have been successful in using this particular method. Nishino and Kasagi (1989) has done measurements in turbulent channel flow and found excellent agreement with direct numerical simulation. In an another work, Kasagi and Matsunaga (1995) has reported a three-dimensional study of flow past a backward facing step using PIV. Brede *et al.* (1996) have studied flow past a circular cylinder using PIV.

Though not an imaging technique, it is appropriate to mention laser Doppler velocimetry (LDV) here, since it is radiation based and is hence non-intrusive. LDV is the measurement of fluid velocities by detecting the Doppler frequency shift of laser light that has been scattered by small particles moving with the fluid (Goldstein, 1997). This particular technique demands the seeding of the flowing fluid to induce scattering and thus creating a frequency shift. It can measure velocity in both isothermal and nonisothermal flows. The frequency shift is independent of fluid temperature and is a major advantage over a thermal transducer. Other advantages of LDV are: (i) ease of operation, (ii) non-

intrusive nature, (iii) good sensitivity at low and high velocities, (iv) linearity in operation, (v) good positional accuracy and (vi) ability to detect reverse flows. The limitations of the LDV are (i) cost, (ii) limited frequency response and (iii) lack of robustness. Early measurements using LDV have been reported by Goldstein and Kreid (1967) for laminar flow of water in a square duct. Other researchers in past have used LDV in their study of turbulent flow (George and Lumley, 1973; Buchave *et al.*, 1979; Heist and Gouldin, 1997). In recent years, LDV has been used for the velocity measurements in complex flows such as flow past a square cylinder (Durão *et al.*, 1988; Lyn *et al.*, 1995), where unsteady reversed flows are encountered.

4.2.2 Intrusive methods

Here, the probe is a detecting element introduced into the fluid, and the flow quantities including turbulent fluctuations are measured by noting the changes in the mechanical, electrical or chemical properties of the element. There are a number of requirements that must be satisfied by the detecting element in the context of turbulent flow. These are:

- The detecting element must be small so that it causes only a small disturbance to the flow pattern.
- The instantaneous velocity distribution must be uniform in the region occupied by the element. This means that the detecting element must be smaller than the dimensions of the smallest eddies of the turbulence.
- The time constant of the probe must be low, so that response to even the most rapid fluctuations is practically instantaneous.
- The measurement system that monitors the state of the probe must be sufficiently sensitive to record small fluctuations.
- The measurement system must be stable, so that no noticeable change occurs in the calibration parameters during at least one test run.

The hotwire anemometer is an example of an intrusive technique whose application for measuring turbulent flow has far outstripped other instruments. The hotwire anemometer measures both fluid velocity and temperature by sensing the changes in heat transfer from a small, electrically heated wire exposed to the fluid motion. This sensor is small in size and coupled with a feedback circuit, it has a very high frequency response.

Its popularity for making turbulence measurements is understandable since it satisfies all the above-mentioned requirements. It has certain limitations since (i) it is not suitable for very small velocities unless proper attention is given for calibration (ii) it is insensitive to the direction of velocity (iii) for velocity measurement, a constant fluid temperature is essential (iv) it is difficult to use because it is fragile and sensitive to contamination and (vi) the calibration, as a rule is nonlinear.

Hotwire experiments have been reported in the present thesis. HWA is thus described in detail in the following section.

4.3 Hotwire Anemometry

A hotwire anemometer responds primarily to the velocity magnitude and is based on the principle of heat transfer. Hence for using a single sensor hotwire anemometer, the flow direction must be known. If three sensors of the hotwire are arranged in such a way that they provide independent output signals, the three components of velocity can be measured and the velocity vector can be determined. In a two-dimensional turbulent flow, a two sensor hotwire, known as crosswire, can measure two components of velocity and velocity fluctuations. The velocity measured by each wire is different from the component of velocity along laboratory coordinates. The velocity sensed by each wire is known as the effective cooling velocity.

In two-dimensional measurements, calculation of velocity components involves solving a pair of nonlinear simultaneous equations. Velocity measurements in varying temperature flows require special calibration. Thus the accuracy of hotwire measurements is affected by the accuracy of the calibration procedure and that of solution procedure that is used to solve the nonlinear simultaneous equations. The calibration methodology is discussed in detail in the present section.

The hotwire is basically a thermal transducer. Simply stated, its principle of operation is as follows. An electric current is passed through a fine filament ($5\text{ }\mu\text{m}$ diameter and 1.25 mm length), which is exposed to cross flow. As the fluid velocity or temperature varies, the heat transfer from the filament varies. This in turn causes a variation in the heat balance of the filament. The filament is made from platinum coated tungsten, tung-

sten having a high temperature-coefficient of resistance. The variation of resistance is monitored by a feedback circuit which passes additional current till the wire temperature becomes a constant independent of the flow velocity or temperature. This temperature is usually much higher than the room temperature and is typically 150-200° C in air flow measurements. Higher temperature enhances the sensitivity of wire but makes the wire fragile. The output of the feedback circuit is a measure of the fluid velocity and temperature. The hotwire and feedback circuit combination is referred as a Constant Temperature Anemometer (CTA).

4.3.1 Convective principles governing the operation of a hotwire

The operation of a hotwire can be explained in terms of convective heat transfer from fine wires. With the assumption of uniform radial temperature distribution within a fine wire, the thermal equilibrium of the wire placed in a fluid gives the following heat balance relation.

$$He + K = i^2 R_w \quad (4.1)$$

where $He = hA_r(T_w - T_f)$ is the convective heat loss from the wire, K is its change in internal energy, and $i^2 R_w$ is the Joule heating of the wire.

The nomenclature employed is:

A_r is the area of hotwire per unit length, m^2 ,

h is the convective heat transfer coefficient, $W K^{-1} m^{-2}$,

T_w is the temperature of wire, K,

T_f is the temperature of fluid, K,

i is the current flowing through wire, amp, and

R_w is the resistance of wire, ohm.

One can write,

$$K = mC_w \frac{dT_w}{dt} \quad (4.2)$$

where m is the mass of wire per unit length, kg/m ,

C_w is the specific heat of the wire material, $J kg^{-1} K^{-1}$

The differential equation governing this convective heat transfer process is

$$mC_w \frac{dT_w}{dt} + A_r h (T_w - T_f) - i^2 R_w = 0 \quad (4.3)$$

The variable of primary interest in hotwire anemometry is the convective heat transfer coefficient, h . The rate of change of internal energy is practically zero for CTA mode of operation of the hotwire. This gives

$$He = 2\pi K_f l (T_w - T_f) Nu \quad (4.4)$$

where, $Nu = \frac{h d_w}{K_f}$ is the Nusselt number,
 d_w is the sensor diameter,
 K_f is the thermal conductivity of fluid and
 $2l$ is the length of sensitive area of hotwire.

The general expression for forced convection Nusselt number in the case of incompressible flow is given by,

$$Nu = f(Re, Pr, \alpha_1, Gr, Ma, \gamma, a_T, 2l/d_w, K_f/K_w) \quad (4.5)$$

where, $Re = \frac{U_e d_w}{\nu}$ is the Reynolds number,
 U_e is the effective cooling velocity,
 ν is the kinematic viscosity of fluid,
 Pr is the Prandtl number,
 α_1 is the angle between freestream flow direction and normal to wire,
 Gr is the Grashof number,
 Ma is the Mach number,
 $\gamma = C_p/C_v$,
 C_p is the specific heat of fluid at constant pressure,
 C_v is the specific heat of fluid at constant volume,
 $a_T = (T_w - T_f)/T_f$ is the temperature loading or overheat ratio.
 K_w, K_f are the thermal conductivities of wire and fluid respectively.

Fortunately, most applications permit a significant reduction in the number of parameters that must be included. The reasons are:

1. Forced convection parallel to the wire is small.

2. Pr depends only on fluid properties, and buoyancy effects can be neglected for $GrPr < Re^2$. Thus, for velocities of air greater than 5.2 cm/s, buoyancy effects can be neglected.
3. For low density and low velocities, Mach number is negligibly small and C_p and C_v can be assumed to be constant.

The general equation governing the operation of the hotwire can be simplified to:

$$Nu = f(Re, a_T) \quad (4.6)$$

In isothermal flows measurements Equation 4.6 can be further simplified as

$$Nu = f(Re) \quad (4.7)$$

Analytical derivation of the functionality between Nu , Re and a_T is difficult. A simplified analytical solution of Equation 4.7 shows that a power law relation is generally valid. The exponent depends on geometric and physical properties of the wire and physical properties of the fluid. An empirical correlation derived using individual (*in situ*) calibration of wire is generally recommended in hotwire applications.

4.3.2 Review of correlations for heat transfer from thin wires

The relationship known as King's law (Bruun, 1995) that permits a significant reduction in the number of parameters is as follows:

$$Nu = A'_c + B'_c Re^{0.5} \quad (4.8)$$

where A'_c and B'_c are empirical constants, usually determined by calibration.

Collis and Williams (1959) suggested an accurate formula for Nusselt number which accounts for the change in properties of the fluid. Their formula can be stated as

$$Nu = (A_c + B_c Re^n) \left[1 + \frac{a_T}{2} \right] \quad (4.9)$$

The constants in the above formula are to be evaluated from the calibration of the wire at different velocities and temperatures. Typical values of the constants for commercial probes used in air are:

$$\begin{aligned} A_c = 0.24, \quad B_c = 0.56 \quad \text{and} \quad n = 0.45 \quad \text{for} \quad 0.02 < \text{Re} < 44. \\ A_c = 0.00, \quad B_c = 0.48 \quad \text{and} \quad n = 0.57 \quad \text{for} \quad 44 < \text{Re} < 140. \end{aligned}$$

Koch and Gartshore (1970) suggested a different formula,

$$\text{Nu} \left(\frac{T_m}{T_f} \right)^a = A_c + B_c \text{Re}^n \quad (4.10)$$

where $T_m = \frac{T_w + T_f}{2}$, $A_c = 0.24$, $B_c = 0.56$, $n = 0.45$ and $a = 0.67$. The correlations given above are in terms of non-dimensional parameters. It is convenient to work in dimensional form as

$$\frac{E^2}{R_w (T_w - T_f)} = A_c \left(\frac{T_m}{T_f} \right)^{a_1} + B_c \left(\frac{T_m}{T_f} \right)^{a_2} U_e^n \quad (4.11)$$

where E is the voltage output of the hotwire.

Collis and Williams (1959), Koch and Gartshore (1970), Davies and Fisher (1964) and Bearman (1971) suggested widely differing values for these constants of the calibration surface given by Equation 4.10. The constants depend on the l/d ratio of the wire, wire material and fluid properties. The choice of the numerical scheme, number of calibration points and range of velocities also affect the overall accuracy of the calibration procedure. The need to generate flows at different velocities and temperatures for calibration is also a source of error. As a result, the overall accuracy of calibration for non-isothermal problems have been reported in the range 90-95%, implying an error of 5-10%.

Hollasch and Gebhart (1972) have suggested an indirect method which does not require uniform flows of different velocities and temperatures, but is valid primarily at low velocities. This method has been extended in the present work and the calibration errors are seen to be less than 1% for a wider range of velocities and temperatures.

Two different calibration techniques which are accurate and suitable for measurements in turbulence are described here.

4.3.3 Calibration methodology

Calibration of a hotwire probe involves two major steps, namely data generation and curve fitting. Calibration data is generated by measuring the output of the anemometer when

the probe is subjected to a flow with known velocity. Specially designed apparatus are used to generate high quality flow with uniform velocity, temperature and very low turbulence level ($< 0.1\%$). DANTEC Instruments supply such calibration equipment. However, a test cell which can produce good quality flow can also be used. This apparatus should be able to produce uniform flow with adjustable velocity. The hotwire probe to be calibrated is kept firmly in the calibration apparatus such that the direction of velocity of uniform flow is normal to the wire. The flow should be steady. The output of the wire is noted at zero flow and successively at various velocities. The calibration data should be repeatable with very low scatter.

In the present study, calibration has been performed in the larger test cell (Section 4.1) itself due to its high quality inflow.

4.3.4 Isothermal calibration of hotwire

DISA hotwire equipment uses a linearizer card (56 N 21) which produces a voltage signal directly proportional to the fluid velocity. The mathematical form of the calibration data used by this card is:

$$y = 10^{A_a + B_b x + E_e y} + C_c x + D_d \quad (4.12)$$

Here A_a , B_b , C_c , D_d and E_e are calibration constants. The constants are selected to give a fluid velocity equal to 10 m/s for a wire output of 10 Volts. In Equation 4.12, y is the linearizer output equal to the normalized velocity defined as,

$$y = 10 \times \frac{U}{U_{max}} \quad (4.13)$$

and x is normalized voltage defined as,

$$x = 10 \times \left[\frac{V - V_0}{V_{max} - V_0} \right] \quad (4.14)$$

where V_0 is the output of the wire measured at zero velocity and V_{max} measured at the maximum velocity U_{max} .

Though the linearizer was not used, its built-in formula has been used as the calibration curve in the present work. The constants A_a , B_b , C_c , D_d and E_e have been obtained by means of iterative least square error approach.

The least square method is applied as follows: For any calibration point (x_i, y_i) , Equation 4.12 will produce an error ϕ_i given by

$$\phi_i = y_i - [10^{A_a+B_b x_i+E_e y_i} + C_c x_i + D_d]. \quad (4.15)$$

The least square approach requires the sum of errors at all calibration points be a minimum, that is,

$$\Phi = \sum_{i=1}^n \phi_i^2 = \sum_{i=1}^n \left\{ y_i - [10^{A_a+B_b x_i+E_e y_i} + C_c x_i + D_d] \right\}^2 \quad (4.16)$$

$$\text{and} \quad \frac{\partial \Phi}{\partial A_a} = \frac{\partial \Phi}{\partial B_b} = \frac{\partial \Phi}{\partial C_c} = \frac{\partial \Phi}{\partial D_d} = \frac{\partial \Phi}{\partial E_e} = 0. \quad (4.17)$$

Equation 4.17 can be used iteratively to calculate A_a, B_b, C_c, D_d and E_e . The calibration strategy described above has been extensively tested by Subbarao (1995).

4.3.5 Explicit non-real time signal analysis

For a single sensor hotwire normal to the flow with its prongs parallel to the flow, the definition of the effective cooling velocity is unambiguous and is equal to the flow velocity. For measurements in two-dimensions, the contribution to the heat loss by the component of velocity along the wire must be included. A crosswire sensor is designed for use in two-dimensional flow measurements. Each wire is separately calibrated and corresponding calibration curve and constants are evaluated. Substitution of the output of the wire in its calibration curve gives the effective cooling velocity sensed by the wire. The components of velocity can be resolved into two components, one normal to the wires and another parallel to them. The effect of cooling by other two components of the velocity is accounted for by a sensitivity coefficient K_T . Experiments of Butler and Wanger (1982) and many others suggested K_T to be in the range from 0.1 to 0.25. The value $K_T=0.20$ has been found to be an optimum in the literature (Perry, 1982). The effective cooling velocity sensed by each wire is defined as

$$V_e^2 = V_N^2 + K_T^2 V_T^2 \quad (4.18)$$

where V_e is the effective cooling velocity, V_N is the velocity component normal to the wire, V_T is the velocity component tangential to the wire. Measurement of two-dimensional

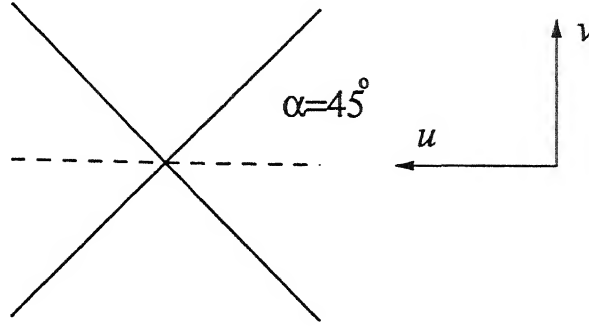


Figure 4.3: Crosswire probe and velocity components.

flows involves calculation of components of velocity in laboratory coordinates. Many techniques are available to calculate these components from known effective cooling velocities.

Chew and Simpson (1988) have proposed an explicit non-real time method of reducing triple sensor hotwire anemometer data to obtain the three mean velocity components and six Reynolds stresses in three-dimensional flow. This method does not require instantaneous signal to calculate the parameters referred above. This method has been applied to a two-wire probe in the present study.

With reference to Figure 4.3, for wire 1 the normal velocity component V_N is $(u \cos\alpha - v \sin\alpha)$ and the tangential velocity component V_T is $(u \sin\alpha + v \cos\alpha)$. The heat transfer coefficient associated with each velocity component is different. Hence the effective velocities v_1 and v_2 sensed by wire 1 and wire 2 are written as,

$$v_1^2 = [(u \cos\alpha - v \sin\alpha)^2 + K_T^2 (u \sin\alpha + v \cos\alpha)^2] \quad (4.19)$$

$$v_2^2 = [(u \sin\alpha + v \cos\alpha)^2 + K_T^2 (u \cos\alpha - v \sin\alpha)^2] \quad (4.20)$$

Generally crosswires are manufactured with the angle between wires $2\alpha = 90^\circ$. With $\alpha = 45^\circ$ above equations can be simplified as

$$v_1^2 = \frac{1}{2} [(u - v)^2 + K_T^2 (u + v)^2] \quad (4.21)$$

$$v_2^2 = \frac{1}{2} [(u + v)^2 + K_T^2 (u - v)^2] \quad (4.22)$$

The factor K_T takes into account the differences in the heat transfer coefficient between cross flow and parallel flow. Let $v_x = \frac{u+v}{\sqrt{2}}$ and $v_y = \frac{u-v}{\sqrt{2}}$. Substituting in

Equations 4.21 and 4.22, we get

$$v_1^2 = v_y^2 + K_T^2 v_x^2 \quad (4.23)$$

$$v_2^2 = v_x^2 + K_T^2 v_y^2 \quad (4.24)$$

Hence, inversion of Equations 4.23 and 4.24 gives,

$$v_x^2 = a_1 v_1^2 + a_2 v_2^2 \quad (4.25)$$

$$v_y^2 = b_1 v_1^2 + b_2 v_2^2 \quad (4.26)$$

where $a_1 = b_2 = \frac{1}{1-K_T^4}$ and $a_2 = b_1 = \frac{-K_T^2}{1-K_T^4}$.

Any variable in the above equations can be split into a mean and a fluctuating part as $v = V + v'$. Splitting all variables in Equations 4.25 and 4.26 and time averaging gives

$$V_x^2 + \overline{v_x'^2} = a_1 (V_1^2 + \overline{v_1'^2}) + a_2 (V_2^2 + \overline{v_2'^2}) \quad (4.27)$$

$$V_y^2 + \overline{v_y'^2} = b_1 (V_1^2 + \overline{v_1'^2}) + b_2 (V_2^2 + \overline{v_2'^2}) \quad (4.28)$$

Let

$$V_{x0}^2 = a_1 V_1^2 + a_2 V_2^2 \quad (4.29)$$

$$V_{y0}^2 = b_1 V_1^2 + b_2 V_2^2 \quad (4.30)$$

$$\overline{v_{x0}^2} = a_1 \overline{v_1'^2} + a_2 \overline{v_2'^2} \quad (4.31)$$

$$\overline{v_{y0}^2} = b_1 \overline{v_1'^2} + b_2 \overline{v_2'^2} \quad (4.32)$$

Then

$$\overline{v_x'^2} = \overline{v_{x0}^2} + V_{x0}^2 - V_x^2 \quad (4.33)$$

$$\overline{v_y'^2} = \overline{v_{y0}^2} + V_{y0}^2 - V_y^2 \quad (4.34)$$

Rewrite Equations 4.27 and 4.28 as

$$V_x + v'_x = [V_{x0}^2 + 2a_1 V_1 v'_1 + 2a_2 V_2 v'_2 + a_1 v_1'^2 + a_2 v_2'^2]^{1/2} \quad (4.35)$$

$$V_y + v'_y = [V_{y0}^2 + 2b_1 V_1 v'_1 + 2b_2 V_2 v'_2 + b_1 v_1'^2 + b_2 v_2'^2]^{1/2} \quad (4.36)$$

Expanding in a binomial series, taking time mean and neglecting terms higher than v'^2 gives

$$V_x = V_{x0} \left[1 + \frac{\overline{v_{x0}^2}}{2V_{x0}^2} - \frac{\sigma_x^2}{8V_{x0}^4} \right] \quad (4.37)$$

Here,

$$\begin{aligned} V_{x0} &= \sqrt{a_1 V_1^2 + a_2 V_2^2} \\ \overline{v_{x0}^2} &= a_1 \overline{v_1'^2} + a_2 \overline{v_2'^2} \\ \sigma_x^2 &= 4 \sum_{i=1,2} \sum_{j=1,2} a_i a_j V_i V_j \overline{v_i' v_j'} \end{aligned}$$

Similarly,

$$V_y = V_{y0} \left[1 + \frac{\overline{v_{y0}^2}}{2V_{y0}^2} - \frac{\sigma_y^2}{8V_{y0}^4} \right] \quad (4.38)$$

where

$$\begin{aligned} V_{y0} &= \sqrt{b_1 V_1^2 + b_2 V_2^2} \\ v_{y0}^2 &= b_1 \overline{v_1'^2} + b_2 \overline{v_2'^2} \\ \sigma_y^2 &= 4 \sum_{i=1,2} \sum_{j=1,2} b_i b_j V_i V_j \overline{v_i' v_j'} \end{aligned}$$

The product of v_x' and v_y' can be calculated using the expression,

$$\overline{v_x' v_y'} = \frac{\left[\sum_{i=1,2} \sum_{j=1,2} a_i b_j \left(V_i^2 V_j^2 + V_i^2 \overline{v_j'^2} + V_j^2 \overline{v_i'^2} + 4V_i V_j \overline{v_i' v_j'} \right) - V_x^2 V_y^2 - V_x^2 \overline{v_y'^2} - V_y^2 \overline{v_x'^2} \right]}{4V_x V_y} \quad (4.39)$$

The velocity components in laboratory coordinates U and V and turbulence quantities u_{rms} , v_{rms} and $u'v'$ can now be calculated from the above variables using the following formulae.

$$U = \frac{V_x + V_y}{\sqrt{2}} \quad (4.40)$$

$$V = \frac{V_x - V_y}{\sqrt{2}} \quad (4.41)$$

$$u_{rms}^2 = \frac{\overline{v_x'^2} + \overline{v_y'^2} + 2\overline{v_x' v_y'}}{2} \quad (4.42)$$

$$v_{rms}^2 = \frac{\overline{v_x'^2} + \overline{v_y'^2} - 2\overline{v_x' v_y'}}{2} \quad (4.43)$$

$$\begin{aligned} \text{and} \\ \overline{u'v'} &= \frac{\overline{v_x'^2} - \overline{v_y'^2}}{2} \end{aligned} \quad (4.44)$$

The method mentioned above does not require equipment to collect instantaneous signals, but involves complex mathematical equations. This method requires measurement of mean output of wire 1 and 2, namely V_1 and V_2 , RMS values of their fluctuations $v_{1\text{ rms}}$ and $v_{2\text{ rms}}$ and the cross product $\overline{v_1'v_2'}$. Inaccurate measurement of these turbulent quantities will produce imaginary numbers owing to the square root sign.

4.4 Measurement of Drag and Vortex Shedding Frequency

Mean velocity profile across the wake, distribution of the streamwise momentum, and the loss of momentum are three important parameters that describe the mean flow structure of the near-wake. In the present work, the momentum loss in the near-wake has been measured and a dimensionless drag coefficient has been calculated. The procedure is analogous to measurement of drag using the *Wake Survey Method*. Generally this method is used to calculate drag coefficient from the velocity profiles measured at positions where there is no static pressure variation across the wake. But in the case of a square cylinder, the static pressure variations have been observed even at twenty cylinder width downstream of the cylinder. Therefore, it is necessary to consider the static pressure variation in the calculations. The drag coefficient is then given by the formula

$$C_d = \frac{\int_{-\infty}^{\infty} (\rho u(y)(U_a - u(y)) + \Delta p) dy}{0.5\rho U_a^2 B} \quad (4.45)$$

where $u(y)$ is the velocity profile in the wake, U_a is the approach velocity, B is the cylinder width and Δp is the static pressure drop between the freestream and the point under consideration. The integrals in Equation 4.45 are evaluated numerically.

The frequency of vortex shedding has been measured with the help of the Spectrum analyzer. The point at which the frequency is determined is at an offset of half-width of the cylinder from the wake centreline. Proper care has been taken to ensure that the hotwire does not act as a control rod which can suppress or enhance the shedding. To avoid confusion, different locations have been examined and the final location has been selected from the spectra having the sharpest peak with minimal noise.

4.5 List of Instruments

Details of instrumentation used with the hotwire equipment are discussed in the present section.

DANTEC CTA Bridge and Accessories

The DANTEC model 56 C 17 CTA has been used in the present study. The main unit 56 C 01 CTA delivers the servo-voltage as the output of the instrument. This voltage is a measure of the fluid velocity. The feed-back circuit of the CTA plays an important role in improving the frequency response of the hotwire from about 100Hz to 10 kHz.

The 56 C 01 CTA contains a function switch with three modes for operation, namely TEMP, STD.BY and FLOW. In TEMP position the resistance of the connected probe can be measured in terms of a current supplied to it. In STD.BY position no current flows through the bridge. In FLOW setting the CTA starts operating with the function of the servo amplifier. A setting named BRIDGE ADJ enables the adjustment of bridge balance for measurement of probe resistance and the setting of the desired overheat resistance. This BRIDGE ADJ has a pair of switches for coarse adjustment of the overheat resistance, and a screw for fine adjustment. Resistance can be varied between 0 and 30 ohm in steps of 0.001 ohm. This adjustment is crucial for setting the overheat resistance for the calibration procedure. CTA in TEMP mode produces a voltage proportional to the resistance of the wire.

The mean-value unit 56 N 22 is a 5.5 digit display voltmeter. The primary purpose of this module is to measure the DC component of the output signal from 56 C 01 CTA. This module has 100 μ volt resolution, 1-1000 seconds integration time and switch selectable 14 inputs. The module 56 N 23 (Analog Processing Unit) is a signal processing module for using with the two 56 C 01 CTA modules. The 56 N 23 APU allows the addition and subtraction of two input signals as well as the calculation of derivative with a variable time step. The 56 N 20 signal conditioner amplifies and filters AC output signals from 56 C 01 CTA. It contains low-pass and high-pass filters which can filter the signal in the required range of frequencies. 56 N 20 signal conditioner can selectively amplify the input signals with gain factors ranging from 1 to 900. This amplification is very important in

the measurement of temperature signals.

In the present work, three 56 C 01 CTA modules which make a 3-channel CTA have been used. Each channel has a separate 56 N 20 signal conditioner and one 56 N 23 APU for a pair of wires. A 3-wire probe can be connected to this setup and outputs of 3 wires can be measured simultaneously. Only 2-wire measurements are reported in this work. 56 N 22 module has been used to measure the mean voltage output of each channel with an integration time constant of 100-1000 seconds. The signal conditioner was set to AC mode with the mean removed from the instantaneous voltage signal. RMS values and other statistics have been measured from long signal traces with a digital oscilloscope and a spectrum analyzer respectively.

Digital Oscilloscope

A Gould 1602 two channel digital storage oscilloscope with a sampling speed of 20 Msam/s and an operating frequency range of 0-20 MHz has been used in this work. This can operate both in storage and non-storage mode. It has advanced features such as menu controlled memory, acquisition/trigger menu and optional features like GPIB (IEEE 488) and RS423 input/output ports for external control by a host computer. A Gould waveform processor 460 provides enhanced measurements and trace processing.

The oscilloscope can acquire very long signal containing data points as many as 10240, simultaneously from two channels. This facility can be used to collect simultaneously long signals of both the components of velocity fluctuations. This oscilloscope with the waveform processor does on-line calculation of rms values of signals in storage mode. This facility was used to measure separately the rms values of the cross-wire outputs.

Spectrum Analyzer

The ADVANTEST R 9211 E is a digital spectrum analyzer that is based on FFT. Wide band as well as high sensitivity measurements can be performed in the frequency range of 10 mHz-100kHz, and input voltage range of 1μ volts_{rms} - 31.6 volts_{rms}. Time-area analysis, frequency analysis, frequency response, time-frequency analysis and function measurement are available in the analyzer.

The analyzer has four different modes of operation. The waveform and spectrum modes are generally used in the turbulence measurement. In waveform mode the spectrum analyzer does on-line measurement of the time signal, histograms (PDF), autocorrelation and crosscorrelation functions. In spectrum mode it measures the power spectrum and the complex spectrum. The analyzer has two single ended/differential input channels. The analyzer also has multiscreen function through which upto four screens can be selected simultaneously. It has different menus such as Math, Setup, Device and Copy. The Math menu does arithmetic operations between two arrays and integration and differentiation of an array. This facility can be used for the measurement of average of product of the two-wire signals (as in the case of Reynolds shear stress). The device menu operates the floppy drive and the GPIB connections. All traces shown on the screen can be stored on a floppy and processed when required. This facility has helped in collecting a large volume of data.

The spectrum analyzer has been used mainly for data collection, ensemble averaging and determination of statistics. Instantaneous traces of statistics can be ensemble averaged. The averaged spectra, PDF, correlation functions can be transferred to a PC through a GPIB interface.

Digital Multimeter

The HP 3457A is a versatile digital multimeter. It can measure DC voltage, AC voltage, AC and DC current and the Resistance. In addition, the HP 3457A has a reading and program storage and is capable of making fast measurements. The HP 3457's math operations manipulate or modify a measured reading before it is displayed. In addition, there is another operation, namely STAT. The STAT operation performs five running calculations on the present series of measurements and stores the results. It evaluates the standard deviation, mean, number of samples, upper reading and lower reading. These facilities can be used to measure mean temperature and the RMS value of the temperature fluctuations.

4.6 Uncertainty Analysis

In a classical sense, it was not possible to repeat precisely identical experiments, mainly due to establishing identical velocity and ambient temperatures. Instead, the approach adopted was to perform the experiments at a nearby Reynolds number, approximately 10% away from the desired value. The two sets of data were then compared in terms of dimensionless velocity and velocity fluctuations. The agreement between the two sets was found to be very good. In this sense, the results reported in the present work have a high degree of repeatability. The extent of repeatability of data over a Reynolds number range of 8700-17625 was found to be $\pm 5\%$ in time-averaged quantities and $\pm 10\%$ in rms quantities, (95% CI). This is discussed in Chapter-5.

It is necessary to comment on the sources of error in every measurements. These errors can arise due to (i) positional accuracy in locating the probe (ii) drift in electronics and consequent errors in voltage measurements (iii) errors in calibration data and inadequate compensation for room temperature (iv) inadequate signal length and sampling rate and (v) errors associated with neglecting the spanwise component of velocity during data reduction. While due care has been taken to minimize errors (i)-(iv), the fifth source of error is likely to cause large localized deviation from numerical predictions. However, Ong and Wallace (1996) have shown two-dimensionality of the near-wake of a circular cylinder at a Reynolds number of 3900. In light of these results the measurements of the present study can be taken as qualitatively meaningful.

Chapter 5

Results and Discussion

The overall features of bluff body wakes have been investigated extensively in the past. Within limits required for engineering design, the predictions of quantities such as the lift and drag coefficient and the Strouhal number are quite satisfactory. Both numerical modeling and experiments yield meaningful data in this regard. There are new technological applications where it has become imperative to understand the nuances of the flow field. Disparities between the theory and the experiments and uncertainties in predictions significantly increase when this next level of detail is explored. The largest uncertainties are associated with each of the local instantaneous flow property. Between these two levels of detail, certain broad conclusions however can be drawn by examining other attributes of the flow structures. The spirit of the present work conforms to this idea, namely a complex time dependent field can be analyzed in terms of measures that preserve several of the flow complexities without averaging them.

Results obtained in the present research can be categorized as (1) temporal and spatial evolution of the wake at low Reynolds numbers, (2) wake characteristics at high Reynolds number and (3) hotwire measurements at low and high Reynolds numbers. Results for (1) and (2) have been obtained from numerical computation. The related code validation and grid independence studies have been reported in the respective sections. The results obtained in the present work have been organized in the following manner:

Low Reynolds number

- Transition and chaos in a two-dimensional wake

- Three-dimensional study of low Reynolds number flow
- Vortex structures and kinetic energy budget in two-dimensional flow
- Comparison of two- and three-dimensional models in low Reynolds number transitional flow
- Influence of inlet shear on the structure of wake

High Reynolds number

- Numerical study of the partially enclosed turbulent unsteady wake using RANS
- Model-free computation of high Reynolds number turbulent flow

Experiments

- Experimental study at low and high Reynolds numbers

5.1 Transition and Chaos in a Two-Dimensional Wake

In the present section, the wake of the square cylinder has been analyzed using the Direct Numerical Simulation (DNS). The Reynolds number range considered here is 40 - 800. The calculations have been carried out in two-dimensions. Consequently, transition to three-dimensionality in the physical problem leads to the appearance of additional harmonics in the numerical simulation. One can expect three-dimensionality of real flow fields to alter the critical Reynolds numbers but not the route to chaos.

The transition scenario of the wake of the square cylinder has been analyzed through different characterization tools applied to velocity traces. These tools are the spectra, autocorrelation functions, time-delay reconstructions, Poincaré maps, Lyapunov exponent and fractal dimension. Calculations have been carried out over a range of Reynolds numbers starting from a steady field, leading finally to a chaotic state of the flow. The issue of the flow topology and its relationship to transition and chaos is addressed. The effect of mesh refinement and time step on the transition have been taken into account to ascertain that the chaos observed in the present analysis has a physical and not a numerical basis. The present study can be viewed as an extension of an earlier work of Guzmán and Amon (1996) to flow past a square cylinder.

Table 5.1.1: Grid Independence Test

Re	Grid size	$\overline{C_D}$	$\overline{C_L}$	C_D'	C_L'
600	218×104	2.27	0.020	0.576	1.35
	436×208	2.35	0.016	0.586	1.49

The two-dimensional geometry (shown in Figure 1.3) for the present analysis has the following dimensions: $L_a=6.0$, $L=26.0$, $H=10.0$ and $B=1.0$. For computation, the flow domain is divided into a number of rectangular cells with a nonuniform mesh throughout the domain. The grid is clustered near the cylinder and then increased in geometric proportion away from it. At the inlet, the streamwise velocity profile is taken as uniform. No-slip boundary conditions have been used at all the solid walls. Free-slip boundary conditions have been applied over the two confining surfaces. The Orlanski boundary conditions (Orlanski, 1976) have been applied on the outflow plane.

The convective terms have been discretized using a second order central differencing scheme. The order of discretization dictates the accuracy of the solution whereas global energy conservation indicates the stability of the time-marching scheme. A more accurate spatial differencing could have been used. However, most higher-order schemes are not energy conserving (Kawamura *et al.*, 1986). Hence, a second order accuracy in space and time has been accepted to be an optimum choice for the present application. To avoid the spurious oscillations associated with central difference of the nonlinear terms, fine grids have been used in the simulation.

The accuracy of a numerical simulation depends on the resolution of the length and time scales associated with the physical problem. The grid resolution should be such that it can properly resolve the smallest length scale of the flow field. In the present work the grid independence study has been carried out to see the effect of grids on the time-averaged and rms values of the lift and drag coefficients. For the grid independence study, two different grid sizes, namely 218×104 and 436×208 have been tested for a Reynolds number of 600. This is the highest Reynolds number employed in the present work. The

Table 5.1.2: Comparison of Drag and Strouhal Number of the Present Study with Published Results

Re	Drag Coefficient, $\overline{C_D}$			Strouhal Number, S			
	Present ¹ (numerical)	Davis <i>et al.</i> ² (1984) (numerical)	Franke <i>et al.</i> ³ (1990) (numerical)	Present ¹ (numerical)	Davis <i>et al.</i> ² (1984) (numerical)	Franke <i>et al.</i> ³ (1990) (numerical)	Okajima ⁴ (1982) (experimental)
100	1.51	1.55	-	0.159	0.154	-	0.141-0.145
200	1.67	-	1.65	0.163	-	0.157	0.138-0.145
250	1.77	1.77	1.72	0.142	0.165	0.141	0.139-0.143
300	1.89	-	1.89	0.146	-	0.130	0.137-0.139
400	2.21	1.88	-	0.167	0.159	-	0.129-0.135

¹ Blockage (B/H) is 10% ² Blockage (B/H) is 0% ³ Blockage (B/H) is 8.3% ⁴ Blockage (B/H) is 0%

comparison of the lift and drag forces computed on these two different grid sizes is listed in Table-5.1.1. The maximum discrepancy in the time-averaged and rms values of drag coefficients are 3.4% and 1.7% respectively. The rms values of the lift coefficients on the two grids differed by 9.4%. Discrepancies at lower Reynolds number can be expected to be smaller. Most computations in the present work have been carried out with the grid size of 218×104 . The rms value of the lift coefficient is a stringent criterion for establishing grid independence at higher Reynolds numbers. The discrepancy reported above is thus not a cause for concern. The effect of grids and the time step on the transition scenario has also been studied and reported in a later section.

The computations have also been conducted for two different time steps, namely 0.0075 and 0.004. These two time steps showed no changes in the time-averaged as well as rms values of the lift and drag coefficients. Finally a time step of 0.0075 has been chosen for all the computations. The computations were started with different initial conditions corresponding to zero and uniform flow conditions. The flow field was seen to converge to the same asymptotic state for each of the initial conditions.

The computer code has been validated through comparison with numerical as well as experimental results over the Reynolds number range of 100 - 400. Table-5.1.2 shows the

comparison of the present computation with those of Davis *et al.* (1984), Okajima (1982) and Franke *et al.* (1990). The present results match well with Davis *et al.* (1984). However, the comparison with the experiments is not as good, probably due to the following reasons. (i) The experiments have a high inlet turbulence (0.5% in Okajima, 1982). This is totally absent in the numerical simulation. Experiments show that the Strouhal number decreases with the increase in inlet turbulence level (Lee, 1975). This trend is consistent with the data of Table-5.1.2. For example, at a Reynolds number of 400, the Strouhal number of 0.129-0.135 reported by Okajima (1982) is less than the numerically determined value of 0.167. (ii) The present study introduces a finite blockage effect through the free slip boundary condition on the side walls. Davis *et al.* (1984) have shown that there is an increase in the drag coefficient and Strouhal number with the increase in blockage ratio, B/H . For example, their results show that at a Reynolds number of 250, the drag coefficient and Strouhal number are 1.77 and 0.165 for zero blockage and 1.79 and 0.177 for a 16.67% blockage. The respective values in the present work are 1.77 and 0.142, the latter being larger than 0.139-0.143 reported by Okajima (1982). Thus the numerical results of the present study are in overall agreement with the published literature.

5.1.1 Analysis of data

Earlier studies of chaos exhibited by a nonlinear dynamical system were facilitated by the fact that the mathematical formulation led to a system of ordinary differential equations. The problem could then be analyzed through qualitative phase-space techniques. This simplification is not available for fluid flow problems. The governing equations, namely the Navier-Stokes equations are nonlinear PDE's. An exact solution of these equations is possible only under restrictive conditions and this generally corresponds to non-chaotic flows. Realistic configurations can only be numerically studied on a prescribed mesh. Consequently, the analysis of chaos is based on time series recorded during time marching of the numerical algorithm, at selected nodes of the mesh.

When the time series approach is adopted, the physical signal can be taken as the streamwise or transverse velocity component, or the instantaneous drag and lift signals. Simultaneously, any one point in the wake could form the basis of analysis. In the present study, it was observed that the transverse component of velocity resembled the lift signal. Similarly, the streamwise velocity showed similarity to the drag signal. In general, the

transverse velocity signal appeared to be less noisy compared to the streamwise component. However, a close examination showed their individual routes to chaos to be practically identical. Results in the present work have been derived using long signal lengths of the transverse velocity. The analysis is based on the long-time behaviour of the time series, *i.e.* the initial transient has been eliminated from consideration. The signals analyzed have been collected at a station $x=2.42$ along the wake centreline ($y=0$). Signals over the near-wake ($x<5$) were found to yield identical routes to chaos.

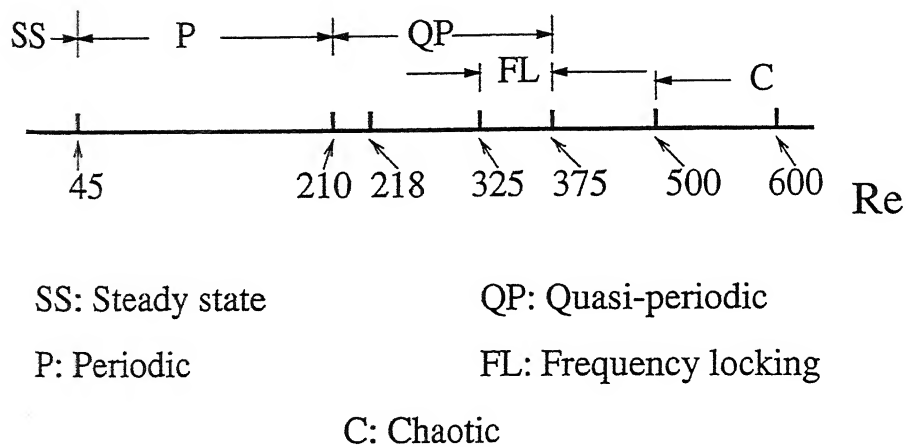


Figure 5.1.1: Schematic diagram of transition scenario in the wake of a square cylinder.

Based on the numerical solution of the unsteady Navier-Stokes equations, identification of transition and onset of chaos in the near-wake of a square cylinder are presented below. The transition characteristics discussed below are specific to the geometry of interest. One can expect the critical points to shift with changes in the blockage ratio as well as the side wall boundary conditions.

Numerical results show that upto a Reynolds number of 40, the flow is steady laminar with twin vortices contained in the recirculation bubble attached to the rear side of the cylinder. For Reynolds number greater than 45, the flow experiences the first Hopf bifurcation leading to a well defined periodicity in the wake. The separated shear layers roll up to become unstable, detach and the vortices are shed downstream. The flow remains periodic with a unique frequency upto a Reynolds number of 210. At

a Reynolds number of 218, the flow shows quasi-periodicity with two incommensurate frequencies following the second Hopf bifurcation. Subsequent frequencies seen in the velocity spectra are linear combination of these two frequencies. The frequency-locking mode, where the frequency ratio is a constant ($=0.5$) has been identified in the Reynolds number range of 325 - 375. The flow goes to a chaotic state probably after the third Hopf bifurcation. It was not easily detectable at Reynolds numbers after the flow comes out of the frequency-locking mode. Hence the onset of chaos is expected to occur in the range of Reynolds numbers 500 - 600. The transition scenario numerically determined in the present study has been summarized through a schematic diagram in Figure 5.1.1.

The transitions taking place in the wake of the square cylinder are explored in greater detail below. Results have been presented under the following heads: (1) Qualitative characterization of the wake dynamics (2) Analysis of chaos through quantitative characterization (3) Instantaneous flow field and (4) Influence of grid size on the chaotic flow.

5.1.2 Qualitative characterization of the wake dynamics

In the present study, the characterization of the wake has been carried out qualitatively in terms of the power spectra, autocorrelation function, time-delay reconstruction and the Poincaré section. The qualitative analysis allows one to visualise the unpredictable nature of the chaotic flow. The topology of the attractor emerges from the tools such as the Poincaré section. Quantification of chaos has been reported through the Lyapunov exponent and the fractal dimension. These parameters assist in a closer prediction of the onset to chaos, the persistence of chaotic flow regimes and the long term unpredictability of the chaotic flow.

5.1.2.1 Power spectra

The time-evolution of the wake has been recorded in the form of velocity signals at selected points in the near-wake and the instantaneous lift and drag acting on the cylinder. It should be noted that the statistical characteristics of the signal were quite similar at all points in the near-wake ($0 < x < 5$). The point chosen for discussion was one that gave the greatest clarity. Between the streamwise and transverse components of velocities, the

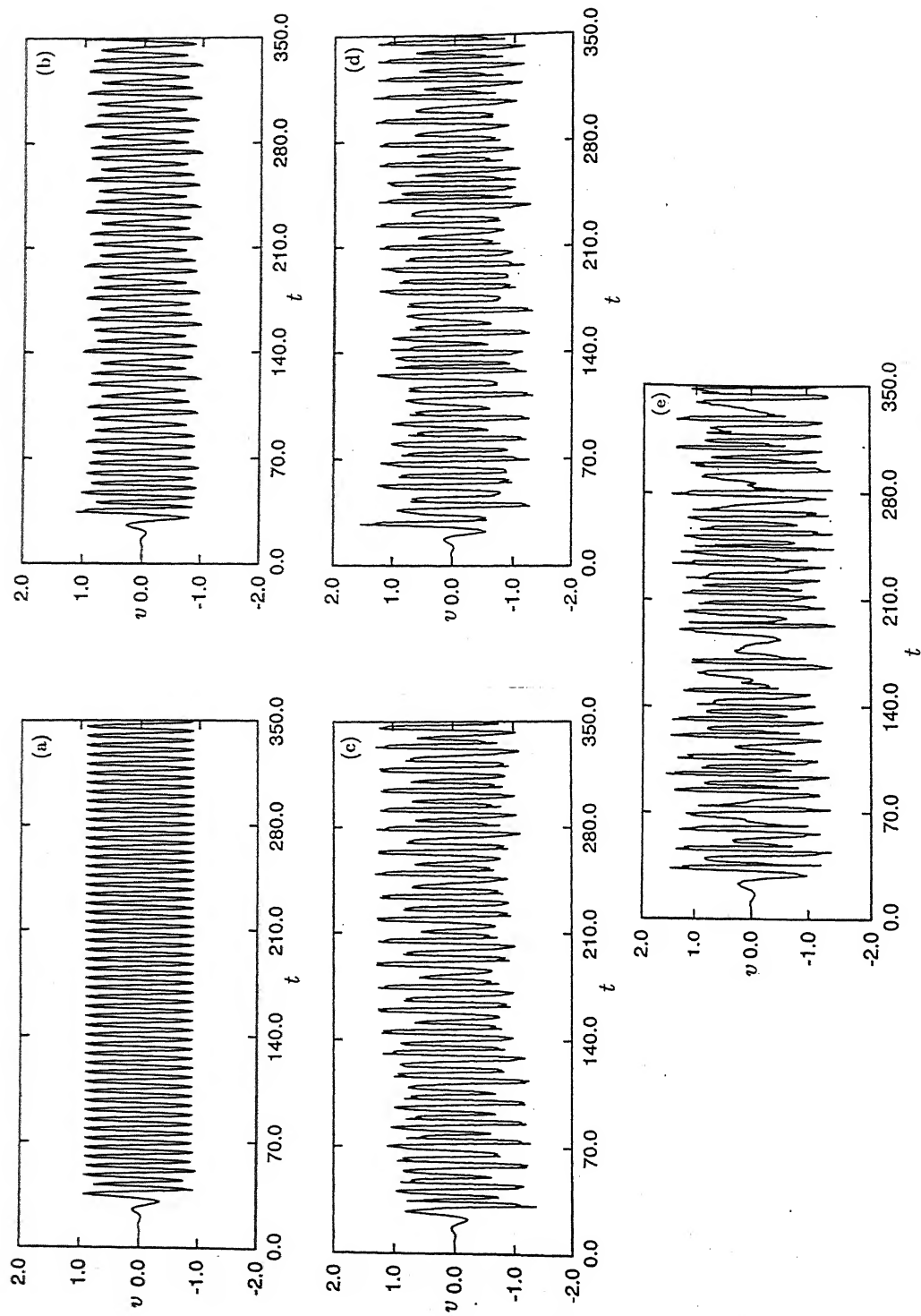


Figure 5.1.2: Transverse velocity signals at (a) $Re=210$ (b) $Re=218$ (c) $Re=300$ (d) $Re=325$ and (e) $Re=600$. With increasing Reynolds number the time trace reveals more harmonics.

former was found to be noisy even when selected peaks were clearly visible. Hence, the present analysis has been carried out primarily using the transverse component of velocity at a selected point on the wake centreline of the cylinder. The FFT algorithm has been used to calculate the power spectra of the time series of the velocity and the forces. The number of data points used for the present study is 2^{15} , with a time step of 0.0075. This corresponds to a minimum frequency of 4.069×10^{-03} , a maximum frequency of 133.33 and a resolution of 4.069×10^{-03} , in dimensionless form. All frequencies seen in the wake were well within this range. Specifically, all calculations were carried out over at least 40 cycles of the dominant harmonic component.

Initial segments of the velocity signals at the different Reynolds numbers in the wake are shown in Figure 5.1.2. The corresponding spectra have been shown in Figures 5.1.3(a-e). It is quite evident that at a Reynolds number of 210 (Figure 5.1.3(a)), the flow is truly periodic in nature with a single dominant frequency, f_1 . At a Reynolds number of 218 (Figure 5.1.3(b)), quasi-periodicity sets in with an additional frequency, f_2 and the linear combination ($m_1 f_1 \pm m_2 f_2$, integer m_1 and m_2) of f_1 and f_2 also being present. The number of frequencies which are linear combinations of the two frequencies f_1 and f_2 increases with the increase in Reynolds number in the quasi-periodic regime. This particular feature is evidenced through the Figure 5.1.3(c) (Re=300). Values of the primary as well as derived frequencies are marked in Figure 5.1.3.

Figure 5.1.3(d) shows the transition to the frequency-locking mode at a Reynolds number of 325. The ratio f_2/f_1 for the geometry of interest is 0.5. Because of the locking phenomenon, all additional frequencies are $(m_1 \pm m_2 f_2/f_1)$ times the dominant frequency, thus resulting in a discrete spectrum. The appearance of frequency-locking means that the strength of the nonlinear interaction between the two frequencies f_1 and f_2 are strong enough to create frequencies of observable spectral peaks. At a Reynolds number of 600 (Figure 5.1.3(e)), the flow is seen to have gone beyond quasi-periodicity and frequency-locking. The spectrum is still not broad-band, but is continuous around the peak frequencies. Other measures discussed later show the flow to have become chaotic at this Reynolds number.

The wake of the square cylinder is thus seen to follow the quasi-periodic/frequency-locking route to chaos. This is analogous to transitions in the wake of a circular cylinder (Vittori and Blondeaux, 1993) as well as the periodic converging-diverging channel (Guzmán and Amon, 1996). The route to chaos for a square cylinder is further investi-

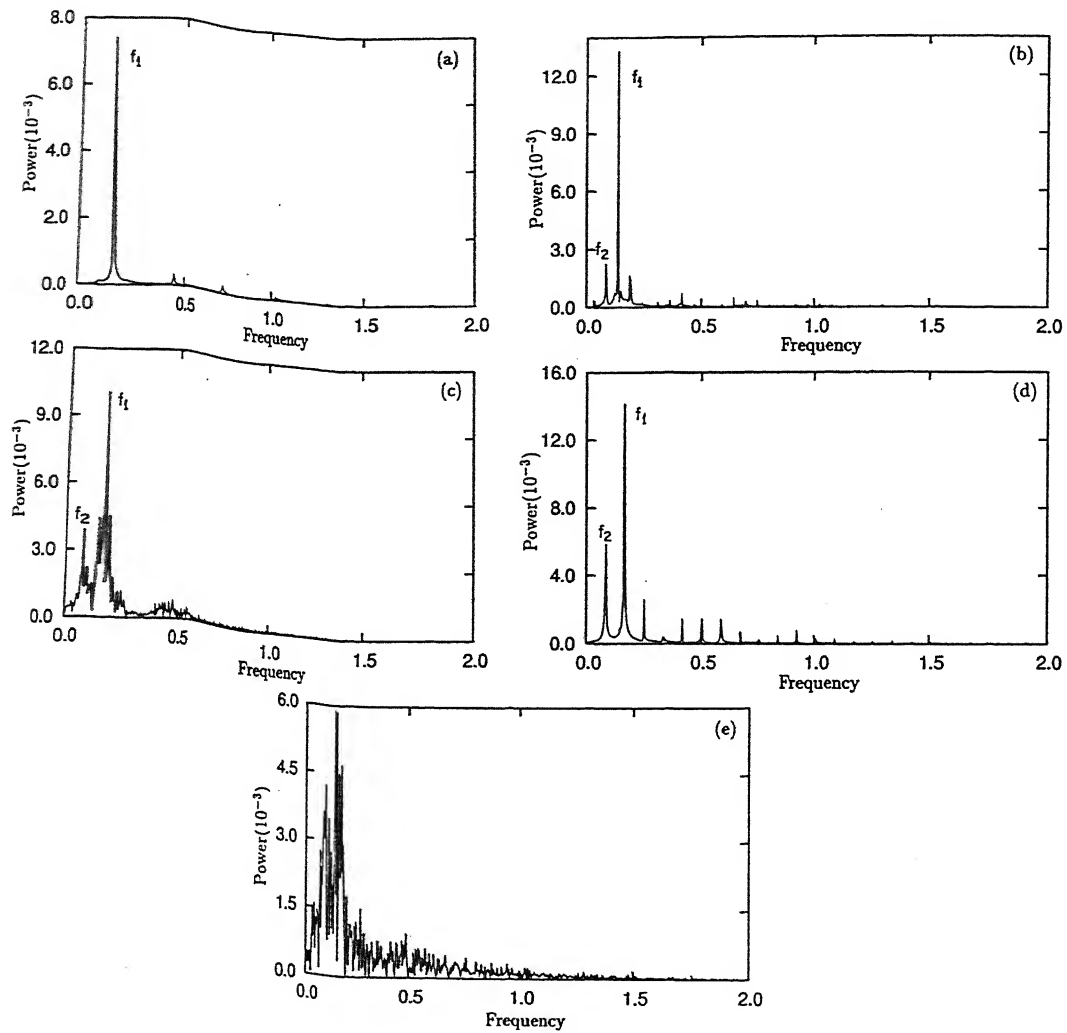


Figure 5.1.3 : Transverse velocity spectra at (a) $Re=210$ (b) $Re=218$ (c) $Re=300$ (d) $Re=325$ and (e) $Re=600$. The spectra show increase in peaks with increasing Reynolds number. The irregular spectrum in (c) becomes organized in (d) due to frequency locking and becomes broadband in (e) as a result of chaotic nature at this Reynolds number.

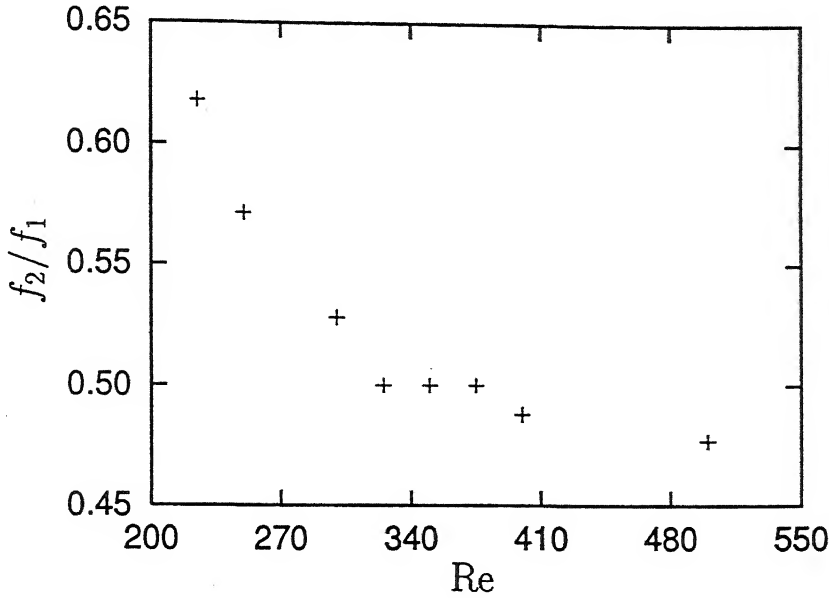


Figure 5.1.4: Variation of the fundamental frequency ratio (f_2/f_1) as function of Reynolds number. The frequency ratio drops to a constant value of 0.5 where frequencies get locked in the Reynolds number range of 325 - 375 and subsequently drop with Reynolds number.

gated below. The quasi-periodicity route to chaos can manifest in one of the following forms (Gollub and Benson, 1980)

1. Steady \rightarrow Unsteady \rightarrow T^2 torus (two frequency quasi-periodicity) \rightarrow Chaos
2. Steady \rightarrow Unsteady \rightarrow T^2 torus (two-frequency quasi-periodicity) \rightarrow T^3 torus (three-frequency quasi-periodicity) \rightarrow Chaos
3. Steady \rightarrow Unsteady \rightarrow T^3 torus (three-frequency quasi-periodicity) \rightarrow Chaos

The T^2 torus is formed in the phase-space when the two independent frequencies are incommensurate in nature. This requires that the ratios f_2/f_1 , f_3/f_1 and f_3/f_2 are irrational and vary continuously with the control parameter (Bergé *et al.*, 1986), the Reynolds number, in the present application. The two frequencies are said to be incommensurate at all time sequences other than the frequency-locked regime if the ratio of f_2 and f_1 decreases smoothly with the increase in Reynolds number. Hence the spectra in Figures 5.1.3(b-c) correspond to a quasi-periodic motion.

Figure 5.1.4 shows the variation of the frequency ratio (f_2/f_1) with Reynolds number. Quasi-periodicity starts at a Reynolds number of 218 but the frequency-locking phenomenon occurs at a Reynolds number of 325. With the increase in Reynolds number beyond a value of 218, the ratio decreases until it reaches the plateau at which the frequencies get locked. This locked frequency ratio (f_2/f_1) is 1/2 in Figure 5.1.4. The frequency-locking phenomenon is sustained upto a Reynolds number of 375. With the further increase in Reynolds number the ratio decreases again and the system goes to a chaotic state as seen in Figure 5.1.3(e). The three-frequency quasi-periodicity route to chaos has not been detected in the present simulation. The detection of the third frequency is difficult. Before the system goes to a chaotic state, the third frequency is generated when the system contains a large number of harmonics. Therefore, detecting the third frequency among the harmonics involves a large uncertainty.

5.1.2.2 Autocorrelation functions

The autocorrelation function, $A(T)$ is a useful tool to analyze fluid motion in the time domain. It is a measure of the maximum time upto which the flow is correlated with itself. If the fluid motion is organized, the correlation function is finite for a longer time *i.e.*, one can accurately predict the fluid motion within this time frame with prescribed conditions for fluid velocity at an arbitrary initial instant of time. For a periodic signal, $A(T)$ is periodic and for a chaotic signal $A(T)$ tends to zero. Thus one cannot predict the future motion of the particle, for $T > T_c$, where T_c is a measure of the time during which the motion is correlated with itself. Chaos can be said to arise beyond the time T_c . The autocorrelation function is defined as

$$A(T) = \frac{\overline{v(t)v(t+T)}}{\overline{v(t)^2}}$$

Here overbar denotes the ensemble average of the product of the instantaneous signals $v(t)$ and its time shifted form $v(t+T)$ (both with zero mean). This average can be calculated as

$$\overline{v(t)v(t+T)} = \lim_{T_p \rightarrow \infty} \frac{1}{T_p} \int_0^{T_p} v(t)v(t+T)dt$$

In practice, it is evaluated using Fourier transforms. The autocorrelation function obtained from the time series of the transverse velocity signal for different Reynolds numbers are shown in Figure 5.1.5. Figure 5.1.5(a) shows the autocorrelation function

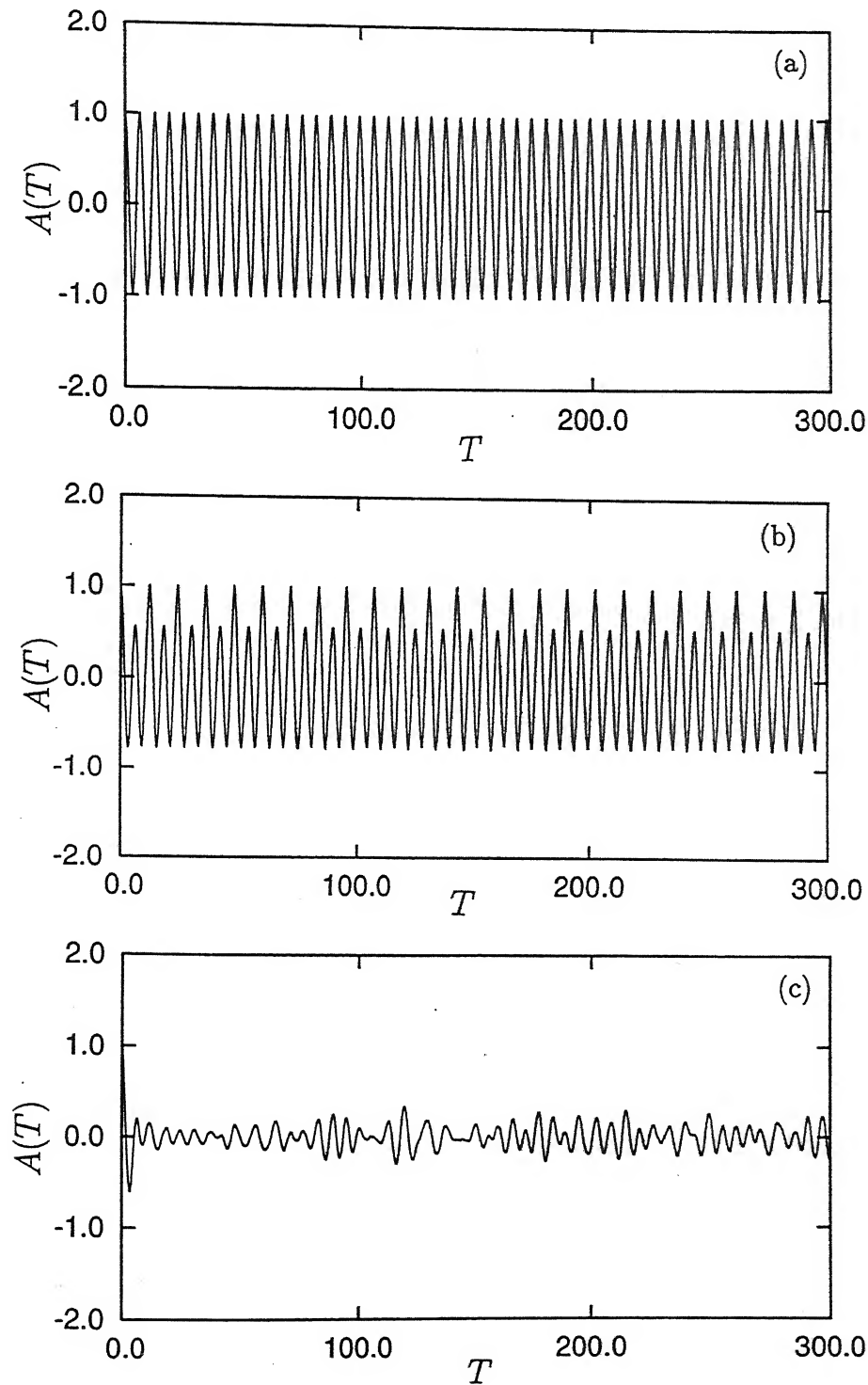


Figure 5.1.5: Autocorrelation function $A(T)$ of the transverse velocity components: (a) $Re=210$ (b) $Re=325$ and (c) $Re=600$. The periodic nature of autocorrelation function shows that the wake has only one frequency. The smaller value of autocorrelation function at a Reynolds number of 600 signifies that the wake is chaotic in nature.

at the Reynolds number of 210 when the wake is periodic with one dominant frequency. The autocorrelation function at a Reynolds number of 325 (Figure 5.1.5(b)) also shows periodicity since at this Reynolds number the flow gets frequency-locked. For a Reynolds number of 600, the autocorrelation function tends to become small rapidly, but persists with small amplitude fluctuations for a sufficiently larger time lag (Figure 5.1.5(c)). The flow can now be classified as chaotic.

5.1.2.3 Time-delay phase-space representation

Phase-space representation is a convenient option available to distinguish between periodic, quasi-periodic and chaotic phenomena. Continuous systems have a particular difficulty in constructing the phase-space. This is because of the absence of the knowledge of the precise number of dependent variables, *i.e.* the number of degrees of freedom in which the phase-space trajectory is to be represented. From an experimental view point, simultaneous measurement of several dependent variables can be difficult. In contrast, extensive information can be obtained for a single dependent variable with accuracy and adequate signal length. A higher dimensional phase-space can be constructed from the time series using the procedure of time-delay reconstruction. This phase-space contains information that is equivalent to the original and is based on the independent degrees of freedom of the system (Baker and Gollub, 1996).

In the present work, the signal recorded is the transverse velocity $v(t)$, a scalar time series. It is now possible to define a vector series whose components are $(v(t), v(t + \tau), \dots, v(t + (m - 1)\tau))$. The equivalence between the original and the reconstructed phase-spaces can be stated as follows: If the system attractor in the original full phase-space is n dimensional, then the m dimensional reconstructed attractor will have the same invariant properties, *e.g.* fractal dimensions or Lyapunov exponents for all m over a minimum value that is not greater than $2n+1$ (Takens, 1981). For the equivalence to be complete, the time-delay τ and the embedding dimension m need to be properly selected. The reconstructed phase-space will be insensitive to this parameter if the time series is infinitely long, is free of noise and has a adequate temporal resolution (Guzmán and Amon, 1996). In the present work the time series had a length of 2^{15} to 2^{16} points with fairly small time steps. Hence the time-delay could have been arbitrarily chosen. However, in the calculation the time-delay was adjusted till the geometric properties of

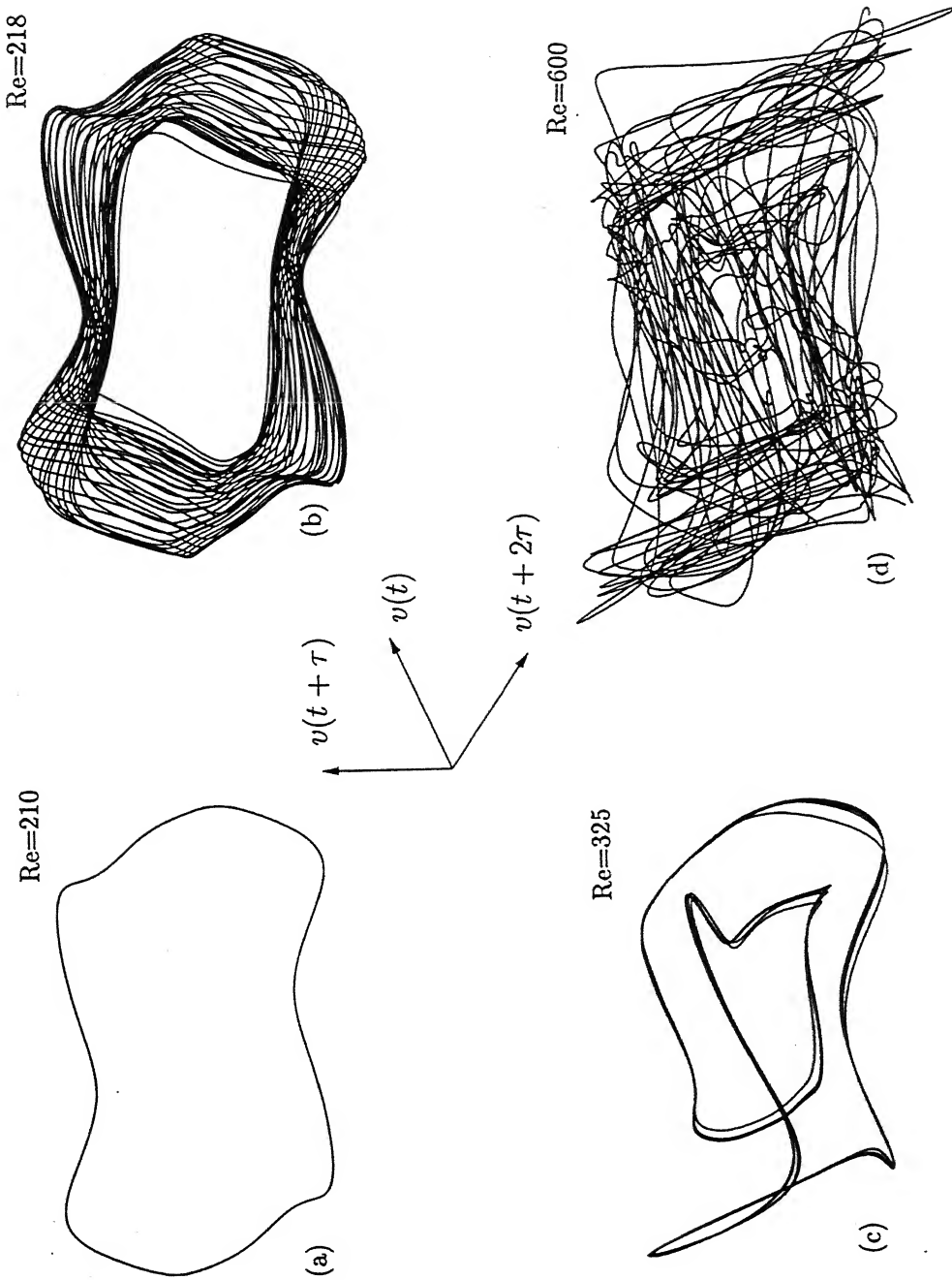


Figure 5.1.6: Three-dimensional time-delay representation of the transverse velocity component: (a) $Re=210$ (b) $Re=218$ (c) $Re=325$ and (d) $Re=600$. The phase-space from a quasi-periodic state in (b) showing more harmonics go to frequency locked organized quasi-periodic state in (c) with strong frequency interactions and becomes totally disorganized at a Reynolds number of 600.

the phase-space attained convergence. Results presented in this section are based on a time-delay of $\tau=0.585$; identical results were seen when the time-delay was increased to $\tau=1.17$. Results were computed with $m=2$ and $m=3$ corresponding to the two- and three-dimensional reconstructed phase-spaces. The pattern that emerged led to identical conclusions for the onset of chaos. Hence, results for $m=3$ alone have been discussed below.

The reconstructed phase-space based on time-delay reconstruction is shown in Figure 5.1.6. The three different axes of the phase-space corresponds to $v(t)$, $v(t + \tau)$ and $v(t + 2\tau)$. Figure 5.1.6(a) is at a Reynolds number of 210 and clearly shows a limit cycle representing periodic flow. The orbit of the attractor is unique and represents the periodic nature of the flow. At a Reynolds number of 218, the flow is quasi-periodic and the attractor surface is deformed. This is shown in Figure 5.1.6(b). The surface has a shape of a T^2 torus. The deformed shape of the attractor can be attributed to the fact that the quasi-periodic attractor is a superposition of two incommensurate fundamental frequencies along with their harmonics (sub- and super-harmonics). At a Reynolds number of 325 (Figure 5.1.6(c)), the attractor becomes more organized and closed owing to the frequency-locking phenomenon. The orbits form a closed loop which confirms the locking of the two fundamental frequencies in the ratio (f_2/f_1) of 0.5. With an increase in the Reynolds number to 600, the attractor becomes disorganized and the pattern seen in the frequency-locking regime is completely disturbed. The possibility of appearance of a strange attractor is explored in the subsequent sections. The orbits do not follow any particular trajectory as in the periodic and quasi-periodic regime.

5.1.2.4 Poincaré section

The phase-space diagram in dimensions higher than three may be needed for a detailed study of chaos. As discussed above, this can be a complicated task. A Poincaré section can be used to simplify the phase-space diagram of systems having higher degrees of freedom. This device enables one to study a system by reducing the phase-space dimensions systematically. This is accomplished by converting a continuous-time evolution into a discrete-time mapping. The reduced attractor is two-dimensional and is not identical to the original attractor. It preserves however the topological properties of the original attractor from which it has been generated (Bergé *et al.*, 1986).

The Poincaré section has been constructed from the time series of velocity by sampling the signal stroboscopically at a particular frequency (Bergé *et al.*, 1986). With this approach the same time signal that has been used earlier to qualify chaos can be utilized. The state vectors $F(t_s) = \{v(t_s), v(t_s + \tau)\}$ are generated and this is similar to the phase-space reconstruction, the only difference being the sampling time. With the above state vectors, the trajectory of the pseudo phase-space is constructed with the variables $\{v(t_s), v(t_s + \tau), t_s\}$. The Poincaré section is then determined by the successive points of intersection between the trajectory and a plane perpendicular to the axis at equal intervals of time $T_s = T_k/4$, where T_k is the fundamental time period of the system corresponding to the dominant frequency.

The Poincaré section is to be determined with a stroboscopic period equal to the time period of the system (Guzmán and Amon, 1996; Bergé *et al.*, 1986). However, in a quasi-periodic state, the fundamental frequency associated with the flow changes as the control parameter is varied. Therefore, for a quasi-periodic flow, the stroboscopic period is taken equal to the fundamental period appropriate for the Reynolds number employed (Guzmán and Amon, 1996). As a result, even the Poincaré section in the periodic state gives a closed trajectory in the place of a point attractor. In the present study, a stroboscopic period equal to one quarter of the fundamental period in the quasi-periodic regime has been chosen. A stroboscopic period equal to the fundamental one was also found to give a similar Poincaré section. The number of points in the time series needed for accurate representation of the Poincaré section was found to be 40000 to 50000.

Figures 5.1.7(a-e) depict the Poincaré sections corresponding to Reynolds numbers in the range of 210 - 600. The periodic solution at a Reynolds number of 210 (Figure 5.1.7(a)) shows a well-organized closed curve. The quasi-periodic flows (Re=218, Figure 5.1.7(b) and Re=300, Figure 5.1.7(c)) show the trajectory points within the pseudophase space and intercept the section at different locations in an organized manner. The pseudophase space is densely covered due to the additional frequencies which are a linear combination of the two incommensurate frequencies f_1 and f_2 and these intersections of the section are bounded. But at a Reynolds number of 325 (Figure 5.1.7(d)), the intersection points on the Poincaré section take a well organized pattern owing to frequency-locking of the flow at this Reynolds number. This particular behaviour of the interceptions on the Poincaré section is related to the commensurate frequency ratio. With further increase in Reynolds number (Figure 5.1.7(e)) the organized behaviour of the Poincaré section breaks down,

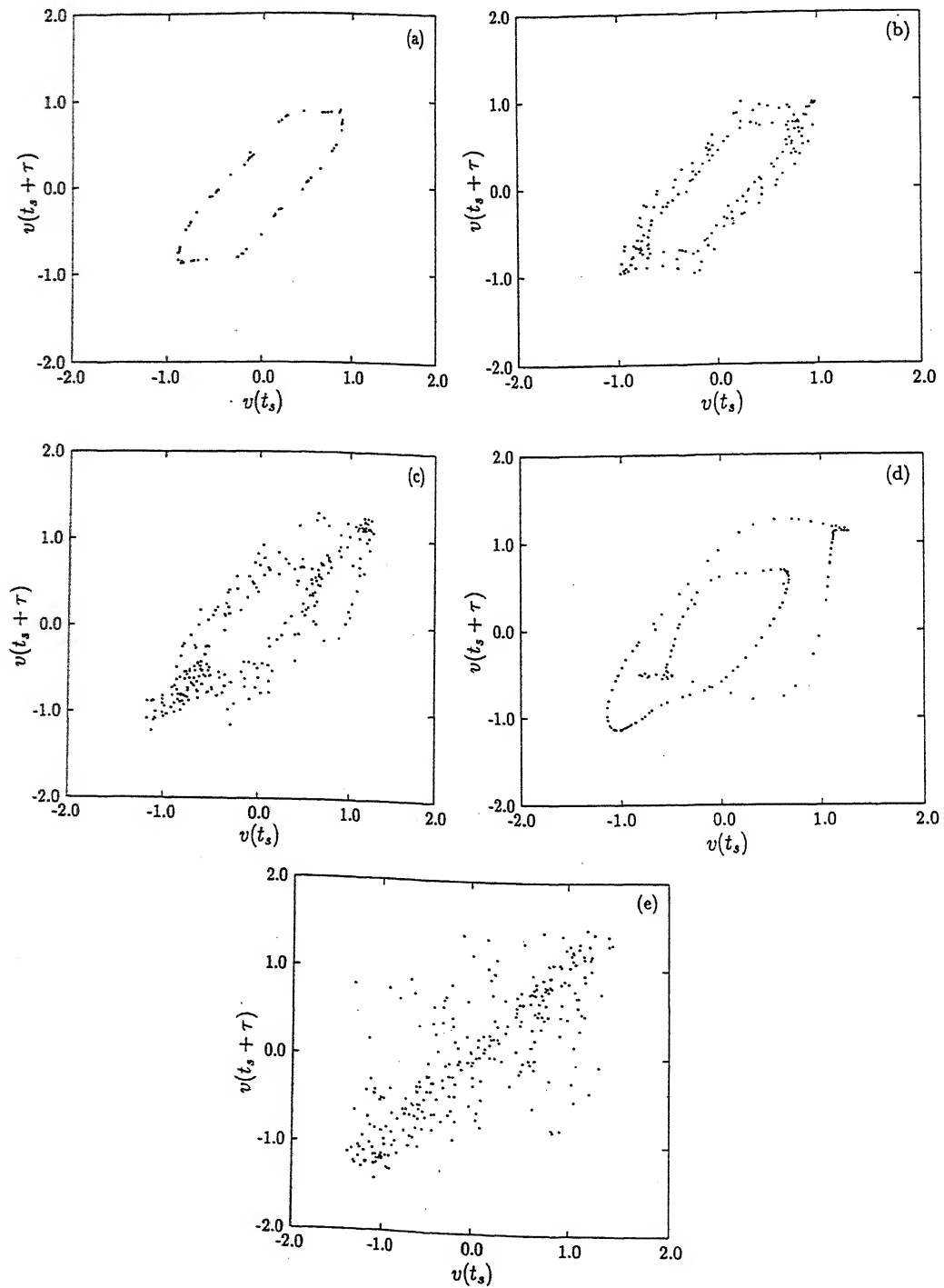


Figure 5.1.7: Poincaré section of the transverse velocity component: (a) $Re=210$ (b) $Re=218$ (c) $Re=300$ (d) $Re=325$ and (e) $Re=600$. The closed orbit in (a) at a Reynolds number signifies periodic wake whereas the total spreading of the attractor at a Reynolds number of 600 in (e) shows chaotic nature. The frequency locked situation is revealed by the organized attractor at a Reynolds number of 325 in (d) with respect to a Reynolds number of 300 in (c) at which the wake shows quasi-periodicity.

and shows signs of the flow entering the chaotic regime.

5.1.3 Analysis of chaos through quantitative parameters

The quantitative analysis of the wake carried out by calculating the Lyapunov exponents and the fractal dimensions are reported below.

5.1.3.1 Lyapunov exponents

The spectrum of Lyapunov exponents is the most complete possible characterisation of the geometric properties of an attractor and the dynamical properties of the flow. This is because of its relationship to the fractal dimension of the attractor and the entropy of the system. The Lyapunov exponents (λ_i) are measures of the long-time average exponential growth or decay of infinitesimal perturbations to a phase-space trajectory. In operational terms, these exponents measure the divergence of two neighbouring states on the time-axis and hence the sensitivity of the system to the initial condition. The number of Lyapunov exponents equals the number of independent phase-space dimensions. Negative Lyapunov exponents correspond to the decay of perturbations towards the attractor. On the other hand the positive Lyapunov exponents imply exponential growth of any infinitesimal perturbations on the attractor leading to the chaotic (strange) attractor. With a given set of ordered Lyapunov exponents $\lambda_1 \geq \lambda_2 \geq \lambda_3 \dots$, the attractor having all negative exponents implies a fixed point attractor while the attractor with all negative value but one with zero implies a limit cycle or periodic attractor. An attractor having one positive Lyapunov exponent is termed as a chaotic attractor. The sign and the number of the Lyapunov exponents thus give detailed information about an attractor. Specifically, the attractor for quasi-periodic flow having four exponents may exhibit the following behaviour (Bergé *et al.*, 1986):

1. quasi-periodic regimes with three frequencies $(0, 0, 0, -)$
2. quasi-periodic regimes with two frequencies $(0, 0, -, -)$
3. periodic regimes with one frequency $(0, -, -, -)$
4. chaotic regime $(+, 0, -, -)$

A positive Lyapunov exponent indicates that there is a direction on the attractor in which perturbations will grow exponentially fast. Here the attractor is bounded within the phase-space, but it is not possible to predict the state of the system at any arbitrary future time instant due to the unavoidable growth of uncertainty.

Different algorithms have been developed to calculate Lyapunov exponents (Wolf *et al.*, 1985; Eckmann *et al.*, 1986; Vastano and Moser, 1991; Keefe *et al.*, 1992). In the present study, the algorithm proposed by Wolf *et al.* (1985) to calculate the largest positive Lyapunov exponent out of the time series data, has been implemented. Extensive trials with different embedding dimensions were carried out to find the reliable one for the calculation of the Lyapunov exponent. The trials with higher dimensions led to similar qualitative behaviour and quantitative differences greater than $\pm 8\%$ were not seen at any Reynolds number.

Figure 5.1.8 shows the time variation of the Lyapunov exponents at different Reynolds numbers. The number of points used in the time series for each of the Reynolds numbers is of the order of 60000. As discussed earlier, a zero value of the Lyapunov exponent has been obtained for non-chaotic flows upto a Reynolds number of 500. The Poincaré section however showed the presence of a strange attractor at a Reynolds number of 500. At a Reynolds number of 600, the flow becomes clearly chaotic with a mean Lyapunov exponent of 0.137 bits/orbit. With an increase in the Reynolds number, the Lyapunov exponent is seen to increase thus showing that the system approaches a higher dimensional chaotic state. The flow at a Reynolds number of 800 gave a mean-Lyapunov exponent of 0.314 bits/orbit (Figure 5.1.8).

5.1.3.2 Fractal dimension

The fractal dimension of chaos is characterized by the stability of the flow on the attractor. Fixed points for steady flows, periodic orbits for one frequency oscillatory flows and N -tori for N -frequency motions are all attractors with trajectories remaining sufficiently close for all time. Therefore, for all the above cases, the flow is stable. The chaotic or strange attractor is characterized by the unstable nature of the flow. Due to the instability, infinitesimal perturbations grow at an exponential rate in one or more directions of the attractor depending on its geometry in the N -dimensional phase-space. An attractor becomes chaotic when it has one positive Lyapunov exponent (Grassberger and Procaccia,

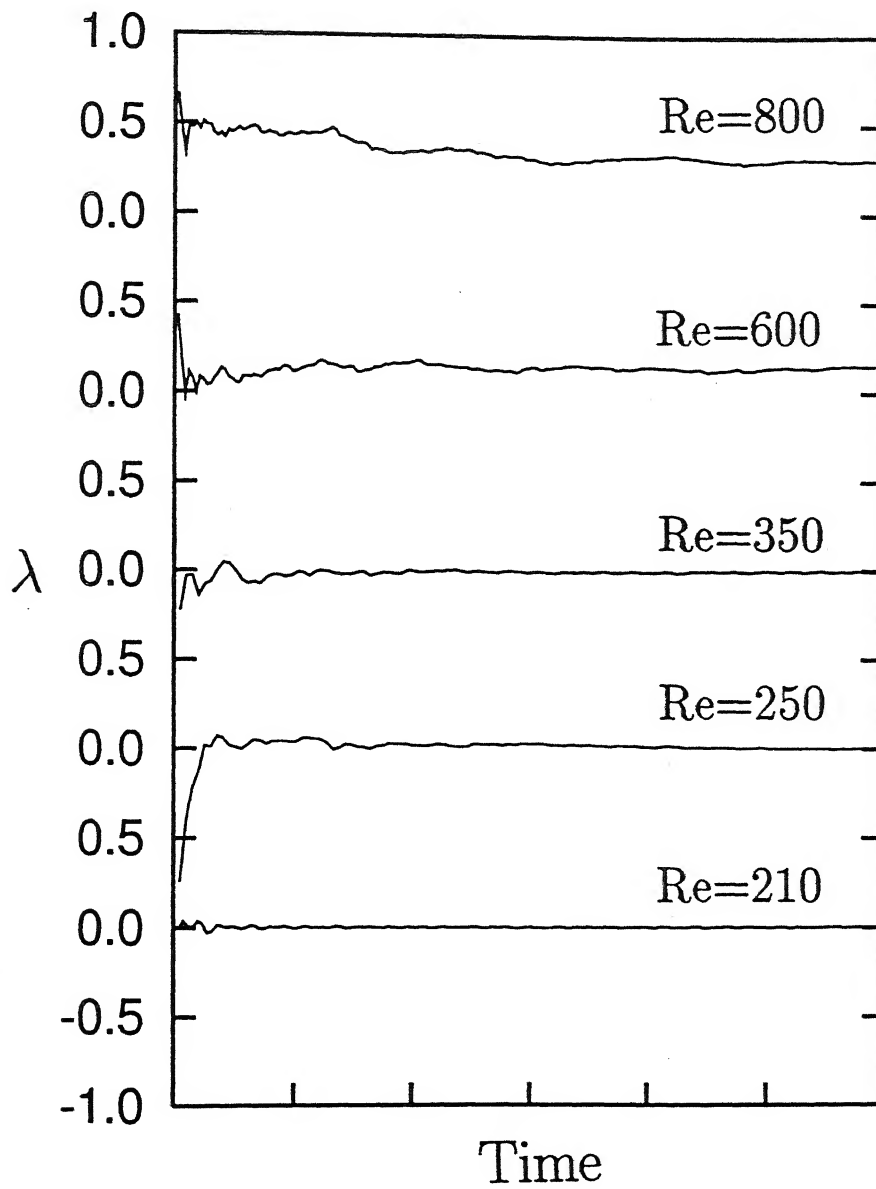


Figure 5.1.8: Temporal variation of the largest Lyapunov Exponent (λ). The positive value of the exponent at a Reynolds number of 600 proves that the flow is chaotic in nature and the magnitude of the exponent increases with increasing Reynolds number.

1983; Vastano and Moser, 1991). The corresponding geometrical property of the attractor is reflected in its fractal dimension.

The fractal dimension is a geometric measure of the space-filling properties of the process being studied. It has been widely used to understand complexity in diverse phenomena. Examples are (a) the topology of the natural rock fractures and (b) intermittency of viscous dissipation at the smallest length scales in turbulence. In the present context, it has been used to understand the fluctuations in the velocity signal (originally one dimensional) and the extent to which it fills the $v(t) - t$ plane due to its chaotic nature. Thus, values of the fractal dimension of the time series greater than unity indicate chaos.

There are different ways to calculate the fractal dimension of an attractor. One such method first measures the correlation dimension and relates it to the fractal dimension (Grassberger and Procaccia, 1983). Another method measures the fractal dimension from the spectrum of Eulerian Lyapunov exponents, λ_i . The fractal dimension is related to the Lyapunov exponents through the Kaplan-Yorke conjecture (Frederickson *et al.*, 1983). Experiments as well as numerical studies of fluid flow systems show that strange attractors are low dimensional at the onset of chaos as well as transitional Reynolds numbers. The dimension of the attractor increases with the Reynolds number, reaching an asymptotic value at the fully developed turbulent state (Pulliam and Vastano, 1993 and Vastano and Moser, 1991).

The temporal flow evolution which shows erratic behaviour on both short and long timescales have been examined in the present work using the Hurst's rescaled range analysis. The Hurst's rescaled range analysis (R/S) is a statistical method for processing a time series and estimating its fractal dimension, d . The records are characterized by the Hurst's exponent, Hr , and the trace of the record can be shown to have a fractal dimension $d=2-Hr$ (Feder, 1988). The fractal dimension of the time series describes the relationship between the variance and the time scale of the time series. Fractal systems have neighbour-to-neighbour correlation at all scale levels. The variance drops less rapidly with the increased resolution of the time series when neighbouring elements are positively correlated. If a signal $\xi(t)$ is divided into intervals of time Δt , and the mean as well as the variance are calculated for each interval, then there will be a lower variance when the interval length is increased. Therefore, the relationship between the variance and the sampling time may fit a power law. The fractal dimension of the time series can then be calculated by the Hurst's rescaled range analysis (Guzmán and Amon, 1996).

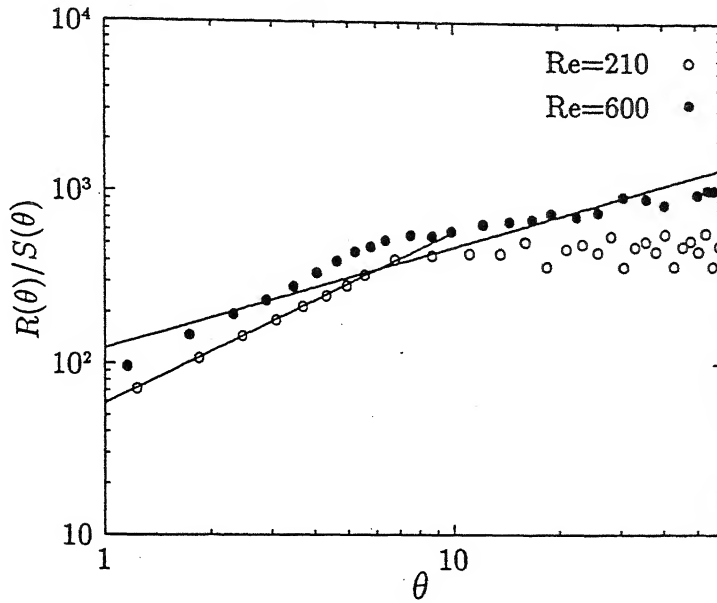


Figure 5.1.9: Logarithmic plot of the rescaled range $R(\theta)/S(\theta)$ vs θ . The slope determines the Hurst's exponent Hr and the fractal dimension $d=2-Hr$. The smaller slope at a Reynolds number of 600 shows that the fractal dimension of the time series is more than one and it is chaotic.

The fractal dimension d of the time series of the transverse component of velocity has been calculated using Hurst's empirical law and the rescaled range analyzes described by Feder (1988). In this approach, the exponent is calculated by measuring the slope of the log-log curve of $R(\theta)/S(\theta)$ vs θ . The term $R(\theta)/S(\theta)$ is the rescaled range:

$$R(\theta) = \max\{X(t, \theta)\} - \min\{X(t, \theta)\}, \quad 1 \leq t \leq \theta$$

It is the range defined as the difference between the maximum and minimum accumulation influx $X(t, \theta) = \sum_{\alpha=1}^t \{\xi(\alpha) - \langle \xi \rangle_\theta\}$ from the mean flow $\langle \xi \rangle_\theta = (1/\theta) \sum_{\alpha=1}^\theta \xi(t)$ for a given interval of time θ ; and, $S(\theta)$ is the standard deviation of the modified series $X(t, \theta)$.

Figure 5.1.9 shows the plot of $R(\theta)/S(\theta)$ vs θ corresponding to Reynolds numbers of 210 and 600. For periodic flows $R(\theta)/S(\theta)$ will be sinusoidal for θ greater than the time-period. Hence, the slopes are calculated using the $R(\theta)/S(\theta)$ data before it becomes periodic. For Reynolds numbers of 210 and 600 the slopes in Figure 5.1.9 have been found to be 1.0 and 0.59. The corresponding fractal dimensions are 1.0 and 1.41. The fractal dimension greater than unity corresponds to the unpredictable nature of the flow and

thus proves that the flow at a Reynolds number of 600 is chaotic in nature.

5.1.4 Instantaneous flow field

The numerical results obtained by solving the two-dimensional, incompressible form of the Navier-Stokes equations have been analyzed to obtain the flow structure and its relationship to transition. Figure 5.1.10(a) shows the vorticity contour for a Reynolds number of 40. At this Reynolds number, the flow is steady with two weak recirculation bubbles behind the cylinder. The flow separates at the leading edges, attaches again and finally separates at the trailing edges. The flow shows the presence of strong vorticity in the separating shear layer and symmetry about the wake centreline. At a Reynolds number of 210 (Figure 5.1.10(b)), the flow shows a pure vortex shedding pattern. The oscillation in all flow properties is sustained by the alternate shedding of vortices from the top and the bottom surfaces of the cylinder. Vortex shedding is initiated as follows: The separating shear layer becomes unstable and rolls up towards the centreline of the wake. The vortices then get detached from the cylinder and convected downstream accompanied by a decay in the peak vorticity. At a higher Reynolds number the flow loses its shedding symmetry. The vorticity contours (Figure 5.1.10(c)) at a Reynolds number of 218 show a minor asymmetry of the shedding due to the quasi-periodic nature of flow. Figure 5.1.10(d) depicts the flow structure at a Reynolds number of 325. The shedding pattern of the flow is quite complex. The regular pattern is seen to have broken but the near-wake shows organized pattern as at lower Reynolds numbers. The far-wake shows irregularity due to nonlinear interactions among the different vortices. The regular near-wake shedding pattern is disturbed with the further increase in the Reynolds number. The contours at a Reynolds number of 600 (Figure 5.1.10(e)) show aperiodic flow behaviour and the complexity of the flow structure is seen in the near-wake itself.

5.1.5 Influence of grid size on the chaotic flow

It is necessary to assess the sensitivity of the results obtained thus far to grid refinement. To study this aspect, flow at a Reynolds number of 600 has been taken up for comparison. At this Reynolds number, the flow is chaotic and hence is expected to exhibit a definite dependence on the grid size. While computations have been performed in the previous

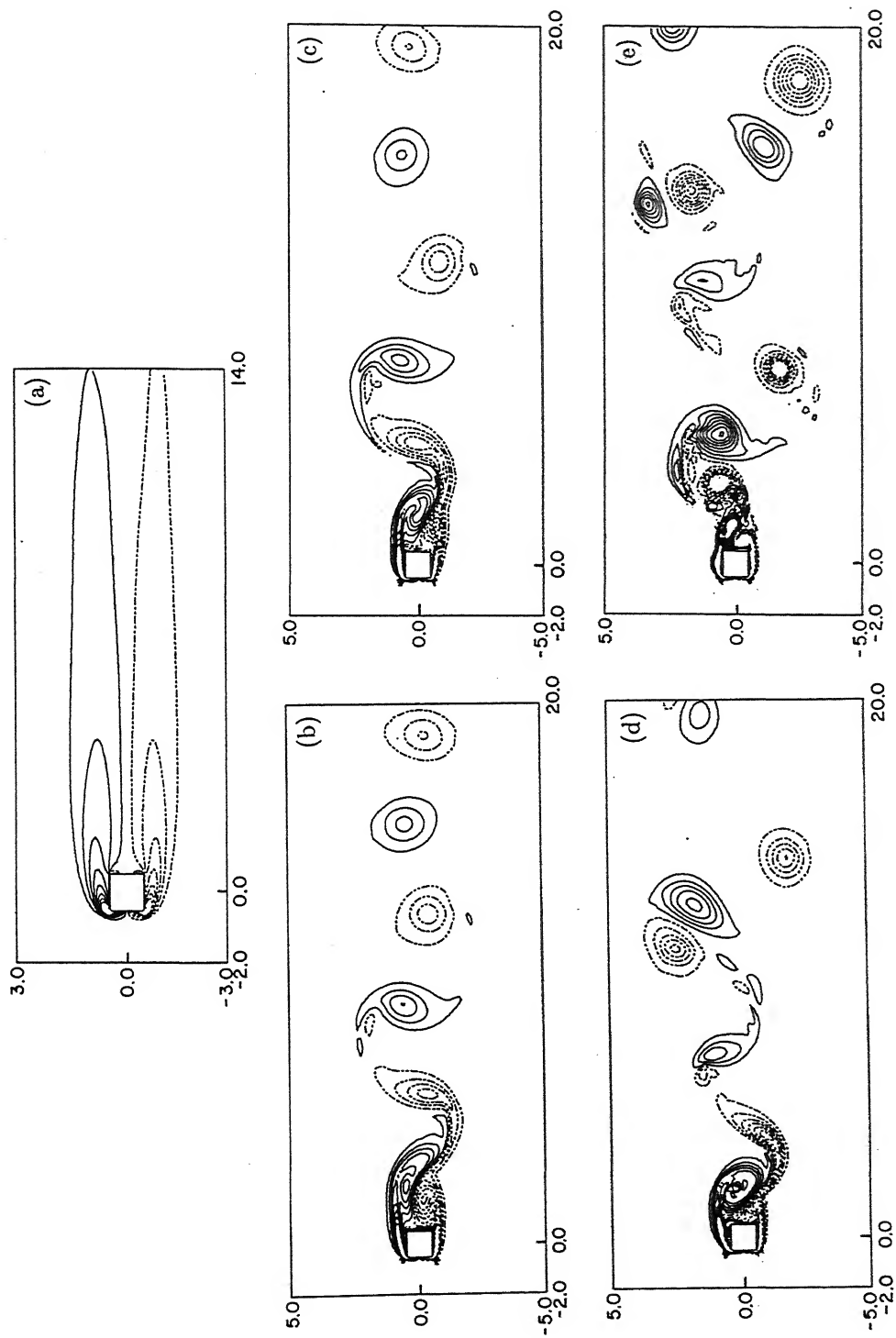


Figure 5.1.10: Instantaneous vorticity contours at different Reynolds numbers: (a) $Re=40$ (b) $Re=210$ (c) $Re=218$ (d) $Re=325$ and (e) $Re=600$. The wake becomes complex with increasing Reynolds number.

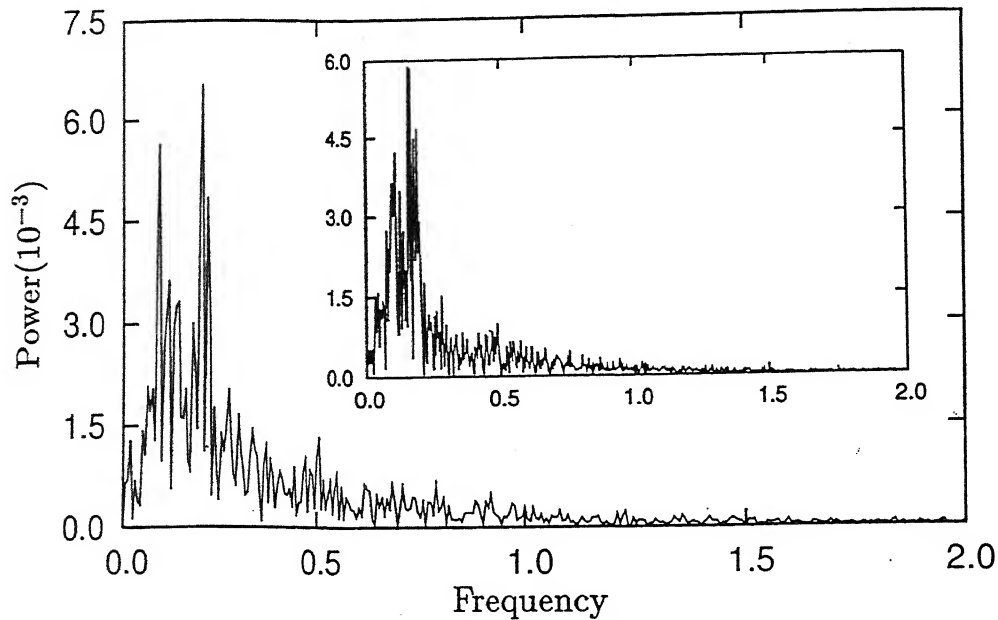


Figure 5.1.11: Power spectrum for a Reynolds number of 600 at grid size of 436×208 ; inset : grid size of 218×104 . The similarity between the two spectra shows that generated chaos in physical in nature.

sections on a 218×104 grid, a grid comprising of 436×208 cells have been employed for comparison. The respective timestep derived on the basis of numerical stability are 0.0075 and 0.005 respectively. Thus the new grid is finer than the original by a factor of 2 in each direction and a factor 1.5 in time. On this grid, the CPU time needed for a single Reynolds number was 15 days of CPU time on the available machines.

Figure 5.1.11 is a comparison of the spectra of the transverse velocity at a predetermined point in the wake. It is clearly seen that the spectra are similar, both in terms of peaks as well as the characteristic frequencies. The Lyapunov exponents on the coarse and the fine meshes are 0.137 and 0.155 bits/orbit respectively. Similarly the corresponding fractal dimensions are 1.41 and 1.32 respectively. Data regarding the lift and drag coefficients are presented in Table-5.1.1.

The above discussion shows that the flow exhibit a small dependence on the grid size and the time step. It is however not large enough to violate any of the conclusions drawn earlier.

5.1.6 Closure

Two-dimensional unsteady flow in the wake of a square cylinder has been numerically analyzed for the sequence of transitions leading to chaos. Major conclusions to emerge from the study are:

1. The periodic \rightarrow quasi-periodic \rightarrow frequency-locking \rightarrow chaotic route to chaos has been established.
2. The critical Reynolds numbers for each transition respectively are 45, 218, 325 and 600.
3. Quasi-periodicity and frequency-locking are clearly brought out in terms of spectra, autocorrelation function, time-delay reconstruction and the Poincaré section. When the flow becomes chaotic, the spectrum is seen to broaden, the autocorrelation function diminishes rapidly towards zero, the Poincaré section is space filling and the time-delay reconstruction becomes completely irregular.
4. Quantitative measures such as Lyapunov exponent and fractal dimension of the time series are consistent with the identified transition sequence. For the Lyapunov exponent the numerical values are $0 \rightarrow 0 \rightarrow 0 \rightarrow 0.137$ corresponding to the transition Reynolds numbers of (2). The fractal dimension was 1.0 at $Re=210$ and 1.41 at $Re=600$.
5. At a Reynolds number of 500, the flow was non-chaotic based on the Lyapunov exponent (which was zero) while the Poincaré section showed a strange attractor.

5.2 Three-Dimensional Study of Low Reynolds Number Flow

In the earlier section time-domain analysis has been carried out to understand the transition route of the wake of a square cylinder. The wake of a square cylinder also undergoes spatial transition from a two-dimensional to a three-dimensional state. In the present section, spatial transition of the wake of a square cylinder has been discussed.

The geometry for three-dimensional analysis is schematically shown in Figure 1.3. The relevant dimensions of the geometry are $L=22.0$, $L_a=7.0$, $A=6.0$ and $H=10.0$. In relation to this figure, the boundary conditions employed for the present investigation are: (i) The confining surfaces are modeled as the free-slip, for example, at the transverse confining surfaces $y=\pm H/2$, $\partial u/\partial y=v=\partial w/\partial y=0$ (ii) At the inlet, a constant streamwise velocity has been used with other velocities being set to zero (iii) convective boundary condition has been employed at the exit plane. For all the solid surfaces on the obstacle, the no-slip boundary condition ($u=v=w=0$) has been used.

For computation, the flow domain is divided into a number of cells. The mesh is nonuniform on the x - y plane but uniform on all x - z planes. The grid is clustered near the cylinder and the spacing is increased by a proper ratio away from the cylinder. The convective terms have been discretized using second order central differencing scheme. The reason for choosing central differencing for the discretization of the convective terms has been discussed in the earlier section.

In the present study, the grid independence study has been carried out with respect to the time-averaged and rms values of the lift and drag coefficients and the Strouhal number. The effect of the grid size and the time step on the transition scenario has been studied and reported in the earlier section. For the grid independence study, three different grid sizes for a Reynolds number of 250, namely $178 \times 80 \times 22$, $178 \times 80 \times 32$ and $218 \times 104 \times 22$ and two different grid sizes for a Reynolds number of 500, namely $178 \times 80 \times 22$ and $218 \times 104 \times 22$ have been employed. The comparison of parameters computed on these grids are listed in Table-5.2.1. The time-averaged quantities, namely the drag coefficient and the Strouhal number show no significant variation for the different grids. However, the rms values of the lift and drag coefficients vary with the grid size. The computations of the present study is highly expensive in terms of time and computer

Table 5.2.1: Grid Independence Test

Re	Grid size	S	$\overline{C_D}$	$\overline{C_L}$	C_D'	C_L'
250	$178 \times 80 \times 22$	0.151	1.69	0.0002	0.032	0.145
	$178 \times 80 \times 32$	0.154	1.69	0.003	0.033	0.193
	$218 \times 104 \times 22$	0.150	1.72	0.003	0.044	0.183
500	$178 \times 80 \times 32$	0.120	2.14	-0.005	0.193	1.442
	$218 \times 104 \times 32$	0.116	2.17	0.005	0.205	1.454

Table 5.2.2: Comparison of present results with published data

Re	Source	S	$\overline{C_D}$
100	2D (present)	0.159	1.51
	3D (present)	0.152	1.50
	Davis <i>et al.</i> (1984)	0.154	1.64
	Franke <i>et al.</i> (1990)	0.154	1.55
	Okajima (1982)	0.139	-
500	2D (present)	0.165	2.34
	3D (present)	0.116	2.17
	Davis <i>et al.</i> (1984)	0.155	1.92
	Okajima (1982)	0.131	-

Table 5.2.3: Code validation at a high Reynolds number

Calculations	Grid Sizes	$\overline{C_L}$	C_L'	$\overline{C_D}$	C_D'	S	l_r
Re=21400 (present)	240×130×32	0.03	1.40	2.65	0.13	0.158	1.30
Wang <i>et al.</i> (1996) (LES)		-0.03 - 0.06	1.23 - 1.48	2.07 - 2.67	0.09 - 0.27	0.13 0.13	0.89 - 1.26
Experiments							
Lee (1975)				2.05	0.23		
Cheng <i>et al.</i> (1992)			0.6	1.9-2.1	0.2		
Durão <i>et al.</i> (1988)						0.138	1.33
Lyn <i>et al.</i> (1995)						0.132	1.38

resources. All the computations have been carried out in a 233MHz and 192MB RAM DEC-ALPHA workstation. The typical CPU time per time step at dynamic steady state on a $178 \times 80 \times 22$ grid at a Reynolds number of 500 is about 9 minutes. Therefore, all computations have been carried out using a grid of size $178 \times 80 \times 22$.

The computer code has been validated through comparison with numerical as well as experimental results over the Reynolds number range of 100 - 21400. Table-5.2.2 shows the comparison of the present numerical results of two- as well as three-dimensional computations with the published numerical results and experiments. The parameters chosen for the comparisons are time-averaged drag coefficient and Strouhal number. There is a good match between the present results and the data in the literature, particularly at low Reynolds number.

The present code has been found to work satisfactorily even at a high Reynolds number of 21400 without any model to take into account the contribution of subgrid scale eddies. The geometry chosen for the high Reynolds number simulation is similar to the present study. The convective terms at the higher Reynolds number have been discretized using third order upwind scheme due to Kawamura *et al.* (1986). Table-5.2.3 shows the summary of the run with the finest grids and the comparisons of the integral parameters such as time-averaged and rms values of the lift and drag coefficients, Strouhal number and the mean recirculation length¹ (l_r). The present results are compared with the results available in the literature at this high Reynolds number. Numerical results using the Large Eddy Simulation (LES) have been chosen for comparison with the present study. It is very clear that the match between our results and those published are good. The minor discrepancies are due to the higher blockage associated with the present work.

The comparison of the streamwise and transverse variation of the time-averaged streamwise velocity at four different locations $x=0.0, 1.0, 1.5$ and 4.0 is presented in a later Figure 5.7.4(a-b). The match among the present results, LES results and experiments are good.

Studies with a circular cylinder show that transition to three-dimensionality can occur at a low Reynolds number even when the overall configuration is two-dimensional. The associated critical Reynolds number is expected to depend on factors such as the inlet

¹The mean recirculation length is the distance beyond the cylinder along the wake centreline over which the time-averaged streamwise component of velocity first attains a positive value.

disturbance level, the shape of the body and the velocity profile in the approach flow.

In the present study for a square cylinder, upstream disturbances are absent and transition is promoted by discretization errors arising from the governing equations along with those from the boundary conditions. These being uniformly distributed over the fluid region, the transition observed in the present computations can be thought of as being natural, rather than forced. The corresponding critical Reynolds numbers can be regarded as upper limits for transitions. Figure 5.2.1(a) exhibits a signal traces of the spanwise component of velocity in the near-wake at Reynolds numbers of 150 and 175. With the passage of time the velocity component at $Re=150$ goes to zero indicating that the flow is two-dimensional. At a Reynolds number of 175, intermittent fluctuations are seen even at longer times. The amplitude of fluctuations in the spanwise velocity increases with increasing Reynolds number. Simultaneously there is a decrease in the intermittency of the fluctuations. The intermittency fades out at a Reynolds number of 250. Beyond, low frequency fluctuations are not present and the signal trace is uniformly noisy. Figure 5.2.1(b) depicts the time variation of the spanwise velocity at a Reynolds number of 325.

The signals in Figures 5.2.1(a) and (b) are a clear indication of transition to three-dimensionality in the wake of the square cylinder. The critical Reynolds number can be taken to lie between 150 and 175. The flow details presented below correspond to a large time, at which a dynamic steady state has been attained.

Results obtained in the present work have been organized as per the following headings:

1. Instantaneous flow field
2. Time-averaged integral parameters
3. Rms values of force fluctuations
4. Effect of three-dimensionality on the instantaneous forces
5. Time-averaged flow field
6. Comparison with a circular cylinder

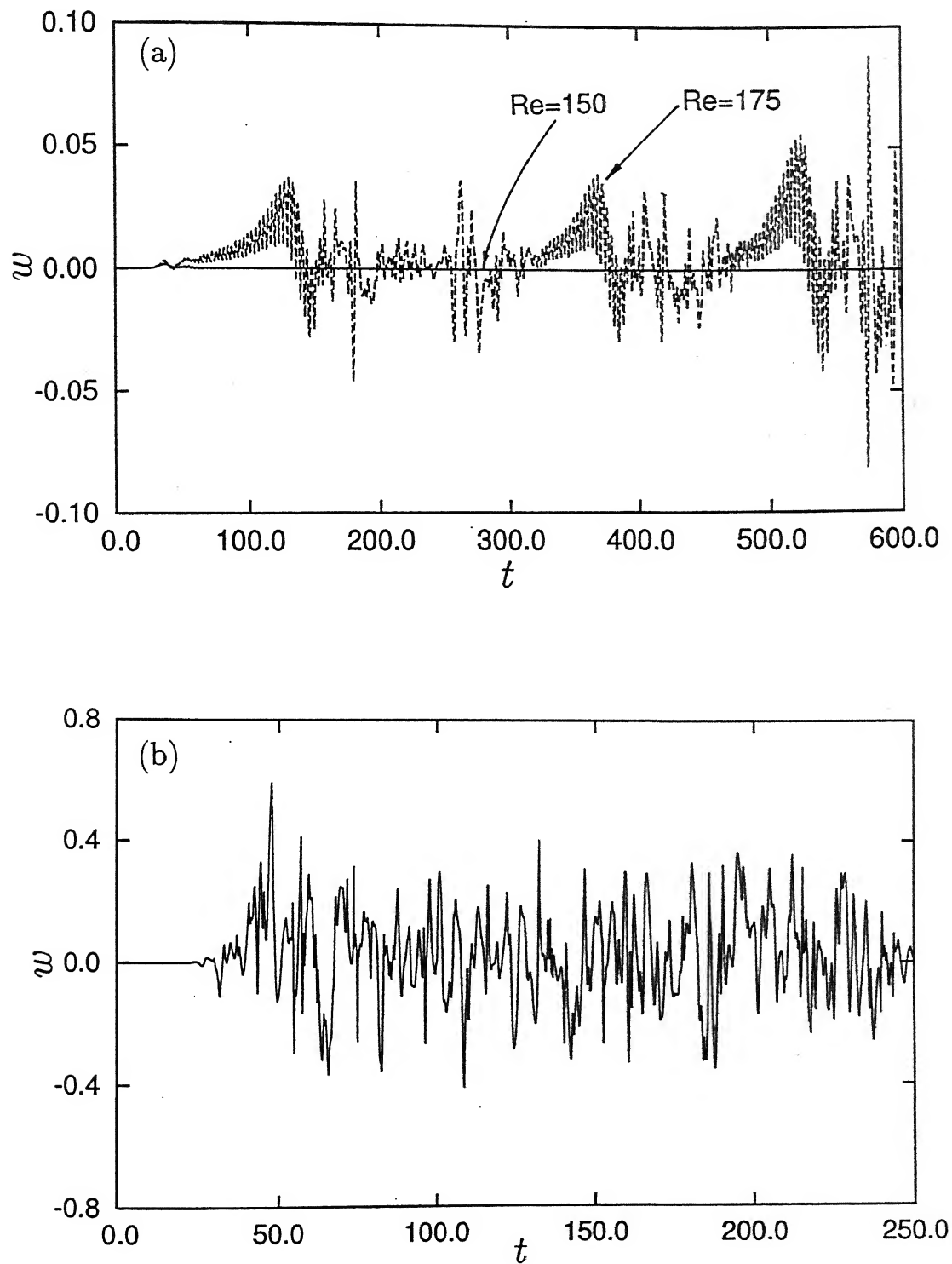
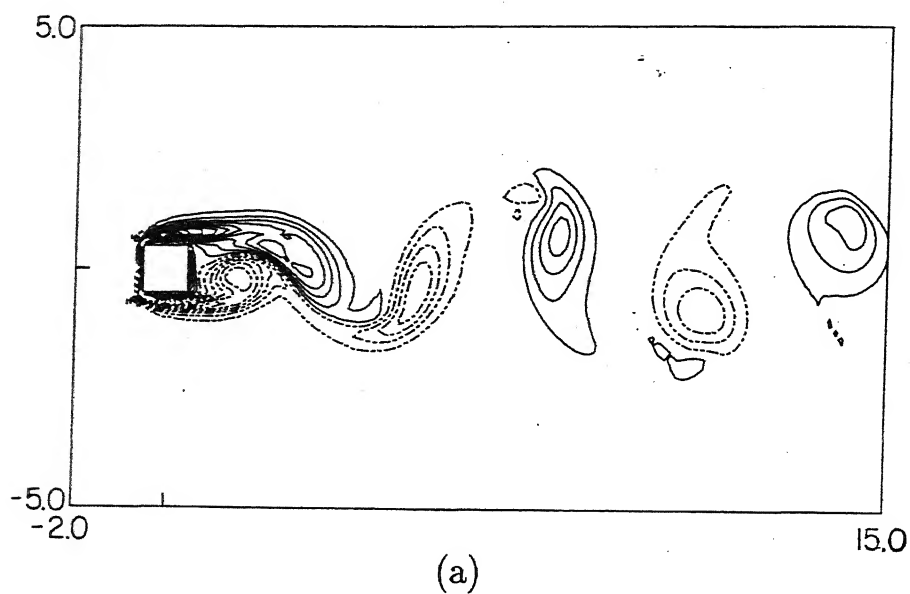
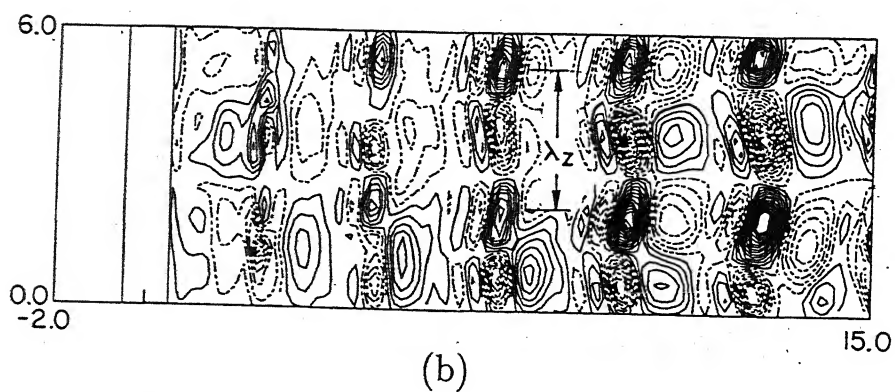


Figure 5.2.1: Time traces of the spanwise component of velocity: (a) $Re=150$ and 175 and (b) $Re=325$.



Broken lines: $(\omega_{z_{\min}}, \omega_{z_{\max}}, \Delta\omega_z) \equiv (0.29, 10.0, 0.57)$

Solid lines: $(\omega_{z_{\min}}, \omega_{z_{\max}}, \Delta\omega_z) \equiv (-9.43, -0.29, 0.57)$



Broken lines: $(\omega_{y_{\min}}, \omega_{y_{\max}}, \Delta\omega_y) \equiv (0.01, 0.4, 0.028)$

Solid lines: $(\omega_{y_{\min}}, \omega_{y_{\max}}, \Delta\omega_y) \equiv (-0.37, -0.01, 0.028)$

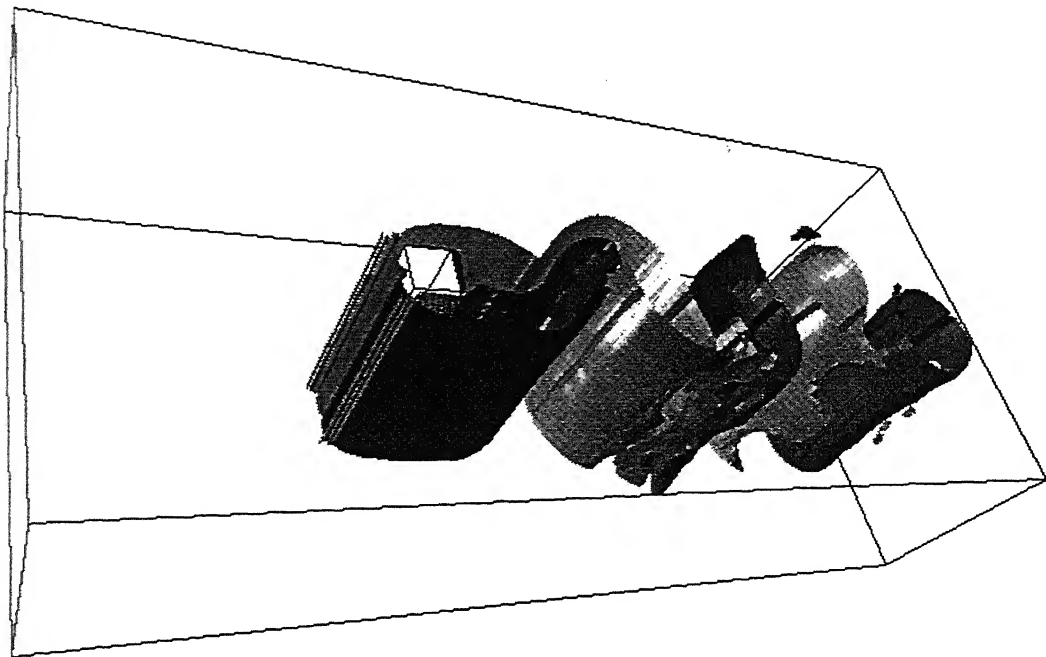
Figure 5.2.2: Vorticity contours at a Reynolds number of 175: (a) spanwise vorticity and (b) transverse (secondary) vorticity. The secondary vortices show Mode-A pattern with a spanwise wavelength of 3.0.

5.2.1 Instantaneous flow field

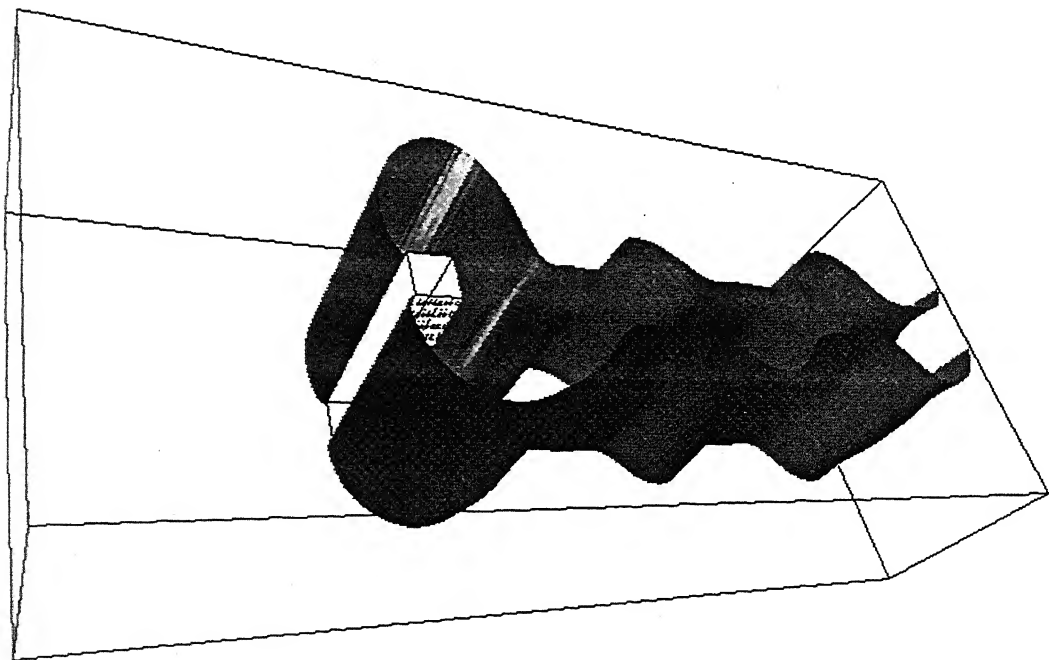
The flow past a square cylinder at low Reynolds numbers is characterized by the formation of a wake of staggered array of vortices. Laminar two-dimensional shedding without any spanwise instability has been observed upto a Reynolds number of 150. With an increase in the Reynolds number to 175, the wake of the square cylinder becomes structurally complex. In addition to the primary spanwise Kármán vortices (ω_z), secondary vortices are also generated in the wake. Two types of secondary vortices are present in the three-dimensional flow field, namely streamwise (ω_x) and transverse vortices (ω_y). Figure 5.2.2(a) shows the instantaneous spanwise vortices on the mid-span ($z=3.0$). The figure reveals the alternate staggered nature of the vortex street, thus signifying dominant periodicity in the flow. The streamwise wavelength of these spanwise vortices is about 6.2, though not a constant along the flow direction. Specifically, the near-wake wavelength is smaller as compared to the far-wake. A possible reason for this result is the higher convective speed of the vortices in the far-wake, the strong interaction between the vortices with opposite signs being absent.

The contours of secondary vortices ω_y are presented in Figure 5.2.2(b). The vortices have been plotted on the vertical mid-plane ($y=0$). The computations of the present study shows that the spanwise wavelength (λ_z) of these vortices is about 3. Figure 5.2.2(b) also shows the presence of the regular large-scale secondary vortices filling the span of the flow domain. At a Reynolds number of 150, the spanwise vorticity plots are similar to Figure 5.2.2(a), but the transverse vorticity is zero everywhere. Thus, Figure 5.2.2(b) is an indication of the flow becoming three-dimensional between Reynolds numbers of 150 and 175.

The three-dimensional iso-surfaces of the spanwise vorticity at a Reynolds number of 175 are shown in Figure 5.2.3(a). This figure shows total uniformity of the vortices across the cylinder span, revealing parallel shedding without discontinuity within the structure. Figure 5.2.3(b) illustrates the three-dimensional iso-pressure distribution at the same instant of time as in Figure 5.2.3(a). A comparison of Figures 5.2.3(a) and (b) shows that pressure minima coincide with the spanwise vorticity peaks. This result is to be anticipated on grounds of physical reasoning and is a useful crosscheck on the numerical computation. The corresponding iso-surfaces for streamwise and transverse vortices have been shown in Figures 5.2.3(c) and (d). These figures demonstrate the existence

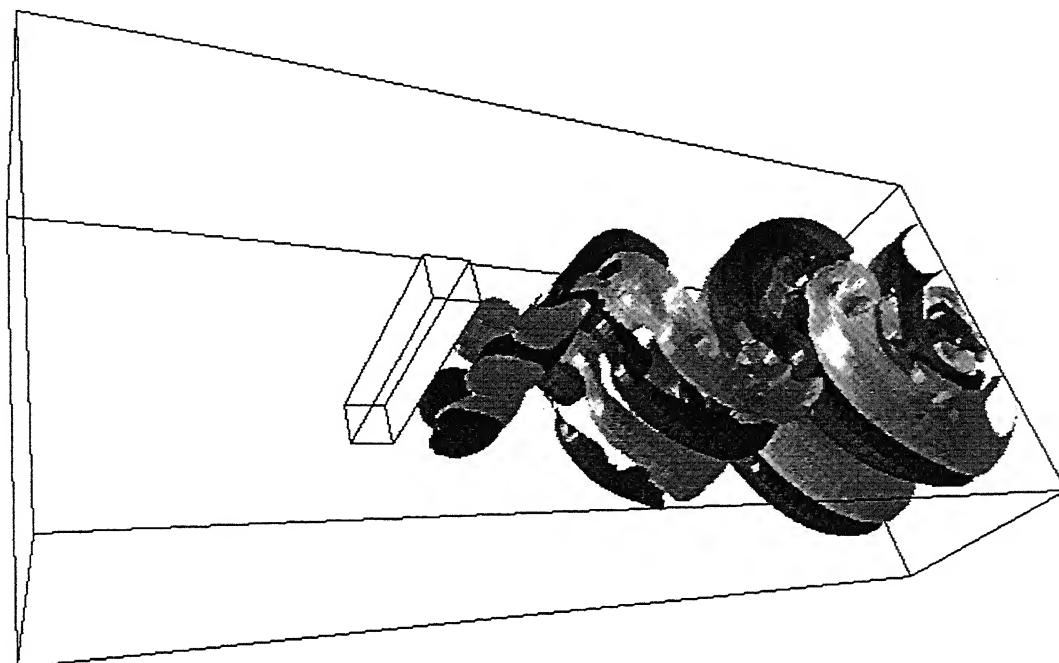


(a)

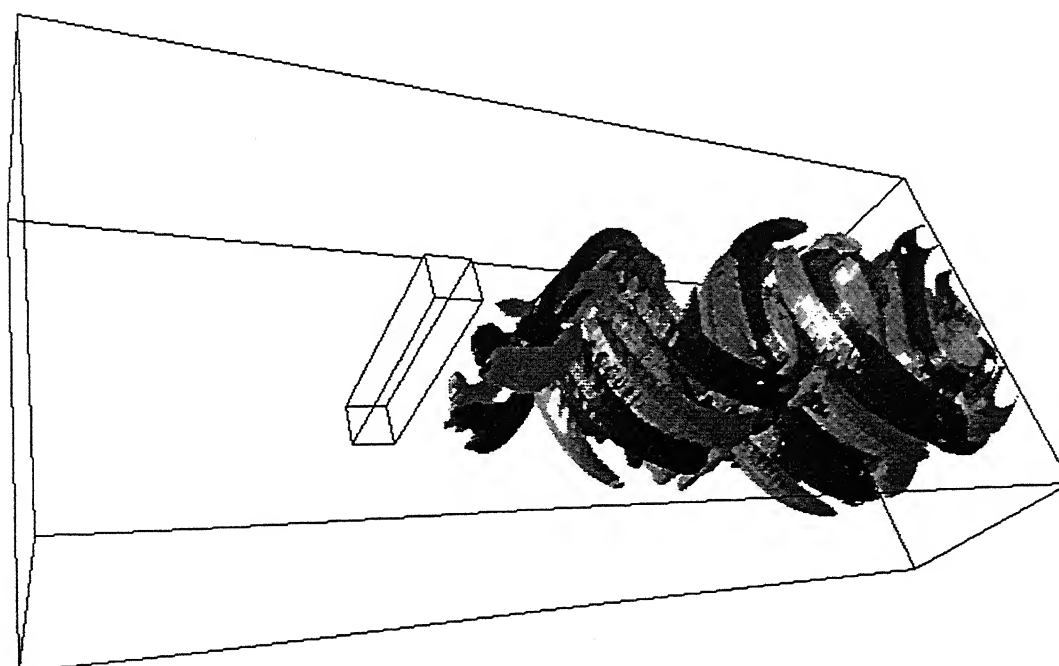


(b)

Figure 5.2.3: for caption see next page



(c)



(d)

Figure 5.2.3: Iso-surfaces at a Reynolds number of 175 with regular shedding mode (Mode-A): (a) spanwise vorticity ($\omega_z=\pm 0.25$) (b) pressure ($p=0.8$) (c) streamwise (secondary) vorticity ($\omega_x=\pm 0.05$) and (d) transverse (secondary) vorticity ($\omega_y=\pm 0.05$).

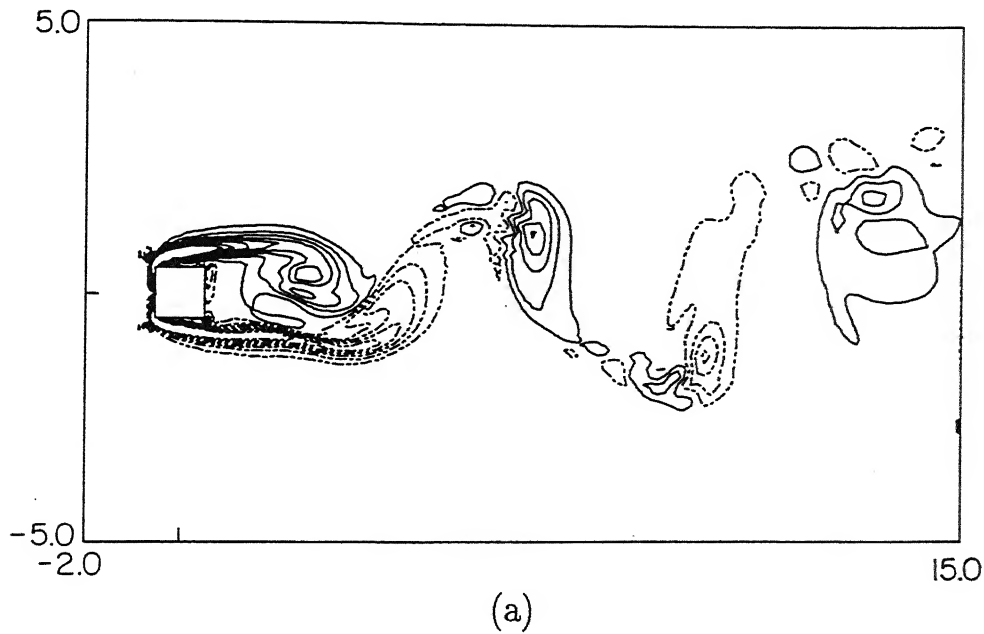
of the secondary flow. This observation confirms the pattern of shedding at a Reynolds number of 175 to be Mode-A¹. The spatio-temporal symmetry of Mode-A clear from the Figure 5.2.3(c) produces a staggered array of streamwise vortices (ω_x) that alternate in sign from period to period at a given spanwise location. The streamwise vortices follow an out-of-phase pattern, *i.e.* within the half period the sign of the streamwise vortices change. Comparing Figures 5.2.3(c) and (d) it can be concluded that the arrangement of vortices are similar, though the transverse component is dense and forms a less regular link between vortices of opposite sign.

Over the Reynolds number range of 175 - 240, three-dimensionality in the form of Mode-A is seen to persist. When the Reynolds number is increased to 250, the large-scale structure in the spanwise direction breaks down to a spanwise wavelength smaller than Mode-A. The mode of shedding resulting in a small-scale structure is labeled Mode-B.

Figure 5.2.4(a) shows the spanwise vorticity contours at the spanwise mid-plane for a Reynolds number of 250 (Mode-B). The wavelength of this component of vorticity is about 6.9 which is larger than that of the Mode-A. The vortices in Figure 5.2.4(a) are structurally complex as compared to Mode-A, Figure 5.2.2(a). The contours of transverse vorticity on the vertical mid-plane ($y=0$) are presented in Figure 5.2.4(b) at the Reynolds number of 250. The spanwise wavelength of these vortices is in the range 1.2-1.4. The vorticity contours give a clear indication of the appearance of irregular finer-scales in Mode-B as compared to Mode-A. Figure 5.2.4(c) shows the spanwise iso-vorticity surfaces at a Reynolds number of 250, while Figure 5.2.4(d) depicts the iso-surfaces of streamwise vorticity. The iso-surfaces of streamwise vorticity show the vortices to be irregular and not a uniformly staggered array as in Mode-A. The streamwise vortices can be seen to have the same sign over all the wavelengths at a particular spanwise location.

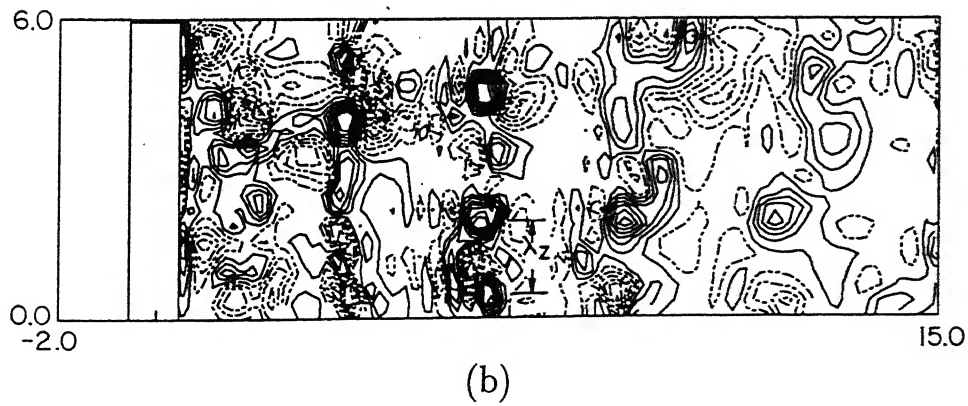
A closer examination of the flow field at a Reynolds number of 175 shows that the vortex dislocation phenomenon reported by Williamson (1992) for a circular cylinder is also present for the square cylinder. Vortex dislocation is the intermittent low-frequency modulation due to the formation of a large-scale irregularity in the near-wake. Figure 5.2.5(a) shows the spanwise vorticity at the mid-span at the instant when the flow suffers vortex dislocation. Compared to Figure 5.2.2(a), the Kármán vortex street is seen to be elongated along with a larger recirculation length. The formation of vortex disloca-

¹A description of Modes-A, A* and B in the context of a circular cylinder is given in Chapters-1 and 2.



Broken lines: $(\omega_{z\min}, \omega_{z\max}, \Delta\omega_z) \equiv (0.33, 5.0, 0.66)$

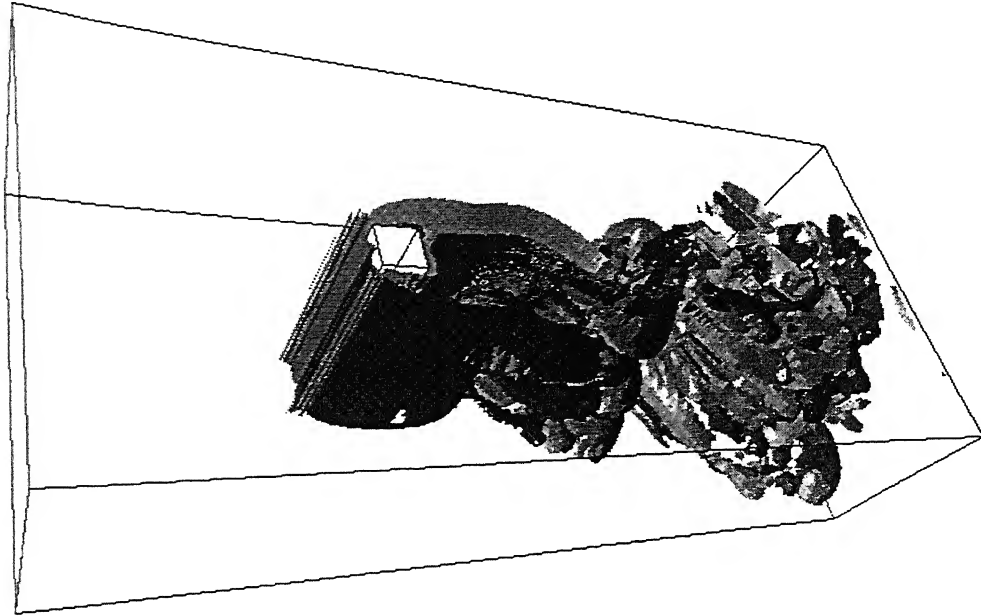
Solid lines: $(\omega_{z\min}, \omega_{z\max}, \Delta\omega_z) \equiv (-4.33, -0.33, 0.66)$



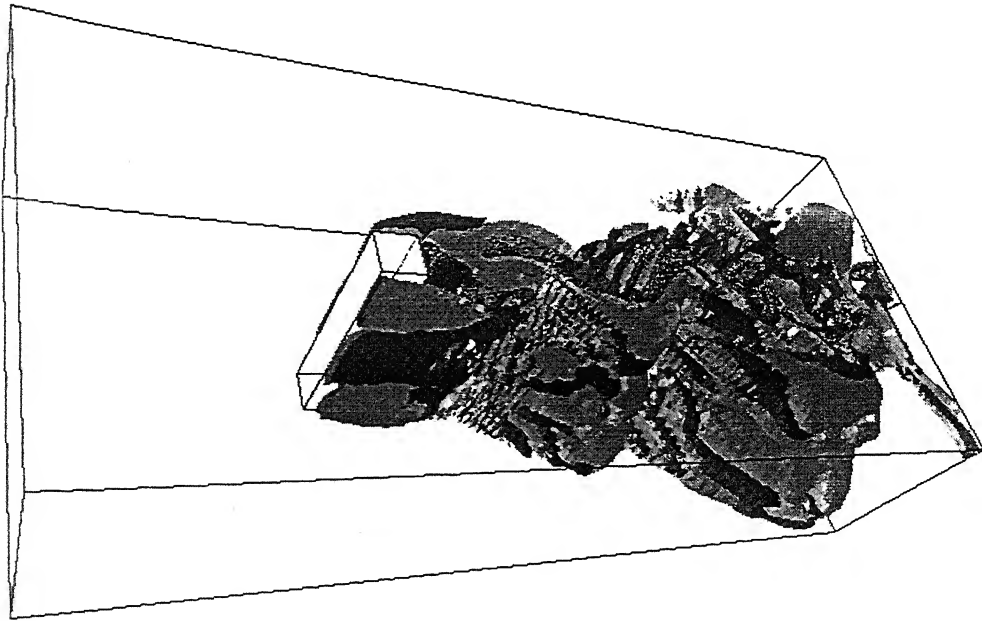
Broken lines: $(\omega_{y\min}, \omega_{y\max}, \Delta\omega_y) \equiv (0.12, 1.8, 0.24)$

Solid lines: $(\omega_{y\min}, \omega_{y\max}, \Delta\omega_y) \equiv (-1.56, -0.12, 0.24)$

Figure 5.2.4: for caption see the next page



(c)



(d)

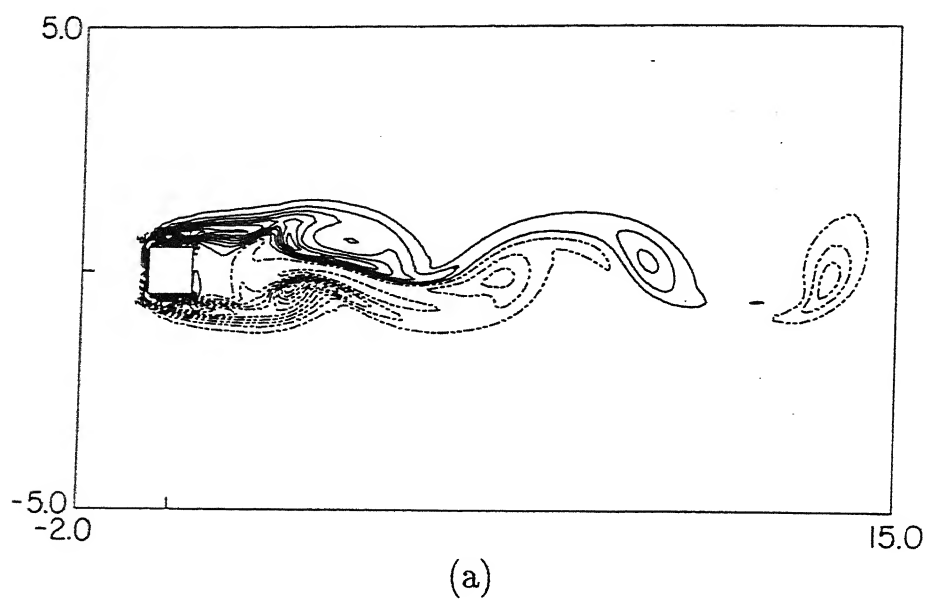
Figure 5.2.4: Vorticity contours and iso-surfaces at a Reynolds number of 250: (a) spanwise vorticity contours (b) transverse (secondary) vorticity contours (c) iso-surfaces of primary vortices ($\omega_z = \pm 0.25$) and (d) iso-surfaces of secondary vortices ($\omega_x = \pm 0.05$). The secondary vortices show Mode-B pattern in (b) with a spanwise wavelength of 1.2-1.4.

tion is understood from Figure 5.2.5(b) where the transverse vorticity on the mid-plane ($y = 0$) is shown. Figure 5.2.5(b) shows the dislocation to be present in the far downstream of the cylinder as well. The dislocated vortex is convected downstream after its formation in the near-wake. Vortex dislocation is generated between the spanwise cells due to the out-of-phase movement of the primary vortex in each cell. A similar effect can be observed if the shedding frequency are slightly different.

Following Williamson (1992), two types of vortex dislocation can be identified. In one, a rather twisted web of vortex linking occurs across the cell boundaries. Such a dislocation is one-sided and lacks symmetry. A two-sided dislocation occurs due to the local phase variation within larger cells of the shed vortices in association with the parallel shedding. It may also occur due to vortex merging along the spanwise direction. The symmetry of the dislocation about the mid-span is a proof that the dislocated vortices are two-sided. Here, dislocation in the spanwise direction undergoes symmetric spreading.

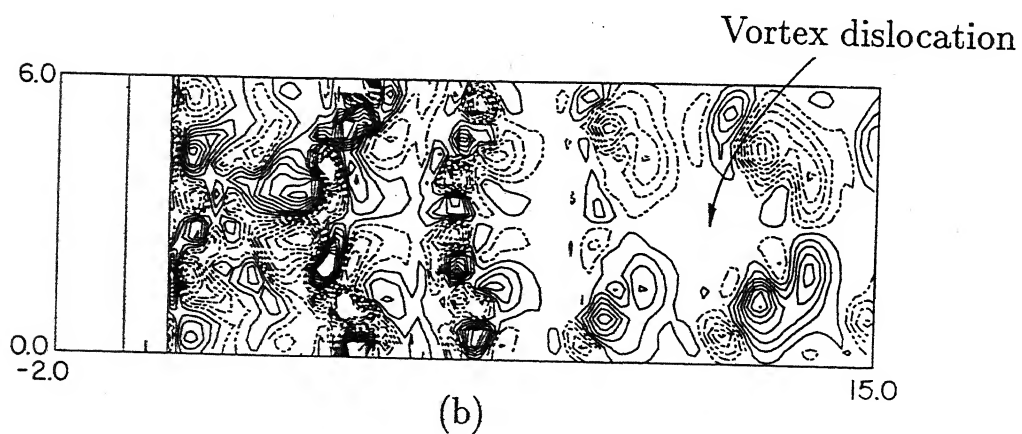
The dislocation in Figure 5.2.5(b) shows that the spreading is two-sided with the frequency and phase of shedding on either side of the dislocation being equal. The two-sided dislocation forms a Λ -structure, evident in Figure 5.2.5(b). In contrast, the out-of-phase two-sided dislocation gives zig-zag symmetry about the cells of dislocation due to shift in either frequency or phase. In a two-sided dislocation, the vorticity concentration and vorticity cancellation can be discerned in Figure 5.2.5(b) due to alternate in-phase and out-of-phase secondary vorticity distribution along the streamwise direction of the flow. Vorticity concentration is seen in the Figure 5.2.5(b) over $13.8 < x < 15.8$, and vorticity cancellation over $11.7 < x < 14.2$ for a particular combination of vorticity cancellation-concentration¹. To show the symmetry of the two-sided dislocation, two other spanwise vorticity contours have been presented in Figures 5.2.5(c) ($z=1.5$) and (d) ($z=4.5$) for the same instantaneous flow field as in Figure 5.2.5(a). Both the figures showing an identical trend in vortex shedding signifies that the dislocation is truly symmetric and two-sided. The vortex formation length at these two spanwise locations are similar as in Mode-A. The only difference is in the knot formation on each vortex downstream. These knots are due to the dislocated spanwise vortices formed at the mid-span. The smaller formation lengths also suggest that the effect of dislocation is not as prominent as at the mid-span since their z -locations are away from the primary dislocation plane ($z=3.0$).

¹When the dislocation spreads over the entire streamwise length beyond the cylinder, alternate arrays of vorticity concentration and cancellation are seen, Figure 5.2.7.



Broken lines: $(\omega_{z\min}, \omega_{z\max}, \Delta\omega_z) \equiv (0.29, 10.0, 0.57)$

Solid lines: $(\omega_{z\min}, \omega_{z\max}, \Delta\omega_z) \equiv (-9.43, -0.29, 0.57)$



Broken lines: $(\omega_{y\min}, \omega_{y\max}, \Delta\omega_y) \equiv (0.06, 1.0, 0.12)$

Solid lines: $(\omega_{y\min}, \omega_{y\max}, \Delta\omega_y) \equiv (-0.88, -0.06, 0.12)$

Figure 5.2.5: for caption see the next page

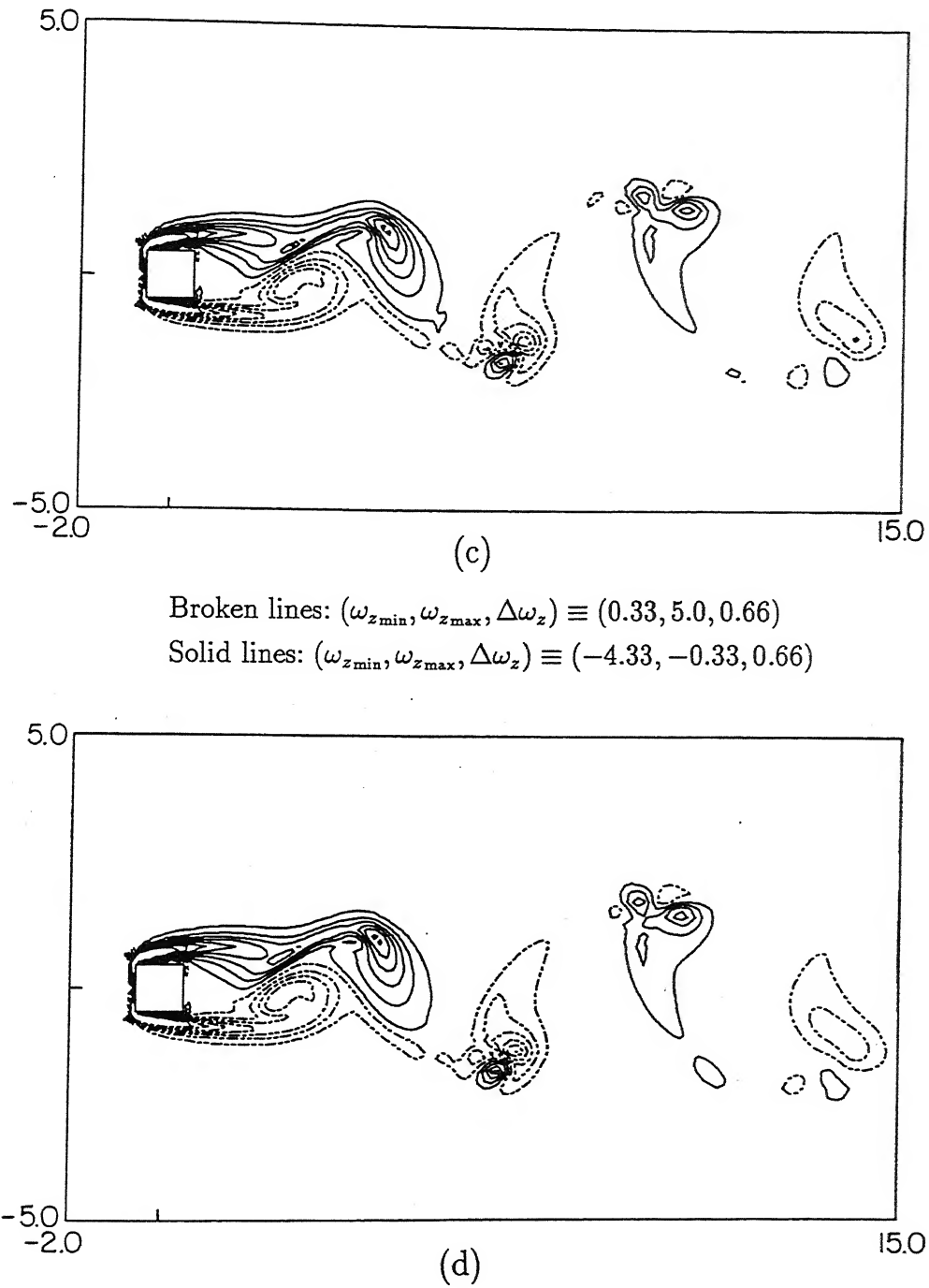


Figure 5.2.5: Vorticity contours at a Reynolds number of 175 when vortex dislocation coexist with regular shedding: (a) spanwise vorticity at mid-span ($z=3.0$) (b) transverse (secondary) vorticity (c) spanwise vorticity at $z=1.5$ and (d) spanwise vorticity at $z=4.5$. The secondary vortices in (b) show the evidence of vortex dislocation shown by an arrow. The figure has been plotted at an instant when the dislocation has propagated in the far-wake.

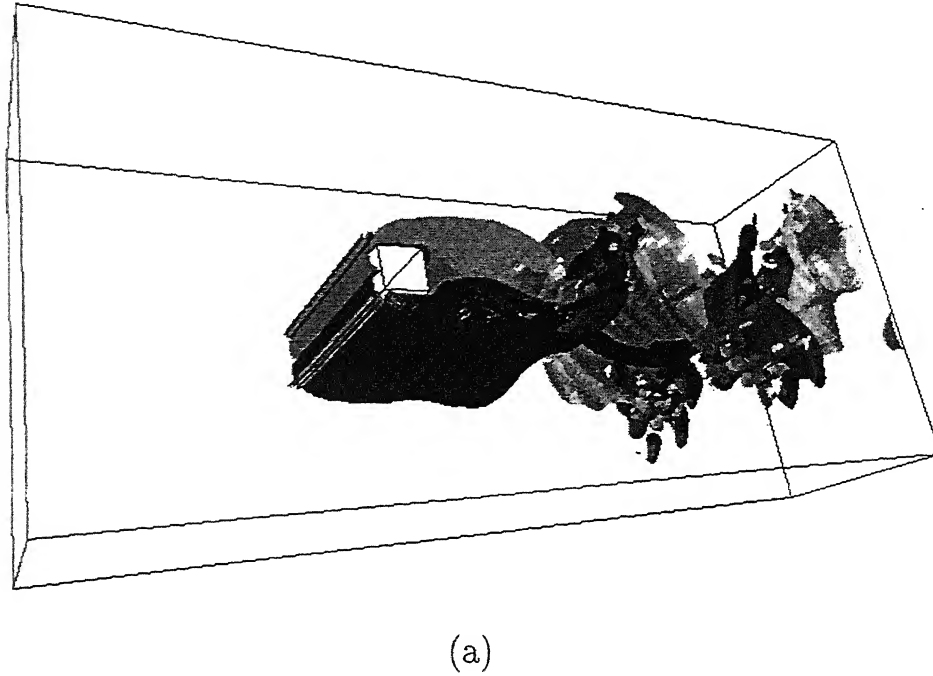
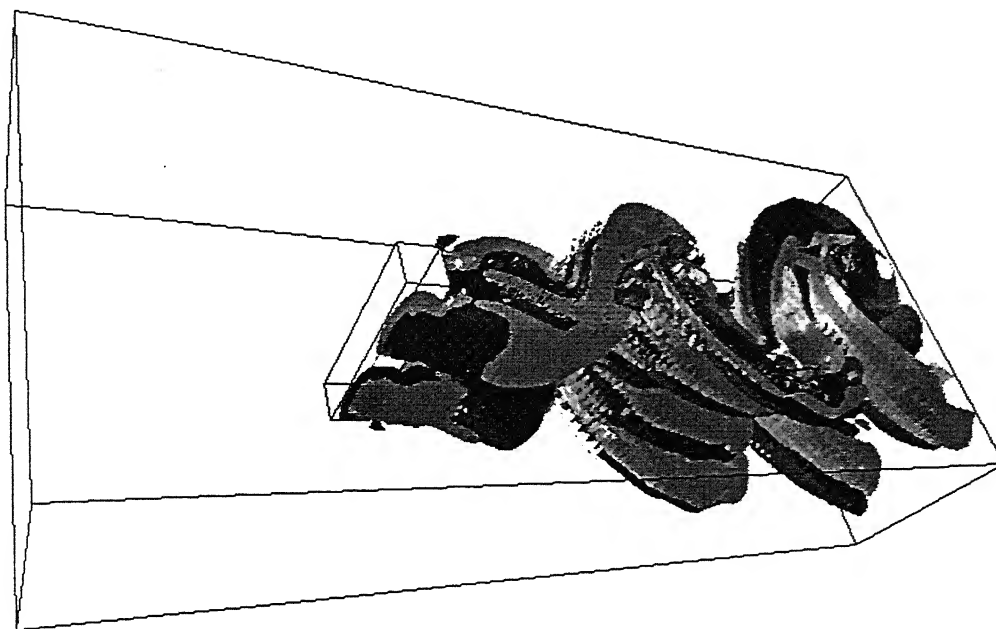
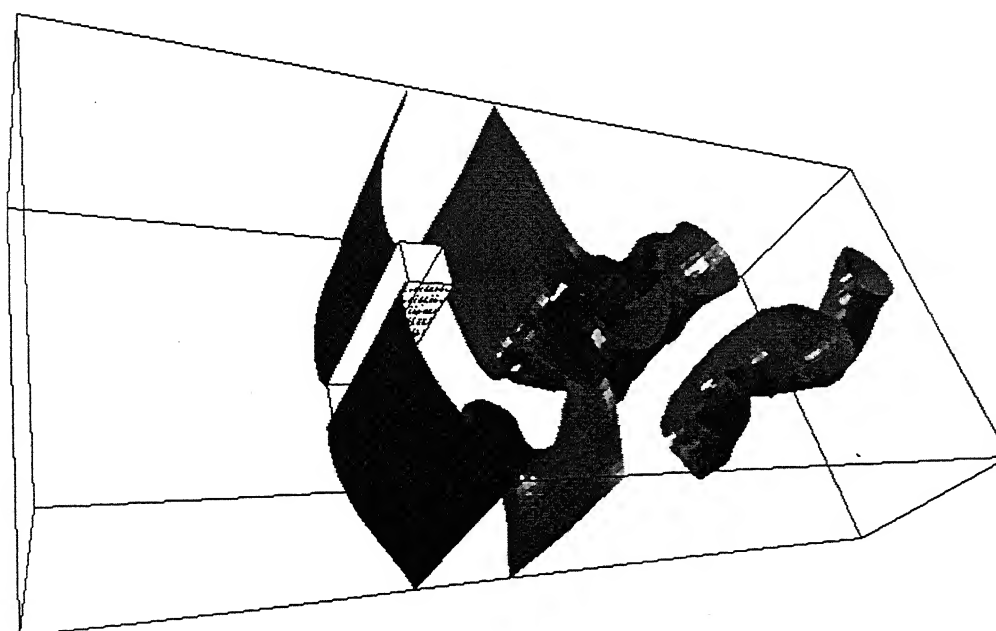


Figure 5.2.6: for caption see next page

Figure 5.2.6 shows the three-dimensional representation of vortex-dislocation through the spanwise (Figure 5.2.6(a)) and streamwise (Figure 5.2.6(b)) vorticity. Figure 5.2.6 illustrates that the dislocation is due to the formation of large-scale structures which are coherent and symmetric in nature. One of the important characteristics of dislocation in the wake is its spreading in the spanwise direction. The spreading occurs due to two major reasons (Williamson, 1992). One is vortex division, *i.e.*, a single spanwise vortex tube divides into two of same sign as the original. The rotation of the single vortex tube twists the other two branched vortex tubes at the point of division about the axis of the single vortex tube. This helical twist of the two vortex tubes leads to flow in the direction of the axis of the main tube and as a consequence the secondary flow is enhanced. The second reason is related to the formation of nonuniform spanwise vortices along the cylinder axis. The nonuniformity of the distribution of vortices results in a helical twisting of the vortex tube and causes secondary axial flow. Owing to nonuniformity in the spanwise vortices, there is a pressure distribution as well. The distribution is such that a higher vorticity corresponds to lower pressure. Therefore, there is net pressure difference along the axis of the spanwise vortex tube. Due to the pressure difference there is a net outward flow of fluid from the mid-span. This outward flow leads to the spreading of the dislocation.



(b)



(c)

Figure 5.2.6: Iso-surfaces at a Reynolds number of 175 when vortex dislocation coexist with regular shedding mode called Mode-A*: (a) spanwise vorticity ($\omega_z = \pm 0.25$) (b) streamwise (secondary vortices) ($\omega_x = \pm 0.05$) and (c) pressure ($p = 0.8$). The regular spanwise vortices in Figure 5.2.3(a) has been deformed.

Vortex division has been established for a higher aspect ratio circular cylinder by Williamson (1992). In the present study the evidence for vortex division is not as clear. The spreading due to nonuniformity of the vortex tube is however clearly seen in the present study. The iso-surfaces of the spanwise vorticity (Figure 5.2.6(a)) show that its distribution is nonuniform along the length. The corresponding iso-surfaces of the streamwise vortices are shown in Figure 5.2.6(b). Similarly the iso-pressure distribution (Figure 5.2.6(c)) shows nonuniformity along the cylinder length, in contrast to the regular shedding mode where pressure is sensibly constant. The nonuniform pressure distribution leads to secondary flow and spreads the dislocation in the spanwise direction.

Figure 5.2.7 shows the temporal evolution of the dislocation through the vorticity contours at a Reynolds number of 175. In this figure, the contours at different times have been plotted with identical maximum-minimum values of vorticity. The instantaneous drag coefficient as a function of time is shown in Figure 5.2.8. The time instances corresponding to the snapshots of Figure 5.2.7 have been marked over the drag-coefficient signal. Figure 5.2.7(a) corresponds to an instance when the vortex dislocation has just been initiated. Comparing Figure 5.2.2(b) and Figure 5.2.7(a), the spanwise wavelength of the secondary vortices can be seen to increase with time. The increase can be related to vortex merging in the spanwise direction. For the dislocation appearing in the present calculation, the vorticity field in the transverse direction is symmetric about the mid-span of the cylinder. Figure 5.2.7(c) shows the spread of dislocation over the entire flow field. During dislocation, the vortices of higher spanwise wavelength are generated in the near-wake. These break down in size as they travel downstream. All the large-scale vortices in the near-wake are oppositely aligned to that in the far-wake. Figure 5.2.7(c) confirms that the spanwise spreading rate of the dislocation is high in the downstream direction. Figure 5.2.7(d) and (e) show that the dislocation process gradually comes to a stop, in the sense that the near-wake is filled by three-dimensional secondary vortices. Thus, unlike the continuous shedding phenomenon, dislocation progress intermittently in time.

Dislocation may originate due to different reasons. Williamson (1992) has demonstrated experimentally the formation of dislocation by forcing a frequency discontinuity with the help of a disc having a diameter larger than the circular cylinder. The formation of a dislocation as a consequence of oblique shedding has also been demonstrated in these experiments. Zhang *et al.* (1995) have documented the vortex dislocation numerically (also called adhesion mode) by introducing spanwise nonuniformity along the cylinder.

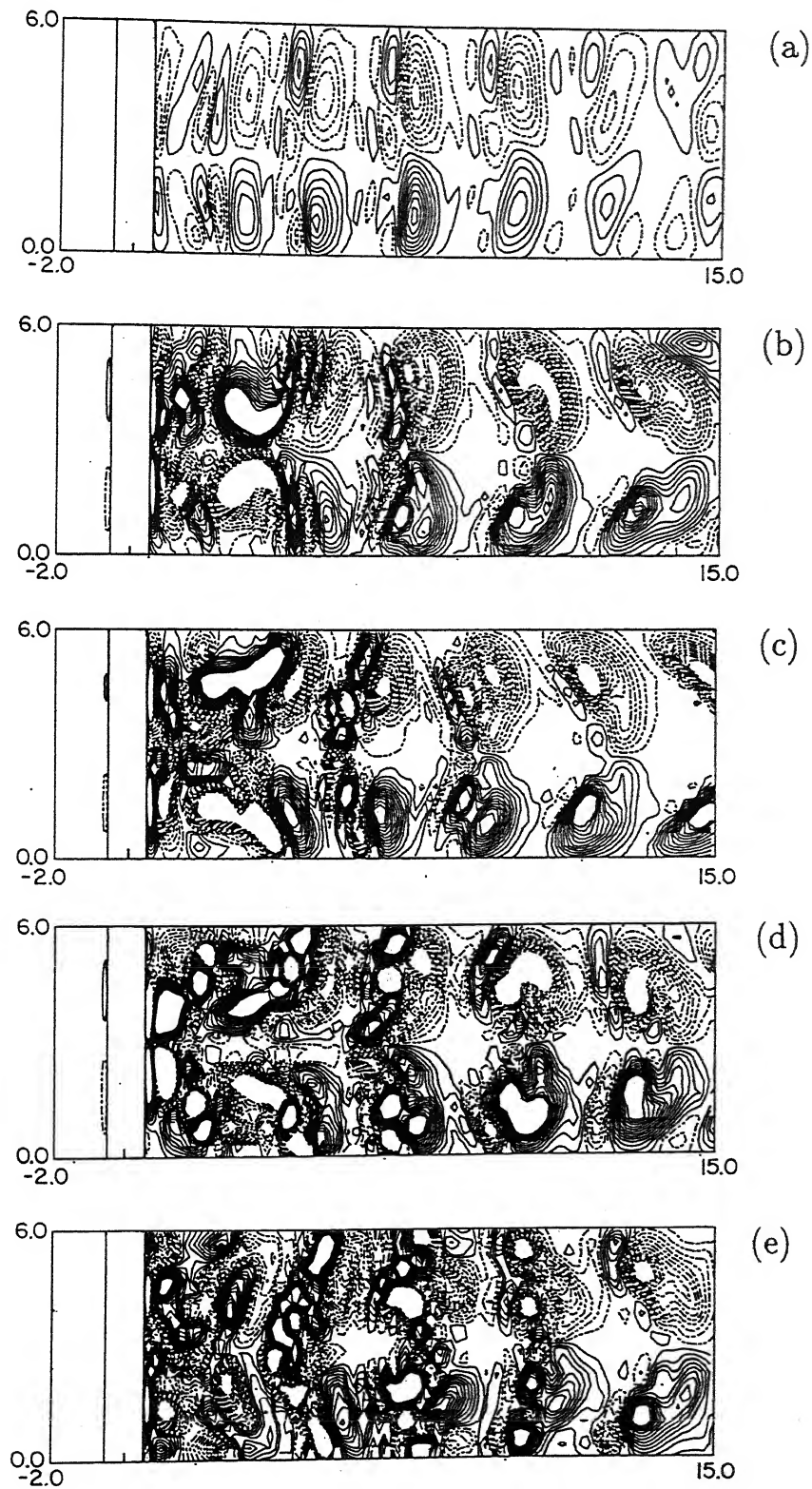


Figure 5.2.7: Temporal evolution of vortex dislocation at various time: (a) $t=510.11$ (b) 541.99 (c) 553.81 (d) 561.59 and (e) 572.23.

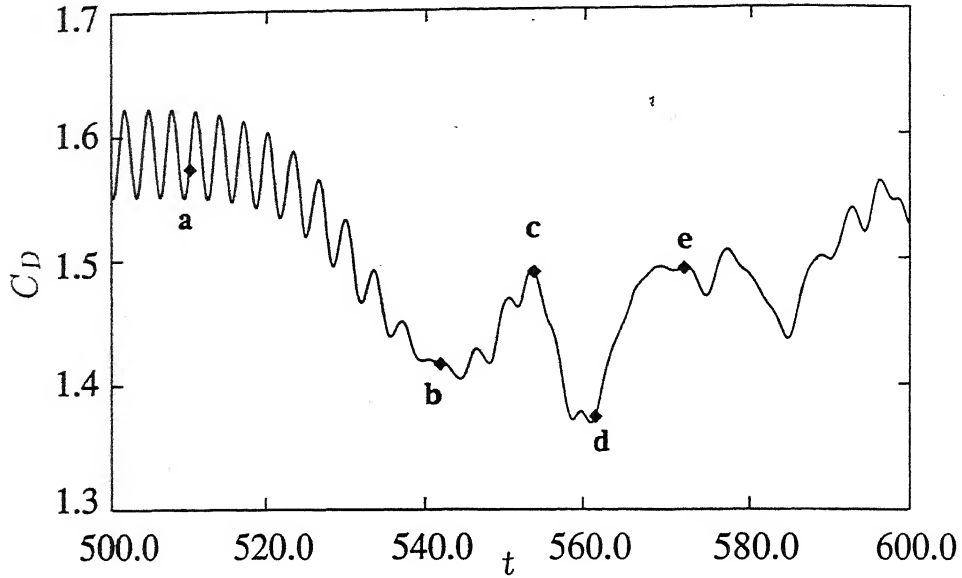


Figure 5.2.8: Drag coefficient signal showing the different instances of the vortex dislocation shown in Figure 5.2.7.

They have used periodic end-boundary conditions. The present study did not employ any external forcing and vortex dislocation was possibly due to the phase variation within the large coherent structures. The other possibility is the merging of the secondary vortices in the spanwise direction. The regular shedding mode (Mode-A) shows a spanwise wavelength of secondary vortices to be 3 units. The spanwise wavelength of the secondary vortices increases during the vortex dislocation by merging. This phenomenon is clear from Figure 5.2.7(a) where the location of the Λ -structure shows an increase in spanwise wavelength. This increase in the wavelength can be associated with a low frequency irregularity seen in vortex dislocation.

The results presented above show that subsequent to transition to three-dimensionality in the wake of a square cylinder two patterns, namely Mode-A and Mode-A* may both appear, the latter involving the vortex dislocation process. Both patterns can coexist over the Reynolds number range 150 - 175. One can broadly conclude that the Mode-A behaviour is more probable in the vicinity of a Reynolds number of 150, while it is Mode-A* around a Reynolds number of 175. To establish the differences between the modes, the signal traces of the relevant quantities have been compared below.

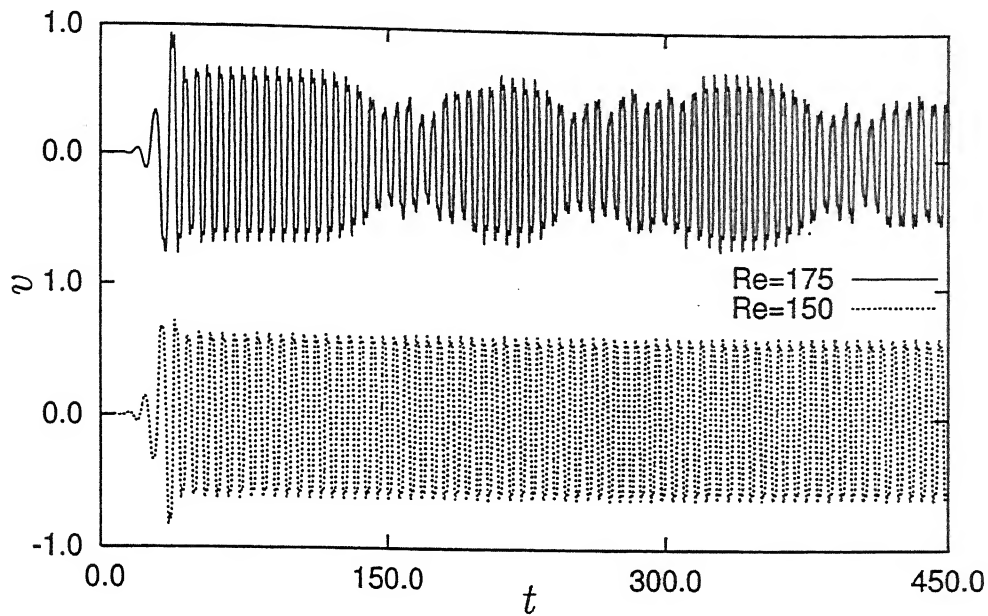


Figure 5.2.9: Time traces of transverse velocity at two different Reynolds numbers. The time signal at a Reynolds number shows the evidence of low frequency intermittent irregularities.

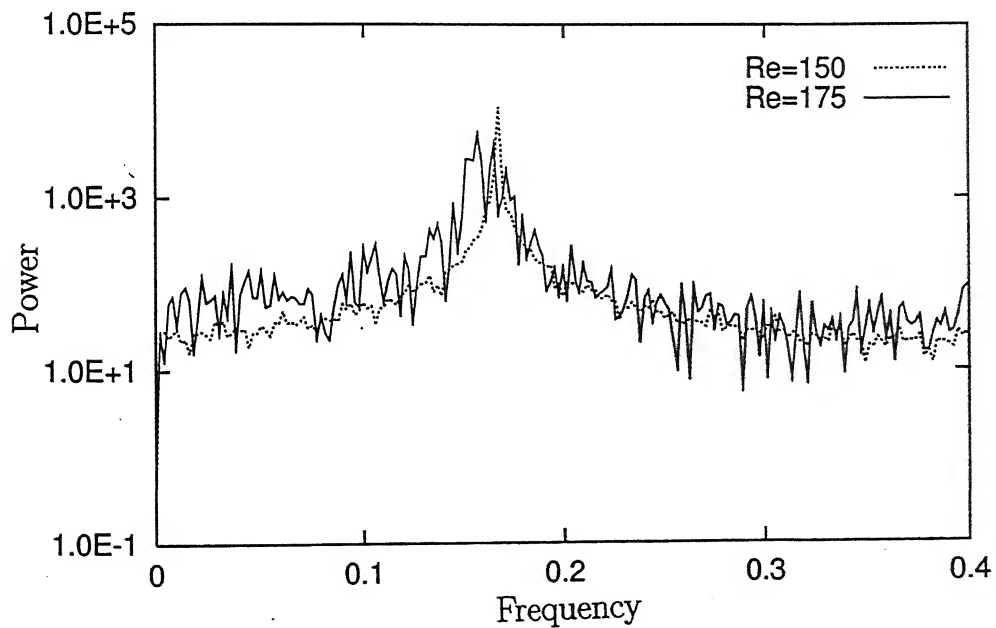


Figure 5.2.10: Spectra at two Reynolds numbers corresponding to time-traces shown in earlier figure (Figure 5.2.9). The spectra at a Reynolds number of 175 shows broadband due to the presence of vortex dislocation.

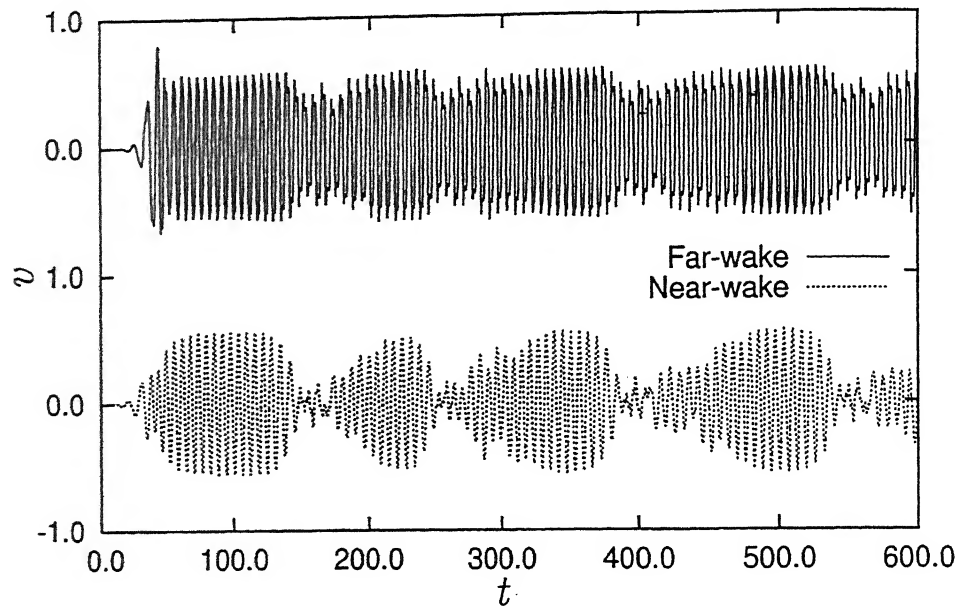


Figure 5.2.11: Time traces in the near- as well as far-wake at a Reynolds number of 175. The little phase-lag of irregularity between the two traces shows the rapid propagation of vortex dislocation in the streamwise direction.

Figure 5.2.9 shows the time traces of the transverse component of velocity at Reynolds numbers of 150 and 175 in the near-wake ($x=1.23$) along the centreline. The dimensionless spectra of the corresponding signals are shown in Figure 5.2.10. The spectrum at a Reynolds number of 175 is broader due to the presence of dislocation. The peak value is smaller since other harmonics related the dislocation have been excited. On the other hand, the spectrum at a Reynolds number of 150 shows a single peak corresponding to the shedding frequency. The frequency of vortex shedding in Mode-A* is smaller due to the presence of the low frequency irregularity of vortex dislocation. The Strouhal frequency of Mode-A matches however the regular shedding frequency at a Reynolds number of 150. A comparison of the two spectra shows that the energy in the higher frequencies are greater in Mode-A* as compared to Mode-A. Thus the spectrum corresponding to Mode-A* is seen to be influenced on the low as well as high frequency ends, in relation to Mode-A.

Figure 5.2.11 shows the signal traces of the transverse velocity component at two locations along the centreline, namely $x=1.23$ and 10.5. The phase-lag between the signals is seen to be small and the low frequency modulation is seen to be small in the far-wake. The propagation of dislocation in the downstream can hence be taken to be rapid.

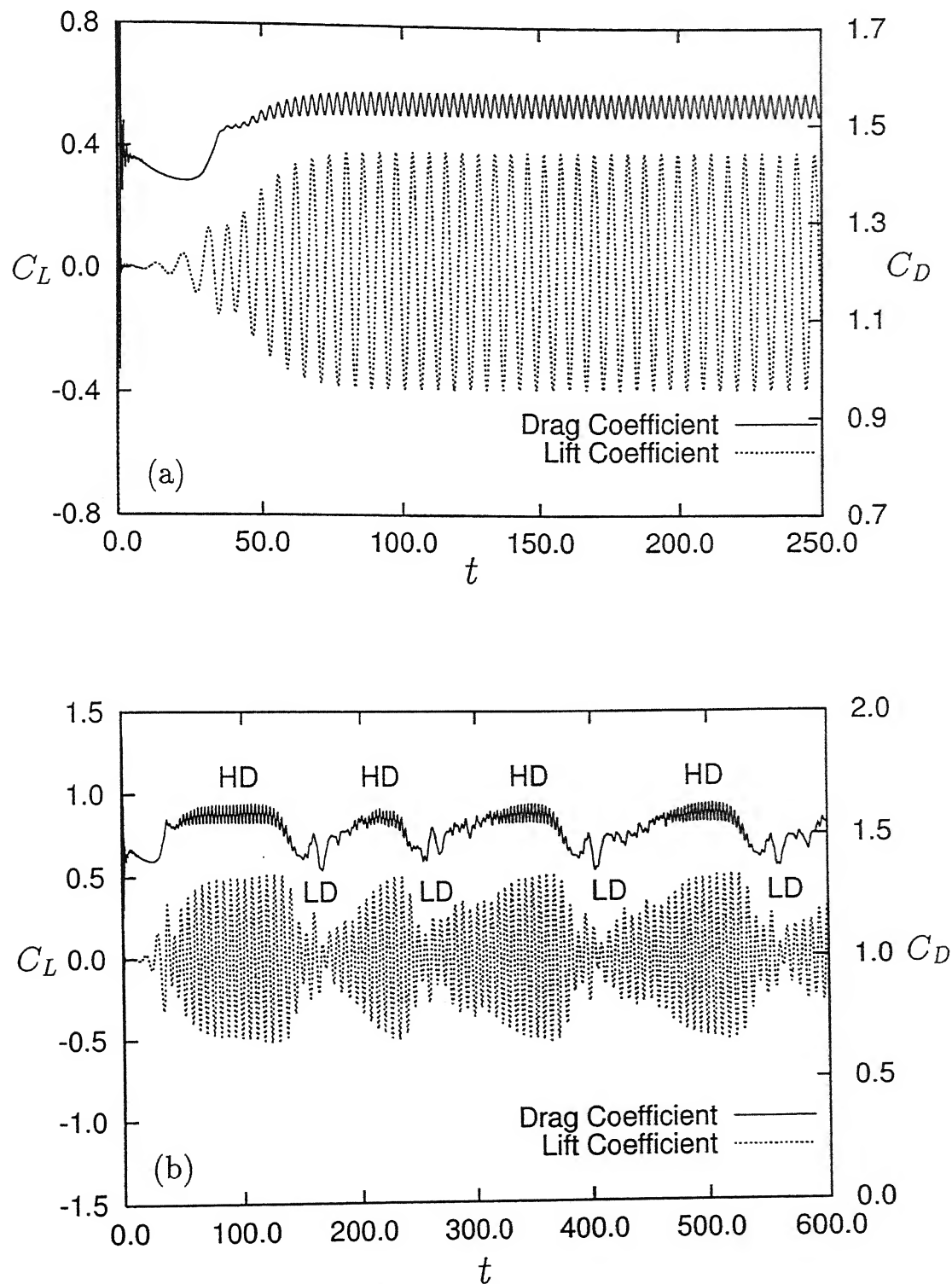


Figure 5.2.12: for caption see the next page

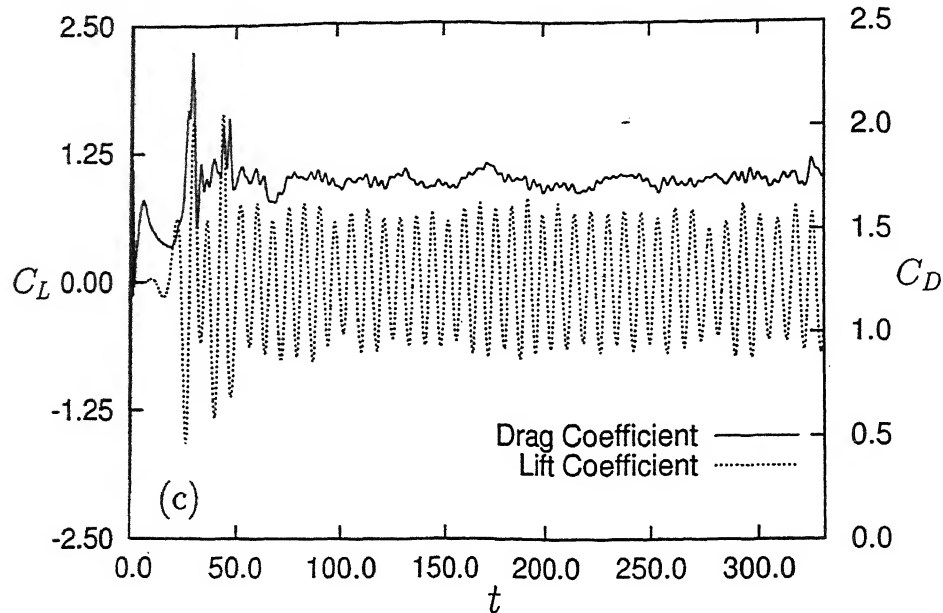


Figure 5.2.12: Temporal variations of drag and lift coefficients at various Reynolds numbers: (a) $Re=150$ (b) $Re=175$ and (c) $Re=290$. Both the drag and lift coefficients at a Reynolds number of 175 show low frequency irregularities which are absent at a Reynolds number of 150. The low frequency intermittent irregularities largely fade away at a Reynolds number of 290.

The variation of the instantaneous drag and lift coefficients with time are shown for a Reynolds number of 150 in Figure 5.2.12(a). At a Reynolds number of 175, the force components exhibit a clear pulsation (Figure 5.2.12(b)). A distinct and intermittent switching of the flow field is clear in this figure. There is a low frequency modulation (marked **LD**, low drag) in the time series with the usual shedding mode (marked **HD**, high drag). The unusual intermittent low frequency modulation can be related to the vortex dislocation. The time-period of the dislocation is approximately fifteen times that of vortex shedding and the duration for which dislocation persists is about 10-12 times the shedding period. The decrease in the drag coefficient during the period of vortex dislocation is due to a longer recirculation length (see Figure 5.2.5(a)) compared to the regular shedding mode. Similarly the decrease in lift coefficient during the vortex dislocation period is also due to a reduced pressure drop across the transverse faces of the cylinder, again owing to a longer recirculation length. In the usual shedding mode there is an increase in the rms values of both the coefficients with Reynolds number. The rms fluctuations momentarily fall for the lift coefficient and rise for the drag coefficient during vortex dislocation. With further increase in Reynolds number, the intermittent

low frequency modulation in the flow decreases, and the pulsation phenomenon fades out, see Figure 5.2.12(c), $Re=290$.

The transition of flow from two- to three-dimensional field affects the decay rate of all vorticity components as they travel downstream (Figure 5.2.13). The spanwise vorticity in Mode-A* ($Re=175$) is higher in the near-wake and shows a faster decay than what is observed during Mode-A with regular shedding. Mode-A at $Re=175$ shows a lower value of the spanwise vorticity and decays slower compared to Mode-B ($Re=250$). The variation of the streamwise vorticity with the downstream direction is shown in Figure 5.2.14. Specifically, the peak values of the streamwise vorticity at a representative instant of time have been shown. Figure 5.2.14 shows the differences in ω_x among Mode-A, Mode-A* at a Reynolds number of 175 and Mode-B ($Re=250$). It is to be noted that any x -location in the near-wake the streamwise vorticity in Mode-A* is about six times higher than the corresponding value for Mode-A. During Mode-A*, vorticity initially increases upto a certain streamwise position and then decreases. However, in Mode-A, the vorticity shows an insignificant variation. The streamwise vorticity for a Reynolds number of 250 (Mode-B) shows a similar variation as in Mode-A*, except that the maximum value is higher and the decay rate is faster. The trends in Figure 5.2.13 are understandable from the following viewpoint. At a Reynolds number of 150, the flow is two-dimensional and the corresponding spanwise wavelength can be taken to be large. In other situations, namely $Re=175$ (Mode-A and A*) and $Re=250$ (Mode-B), the flow is three-dimensional with finite spanwise wavelength. If one can relate three-dimensionality to vortex stretching, it follows that the initial vorticity for small distances in the x -direction will be higher for three-dimensional flows compared to the two-dimensional one. Thus, the vorticity in a three-dimensional field is initially larger, but it decays rapidly due to the formation of smaller structures. The decay rates are the smallest for two-dimensional flow ($Re=150$). At a Reynolds number of 175, the peak vorticity in the presence of vortex dislocation is higher, though the wavelength is also higher compared to Mode-A. This suggests a fine-grained structure contained within a larger vortex, which decays rapidly with distance. At $Re=250$, the vortex has a smaller spanwise wavelength of unity but a uniform distribution of vorticity. This results in a decay faster than in two-dimensional flow but slower than Mode-A*.

The distribution of the transverse vorticity is shown in Figure 5.2.15. The figure shows the peak vorticity determined at a representative instant of time on the mid-plane

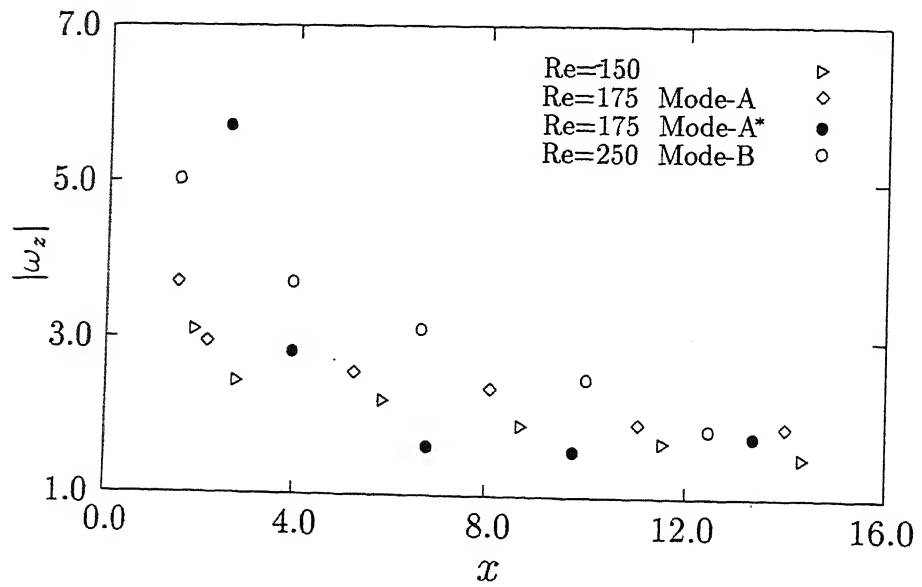


Figure 5.2.13: Streamwise variation of spanwise vorticity with Reynolds numbers.

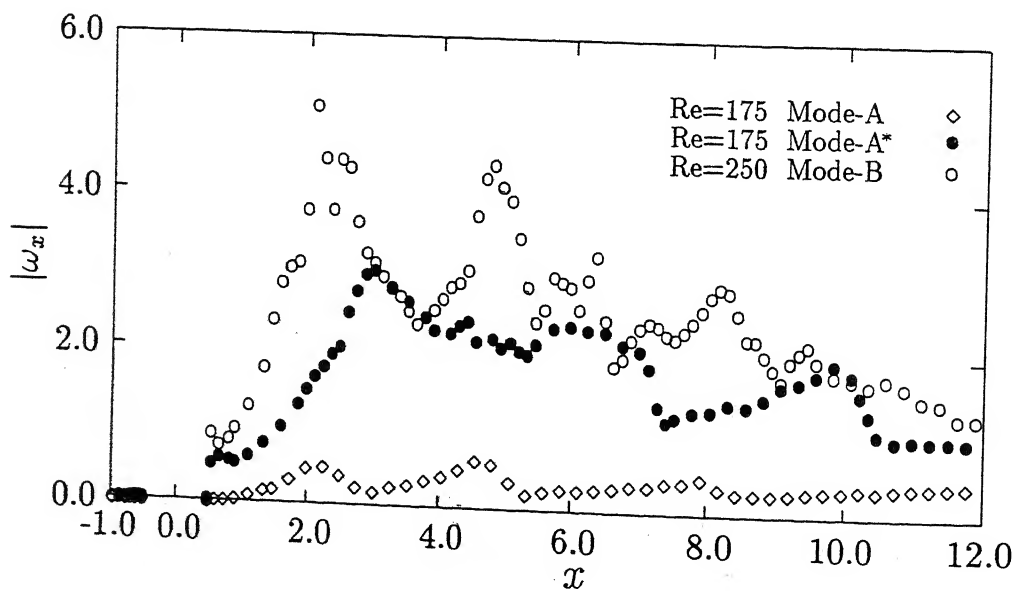


Figure 5.2.14: Streamwise variation of streamwise vorticity with Reynolds numbers.

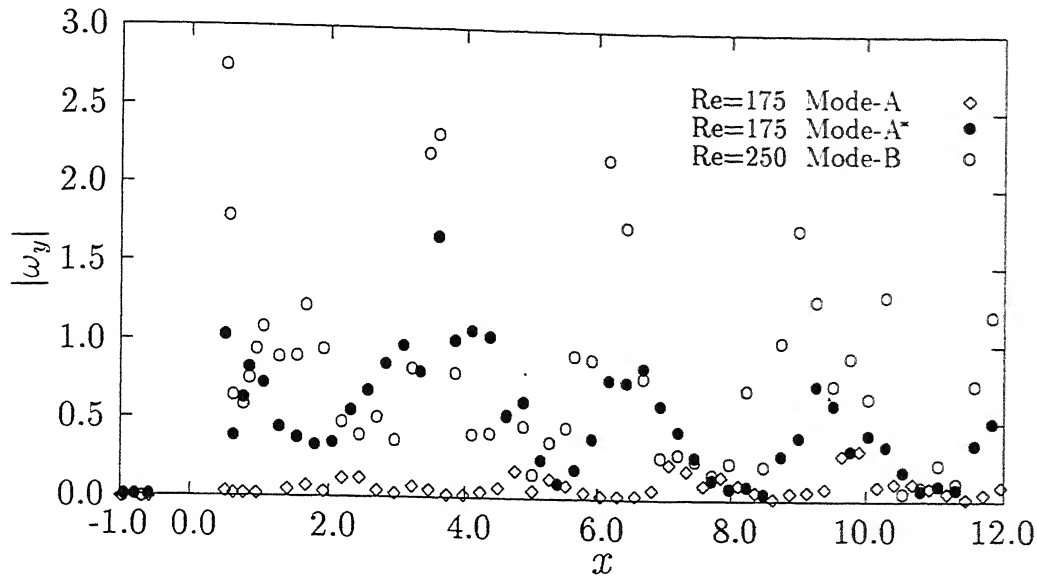


Figure 5.2.15: Streamwise variation of transverse vorticity with Reynolds numbers.

along the flow direction. No clear trend is discerned for any of the modes, except that for Mode-A, ω_y gradually increases with x while for A* and B, the dominant change is one of decay.

Transition in the wake of a square cylinder can now be characterized as follows: The flow is two-dimensional upto a Reynolds number of 150. At a Reynolds number of 175, the flow becomes three-dimensional. This particular Reynolds number is also characterized by the presence of intermittent low frequency oscillations together with the three-dimensional shedding mode (Mode-A). The combination of the two different phenomena has been called Mode-A*. There may exist a small range of Reynolds numbers in which the flow shows Mode-A behaviour without any intermittent low-frequency, but this could not be detected in the present work. The sequence of transition to three-dimensionality is thus expected to be:

$$2D \rightarrow A^* (3D) \rightarrow B (3D)$$

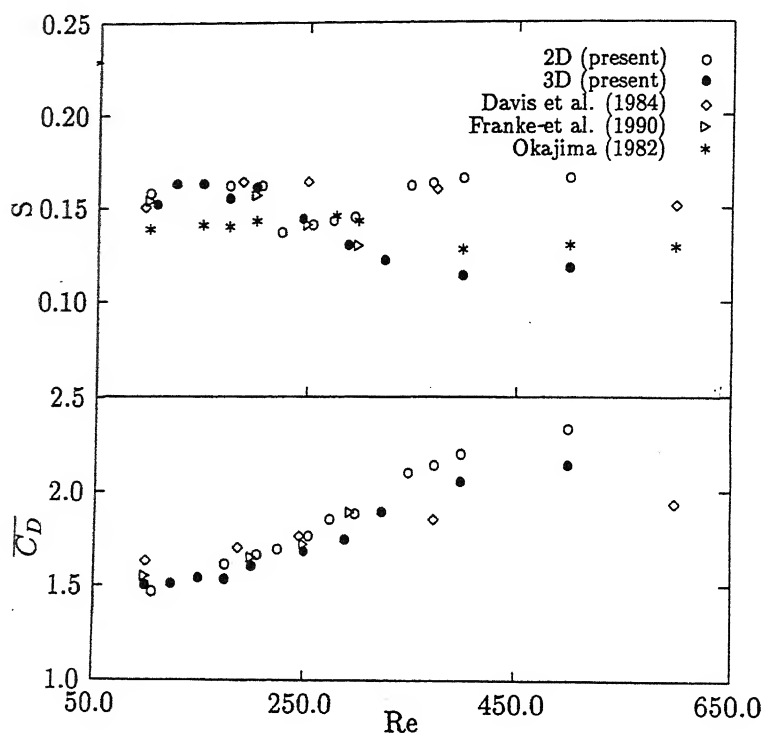


Figure 5.2.16: Variation of Strouhal number and drag coefficient with Reynolds number.

5.2.2 Time-averaged integral parameters

The present section is concerned with the consequences of vortex dislocation on time-averaged quantities. Figure 5.2.16 is a comparison between the present two- and three-dimensional simulation with the computational results of Davis *et al.* (1984) and Franke *et al.* (1990), and the hotwire experiments of Okajima (1982). This figure shows that at a Reynolds number of 175, the Strouhal number decreases. Beyond a Reynolds number of 250 for two-dimensional and 450 for three-dimensional calculations, there is an increase in Strouhal number. The reduction in the Strouhal number at a Reynolds number of 175 can be related to formation of vortex dislocation. The experimental points of Okajima (1982) show significant scatter and preclude a precise investigation of this effect. The data points shown in Figure 5.2.16 are averages determined from the reported experiments. The numerical simulation referred in Figure 5.2.16 are two-dimensional in nature and also fail to capture this trend. Specifically at a Reynolds number of 175, the computed value of the Strouhal number is 0.158, when dislocation coexists with the regular shedding mode and is lower than the value without dislocation ($=0.163$). A Strouhal number of 0.163 is

also obtained at a Reynolds number of 150 when the transition to three-dimensionality has not occurred. The Strouhal number increases to 0.161 at a Reynolds number of 200 when the dislocation fades away at this Reynolds number.

The variation of the time-averaged drag coefficient, $\overline{C_D}$ with Reynolds number is also shown in Figure 5.2.16. The present three-dimensional computation shows a close association between the drag coefficient and the Strouhal number. The inverse of the Strouhal number correlates with the time-averaged drag coefficient over the entire range of Reynolds number. The time-averaged lift coefficient was found to be less than 10^{-3} at all the Reynolds numbers studied.

Table 5.2.4: Rms values of lift and drag coefficients

Re	C'_L	C'_D
100	0.122	0.003
125	0.223	0.011
150	0.274	0.017
175	0.268	0.062
200	0.305	0.026
250	0.150	0.032
290	0.473	0.033

5.2.3 Rms values of force fluctuations

The rms values of the lift and drag coefficients as a function of Reynolds number are presented in Table-5.2.4. There is a steady increase in the rms values upto a Reynolds number of 150. At a Reynolds number of 175, an increase in the rms value of drag coefficient and a simultaneous decrease in that of lift coefficient are seen. This behaviour can also be traced to vortex dislocation. During this process, the elongation of the shear layer leads to a lower value of the instantaneous drag coefficient. Thus the rms value is higher though the time-averaged value is unaffected. The drop in the rms value of the lift coefficient can be explained by the lower transverse rms velocity fluctuation (Figure 5.2.9) experienced by the cylinder during vortex dislocation. A second discontinuity is observed

at a Reynolds number of 250. This can be attributed to the switching of the flow from Mode-A (or Mode-A*) to Mode-B. Mode-B contains fine-scale structures when compared to Mode-A. These small-scales also lead to smaller transverse fluctuation. The higher rms value of the drag coefficient is a consequence of the higher pressure drop across the cylinder in the streamwise direction due to the formation of small-scale structures. The rms values of the lift and drag coefficients subsequently show a steady increase with increasing Reynolds number¹.

5.2.4 Effect of three-dimensionality on the instantaneous forces

The three-dimensional flow has an effect on the pressure distribution around the cylinder. Due to the nonuniform pressure distribution along the span of the cylinder, there is a remarkable effect on the instantaneous forces acting on the cylinder. Figure 5.2.17(a) shows the temporal variation of the lift coefficient at three different locations ($z=1.5, 3.0$ and 4.5) along the span of the cylinder at a Reynolds number of 325. The three different lift coefficient curves are seen to be in phase though the peak values are affected. The drag coefficient behaves altogether in a different manner. Figure 5.2.17(b) depicts the phase shift among the three different drag coefficients calculated at the three locations. The point to be noted is that the cylinder may experience a bending moment, if two or more drag coefficients go out of phase. It is also evident that variations in the shedding frequency lead to variations in the drag amplitude. As a result, the bending moments at various spanwise locations are different. The flow without any prominent three-dimensional effect will not experience bending as there is no spanwise variation of lift and drag.

5.2.5 Time-averaged flow field

The wake of a square cylinder is unsteady even at a Reynolds number of 45. Hence a comparison of the wake behaviour at different Reynolds numbers in terms of entrainment and wake size is not appropriate if the instantaneous flow field is chosen. The time-averaged flow field better reveals the physical phenomenon at the large-scale. It is interesting to know if time-averaging suppresses the intricate phenomena such as vortex dislocation in

¹At a Reynolds number of 325, C'_L and C'_D were found to be 1.015 and 0.113 respectively. This sudden increase is consistent with the higher velocity fluctuations in the near-wake of Figure 5.2.20. A possible explanation is the resonance due to interaction between the shear layer and Kármán frequencies.

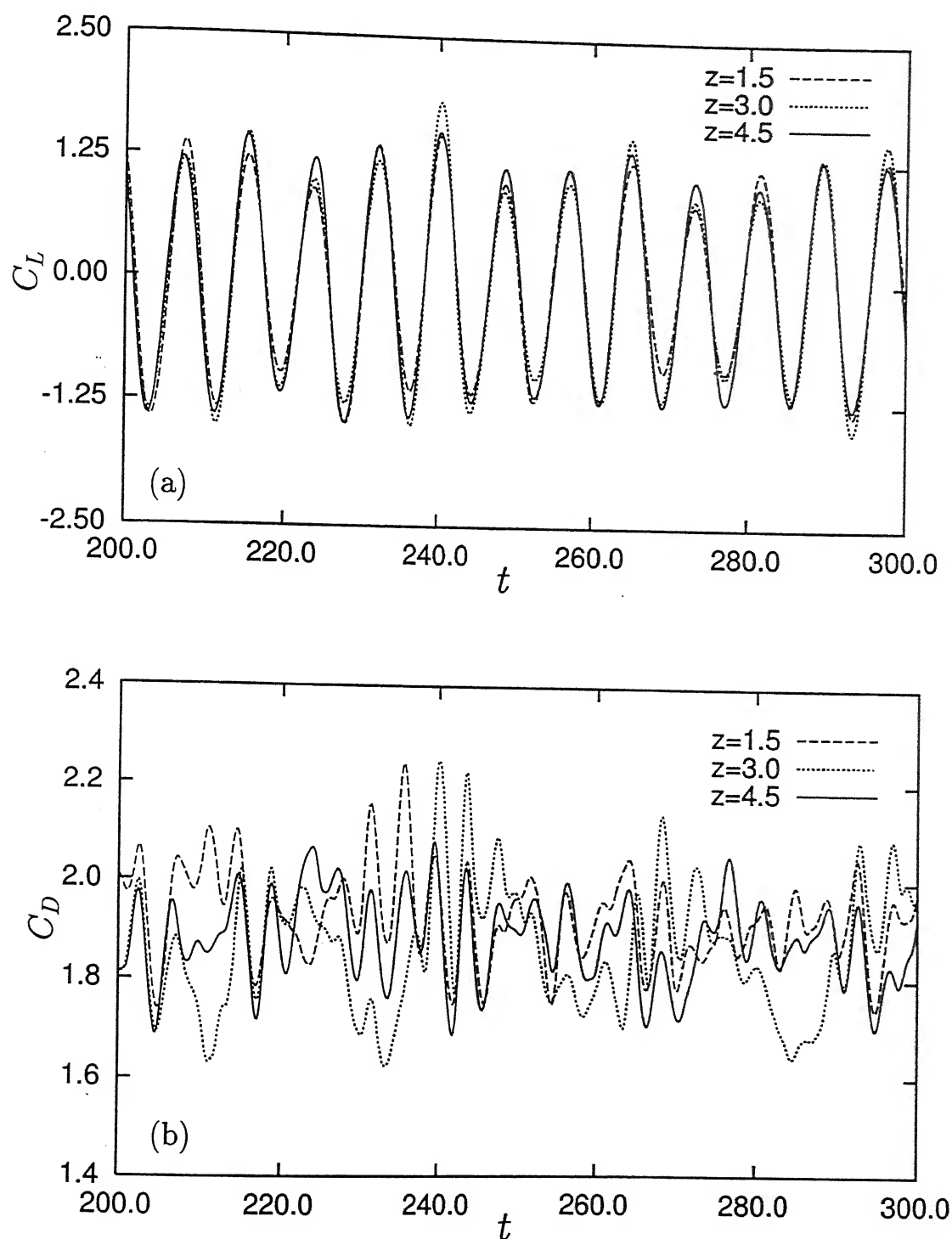


Figure 5.2.17: Variation of force coefficients at various spanwise locations at a Reynolds number 325: (a) lift coefficient and (b) drag coefficient. The drag coefficient shows severe three-dimensionality in terms of phase shifts among different spanwise locations whereas the lift coefficient does not suffer from such an effect.

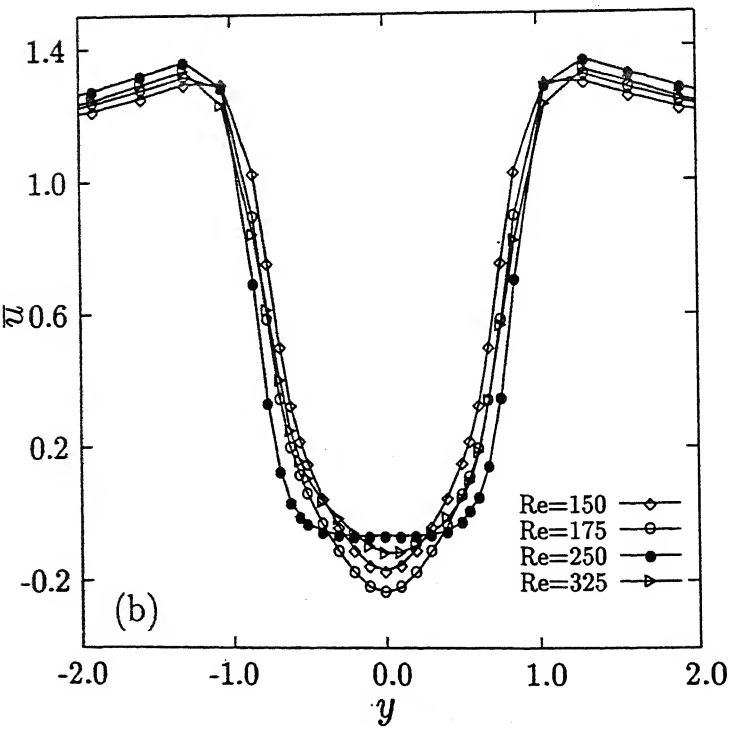
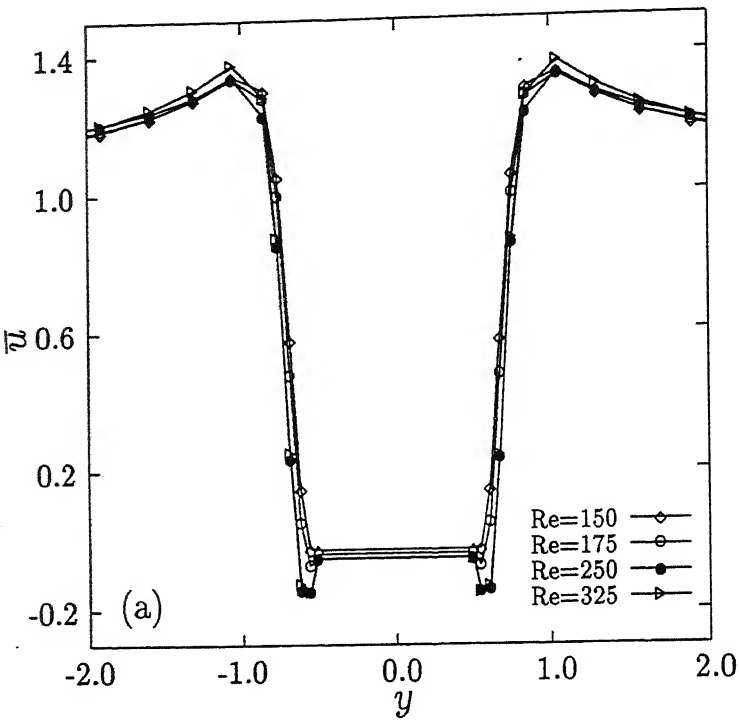


Figure 5.2.18: for caption see the next page

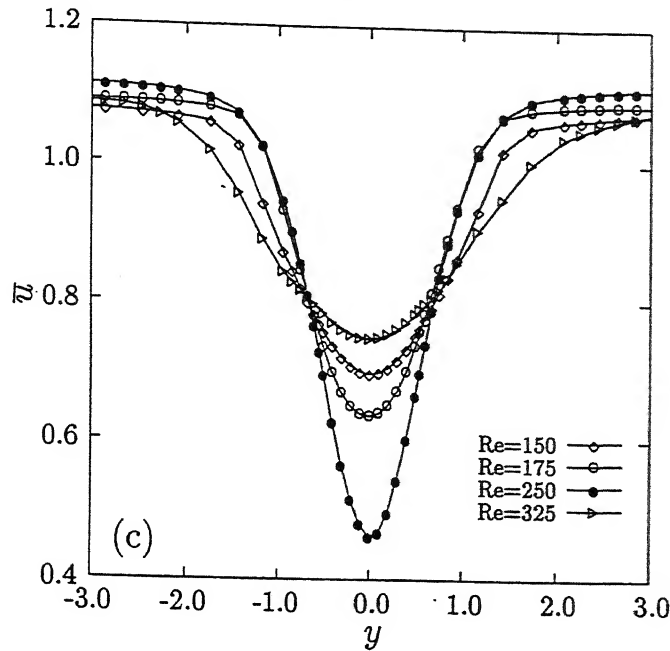


Figure 5.2.18: Variation of time-averaged streamwise velocity for various Reynolds numbers at different locations: (a) $x=0$ (b) 1.0 and (c) 4.0.

the portrait of the flow field. In the present study, the flow field has been time-averaged with twenty or more cycles after the dynamic steady state has been reached.

Figure 5.2.18 shows the time-averaged profile of the streamwise component of velocity for the four Reynolds numbers. Figure 5.2.18(a) has been drawn for a streamwise location of $x=0$. All the four profiles look similar except that at lower Reynolds numbers, very little backflow is observed above and below the cylinder. With the increase in Reynolds number, the extent of backflow increases. The streamwise velocity component at a location $x=1.0$ is shown in Figure 5.2.18(b). The centreline velocity is negative for all the Reynolds number at this location. The recovery of velocity is directly related to the wake-width which in turn depends on the entrainment at the edge of the wake. Since no difference is seen in wake-width, the recovery rates at different Reynolds numbers are practically identical. At an axial location $x=4$ (Figure 5.2.18(c)), the wake-width varies considerably with the Reynolds number. The wake-width initially decreases with the increase in Reynolds number to 175 possibly due to the increase in entrainment from the outer flow. With the increase in Reynolds number to 325, the wake-width again increases as the entrainment decreases.

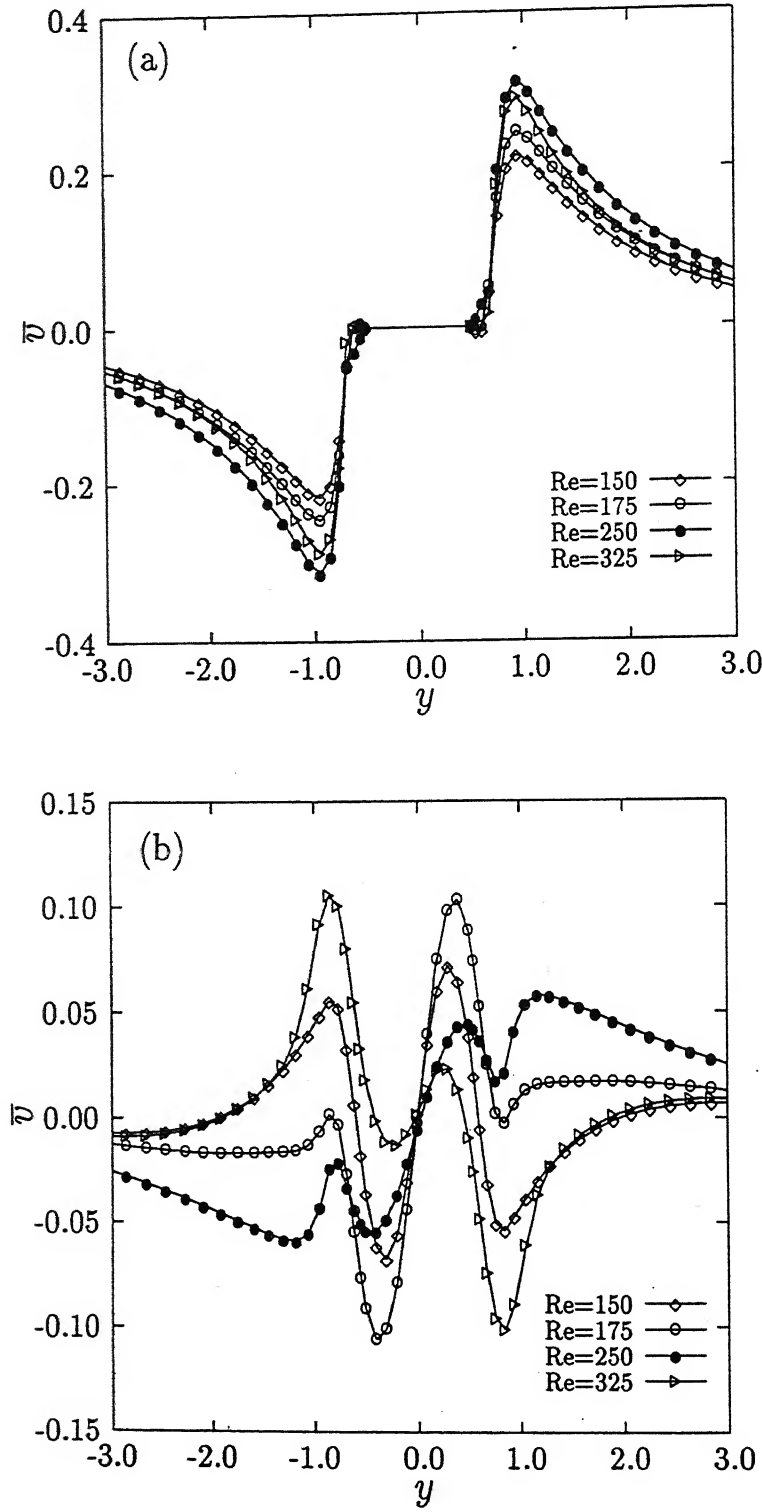


Figure 5.2.19: for caption see the next page

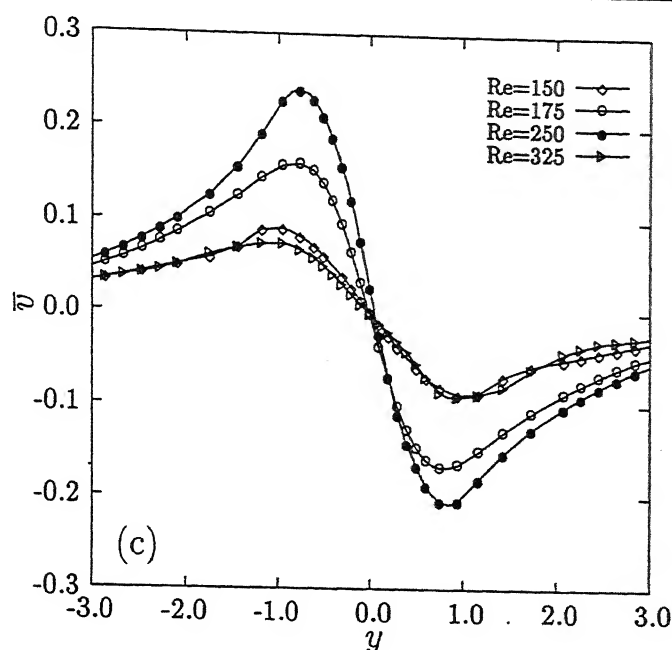


Figure 5.2.19: Variation of time-averaged transverse velocity for various Reynolds numbers at different locations: (a) $x=0$ (b) 1.0 and (c) 4.0.

The time-averaged transverse component of velocity, in turn a measure of entrainment have been presented in Figure 5.2.19. Though all profiles at $x=0$ (Figure 5.2.19(a)) look similar, the maximum velocity attained at $y = \pm 1$ shows differences with Reynolds number. Figure 5.2.18(b) demonstrates the entrainment within the recirculation bubble of the mean flow at $x=1.0$, a position close to the cylinder. The entrained fluid mass from either side of the wake crosses the centreline of the wake indicating positive and negative transverse velocity above and below the centreline respectively. Figure 5.2.19(c) also confirms the occurrence of entrainment of fluid mass in the wake at $x=4$. The entrainment mechanism into the wake is due to oppositely oriented spanwise vortices generated by the separating shear layer. The resulting motion takes the fluid inwards, closer to the wake centreline. As a consequence, the size of the wake grows in the downstream direction. This is consistent with the data of Figure 5.2.18.

The behaviour of the dimensionless fluctuating components in the wake shows interesting patterns. The fluctuations in general increase with the Reynolds number. However, over a narrow range of the Reynolds number, the spanwise wavelength changes from 3 to a value in the range 1.2-1.4 and leads to a drop in magnitude of the fluctuations. Figure 5.2.20(a) depicts the profiles of the streamwise normal stress $\overline{u'^2}$ at $x=0$. It can be seen

that the region occupied by the fluctuations on each side of the cylinder increases with the increase in the fluctuations. This transverse distance determines the wake-width in terms of the velocity fluctuations. The profile of $\overline{u'^2}$ at $x=1.0$ is presented in Figure 5.2.20(b). It is interesting to note that at each location, the fluctuations in the streamwise component of velocity at a Reynolds number of 175 are higher compared to a Reynolds number of 150. One should have expected the fluctuations at a Reynolds number of 175 to be smaller due to its three-dimensionality. Instead, the fluctuations at this Reynolds number are higher due to vortex dislocation. Subsequently, there is a sudden drop in the level of fluctuations at a Reynolds number of 250, though the trend is one of continuous increase in fluctuations with Reynolds numbers.

The drop in the level of fluctuations for Reynolds number range of 200 - 250 has been reported by Williamson (1996b) for a circular cylinder. The reason is conjectured to be the following. The change from Mode-A* to Mode-B instability is characterized by the change in the spanwise wavelength from 3 to a range 1.2-1.4. This change in wavelength from a higher to a lower value reveals the presence of finer or smaller scales in Mode-B. These finer scales correspond to smaller spatial fluctuations and high frequency eddies. On the other hand, the higher wavelengths correspond to low frequency eddies. These are related to larger coherent structures which are responsible for larger fluctuations at the transitional Reynolds number, *i.e.*, when three-dimensionality is initiated. With the further increase in Reynolds number, the fluctuations increase owing to the stretching of the primary vortices.

Another reason for higher fluctuations at higher Reynolds numbers (>300) can be attributed to the following: The primary vortices with opposite sign come closer to each other near the wake centreline and interact more intensely as compared to the case when they are apart. The interaction of the coherent structures is governed by tearing and pairing (Hussain, 1983). These produce newer structures at other scales. As a result of this complex interactions, the size of the fluctuations increase. In most cases, twin peaks are present in the near-wake. At $x=6.0$ (Figure 5.2.20(c)), there are twin peaks in the fluctuations at all Reynolds number except 250. The far-wake however shows different behaviour. The streamwise fluctuations far downstream ($x=14.0$) show two or more peaks (Figure 5.2.20(d)) upto a Reynolds number of 175, beyond which only single peak is observed. This phenomenon may be explained in the following way. At a lower Reynolds number, two rows of vortices of opposite sign are shed from the top and the

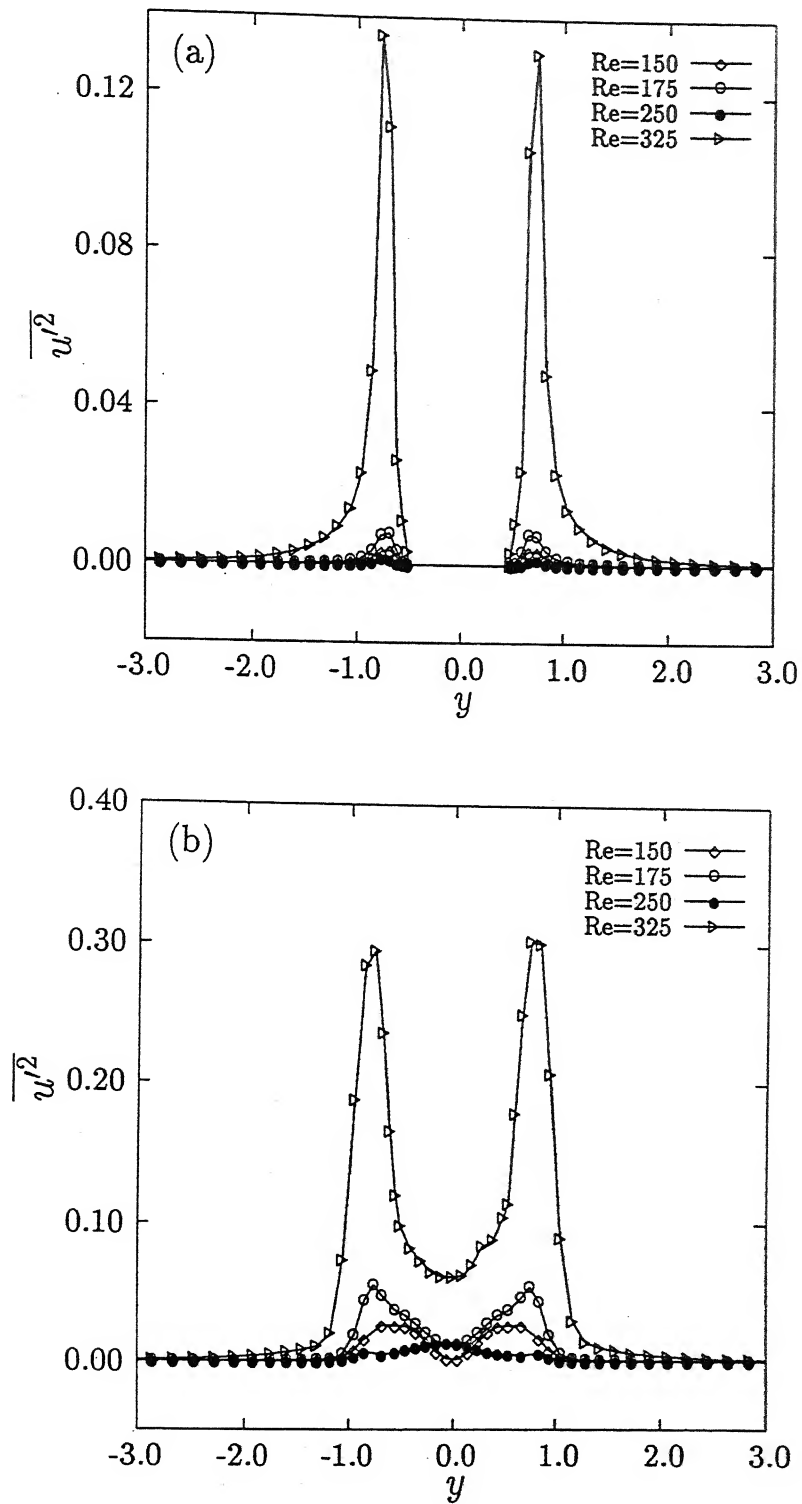


Figure 5.2.20: for caption see next page

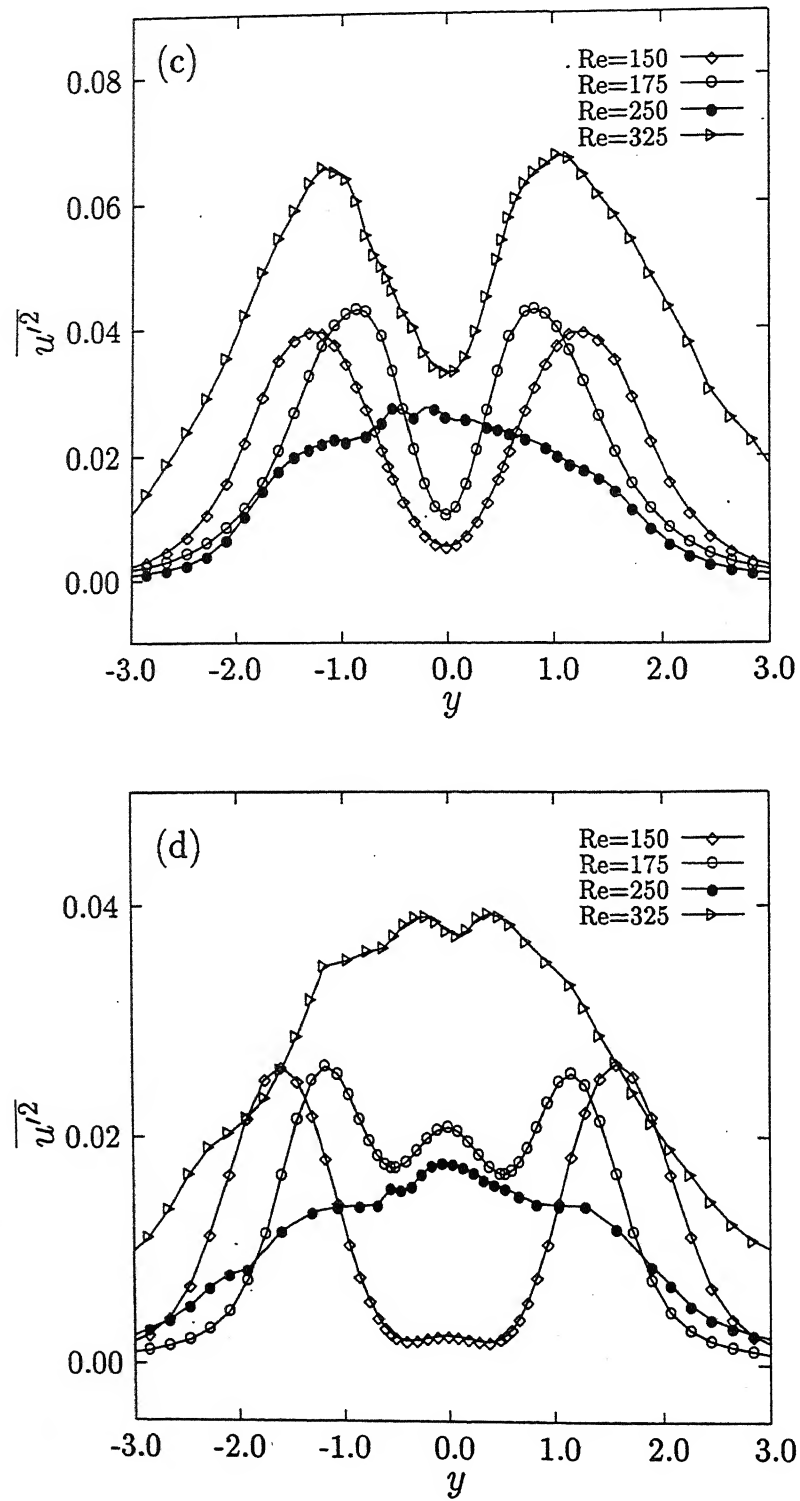


Figure 5.2.20: Variation of the streamwise velocity fluctuation for different Reynolds numbers at different locations: (a) $x=0$ (b) 1.0 (c) 6.0 and (d) 14.0.

bottom surfaces of the cylinder. These vortices travel downstream parallel to the wake centreline. The flow structure is predominantly non-overlapping. But at higher Reynolds numbers (>200), the vortices with opposite sign come closer in the far-wake and move along or parallel to the centreline. As a result, the net fluctuations are high and show a single peak.

The evolution of the streamwise component of velocity is shown in Figure 5.2.21(a). The magnitude of the negative velocity in the recirculation bubble is high for the transitional Reynolds number of 175. The recovery rates for each Reynolds number are practically equal and the streamwise velocity reaches its asymptotic limit at around $x=5$. There is a trend of slight decay for the Reynolds numbers of 150 and 175. The length of the recirculation region varies considerably with Reynolds number. It is the smallest for a Reynolds number of 325 ($=1.74$) and highest for a Reynolds number of 250 ($=3.1$). Figure 5.2.21(b) depicts the evolution of the streamwise normal stress ($\overline{u'^2}$) with Reynolds number. As discussed earlier, the fluctuations increase with Reynolds number with the exception at a Reynolds number of 250 where the fluctuations locally get reduced. It is interesting to see that there are two peaks in the fluctuations at a Reynolds numbers of 250 whereas at other Reynolds numbers, only a single peak is seen. It is to be noted that for the Reynolds number of 175, there is an increase in the streamwise fluctuations in the far-wake. The reason for this trend may be attributed to vortex dislocation which creates large-scale structures. Such structures spread rapidly along both the spanwise and streamwise directions. The asymptotic limit of the fluctuations following the initial decay near the peak is greater at higher Reynolds numbers. In summary, vortex dislocation does not affect the time-averaged flow field, though its influence is prominently seen in the time-averaged fluctuations.

5.2.6 Comparison with a circular cylinder

The transition phenomena in a bluff body wake particularly for a circular cylinder has been studied extensively in the past. Though the macroscopic flow past a square cylinder resembles to that of circular cylinder, there are major differences as far as the separation mechanism and the related integral parameters such as Strouhal number, lift and drag coefficient are concerned. In this context, it is surprising to note that there is similarity between the circular and square cylinders in their transition sequence at low Reynolds

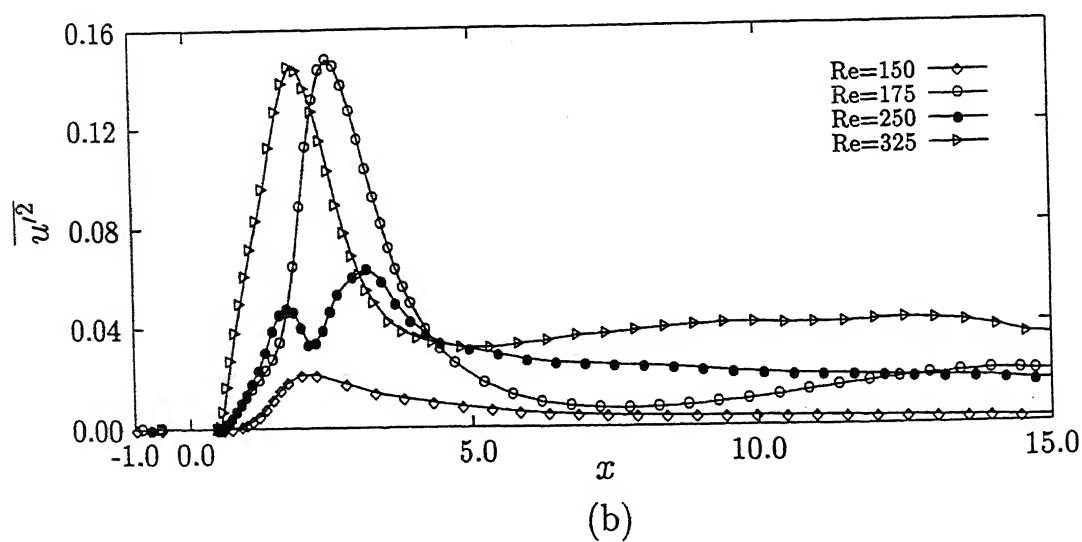
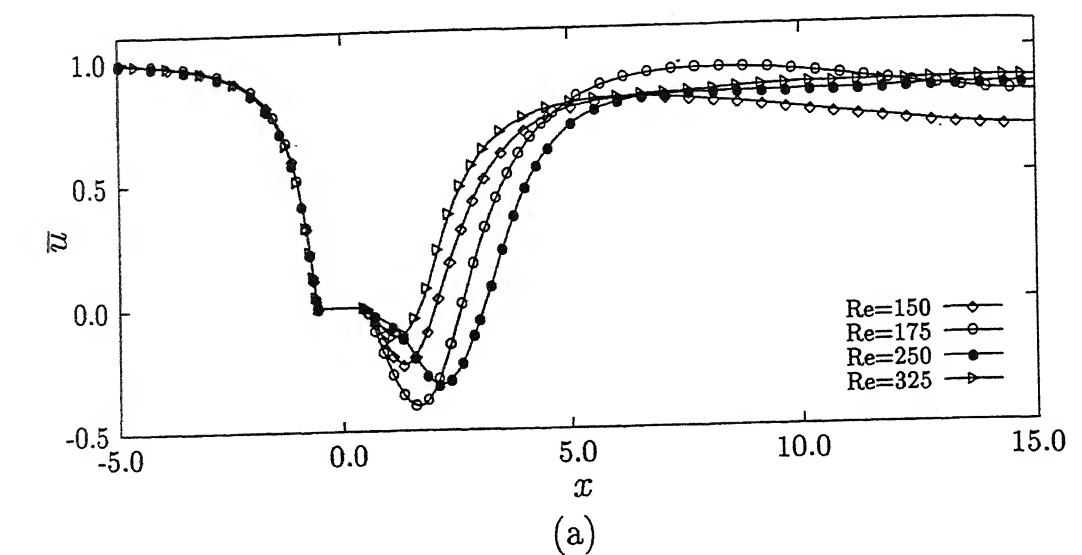


Figure 5.2.21: Streamwise variations of (a) streamwise time-averaged velocity and (b) streamwise velocity fluctuations at various Reynolds numbers.

numbers.

The flow past a circular cylinder experiences a transition to three-dimensionality at a Reynolds number of 180 (Williamson, 1988b). Noack and Eckelmann (1994) have found analytically this Reynolds number to be 170. The Floquet stability analysis carried out by Henderson and Barkley (1996) shows that the critical Reynolds number corresponding to three-dimensionality is 188.5. The present study indicates that the critical Reynolds number lies between 150 and 175 for a square cylinder.

The wake of a circular cylinder undergoes a series of transition with respect to the formation of the secondary spatial structures having different spanwise wavelengths. The transition to three-dimensionality is sensitive to various factors such as upstream conditions and end conditions of the cylinder. Williamson (1996a) has reported a spanwise wavelength of 3.0-4.0 at a Reynolds number of 189-194 for Mode-A and 1.0 at a Reynolds number of 250 for Mode-B for flow past a circular cylinder. Numerical calculation and experiments of Zhang *et al.* (1995) have shown that the wavelengths are 4 for Mode-A and 1 for Mode-B at Reynolds numbers of 200 and 240 respectively. Henderson (1996) has found that Mode-A is triggered at a Reynolds number of 195 and the corresponding wavelength is 3.96. This study also shows that the wake of the cylinder has a Mode-B pattern at a Reynolds number of 265 with a spanwise wavelength of 0.822. Brede *et al.* (1996) have reported Mode-A at a Reynolds number range of 160-240 for flow past a circular cylinder and the corresponding wavelength is 4.5. At a Reynolds number greater than 240 the pattern was found to be Mode-B with a spanwise wavelength of 1. The spanwise wavelength in the present study has been found to be 3.0 for Mode-A and the corresponding Reynolds number is 175. Mode-B does not have a constant spanwise wavelength but falls in the range of 1.2-1.4 at a Reynolds number of 250.

The instantaneous contours of the secondary vortices (ω_y) in Mode-A have been found to be of alternate sign along the cylinder axis (Figure 5.2.2(b)). These contours are similar to those observed by Zhang *et al.* (1995) for a circular cylinder. The structures of secondary vortices in Mode-B of the present study (Figure 5.2.4(b)) are also similar to those of Zhang *et al.* (1995).

The wake of the square cylinder experiences intermittent low frequency pulsation at definite Reynolds numbers. This phenomena has been attributed to the formation of large-scale irregularities, namely vortex dislocation. The flow irregularity has been

reported by many researchers in the past. Roshko (1954) observed a low frequency intermittency in the wake of a circular cylinder. Subsequently, Bloor (1964) explained the low frequency pulsation as the cause of three-dimensionality. Williamson (1992) has also observed low frequency fluctuations in an extensive set of experiments. This is clear from the Figure 4 of his paper which describes the downstream decay of streamwise fluctuations at a Reynolds number of 183. Henderson (1996) has reported similar fluctuations in lift and drag coefficient at a Reynolds number of 1000. The fluctuations of lift coefficient (Figure 20, Henderson (1996)) are similar to Figure 5.2.9 of the present study. The contours of the secondary vortices of the present study clearly show the formation of dislocation at the mid-span. A similar pattern has been reported from experiments by Towfighi and Rockwell (1994) for dislocation in flow past an oscillating cylinder. An important characteristic of a dislocation is its high spanwise spreading rate. Figure 6(b) of Williamson (1992) shows this phenomenon and is remarkably similar to Figure 5.2.7(c) of the present study.

The transition sequence to three-dimensionality reported by Williamson (1996b) for circular cylinder is $2D \rightarrow A \rightarrow A^* \rightarrow B$. In contrast, the present study shows that this particular sequence for a square cylinder to be $2D \rightarrow A^* \rightarrow B$.

5.2.7 Closure

A numerical study of three-dimensional flow past a square cylinder in the Reynolds number range of 150 - 325 has been reported. The flow is seen to be predominantly two-dimensional at a Reynolds number of 150. At a Reynolds number of 175, the flow is three-dimensional, with two possible modes labeled Mode-A and Mode-A*. In Mode-A, a three-dimensional structure with a spanwise wavelength of 3 is formed. In Mode-A*, this is accompanied by intermittent large-scale irregularities identified as vortex dislocation. The time for which vortex dislocation persists is 10-12 times the shedding period. At all Reynolds numbers, the flow is shedding dominated, and hence by the spanwise vortices, three-dimensionality being superimposed on this flow field.

It is important to know the extent of influence of three-dimensionality on the time-averaged flow field, forces and decay rates of vorticity. The numerical results of the present work show that:

1. Transition to three-dimensionality occurs at a Reynolds number between 150 and 175.
2. Flow at a Reynolds number of 175 shows intermittent low frequency irregularities and consequent two distinct modes namely, Mode-A and Mode-A*.
3. Vortex dislocation possibly occurs as a result of vortex merging in the spanwise direction.
4. Flow at a Reynolds number of 250 reveals Mode-B having a finer-scale compared to Mode-A.
5. The spanwise wavelengths corresponding to Mode-A and Mode-B are 3 and 1.2-1.4 respectively.
6. The effect of three-dimensionality is prominent for the drag coefficient because of phase shifts along the length of the cylinder.
7. The various three-dimensional modes affect the time-averaged fluctuations though these do not have any effect on time-averaged flow field.

5.3 Vortex Structures and Kinetic Energy Budget in Two-Dimensional Flow

This section is aimed at understanding the role of the periodic components on momentum transfer in laminar wake of a square cylinder. Further, their similarity to the periodic components in turbulent flow, obtained by phase averaging has been explored. To undertake this study, the square cylinder is taken to be exposed to a fully developed approach flow at the inflow plane of the channel. The Reynolds number based on the cylinder width and the average velocity considered in the numerical study is 100. The results of the numerical simulation have been analyzed to determine the characteristics of vortices, the statistics of the velocity fluctuations, the overall topology of the wake and the individual contributions to the kinetic energy budget.

The relevant dimensions pertaining to the present study are: $L=40$, $L_a=6.0$, and $H=10$ (Figure 1.3). The boundary conditions employed for the present investigation are:

- Top and bottom boundaries (at $y=\pm H/2$): $u=v=0$ (no-slip condition)
- Channel inlet: $u=u(y)$ (fully developed), $v=0$.
The experiments of Cantwell and Coles (1983) were conducted in a wind tunnel, with the approach velocity being a constant and no confining boundaries. Numerical experiments carried out in the present work show only a weak influence of the side walls on the near-wake structure.
- Channel exit: Convective boundary conditions of the Orlanski type (Orlanski, 1976) has been used.
- Obstacle: No-slip boundary conditions are used for the velocities on the obstacle surface.

The discretization of the convective terms in the momentum equations are performed by a third order scheme (Kawamura *et al.*, 1986). The time step employed in the computation is of the order of 10^{-3} .

For the computation, the flow domain is divided into a number of cells, the cell aspect ratio being unity in all the calculations. A uniform mesh has been used throughout

the domain. In order to achieve a grid independent solution, computations have been performed for two different meshes with 642×162 and 402×102 grids. The time-averaged drag coefficient ($\overline{C_D}$) on a 642×162 grid was found to be 2.97 and on a 402×102 grid was 2.92, a difference of less than 2 percent. Results presented here are for a 402×102 grid at Reynolds number of 100. The entire set of calculations was repeated at a Reynolds number of 150 and the results obtained were found to be practically identical to those of a Reynolds number of 100. Hence the present study may be considered to have a range of validity of $100 < Re < 150$. For $Re > 180$, Williamson (1988b) has shown a transition to three-dimensionality for a circular cylinder¹ and the results of the present work are not expected to carry over.

The full code has been extensively tested against other numerical solutions and experimental data. The comparison for flow past a square cylinder at a Reynolds number of 21400 is presented in Section 5.7. For example, Figure 5.7.4(a) shows the comparison of the time-averaged streamwise component of velocity at different locations downstream of the cylinder. The experimental data of Lyn *et al.* (1995) and the LES calculation of Wang *et al.* (1996) are also superposed on this figure. The agreement between the present computations and the reference data can be seen to be good.

Calculations for this study were carried out on a DEC-ALPHA machine with 32MB RAM and 125MHz processor speed. The typical CPU time on a 402×102 grid was found to be 2 hours per cycle of vortex shedding. All results have been discussed on the basis of data generated after 30 such cycles.

As already discussed, in the wake of a bluff-body flow the time-varying component ϕ (for example, velocity and pressure) may be written as the combination of the global mean component $\overline{\phi}$, a periodic component $\tilde{\phi}$ and a random component ϕ'' (Hussain, 1983). ϕ'' refers to turbulent flow alone whereas $\overline{\phi}$ and $\tilde{\phi}$ are common for both laminar and turbulent flows. In the present study, ϕ'' is negligible at a Reynolds number of 100 and correlations that defines the stress tensor have been formed using $\tilde{\phi}$. Specifically, a terms such as $\tilde{u}\tilde{v}$ is calculated as $\frac{1}{T} \int_0^T (u - \overline{u})(v - \overline{v})dt$, where the integral is evaluated by direct summation over 30 (or greater) cycles.

Results obtained by direct numerical simulation are discussed here for the flow past a square cylinder placed centrally in a parallel plate channel at a Reynolds number of

¹Section 5.2 shows transition to occur for a square cylinder when $150 < Re < 175$.

100. The flow past a circular cylinder beyond a Reynolds number of 180 has been shown to be three-dimensional by Williamson (1988b). Hence the flow pattern in the present work is expected to be two-dimensional at a Reynolds number of 100. Further, the flow is expected to be laminar in the sense that the flow variables are composed of a time mean and a periodic part, the random component being zero.

For the present configuration, the Strouhal number and drag coefficient were determined as follows. The Fourier transform of the signal of the transverse component of velocity in the near-wake was computed and the power spectrum was determined. The spectrum was seen to have only one dominant peak corresponding to the vortex shedding frequency. This confirmed the periodicity of the flow field. The Strouhal number based on this frequency was found to be 0.238 for fully developed and 0.17 for uniform inflow conditions. The drag coefficient was determined by integrating pressure on the forward and rear faces of the cylinder. The viscous contribution was found to be negligible in the present work (around 5% for parabolic and 8% for uniform flow condition at inlet). The drag coefficient was calculated to be 2.92 for fully developed and 1.62 for uniform inflow conditions. The rms values of fluctuating lift and drag were calculated as 0.52 and 0.04 respectively. Detailed experimental results at such a low Reynolds number as 100 are not available. Okajima (1982) has obtained a value of 0.15 for Strouhal number at a Reynolds number of 100 in an unconfined wake. This is consistent with the value of 0.17 obtained by the present authors, the increase being due to the wake confinement in a channel. Davis *et al.* (1984) report a drag coefficient of 1.6 at $Re=100$ from numerical studies. Hence the present calculation is generally in agreement with the published data.

5.3.1 Wake dynamics at a low Reynolds number

The present study is concerned with the structure and energetic interactions in the wake. Thus, the focus is primarily on the flow details and are discussed in detail below. Figure 5.3.1 shows the trajectory of the point of peak vorticity with time. It is clear from the figure that the vortices move away from the centreline at the very beginning. Subsequently, they come closer to the centreline and finally travel away and leave the domain in a direction parallel to the main flow. Hence, a vortex shed on the lower side of the cylinder leaves the physical region at a point above the cylinder axis (also see Figure 5.3.9). Initially, the vortices at the base of the square cylinder, namely the region between the

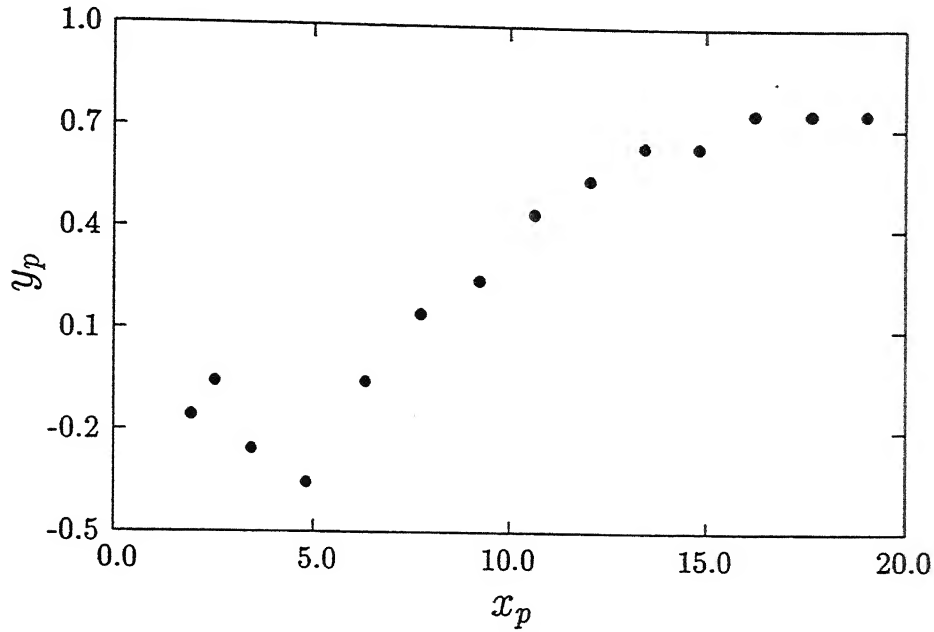


Figure 5.3.1: Trajectory of vortex peaks. The vortex moves parallel to the wake centreline in the far-wake.

wake stagnation point and the rear surface remain relatively inactive. Later these vortices accelerate and move with constant velocity into the far-wake. Figure 5.3.2 shows a plot of the x -coordinate of the peak vorticity (x_p) with time. The slope of the x_p-t graph gives the celerity (c_x) of the vortex associated with the peak vorticity. In the base region (approximately $x < 2.5$) the celerity c_x is found to be 0.69 whereas in the near- and far-wake ($x > 2.5$) the value remains a constant at 1.30. This value is somewhat higher compared to a value of 0.85 presented in the literature (Lyn *et al.*, 1995). The reason is that in the present computation, the inflow condition has been taken to be fully developed and not a constant. The y -direction celerity c_y fluctuates as the vortices travel downstream and becomes zero before the vortices leave the physical domain.

Figure 5.3.3 depicts the decay of peak vorticity ($|\omega_p|$) of the total flow field with the downstream direction. The decay is related to viscous diffusion primarily in the transverse direction. In the base region the decay rate is very high. The decay of vorticity with distance (Figure 5.3.3) has been fitted with a curve of the form $|\omega_p| = 4.79e^{-0.125x} + 0.3x^{0.45}$, $\pm 4.6\%$. The decay rate calculated from this curve by differentiation is presented in Table-5.3.1. The decay rate itself diminishes with distance, showing that vortices are

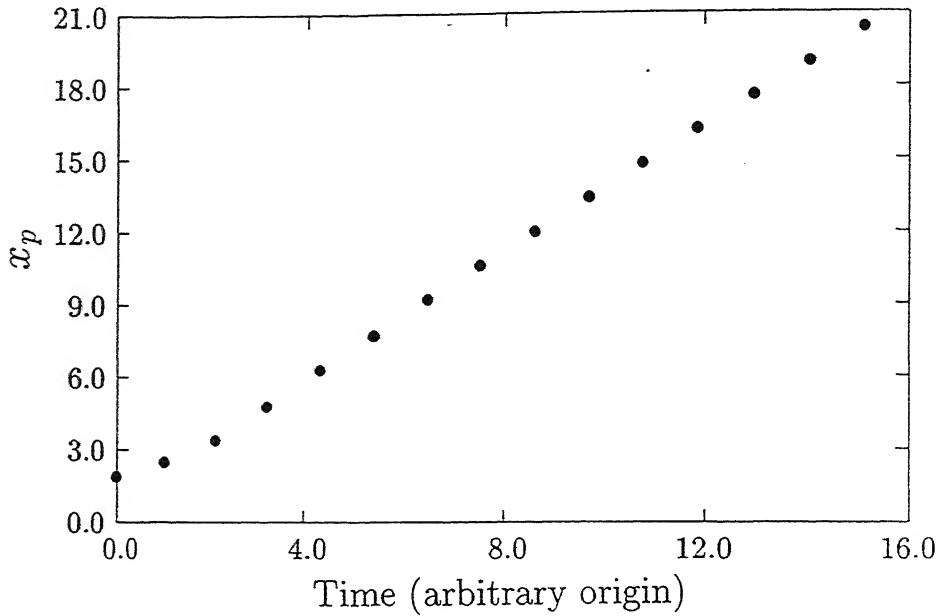


Figure 5.3.2: Variation of streamwise location of vortex peaks with time. The streamwise vortex celerity near the cylinder (base region) is less than that in the near- and far-wake ($x > 2.5$).

transported by advection in the far-wake.

5.3.2 Profiles of time-averaged flow field and stresses

The time-averaged velocity profiles behind the cylinder at specified downstream locations have been exhibited through Figures 5.3.4 and 5.3.5. The velocity profiles were seen to be symmetric about the centreline of the channel. Hence only the lower half of the channel has been shown in these figures. Results have been presented for the near-wake alone, that is $x \leq 7$, where x is measured from the centre of the cylinder. An examination of Figures 5.3.4 and 5.3.5 shows the following: Just above the cylinder ($x=0$), the acceleration of flow due to blockage of the channel produces streamwise velocities greater than 1.5 and transverse velocities in the negative direction. The blockage effects continue to be felt in the base region ($x=1.0$) but for $x \geq 2$, a wake-like behaviour is seen. In particular, one can notice reversed flow conditions and positive values of the transverse velocity, characteristic of fluid entrainment by the wake. This is consistent with an increase in wake size with distance. At $x=7$, the velocity profiles attain an element of similarity. In particular,

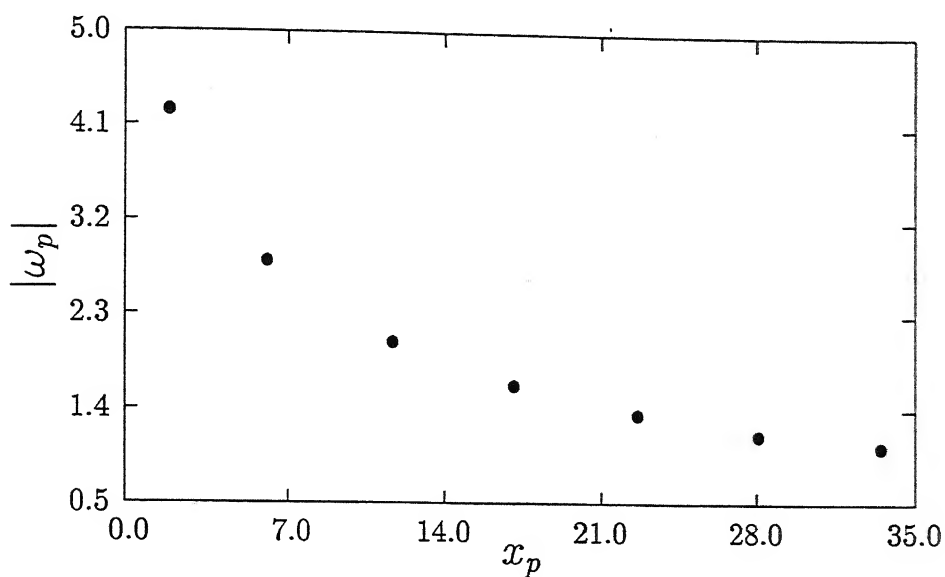


Figure 5.3.3: Downstream decay of peak vorticity. The decay of vortices in the downstream direction is attributed to viscous diffusion at low Reynolds number.

Table 5.3.1: Decay Rate of Peak Vortices

Streamwise Location	Peak Vorticity	% of Decay
1.95	4.16	9.06
3.45	3.63	8.85
6.35	2.85	7.80
9.25	2.32	6.42
12.05	1.98	4.98
14.85	1.76	3.59
17.65	1.61	2.36
19.05	1.57	1.83

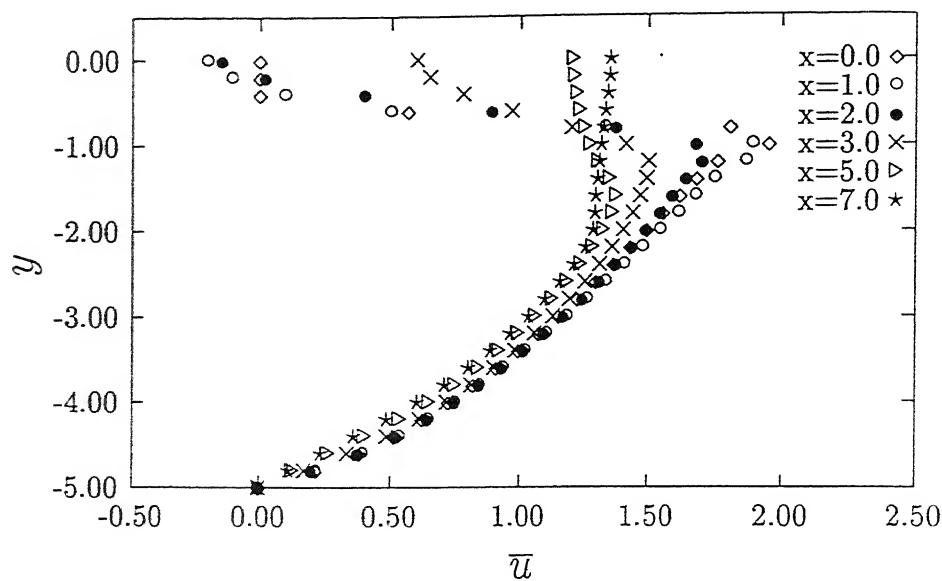


Figure 5.3.4: Time-averaged profiles of streamwise velocity component at different x -locations.

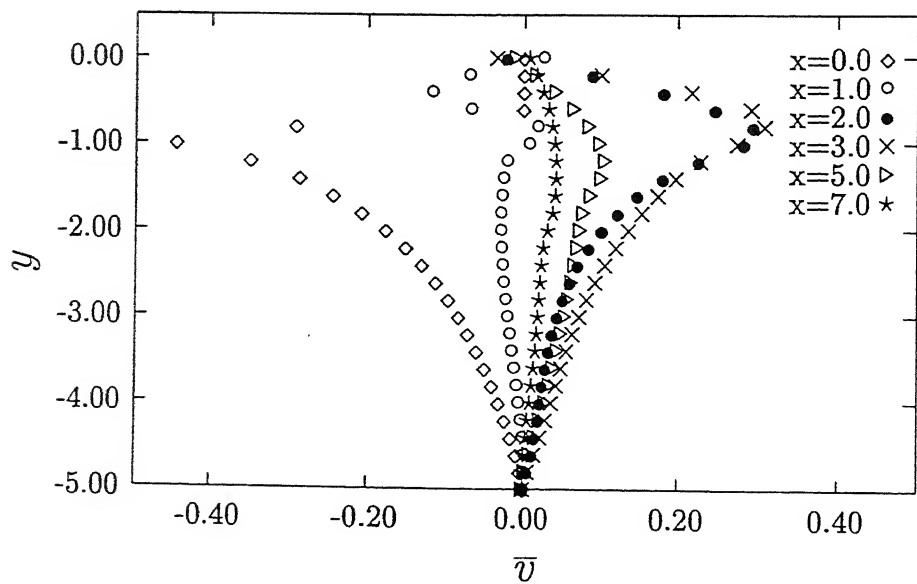


Figure 5.3.5: Time-averaged profiles of transverse velocity component at different x -locations.

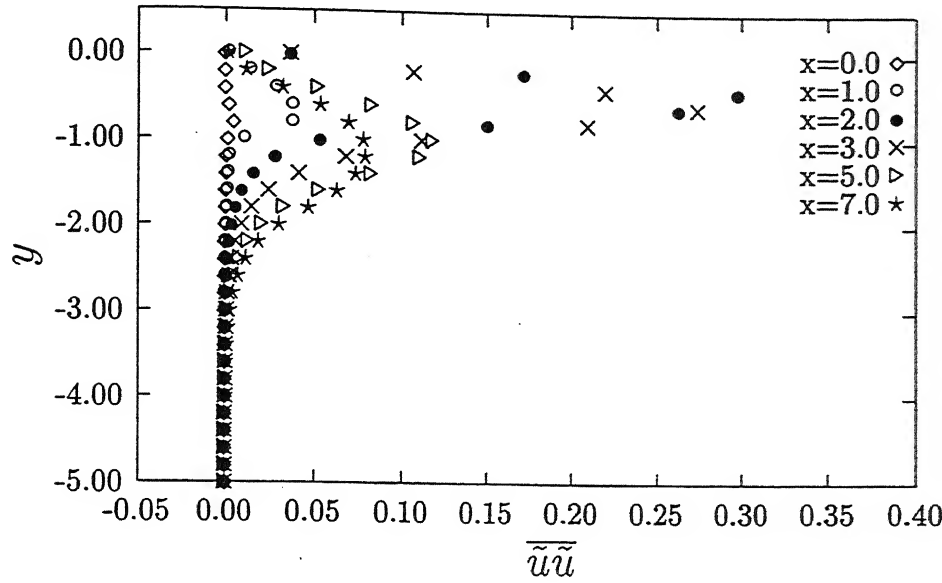


Figure 5.3.6: Time-averaged profiles of streamwise normal stress component at different x -locations.

the transverse velocity component becomes small and the streamwise component displays a wake region near the centreline and the related velocity deficit, while the outer region appears parabolic and fully developed. Over a distance of $x=1$ to 7, the centreline velocity changes from -0.035 to 1.36 , the variation being very rapid upto $x=3$. Using eye judgment, one can deduce the wake size at $x=7$ based on the mean flow to be around 4 units, 2 units on each side of the centreline.

The profiles of the stress terms $\overline{u'u'}$, $\overline{v'v'}$, $-\overline{u'v'}$ associated with the periodic components of velocity have been shown in Figures 5.3.6, 5.3.7 and 5.3.8. The streamwise and transverse normal stresses $\overline{u'u'}$ and $\overline{v'v'}$ are both large in the near-wake ($x \geq 2$) but decay rapidly with distance in the flow direction. The transverse profiles show that $\overline{u'u'}$ is small on the centreline and attains a maximum away from it. This point moves outwards for locations further downstream. In contrast, peak values $\overline{v'v'}$ occur at the axis itself. The shear stress $-\overline{u'v'}$ is zero at the axis and attains its highest magnitude away from it. This maximum value also decays with the downstream distance. All three stresses clearly demarcate the wake boundary, outside which they are zero. The wake sizes corresponding to $\overline{u'u'}$, $\overline{v'v'}$ and $-\overline{u'v'}$ are 5.0, 4.0 and 4.2 respectively and thus marginally higher than the wake

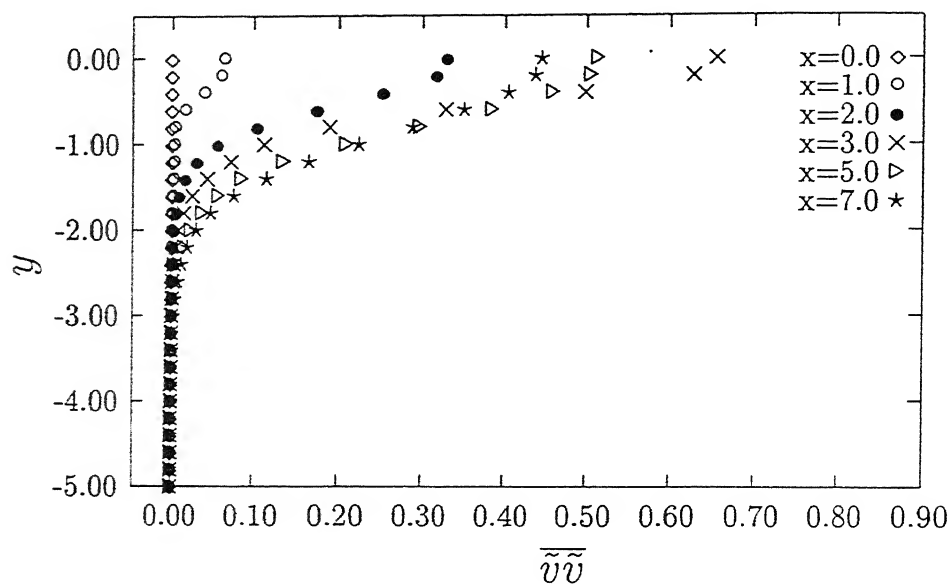


Figure 5.3.7: Time-averaged profiles of transverse normal stress component at different x -locations.

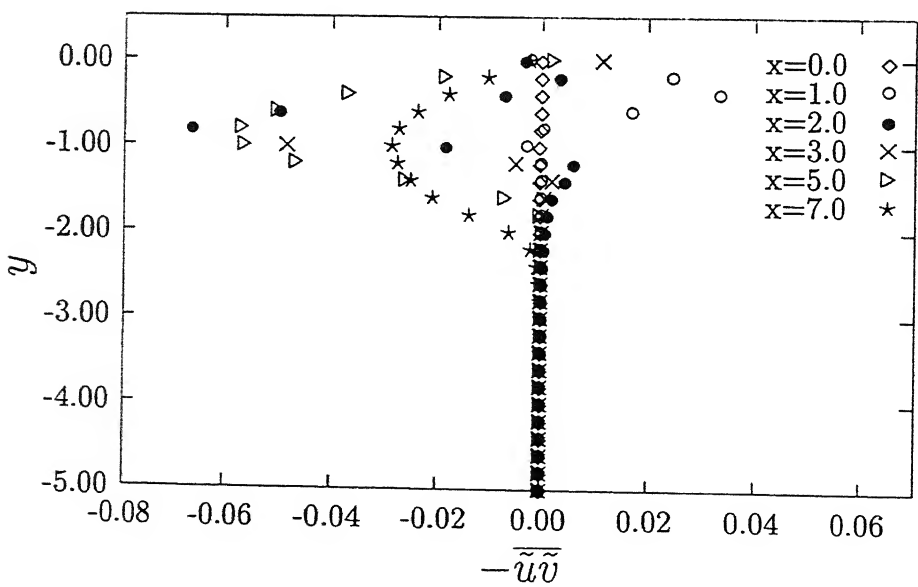


Figure 5.3.8: Time-averaged profiles of shear stress at different x -locations.

size for mean flow. Thus velocity fluctuations penetrate deeper into the outer flow. This could be due to shear in the mean flow associated with fully developed inflow conditions.

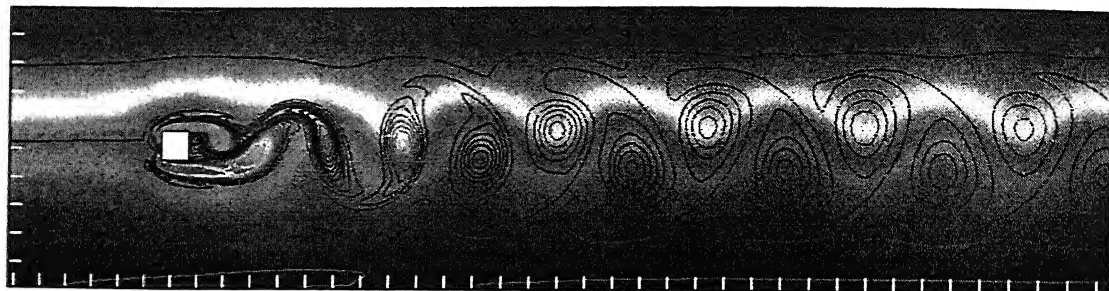
It is of special interest to relate the sign of the time-averaged streamwise velocity gradient ($\frac{\partial u}{\partial y}$) with that of $-\overline{u'v'}$. Comparing Figures 5.3.4 and 5.3.8, the signs of each of them can be seen to be negative. One can then conclude that the generation of velocity fluctuations in the wake follows a process akin to that in near-parallel shear flows, boundary-layers for example.

The decay of the periodic components with distance does not automatically indicate the process of viscous dissipation. As proposed by Townsend (1949) for turbulent flows, the decay in the downstream direction can be associated with transport of fluctuations in the transverse direction. Figures 5.3.6-5.3.8 convincingly show an increase in the magnitude of the stress terms for a given y -location, as one moves downstream. It is interesting to note that the trends seen in these figures are similar to those of Lyn *et al.* (1995) and Cantwell and Coles (1983) for turbulent flow.

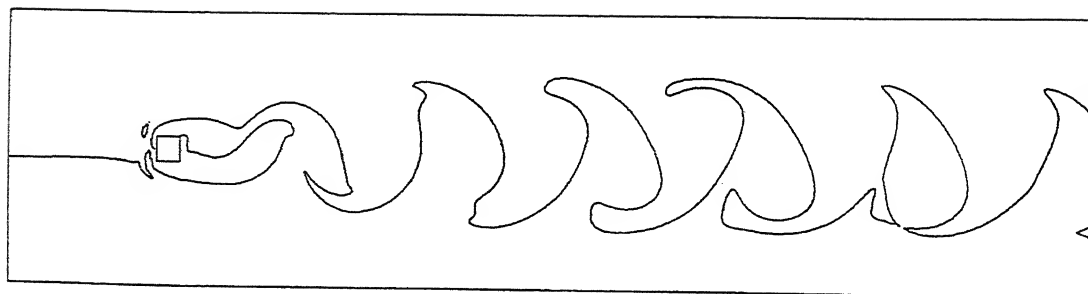
5.3.3 Instantaneous flow field

Figure 5.3.9(a) depicts the instantaneous vorticity contours and streamlines for a Reynolds number of 100 at a nondimensional time of 213 (around 35 cycles). The two quantities have been superimposed on each other, with the streamlines shaded. The contour plot clearly reveals the alternate shedding of vortices from each side of the cylinder. The repeated rollup of fluid masses are discerned and are visible in the figure. Figure 5.3.9(b) demonstrates the threading of the Kármán vortex street, namely the continuity of iso-vorticity lines over a long distance. Such threading has also been experimentally observed by Perry *et al.* (1982) and Gerrard (1978) for circular cylinders at Reynolds numbers of about 100. A major difference between the present calculation for the laminar case and the general problem of turbulent flow should be noted. As in Figure 5.3.9, the laminar wake remains strongly coherent over a larger distance, at least upto $x=33$ at $Re=100$, while the degree of coherence is expected to be diminished over a smaller distance, perhaps $x>7$ at higher Reynolds numbers.

It is clear from the discussions above that the flow in the wake is unsteady, with a dominant periodic component superimposed on the mean velocity field. Rms values of



(a)



(b)

Figure 5.3.9: (a) Instantaneous vorticity contours and (b) Schematic of threading process. The vorticity contour shows coherency of the vortex structure way upto the exit of the flow domain.

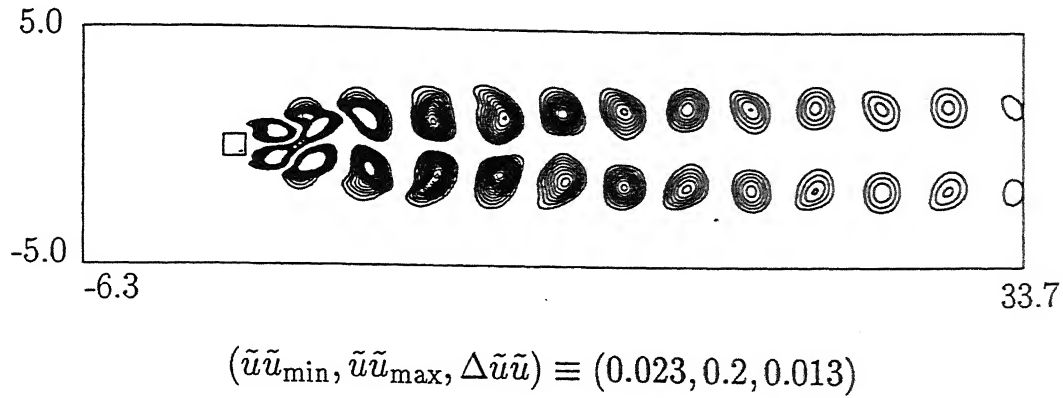


Figure 5.3.10: Contours for instantaneous streamwise normal stress. The the instantaneous stress itself show the evidence of the double peaks in the time-averaged profiles of streamwise normal stress.

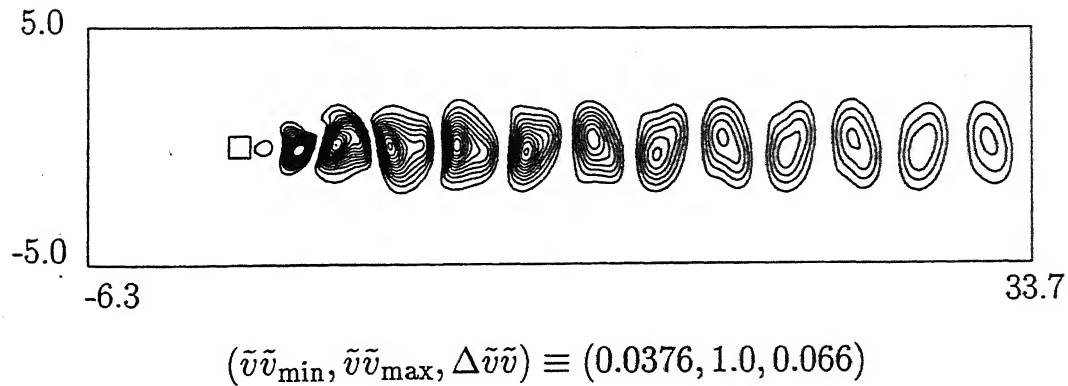


Figure 5.3.11: Contours for instantaneous transverse normal stress. The the instantaneous stress itself show the evidence of the single peak in the time-averaged profiles of transverse normal stress.

the periodic component further show cross-wake variations that resemble turbulent flow. To explore this aspect further, contours of the stress components associated with the velocity fluctuations have been analyzed. Figures 5.3.10, 5.3.11 and 5.3.12 show contours of the instantaneous normal stresses $\tilde{u}\tilde{u}$, and $\tilde{v}\tilde{v}$ as well as the shear stress $\tilde{u}\tilde{v}$ for a Reynolds number of 100. As stated earlier, these structures are purely laminar, there being no turbulence present in the flow. The streamwise as well as the transverse normal stresses are purely positive everywhere. They attain a maximum at the centre of each set of closed contours. The peaks in $\tilde{u}\tilde{u}$ above and below the centreline (Figure 5.3.10) indicate rotation of the fluid particles with respect to the mean flow. The simultaneous appearance of contours of $\tilde{u}\tilde{u}$ above and below the wake centreline is a confirmation of this quantity becoming zero on the centreline. In contrast, the transverse stress $\tilde{v}\tilde{v}$ attains a maximum on the centreline. The consecutive sets of $\tilde{v}\tilde{v}$ (Figure 5.3.11) form closed contours spanning both halves of the wake. Clearly positive and negative peaks in the time trace of \tilde{v} occur only along the centreline. Figures 5.3.10 and 5.3.11 show symmetry of the normal stresses about the centreline of the wake. This is generally in agreement with experiments of Cantwell and Coles (1983) for a circular cylinder at a Reynolds number of 140000. However, the water tunnel experiments of Lyn *et al.* (1995) with LDV for a square cylinder ($Re=21400$) show asymmetry in the streamwise normal component of the stresses to an extent of 50%. A possible reason for the discrepancy could be a high inlet turbulence level ($\sim 2\%$) in these experiments.

A detailed comparisons of contours of the instantaneous shear stress $\tilde{u}\tilde{v}$ between the present computation and the experiments in the turbulent flow is presented next. The experimental contours have been obtained by phase-averaging the instantaneous signals recorded at different points in the wake. The contour plots of experimental and numerical data are shown in Figures 5.3.12(a-c). The numbers mentioned at the bottom of the figure are purely dimensionless. In the computational results (Figure 5.3.12(a)), positive and negative contours are respectively marked by solid and dashed lines. Essentially, two contour shapes are to be demarcated in Figures 5.3.12. One is an elongated shape spanning the entire width of the wake and the other is a closed contour on one half of the wake alone. The slope of the elongated contour alternates in sign but is generally has the same magnitude in the flow direction. Many of these features are seen to carry over to the experimental results, though the magnitudes of the dimensionless shear stress increase with Reynolds number. The instantaneous shearing stresses ($\tilde{u}\tilde{v}$) determined numerically (Figure 5.3.12(a)) are antisymmetric about the wake centreline. These can be explained

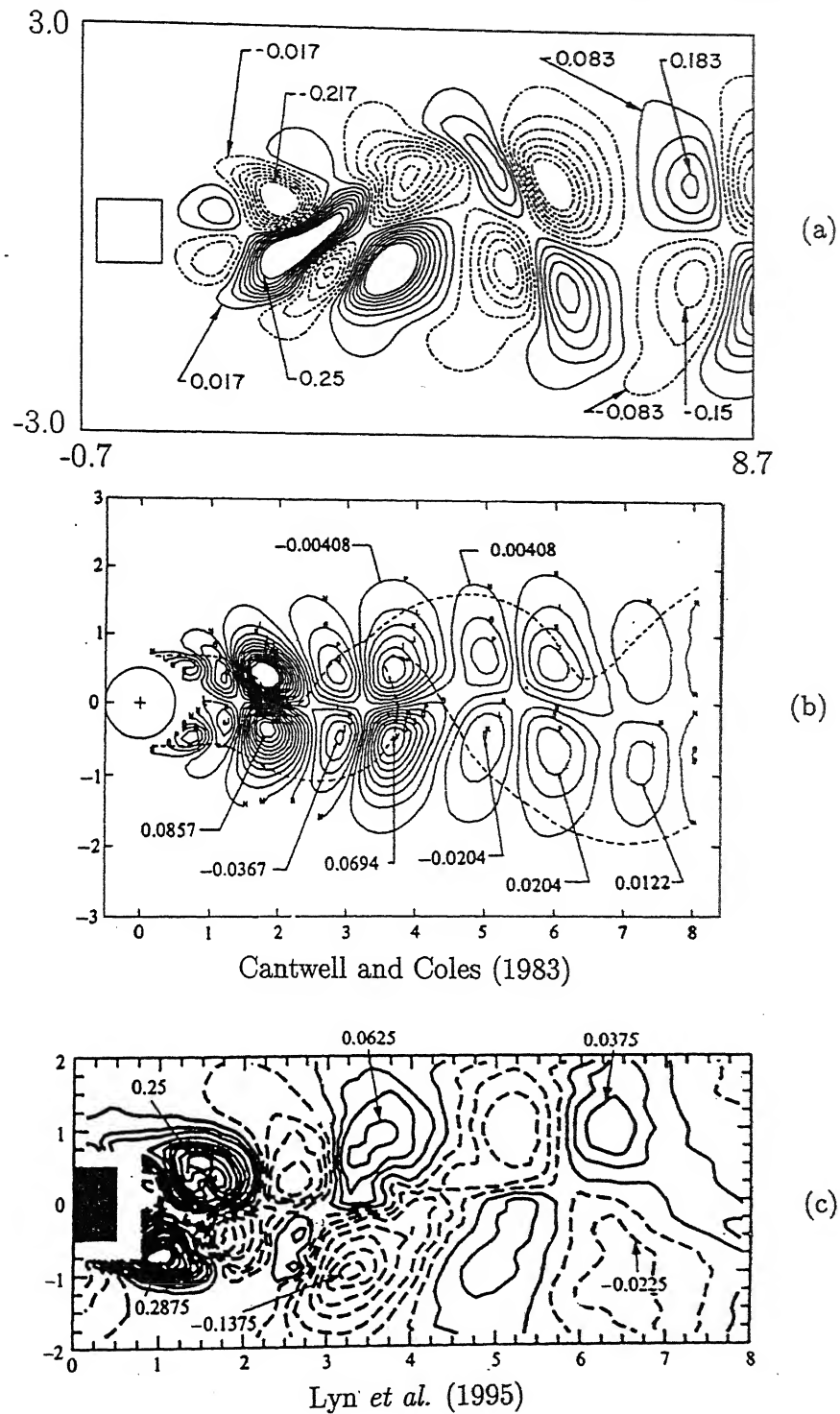


Figure 5.3.12: Contours for instantaneous shear stress: (a) present computation, (b) Cantwell and Coles (1983) (c) Lyn *et al.* (1995). The stronger instantaneous shear stress in the present calculation is due to the following: (i) the inflow is parabolic whereas the data of Lyn *et al.* (1995) is for uniform inflow (ii) the phase-averaged far-wake flow field at higher Reynolds number becomes weak because of higher incoherence and the large number frequencies present in the far-wake.

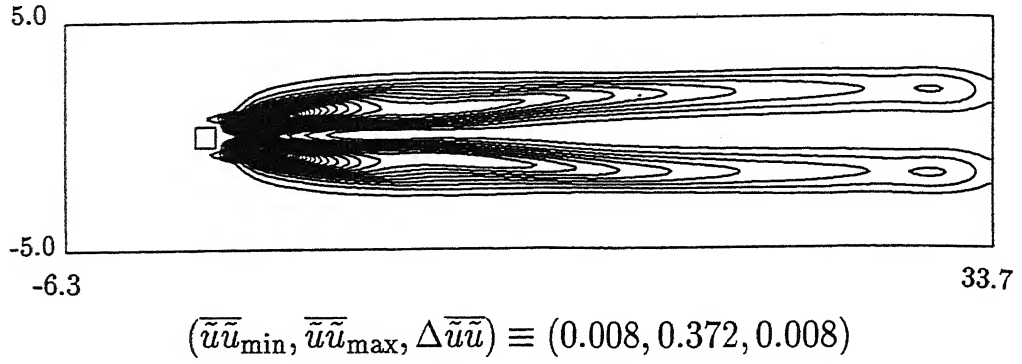


Figure 5.3.13: Contours for time-averaged streamwise normal stress. The symmetry about the centreline with double peaks on either side of the cylinder shows the two array of vortices traveling parallel to the wake centreline.

as being due to the independent influences of a strong and a weak x -momentum fluxes towards and away from the wake centreline respectively.

Further appreciation of Figures 5.3.9-5.3.12(a) can be gained from the fact that the numerical results have been plotted for a particular time instant. Hence they are in complete correspondence with one another. Figures 5.3.12(b) from the experiment of Cantwell and Coles (1983) and Figures 5.3.12(c) from the experiments of Lyn *et al.* (1995) may be compared with Figure 5.3.12(a). The experiments were conducted at a much higher Reynolds number of 10^5 where the wake was definitely turbulent. As stated earlier, the experimental results in Figures 5.3.12(b) and 5.3.12(c) show phase-averaged contours and consequently that the random components do not appear in these figures. It is for this reason that the laminar flow computations of the present study can be directly compared with the experimental data of turbulent flow. An important conclusion to emerge here is that the flow structures in the turbulent flow reveal a striking similarity with those of the fluctuations in the laminar flow.

An overlapping comparison of Figures 5.3.9, 5.3.10 and 5.3.11 reveals that vorticity peaks coincide with regions where $\tilde{u}\tilde{u}$ and $\tilde{v}\tilde{v}$ are small. In other words, the flow properties remain correlated at all instants of time and further, from one cycle to the next. In view

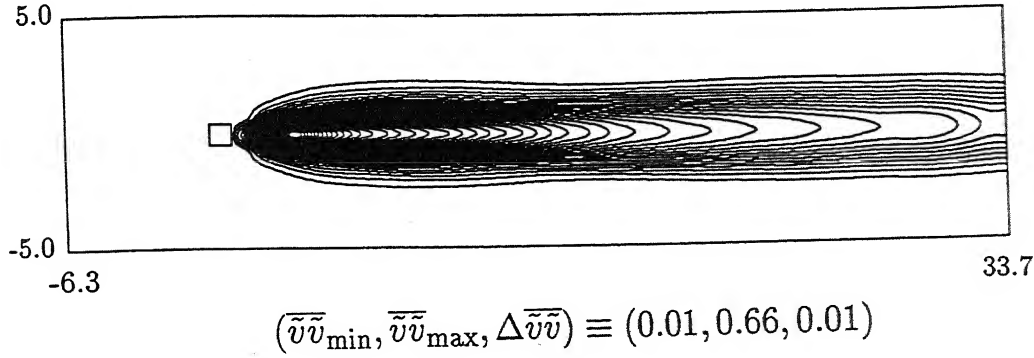


Figure 5.3.14: Contours for time-averaged transverse normal stress. The single peak along the centreline of the wake is the consequence of the contribution of transverse velocity from either row vortices moving parallel to the wake centreline.

of the periodicity of the fluid motion, the time-averaged quantities of all the three stresses show significant contributions from the fluctuations. This point is taken up next for analysis.

5.3.4 Time-averaged flow fluctuations

Figure 5.3.13 shows contours of time-averaged streamwise normal stress $\bar{u}\bar{u}$ in the wake of the square cylinder. This quantity is zero at the centreline throughout the shedding cycle. As a result the map is symmetric about the wake centreline and exhibits a peak on each side. The contribution of the normal stresses $\bar{v}\bar{v}$ at the centreline is positive, as the instantaneous counterpart has nonzero values throughout the shedding cycle (Figure 5.3.14) and consequently shows a single peak over the entire wake width. The shear stresses are similar to the streamwise component and make zero contribution at the wake centreline (Figure 5.3.15(a)). This data can be compared with the experiments of Cantwell and Coles (1983). Figure 5.3.15(b) shows that the experiments exhibit trends similar to the laminar computation. Results for the shear stresses have not been reported by Lyn *et al.* (1995) and hence have not been taken up for comparison. In the present study, all quantities, namely fluctuations $\tilde{u}\tilde{u}$, $\tilde{v}\tilde{v}$ as well as the time-averaged parts $(\bar{u}\bar{u}, \bar{v}\bar{v}, \bar{u}\bar{v})$ are

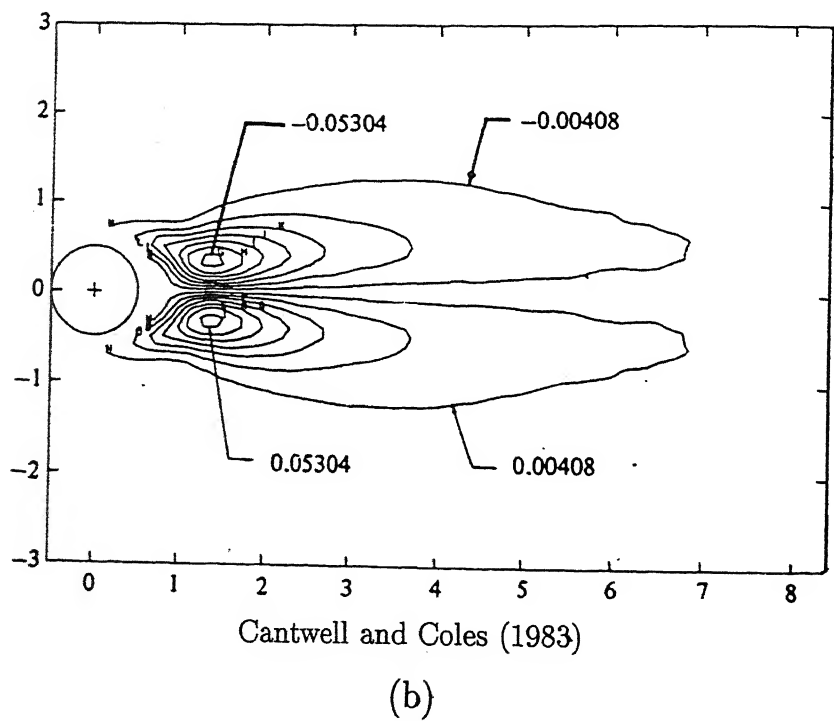
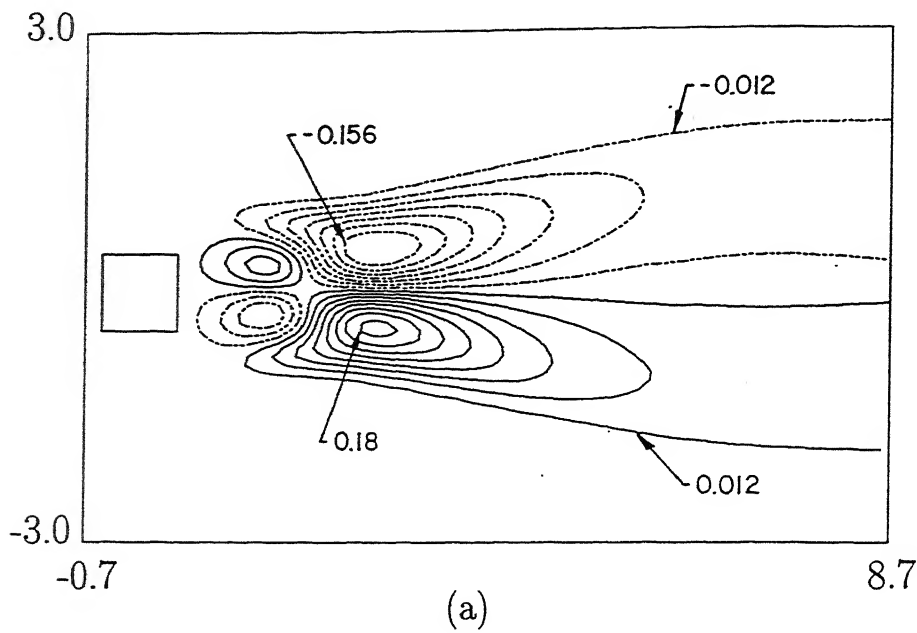


Figure 5.3.15: Contours for time-averaged shear stress: (a) present computation and (b) Cantwell and Coles (1983).

found to be symmetric about the centreline. This is supported by the circular cylinder experiments but not those with the square cylinder. On the whole however, the conclusion to emerge from the present study is that laminar periodic flow behaves qualitatively the same way as fully turbulent phase-averaged flow.

Zhou and Antonia (1993) have reported the magnitude of circulation and its decay in the wake of a circular cylinder at a Reynolds number of 5600. Circulation being the integral of vorticity over a closed contour, vorticity and circulation are interrelated. It may however so happen that with the decrease in peak vorticity there will be no change in the circulation. The reason could be that there is an increase in vortex area (example, wakes where fluid entrainment causes the vortex to grow in size) while there is the decrease in peak vorticity. On the contrary, the decrease in circulation means the decrease in peak vorticity. Subject to these conditions, circulation reported can be immediately compared with data in Figure 5.3.3. A direct comparison between the two sets of data shows that the dimensionless vorticity in laminar flow (present) is higher compared to turbulent flow in Zhou and Antonia (1993). A possible explanation for this result is that flow at low Reynolds number is two-dimensional in nature and does not encounter the three-dimensional vortex-stretching mechanism. The latter is present in all experiments, and can be dominant at high Reynolds numbers. Other relevant factors are: (i) Vortex cores of opposite sign overlap and lead to cancellation of vorticity. This is more probable in turbulent flow owing to the random fluctuations. (ii) Vortex interactions such as tearing and pairing are primarily responsible for a faster vortex decay in turbulent flow. On the other hand, vorticity diffusion is the only mechanism available in laminar flow to increase the vortex-area, reduce the peak-vorticity but keep the circulation relatively constant.

5.3.5 Analysis of the kinetic-energy equation of velocity fluctuations

In light of certain similarities between time-periodic laminar flow and turbulent flow in the wake of a square cylinder, it is pertinent to examine the kinetic energy equation of the velocity fluctuations for the present problem. The time-averaged kinetic energy equation for the fluctuating, self-sustained oscillatory component of the velocity is given

by (Majumdar and Amon, 1997)

$$\underbrace{\frac{D}{Dt} \left(\frac{q^2}{2} \right)}_{\text{I}} = - \underbrace{\frac{\partial}{\partial x_j} \left\{ \tilde{u}_j \left(\bar{p} + \frac{\tilde{u}_i \tilde{u}_i}{2} \right) \right\}}_{\text{II}} - \underbrace{\tilde{u}_i \tilde{u}_j \frac{\partial \bar{u}_i}{\partial x_j}}_{\text{III}} \quad (5.3.1)$$

$$+ \underbrace{\frac{1}{\text{Re}} \frac{\partial}{\partial x_j} \left\{ \tilde{u}_i \left(\frac{\partial \tilde{u}_i}{\partial x_j} + \frac{\partial \tilde{u}_j}{\partial x_i} \right) \right\}}_{\text{IV}} - \underbrace{\frac{1}{\text{Re}} \frac{\partial \tilde{u}_i}{\partial x_j} \left(\frac{\partial \tilde{u}_i}{\partial x_j} + \frac{\partial \tilde{u}_j}{\partial x_i} \right)}_{\text{V}}$$

In the above equation, $q^2/2$ ($=\tilde{u}_i \tilde{u}_i/2$) is the fluctuating kinetic energy, $-\tilde{u}_i \tilde{u}_j$ is the shear stress associated with oscillatory motion, \bar{u}_i is the time-averaged velocity of the base flow and Re is the Reynolds number. Term I signifies the rate of change of kinetic energy associated with the fluctuating components of velocity of a fluid particle as it moves from one location to the next. Term II relates to the work due to the total pressure (static+dynamic) on the fluctuations. Term III represents the production mechanism of the fluctuating velocities mainly from the shear in the base flow. Production due to normal and shear stresses are also accounted for in Term III. Term IV represents viscous diffusion, a quantity generally not of importance at high Reynolds numbers. This term, however, is important in certain regions of the wake at low Reynolds numbers. Term V accounts for the viscous dissipation of the kinetic energy to the internal energy of the fluid.

It is well known that as the wake evolves with distance, it approaches equilibrium in the sense that the production and dissipation terms (III and V) become close to each other and other terms become negligibly small. This is the condition of a fully developed turbulent flow. In the near-wake, both diffusion and dissipation are small (except in narrow regions such as shear layers) and energy transfer mechanism involves advection (I), the work done by pressure fluctuations (II) and production (III). The near-wake features are common to both laminar and turbulent wakes.

Term II is not properly understood and permits several interpretations. For example, it can be thought of as work done by pressure fluctuations, transport of total pressure by velocity fluctuations or simply as diffusion of kinetic energy. Application of divergence theorem on this term will yield the following situation. The volume integral will be expressible in terms of a surface integral. The integral will be zero if the stresses do not perform any work on the surface. This explains why Term II can be associated with the

work done by pressure fluctuations. For any general flow situation scaling may be used to establish the relative importance of the different terms in Equation 5.3.1. For example, the pressure work can be estimated as

$$\frac{\partial}{\partial x_j}(\tilde{u}_j \tilde{p}) \sim \frac{(\sqrt{k})^3}{l}$$

where, \sqrt{k} is a measure of fluctuations. The pressure fluctuations are of the order of $(\sqrt{k})^2$ and l is the local length scale of the flow, which determines the gradients of averaged quantities, should be of the order of the large eddy size. Similarly the mean transport of the fluctuating kinetic energy by oscillatory motion may be expressed as

$$-\frac{\partial}{\partial x_j} \left(\frac{1}{2} \tilde{u}_i \tilde{u}_i \tilde{u}_j \right) \sim \frac{(\sqrt{k})^3}{l}$$

The above two terms have the same order of magnitude and together can be called the work due to the total pressure. In this study, the numerical results have been analyzed to appreciate the influence of this term in the kinetic energy budget for the oscillatory velocity components in the near-wake. As mentioned earlier, the oscillations are of a low frequency; high wave-number, small-scale eddies have not been considered in the analysis.

Individual terms in Equation 5.3.1 have been determined in the present work as a part of the numerical simulation. The contour plot of the production of kinetic energy of the fluctuating components (Term III) is shown in Figure 5.3.16. The contour lines show two different zones. The wake region beyond a downstream distance of $x=3$ from the obstacle shows uniformly positive values. This indicates that energy from the mean flow is being passed on to the fluctuating components by the mechanism of shear. The zone very near the trailing edge of the cylinder exhibits negative values signifying a transfer of kinetic energy from the fluctuating components to the mean flow and is consistent with the initially high decay rates of $\overline{\tilde{u}\tilde{u}}$, $\overline{\tilde{v}\tilde{v}}$ and $\overline{\tilde{u}\tilde{v}}$.

The contours of the diffusion contribution (Term IV) of the fluctuating components are shown in Figure 5.3.17. The contours of the diffusion term depict a complex structure but show overall symmetry about the centreline. Figure 5.3.17 shows that diffusion is significant only in the transverse direction since the wake size is small. More specifically, the shear layers, on each side of the centreline are regions having a significant presence of diffusion.

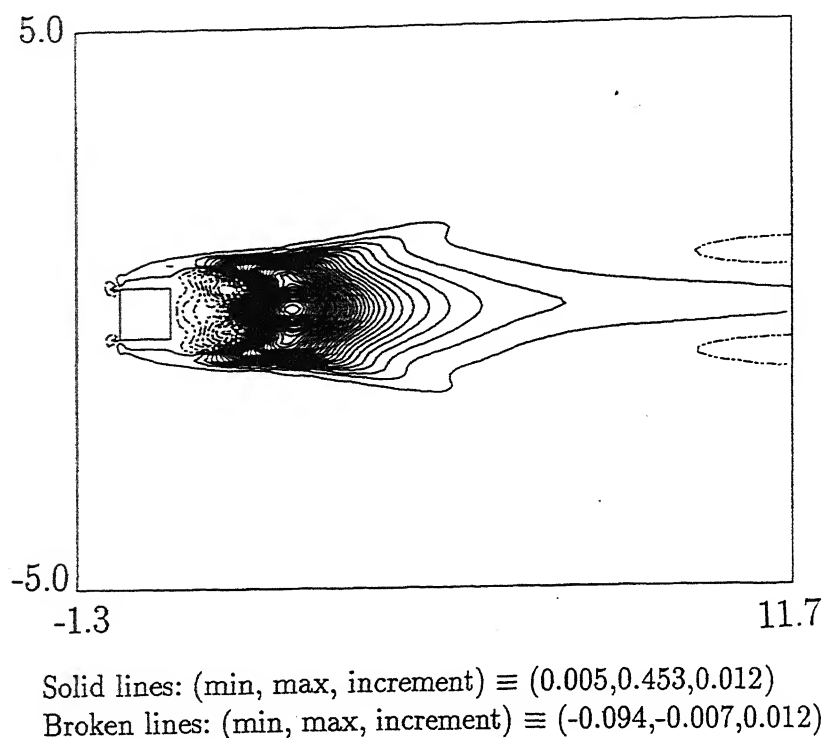


Figure 5.3.16: Contours of the production of kinetic energy of fluctuating velocities.

Figure 5.3.18 depicts the contours of the rate of dissipation of the fluctuating kinetic energy (Term V). Dissipation in the near-wake is a small quantity when compared to production and advection. It becomes even smaller (along with diffusion) at higher Reynolds numbers. The presence of a strong gradient of the fluctuating velocity in the shear layer region is revealed through the contours of diffusion in Figure 5.3.17. Dissipation leads to loss of kinetic energy and is dominant at sites of large diffusion. This particular fact which is evident on comparing terms IV and V is also revealed through the Figure 5.3.18. The core of the wake is a region of high mixing and shows a low rate of dissipation. Although the magnitude of dissipation is small in comparison to other terms, it extends to a larger downstream distance as compared to other quantities in the kinetic energy equation.

The time-averaged profiles of individual terms of the kinetic energy equation are respectively shown in Figures 5.3.19(a) and 5.3.19(b) at two different streamwise locations, namely $x=1$ (base region) and $x=3$ (near-wake) downstream of the cylinder. From

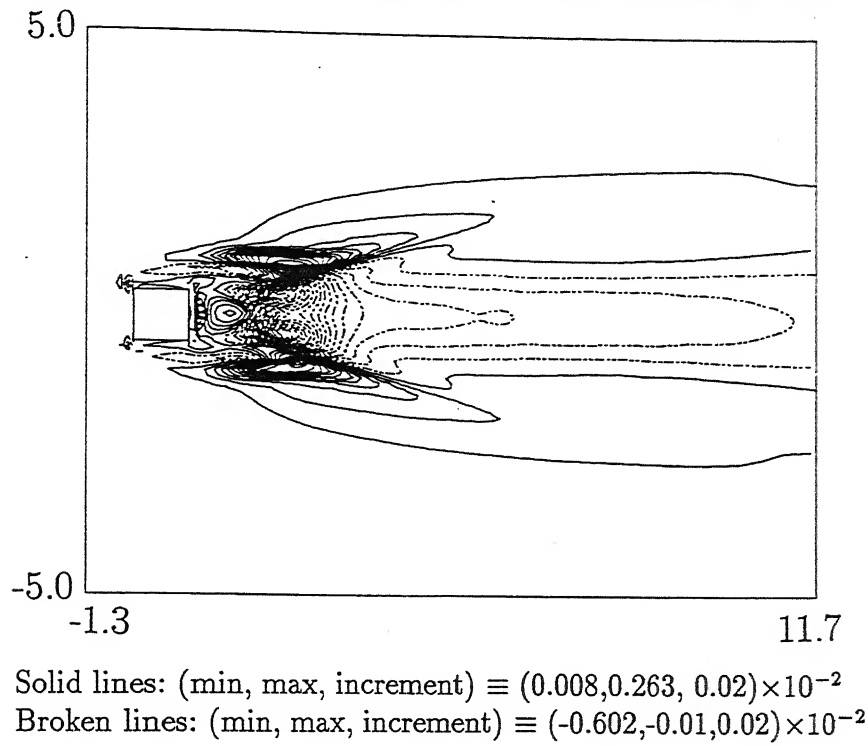


Figure 5.3.17: Contours of the diffusion of kinetic energy of fluctuating velocities.

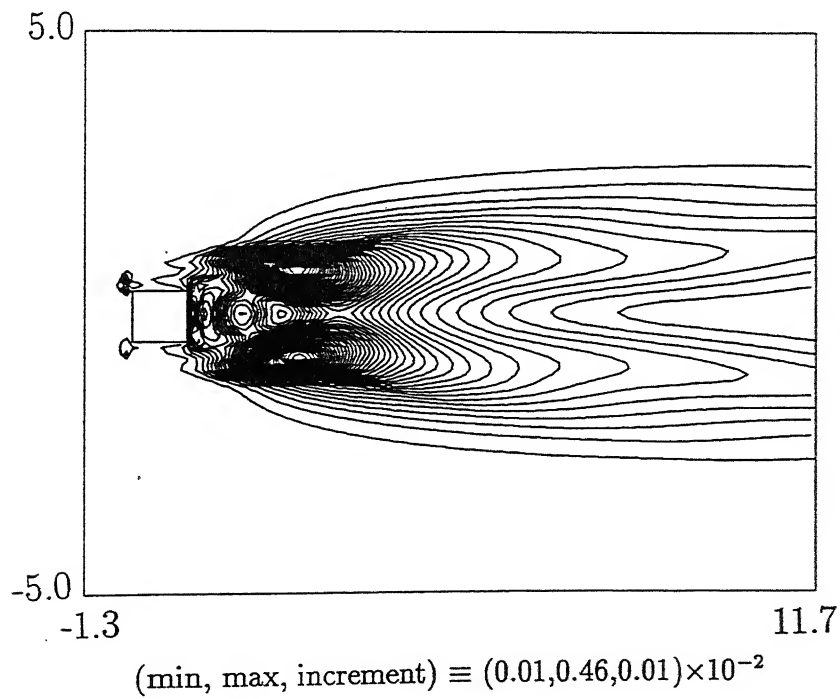
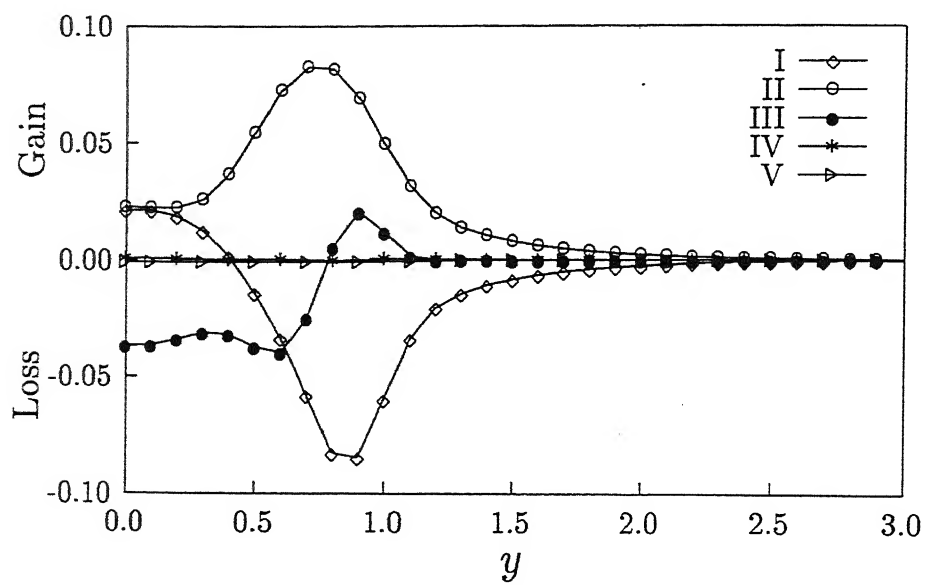
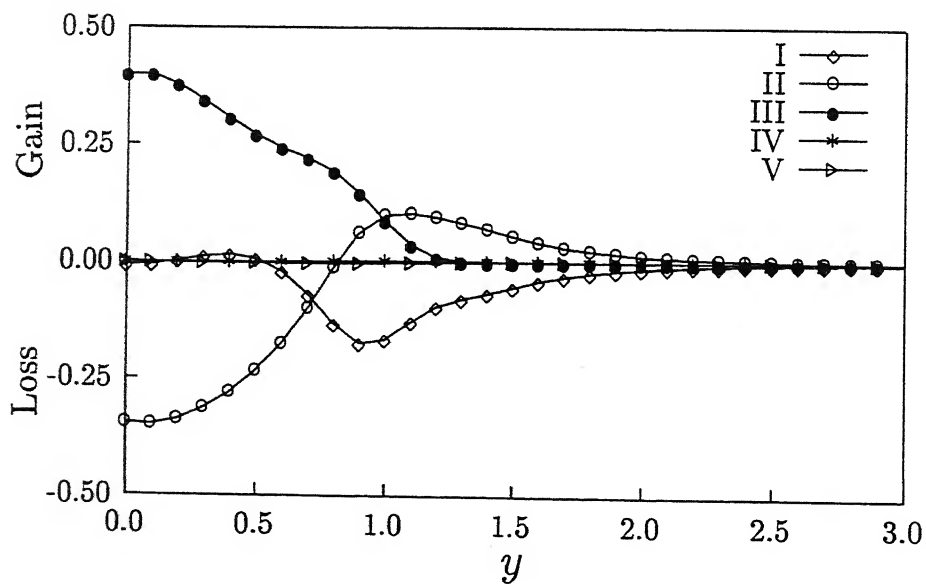


Figure 5.3.18: Contours of the dissipation of kinetic energy of fluctuating velocities.



(a)



(b)

Figure 5.3.19: Transverse variation of different terms of kinetic energy equation at (a) $x=1.0$ and (b) 3.0 .

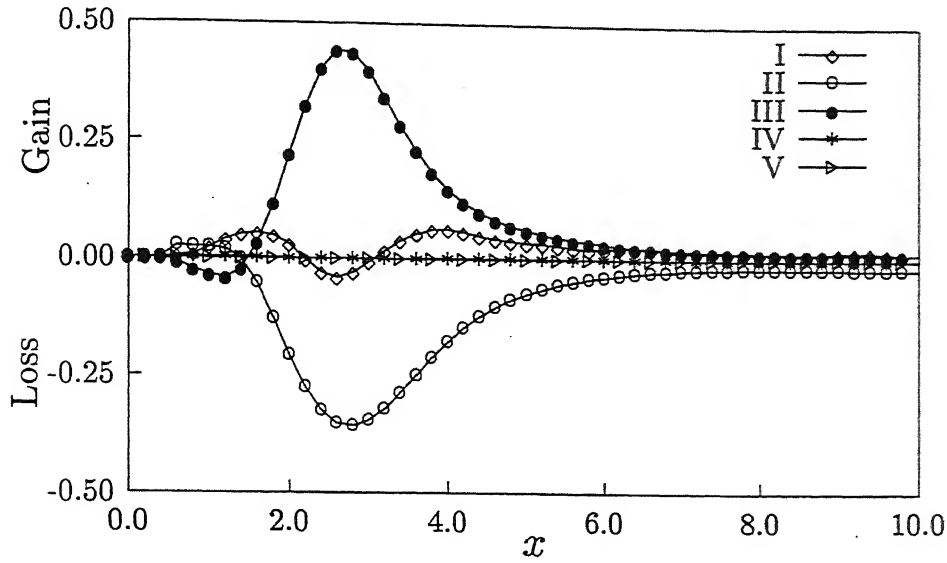


Figure 5.3.20: Streamwise variation of different terms of kinetic energy equation at $y=0$.

Figure 5.3.19(a) it is observed that the production (Term III) is quite high and negative at the centre ($y=0$). At point $y=0.79$, the production is negligible and the gain by convection is balanced by the work due to total pressure (Term II). Figure 5.3.19(b) reveals that the production reaches maximum positive value near the centre ($y=0$) and is practically balanced by the work due to total pressure. At a point $y=1.85$, the production is negligible and the gain by convection (Term I) is balanced by the work due to total pressure (Term II).

The kinetic energy budget along the streamwise direction at the centreline is presented in Figure 5.3.20. Convection due to mean motion is significant only in the transverse direction (as in Figure 5.3.19) and there is no major contribution to the streamwise variation of total energy. In contrast, the work of pressure fluctuation and the advection term are equal but opposite in sign over the length considered. Hence they represent the primary mechanisms of energy transport in the streamwise direction in the wake. From the above discussions, it is evident that the work done by the total pressure fluctuation, convection due to mean motion and the production terms are primarily responsible in the near-wake for the exchange of energy between the mean flow and the fluctuations.

5.3.6 Closure

A direct numerical simulation of two-dimensional Navier-Stokes equations for flow past a square cylinder placed in a channel at a Reynolds number of 100 has been performed using a high order finite difference scheme. The instantaneous flow field has been recorded after the passage of sufficient amount of time. The results obtained in the study show the following.

1. The wake of the square cylinder is driven by a clear vortex shedding frequency. The instantaneous flow field at a low Reynolds number is spatially coherent in nature.
2. The x -direction celerity is found to vary from 0.69 in the base region to a constant value of 1.30 in the far-wake. In the y -direction, celerity fluctuates in the base region due to interaction among vortices and becomes zero in the far-wake.
3. The phenomenon of sharp attenuation of peak vorticity is observed at the base and the near-wake region.
4. An important result to emerge from the study is that the unsteady periodic oscillatory flow in the wake has great similarity with the phase-averaged high Reynolds number turbulent flow. The similarities are in terms of vortex decay owing to transverse diffusion of the stress components $\overline{u_j u_j}$, instantaneous isovorticity contours, instantaneous stress contours and time-averaged contours of the stress components. Differences are however seen in terms of the decay rate of circulation downstream of the cylinder.
5. The kinetic energy budget of the oscillatory components reveals that the convection due to mean motion, the production term and the pressure fluctuations play a vital role for the energy exchange between the mean and the fluctuating motion. The dissipation and diffusion terms are uniformly negligible, except in the region of the shear layers.

5.4 Comparison of Two- and Three-dimensional Models in Low Reynolds Number Transitional Flow

The transition of the two-dimensional to three-dimensional shedding in the wake of the square cylinder (Section 5.2) occurs after a Reynolds number of 150. Therefore, above this Reynolds number three-dimensionality plays a significant role in determining the structure of the wake. Studies show that a two-dimensional simulation cannot resolve the effect of the three-dimensionality and predicts higher velocity fluctuations. Thus, the drag and lift coefficients are also over-predicted. Consequent to the early transition to three-dimensionality, results obtained from a two-dimensional simulation past a bluff body above a Reynolds number of 150 can be expected to be inaccurate.

The possible reasons for higher forces in a two-dimensional calculation has been demonstrated by different researchers. Chua *et al.* (1990) reported that the discrepancy could be due to the end effects from the termination of the body at the walls of the wind tunnel or at the end plates. It has now been established that the end effects can lead to different shedding modes, namely oblique and parallel. These in turn may lead to the discrepancy between the two- and three-dimensional simulations. In particular, the two-dimensional simulation cannot have a spanwise velocity component that is responsible for the Modes-A and B shedding as discussed in Section 5.2. It has been argued that the recirculation bubble remains stable due to the equilibrium between pressure and the shear stress acting on the bubble. The length of recirculation bubble in turn determines the forces on the cylinder. Three-dimensional simulation shows lower shear stresses because it can resolve the spanwise component of velocity and diminishes the fluctuations in other directions through its mass and momentum conservations across any given control volume. Williamson and Roshko (1990) showed that reduction in the measured in-plane shear stress with increasing three-dimensionality leads to a reduction in base suction and thus a reduction in drag.

The bluff body wake is characterized by the roll up of the separated shear layer. In a two-dimensional simulation, the vortices roll up very close to the bluff object. This closer rolling leads to the smaller vortex formation length¹. Chua *et al.* (1990) have shown that

¹The vortex formation length is the distance beyond the cylinder along the wake centreline over which the streamwise component of velocity fluctuations attains a maximum value.

this smaller vortex formation causes higher suction and thus higher drag. Tamura *et al.* (1990) have concluded that the higher suction and consequently the higher aerodynamic forces are due the formation of a larger number of secondary vortices around the bluff object. Mittal and Balachandar (1995a) demonstrated the higher aerodynamic forces as a direct consequence of the higher shear stresses in a two-dimensional simulation.

The present study is aimed at the comparison of flow structures in the wake of a square cylinder by solving numerically the two- and three-dimensional Navier-Stokes equations. The possible cause for the differences between the two paradigms has been investigated with the help of the mean flow and pressure equations and the vortex stretching mechanism. The comparison has been presented in terms of the normal and shear stresses, mean flow, instantaneous flow and signal traces. The Reynolds number considered in the analysis is 250. The specific reason for choosing this Reynolds number is the fact that it is within the transitional regime where large differences in the flow structures, the rms values of the velocity fluctuations and the aerodynamic forces are observed.

The geometry (Figure 1.3) for the present study is the same as that considered in Section 5.1 for the two-dimensional model. However, the three-dimensional model has a spanwise length of 6 cylinder widths while the other dimensions are similar to the two-dimensional model. Both the two- and three-dimensional computations have been carried out over a grid having 218×104 cells. For the latter, the third dimension overlaps the span of the cylinder and has been divided into 22 uniformly spaced planes. The other two directions have nonuniform grids generated by a proportional increase in the grid size. For grid independence test, the two different grids used are 218×104 and 436×208 in two-dimension and $178 \times 80 \times 22$ and $218 \times 104 \times 22$ in three-dimensions. Grid independence tests described in Sections 5.1 and 5.2 show that both the computations are grid independent with a maximum discrepancy in their respective time-averaged drag coefficients of less than 2%. The boundary conditions used in the present section has been discussed in Section 5.1 for the two-dimensional model and Section 5.2 for the three-dimensional model.

5.4.1 Time traces of selected flow properties

Figure 5.4.1(a) shows the comparison of the time evolutions of the lift coefficient obtained by the two- and three-dimensional simulation. It is evident that amplitude of the force

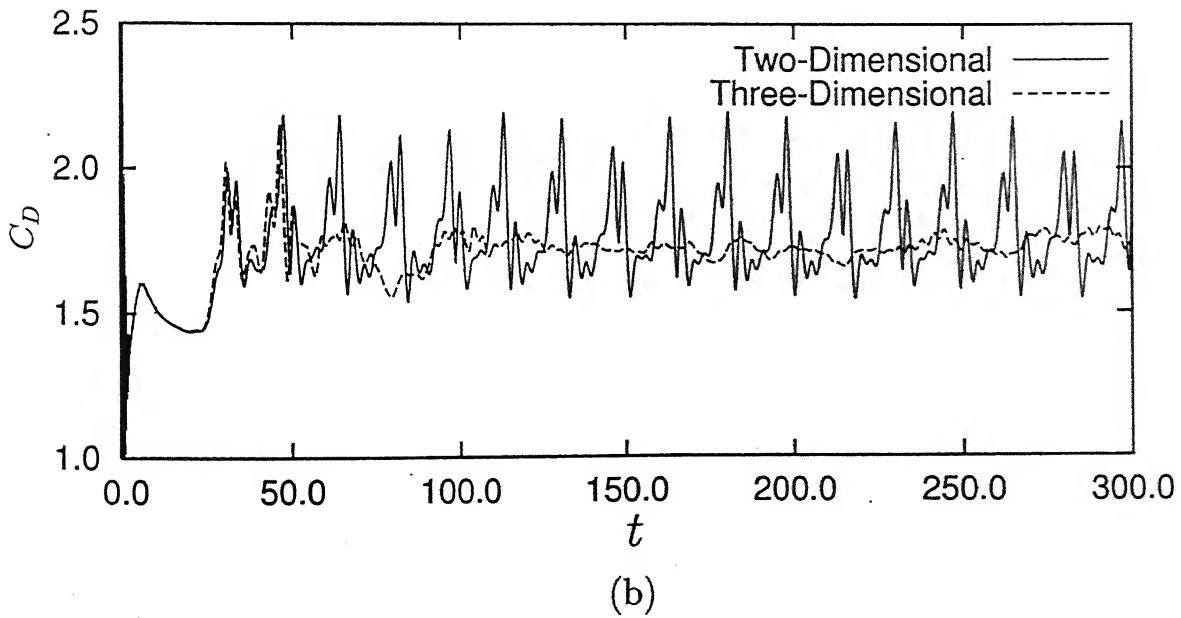
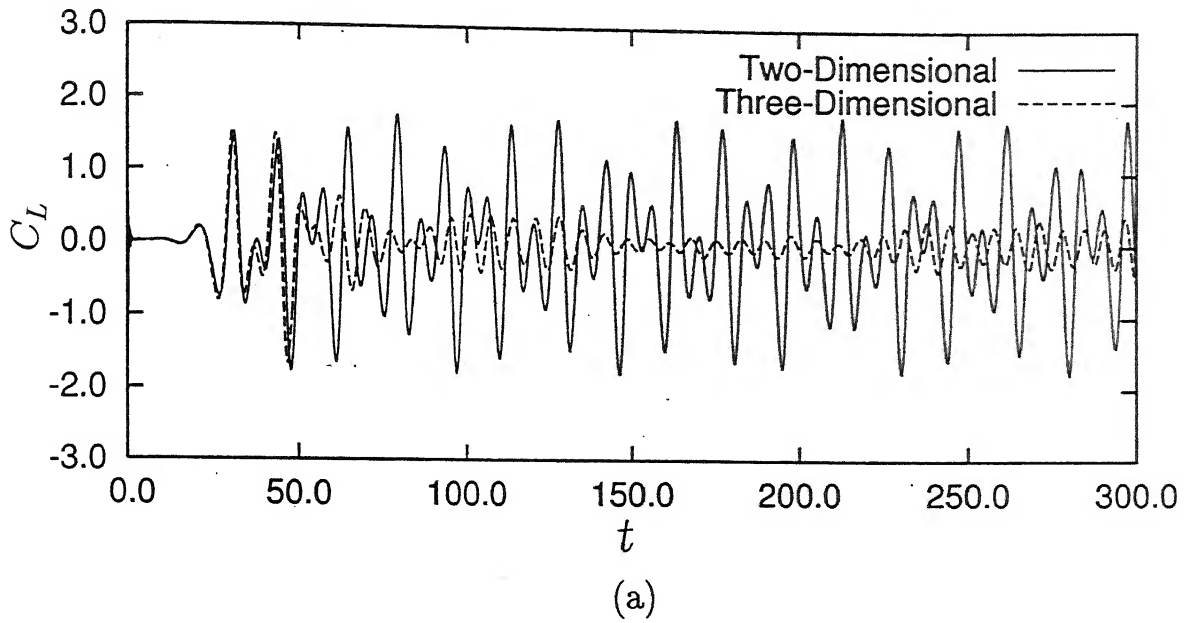


Figure 5.4.1: Comparison of time evolution of (a) lift and (b) drag coefficients obtained by two- and three-dimensional simulation. Though the time-averaged values are nearly equal for the two, the rms values are higher in two-dimensions.

Table 5.4.1: Comparison of Lift & Drag Coefficient and Strouhal Number

	S	$\overline{C_D}$	C'_D	C'_L
2D	0.142	1.77	0.145	0.830
3D	0.150	1.72	0.044	0.183

fluctuations is greater in the two-dimensional case compared to the three-dimensional. The possible reason for the higher amplitude of lift coefficient is discussed later. Figure 5.4.1(b) depicts the time signal of drag coefficient for the two cases. Though there is little difference in their time-averaged values, two-dimensional computation gives a higher amplitude. It is of great interest to note that both the lift and drag coefficients initially (after the computation has been started with identical quiescent conditions) show similar temporal variation upto a nondimensional time of 50. This is due to the fact that flow is initially two-dimensional even in a three-dimensional geometry. Once three-dimensionality sets in, the behaviour of the flow becomes different from that of the two-dimensional counterpart.

The evolution of three-dimensional flow from a two-dimensional state is shown in Figure 5.4.2 through the time-trace of spanwise component of velocity at two different locations ($x=2.4$ and 13.7). Below a nondimensional time of 50, the flow is two-dimensional in nature and the spanwise component of velocity is zero. Figures 5.4.1 and 5.4.2 confirm two-dimensionality of the three-dimensional computation at an early time. Table-5.4.1 shows the comparison of different parameters computed in two- as well as three-dimensional geometries. Since the Reynolds number chosen is very close to transitional, there is only a small change in the time-averaged drag coefficient. The rms values of the lift and drag coefficients however vary significantly. The reasons for these differences can be explained as follows.

The Poisson's equation for pressure can be written after taking the derivative of each momentum equation with respect to its direction and adding them up as

$$\frac{\partial^2 p}{\partial x_k^2} = -\frac{\partial^2}{\partial x_i \partial x_j} (u_i u_j) \quad (5.4.1)$$

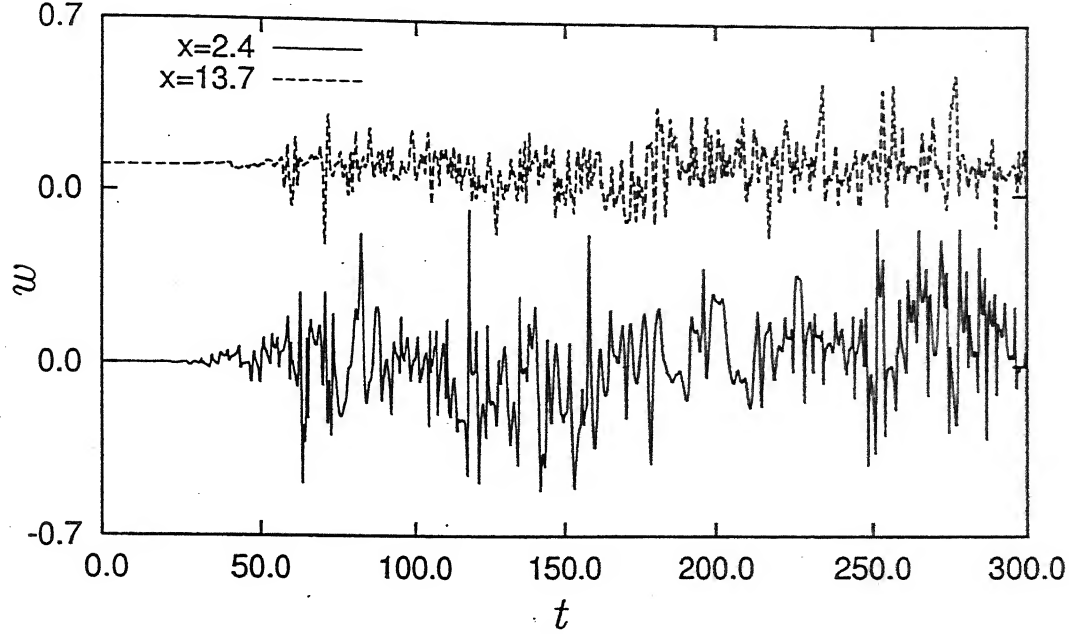


Figure 5.4.2: Evolution of spanwise velocity at locations $x=2.4$ and 13.7 . The fluctuations in the far-wake is damped down due to nonlinear interactions leading to tearing of the larger vortices.

The instantaneous pressure in the above equation can be written as the sum of the time-averaged and fluctuating parts. Time-averaging this equation gives the Poisson's equation for mean pressure. The fluctuating pressure equation for incompressible flow can be obtained by subtracting the time-averaged equation from the instantaneous equation as

$$\frac{\partial^2 p'}{\partial x_k^2} = -2 \frac{\partial \bar{u}_j}{\partial x_i} \frac{\partial u_i'}{\partial x_j} - \frac{\partial u_j'}{\partial x_i} \frac{\partial u_i'}{\partial x_j} + \frac{\partial^2}{\partial x_i \partial x_j} (\overline{u_i' u_j'}) \quad (5.4.2)$$

But on the wall or very near it the above equation simplifies to

$$\frac{\partial^2 p'}{\partial x_k^2} = \frac{\partial^2}{\partial x_i \partial x_j} (\overline{u_i' u_j'}) \quad (5.4.3)$$

On the other hand the mean flow equation can be written as

$$\frac{\partial}{\partial x_j} (\bar{u}_i \bar{u}_j) = -\frac{\partial \bar{p}}{\partial x_i} + \frac{1}{\text{Re}} \frac{\partial^2 \bar{u}_i}{\partial x_j^2} - \frac{\partial}{\partial x_j} (\overline{u_i' u_j'}) \quad (5.4.4)$$

The above equation for mean momentum can also be written in terms of normal

stresses and the vorticity components as

$$\frac{\partial}{\partial x_j}(\overline{u_i u_j}) = -\frac{\partial \overline{p}}{\partial x_i} + \frac{1}{\text{Re}} \frac{\partial^2 \overline{u_i}}{\partial x_j^2} - \frac{\partial}{\partial x_i} \left(\frac{1}{2} \overline{u'_j u'_j} \right) + \epsilon_{ijk} (\overline{u'_j \omega'_k}) \quad (5.4.5)$$

Comparing Equations 5.4.4 and 5.4.5, we get

$$-\frac{\partial}{\partial x_j}(\overline{u'_i u'_j}) = -\frac{\partial}{\partial x_i} \left(\frac{1}{2} \overline{u'_j u'_j} \right) + \epsilon_{ijk} (\overline{u'_j \omega'_k}) \quad (5.4.6)$$

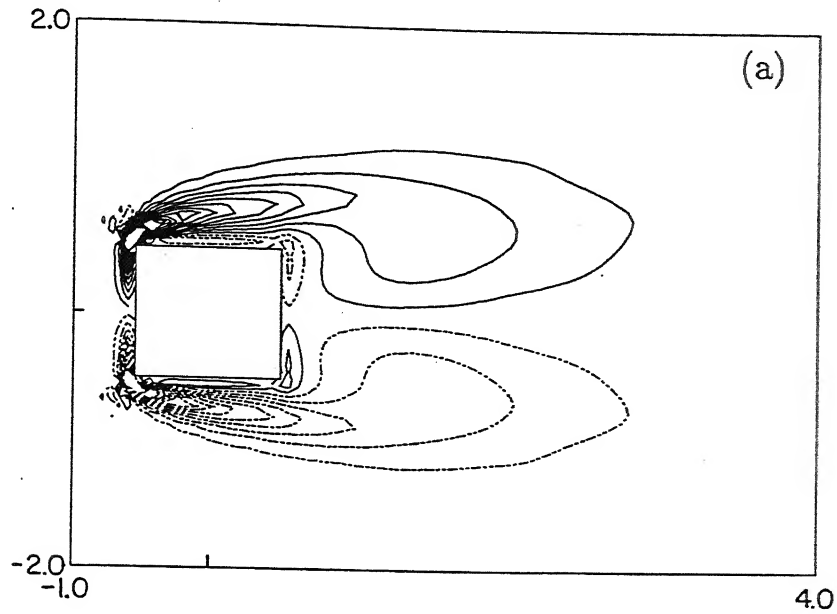
The second term on the right hand side in Equation 5.4.6 is like a Reynolds stress term and the gradient of which can be thought as representing a diffusion phenomenon. The two-dimensional model has a higher value of this term compared to the three-dimensional model. The two-dimensional model shows higher Reynolds stresses because (1) it has less diffusion due to non-availability of the third direction, and (2) all components of vorticity are active in three-dimensions. In effect, the right hand side of Equation 5.4.3 is lowered in two-dimensions. Since Equation 5.4.3 is of a Poisson type, one can directly conclude¹ that the magnitude of pressure fluctuation is higher in a two-dimensional model.

The shear stress is related to normal stresses $(\frac{1}{2} \overline{u'_j u'_j})$ and vortex stretching forces $(\epsilon_{ijk} \overline{u'_j \omega'_k})$. In the two-dimensional simulation, the spanwise component is absent and the vortex stretching force terms can be written as $\overline{v' \omega'_z}$ and $\overline{u' \omega'_z}$ for the u - and v -momentum equations respectively. But in three-dimensions, all the terms of vortex stretching force are retained. Due to the presence of all the terms in Equation 5.4.6, the difference in shear stresses is evident in two- and three-dimensions.

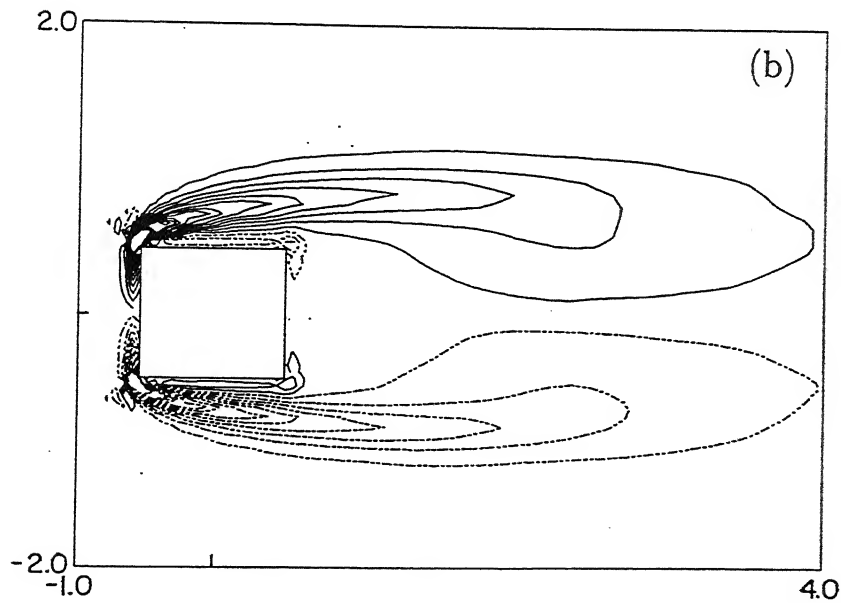
5.4.2 Evaluation of vorticity and pressure fields

The spanwise time-averaged vorticity contours for the two- and three-dimensional simulation are shown in Figures 5.4.3(a) and 5.4.3(b) respectively. Both the contours reveal the formation of separated shear-layers from the top and bottom leading edges of the square cylinder. The separated shear layer in the case of a three-dimensional simulation extends to a larger streamwise distance compared to the two-dimensional counterpart. The elongated shear layer which gives a longer mean recirculation region in the three-dimensional

¹by recourse to the maximum principle for PDEs.



Broken lines: $(\omega_{\min}, \omega_{\max}, \Delta\omega) \equiv (0.6, 15.0, 1.2)$
 Solid lines: $(\omega_{\min}, \omega_{\max}, \Delta\omega) \equiv (-13.8, -0.6, 1.2)$



Broken lines: $(\omega_{\min}, \omega_{\max}, \Delta\omega) \equiv (0.6, 15.0, 1.2)$
 Solid lines: $(\omega_{\min}, \omega_{\max}, \Delta\omega) \equiv (-13.8, -0.6, 1.2)$

Figure 5.4.3: Time-averaged vorticity contours for (a) two-dimensional and (b) three-dimensional simulation. The larger length of the shear layer in case of three-dimensional simulation shows the presence of streamwise diffusion due to velocity-vorticity interaction.

simulation contributes a smaller drag coefficient compared to two-dimensions. This elongation is due to the increased diffusion in the three-dimensional flow, as can be seen in the following mathematical argument:

The vorticity equation can be written as (Tennekes and Lumley, 1983):

$$\frac{\partial \omega_i}{\partial t} + u_j \frac{\partial \omega_i}{\partial x_j} = \omega_j \frac{\partial u_i}{\partial x_j} + \nu \frac{\partial^2 \omega_i}{\partial x_j^2} \quad (5.4.7)$$

Decomposing the instantaneous vorticity and velocity components into the time-averaged and fluctuating components and time-averaging, one can get the mean vorticity equation as

$$\bar{u}_j \frac{\partial \bar{\omega}_i}{\partial x_j} = -\frac{\partial}{\partial x_j} (\overline{u'_j \omega'_i}) + \frac{\partial}{\partial x_j} (\overline{u'_i \omega'_j}) + \bar{\omega}_j \frac{\partial \bar{u}_i}{\partial x_j} + \nu \frac{\partial^2 \bar{\omega}_i}{\partial x_j^2} \quad (5.4.8)$$

The first two terms on the right hand side behave like diffusion terms since they resemble Reynolds stresses. The second term is due to vortex stretching and is completely absent in two-dimensional flow. This indicates the higher diffusion in a three-dimensional flow leading to a lengthening of the shear layer.

Figure 5.4.4 shows the instantaneous spanwise vorticity contours in two- (Figure 5.4.4(a)) as well as three-dimensions (Figure 5.4.4(b)). There are significant differences between these two instantaneous fields in many respects. The vortices in the three-dimensional geometry are closer to being symmetric about the wake centreline throughout the domain whereas in two-dimensions, no such symmetry is seen. The coherence of the vortices in the two-dimensional simulation is evident along the length of the physical domain. However, three-dimensional simulation shows coherence only in the near-wake ($x < 10$) and far-wake reveals complex interactions such as pairing and tearing of vortices. Such complex interactions are possible due to the presence of other two secondary vortices which distort the primary vortices. The faster decay of spanwise vortices (Figure 5.4.4) in the three-dimensional simulation is due to the fact that the complex interactions tear off the primary vortices to multiple smaller vortices. These smaller vortices decay faster owing to the viscosity of the fluid. It is also seen that the wake width is larger in the three-dimensional simulation. This observation is supported by the mean velocity profiles discussed in a later paragraph.

Figure 5.4.5 illustrates the instantaneous pressure contours at a predetermined instant of time. The pressure contours corresponding to the two-dimensional case do not

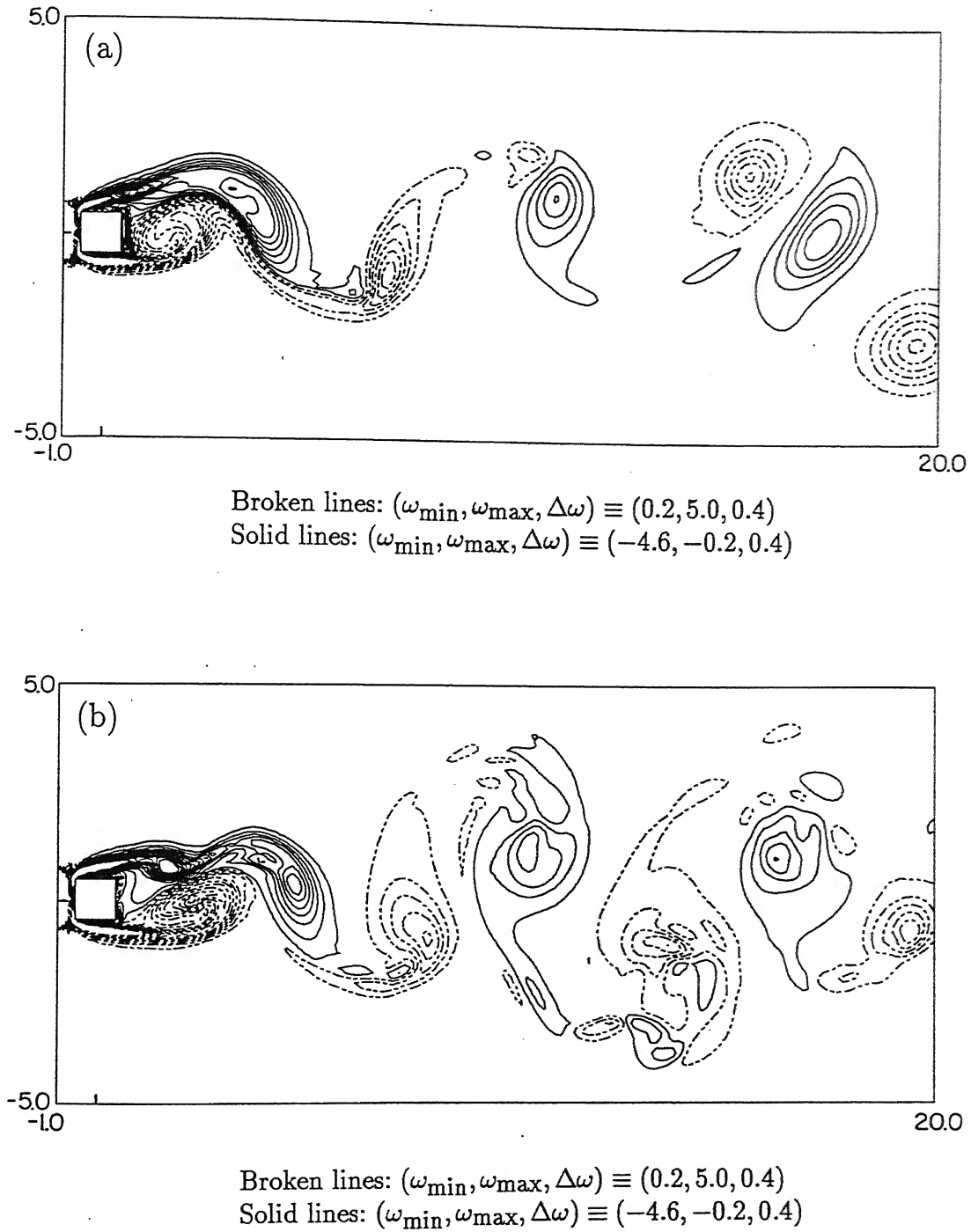
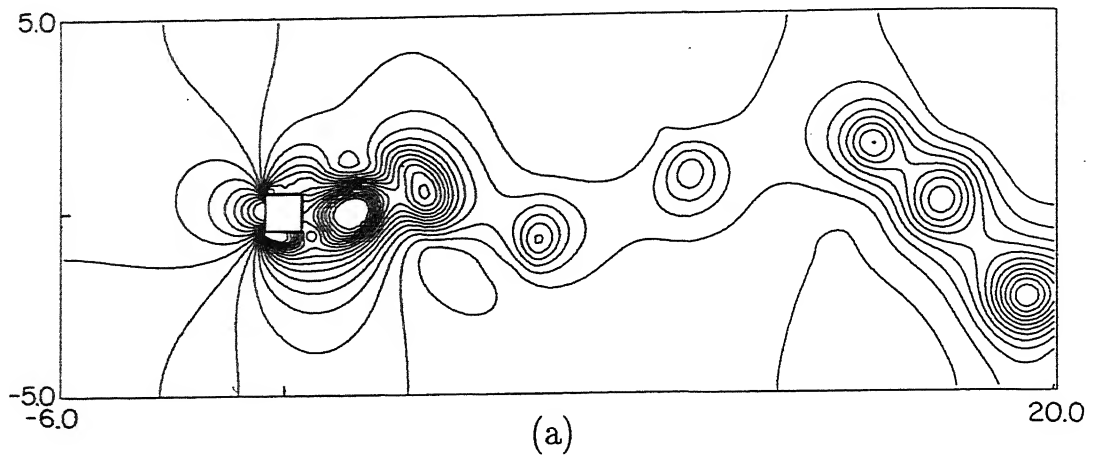
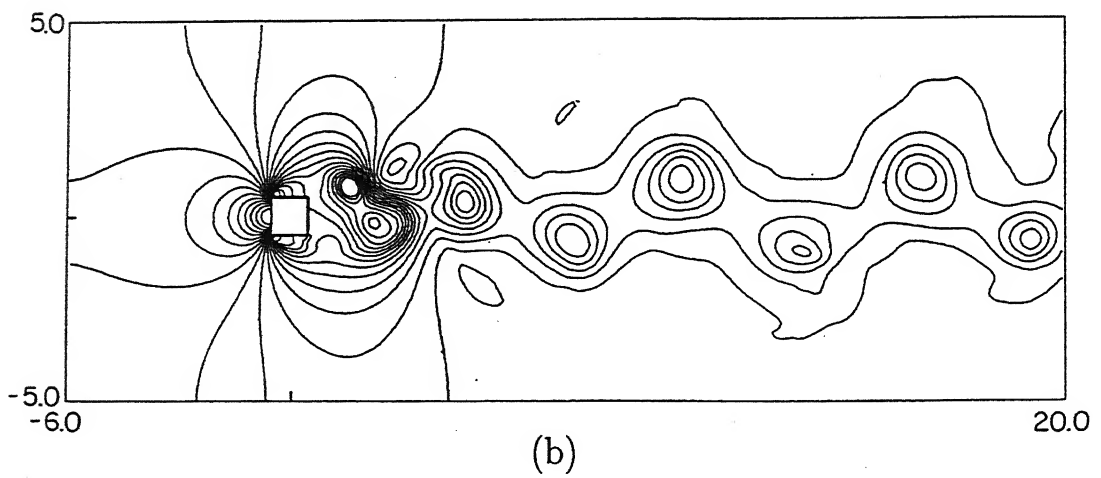


Figure 5.4.4: Instantaneous vorticity contours for (a) two-dimensional and (b) three-dimensional simulation. Two-dimensional flow shows higher coherence and asymmetry compared to three-dimensions. The higher coherence is due to the absence of three-dimensionality which leads to vortex stretching and make the flow field complex by generating secondary vortices.



$$(p_{\min}, p_{\max}, \Delta p) \equiv (0.06, 1.5, 0.06)$$



$$(p_{\min}, p_{\max}, \Delta p) \equiv (0.16, 1.5, 0.056)$$

Figure 5.4.5: Instantaneous pressure contours for (a) two-dimensional and (b) three-dimensional simulation. The coincidence of pressure minima with vorticity maxima shows the correctness of the numerical simulation.

show any regular pattern of vortex shedding and reveal that there is no uniformity in the decay of pressure along the streamwise direction. Similar to vorticity contours, these distributions also show asymmetry about the wake centreline. On the other hand, three-dimensional simulation predicts a uniform decay of pressure maxima and shows the alternate staggered array of pressure contours whose minima coincide with that of peak vorticity. The correlation between the peak vorticity and pressure minima is a confirmation of the correctness of the numerical simulation.

5.4.3 Time-averaged flow field

There are significant differences between the flow fields of the two- and three-dimensional simulation, Figure 5.4.6. The streamwise velocity profiles (Figure 5.4.6(a)) in the transverse direction at some selected locations ($x=0, 1, 2, 4$ and 6) have been compared. There is no difference at $x=0$ between the two simulations whereas at other locations, differences specially near the wake center can be seen. The reason for a good match at $x=0$ can be understood by the fact that the incoming flow is almost two-dimensional¹. The velocity profile at $x=1$ for the three-dimensional simulation is a flatter in the central region of the wake. The minimum value of the velocity at this location is higher compared to the two-dimensional counterpart. The comparison in terms of the transverse velocity profiles gives more insight into these differences. The transverse velocity profile is presented in Figure 5.4.6(b). At all the streamwise locations, differences between the two simulations can be seen. The transverse velocity at $x=0$ and 1 are in the outward direction away from the wake centreline. But the direction of this component of velocity reverses for $x=2$ onwards. The extent of entrainment of fluid into the wake ($x \geq 2$) differs between the two simulations and gives rise to a longer recovery length for the three-dimensional case. Figure 5.4.6(c) depicts the centreline recovery of the streamwise velocity. The mean recirculation length (as determined from the recovery graph) for the three-dimensional simulation is more than that for the two-dimensional case. The recirculation lengths in the two cases are 2.98 and 2.08 respectively. However, two-dimensional simulation shows a stronger back flow. The recovery rates of the streamwise velocity in both cases are nearly equal and both the simulations attain an asymptotic value of 0.84 (two-dimensional) and 0.81 (three-dimensional) in the intermediate-wake.

¹Transition to three-dimensionality occurring in the wake of the cylinder.

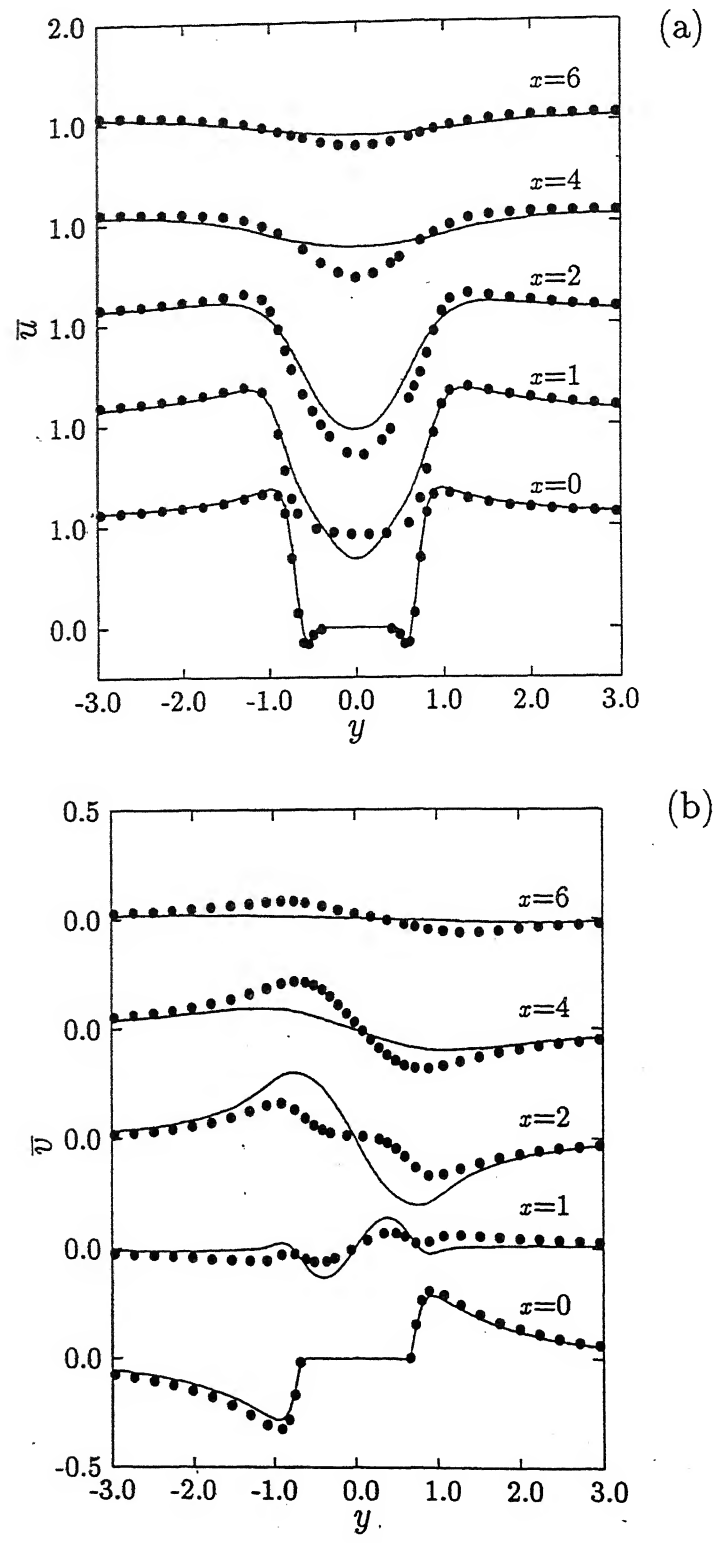


Figure 5.4.6: for caption see next page

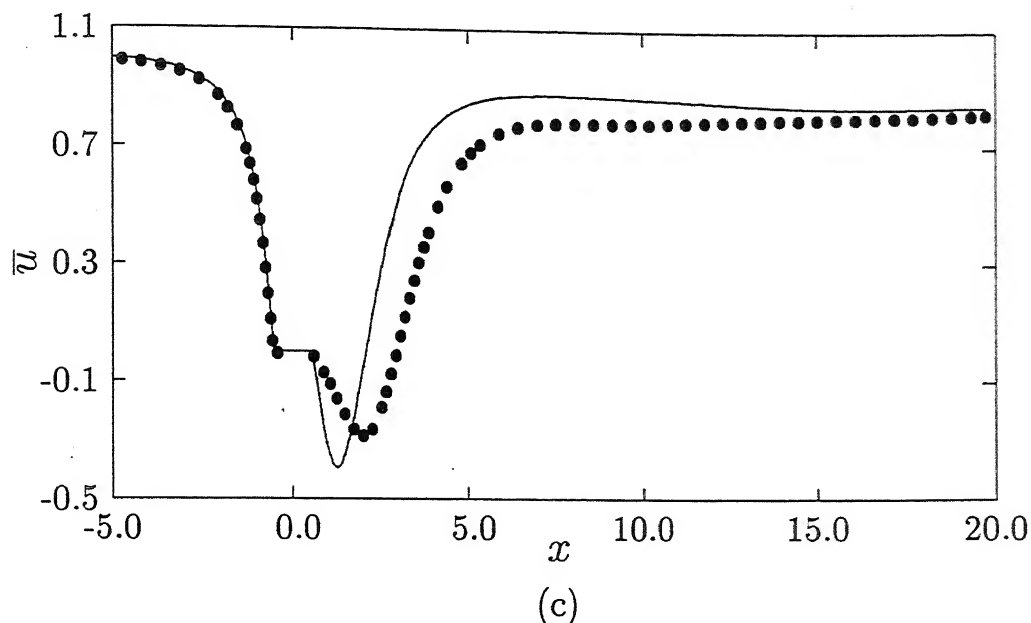


Figure 5.4.6: Comparison of time-averaged profiles: (a) streamwise velocity and (b) transverse velocity at various locations and (c) centreline recovery of streamwise velocity. (Line: Two-dimensions, Symbol: Three-dimensions)

The fluctuating field shows remarkable differences if the three-dimensional flow past the square cylinder is simulated by using the two-dimensional Navier-Stokes equations. The velocity fluctuations play a major role in determining the lift and drag forces and the mean flow distribution through an indirect influence on pressure. Specifically, the three-dimensional flow involves vortex stretching, and determines the proper distribution of the shear stresses. Though the consequences of vortex stretching are more significant in turbulent flow, they should also be considered in the case of self-sustained oscillations as in the bluff body wake. The vortex stretching phenomenon is intense in the base region ($x < 4$) where all the three components of the vortices are present. Here the vortices are produced and grow to maturity. Thus, three-dimensionality of the near-wake becomes prominent.

Figure 5.4.7 shows the distribution of two normal stresses and the shear stress in the wake. The plot of the streamwise velocity fluctuation (Figure 5.4.7(a)) shows that the three-dimensional fluctuations are weaker compared to the two-dimensional counterpart. From Figure 5.4.7(a), it is also evident that all the locations reveal similar variations, with differences seen only in their magnitudes. The possible reason for lower values of $\overline{u'^2}$

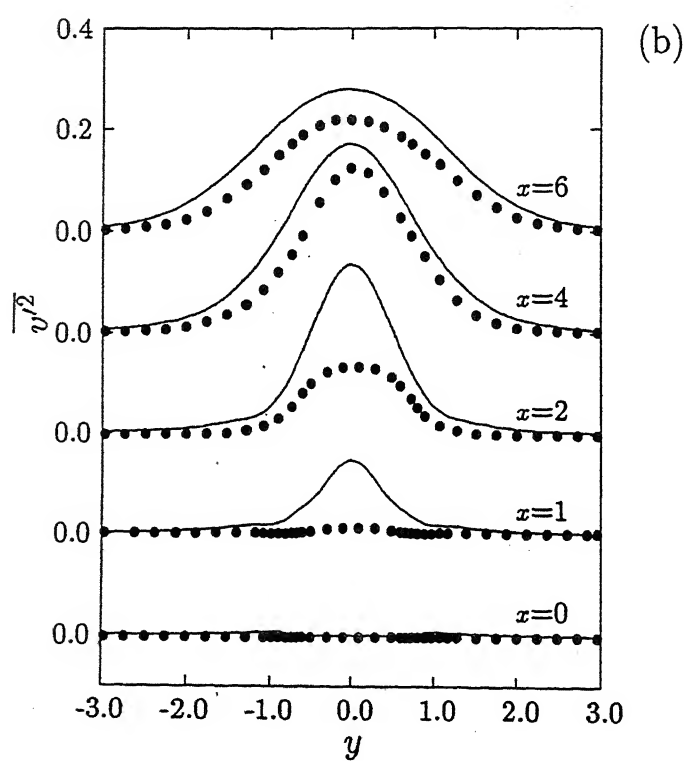
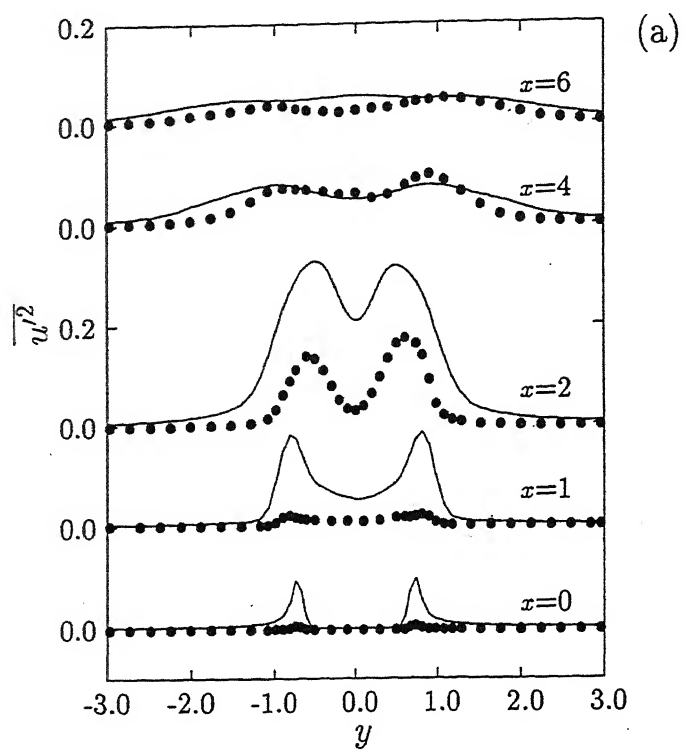


Figure 5.4.7: for caption see next page

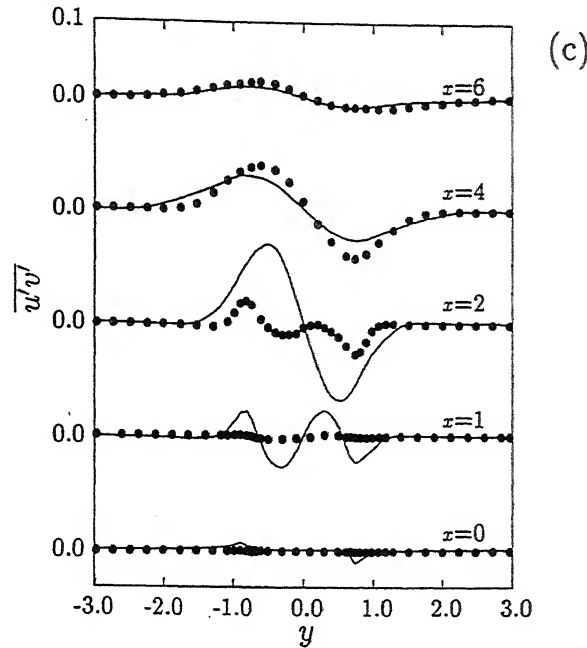


Figure 5.4.7: Comparison of time-averaged profiles of (a) streamwise normal stress (b) transverse normal stress and (c) shear stress. (Line: Two-dimensions, Symbol: Three-dimensions)

in the case of the three-dimensional simulation is that the two shed vortices (also present in two-dimensions) are damped through stretching of the core vortex, thus leading to fluctuations in the direction orthogonal to the two-dimensional case.

It is to be noted that the wake-width in terms of fluctuating streamwise velocity is greater in the two-dimensional simulation compared to the three-dimensional. Both two- as well as three-dimensional simulations show that the streamwise velocity fluctuation exhibits symmetric double peaks about the wake centreline. The magnitude of fluctuations in both the simulations initially grows with the downstream direction (upto the vortex formation length). However, the fluctuations diminish with further increase in downstream distance. The variation of the transverse component of velocity fluctuations in the transverse direction has been depicted in Figure 5.4.7(b). Unlike the streamwise component, the transverse velocity fluctuation shows a single peak and is also symmetric about the wake centreline. As with the streamwise component, it is lower in magnitude in three-dimensions in comparison to two-dimensions. Figure 5.4.7(c) demonstrates the transverse variations of shear stress at different locations. Within the mean recirculation zone, the shear stress in the two- and three-dimensional computations differ significantly. However,

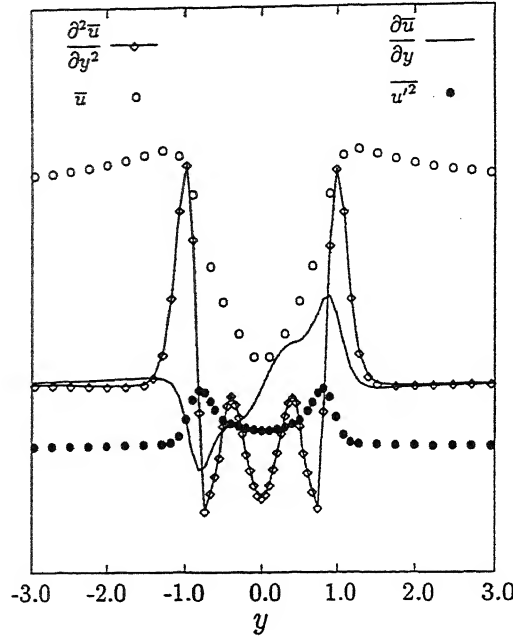


Figure 5.4.8: Transverse variation of $\frac{\partial \bar{u}}{\partial y}$, $\frac{\partial^2 \bar{u}}{\partial y^2}$ and $\overline{u'^2}$ at a location $x=4.0$. It is interesting to see that fluctuations are the highest at the points of inflexion ($\frac{\partial^2 \bar{u}}{\partial y^2} = 0$).

good comparison between the two is observed outside the recirculation zone. The weaker normal and shear stresses within the recirculation zone may be due to the severe three-dimensionality in the transitional three-dimensional flow in the base region of the wake. This phenomenon can be attributed to the fact that the spanwise velocity fluctuation is the highest in the recirculation region and drops subsequently in the downstream. It is interesting to note that the wake-width varies with respect to each component of velocity fluctuations in the case of two-dimensional computations and gives wider wake-widths in terms of the streamwise normal stress and shear stress than that in terms of the transverse normal stress. However, three-dimensional computations consistently show equal wake-width for each component of velocity fluctuations.

It has been noted earlier that the normal and shear stresses in the three-dimensional model are smaller compared to two-dimensions. There is well-established theorem in stability analysis that two-dimensional disturbances have a higher growth rate compared to three-dimensional disturbances (Squire's theorem; Drazin and Reid, 1984). This theorem is valid for the initial period of the growth of disturbance. In the near-wake of a square cylinder (where vortex formation takes place), disturbances in the form of fluctuations can

be thought of growing from a small to mature fully developed fluctuations in the downstream. It is thus to be expected that the fluctuations are higher in the two-dimensional simulation compared to three-dimensions.

The present computation shows that the peaks in the streamwise velocity fluctuation is located at a transverse location which corresponds to the point of inflexion of the mean streamwise velocity profile. Figure 5.4.8 shows the transverse variation of $\frac{\partial \bar{u}}{\partial y}$, $\frac{\partial^2 \bar{u}}{\partial y^2}$ and $\overline{u'^2}$ at a location $x=4$. It is evident from the figure that the maximum of $\overline{u'^2}$ occurs at the transverse locations where $\frac{\partial^2 \bar{u}}{\partial y^2}$ changes its sign and $\frac{\partial \bar{u}}{\partial y}$ is a maximum (or a minimum below the wake centreline). At other locations, similar variations have been observed. It can be proved mathematically that at the point of inflexion, the production of the streamwise normal stress is the highest. The proof of this maxima is clear from the following discussion:

The production of streamwise normal stress for a two-dimensional flow can be written as (Amano and Goel, 1984):

$$P_{u'^2} = -\overline{u'^2} \frac{\partial \bar{u}}{\partial x} - \overline{u'v'} \frac{\partial \bar{u}}{\partial y} \quad (5.4.9)$$

The cross-gradient of the production term is

$$\frac{\partial}{\partial y} (P_{u'^2}) = -\overline{u'^2} \frac{\partial^2 \bar{u}}{\partial x \partial y} - \frac{\partial \overline{u'^2}}{\partial y} \frac{\partial \bar{u}}{\partial x} - \frac{\partial \overline{u'v'}}{\partial y} \frac{\partial \bar{u}}{\partial y} - \overline{u'v'} \frac{\partial^2 \bar{u}}{\partial y^2} \quad (5.4.10)$$

The shear stress $\overline{u'v'}$ may be written as $\nu_t (\frac{\partial \bar{u}}{\partial y} + \frac{\partial \bar{v}}{\partial x})$, where $\nu_t > 0$ in a shear flow configuration. Quantities such as $(\frac{\partial \bar{u}}{\partial x}, \frac{\partial \bar{v}}{\partial x}, \text{ and } \frac{\partial^2 \bar{u}}{\partial x \partial y})$ are small at distances away from the wake centreline. Further, at the point of inflexion the quantity $\frac{\partial^2 \bar{u}}{\partial y^2} = 0$. Therefore, at the point of inflexion

$$\frac{\partial}{\partial y} (P_{u'^2}) = 0$$

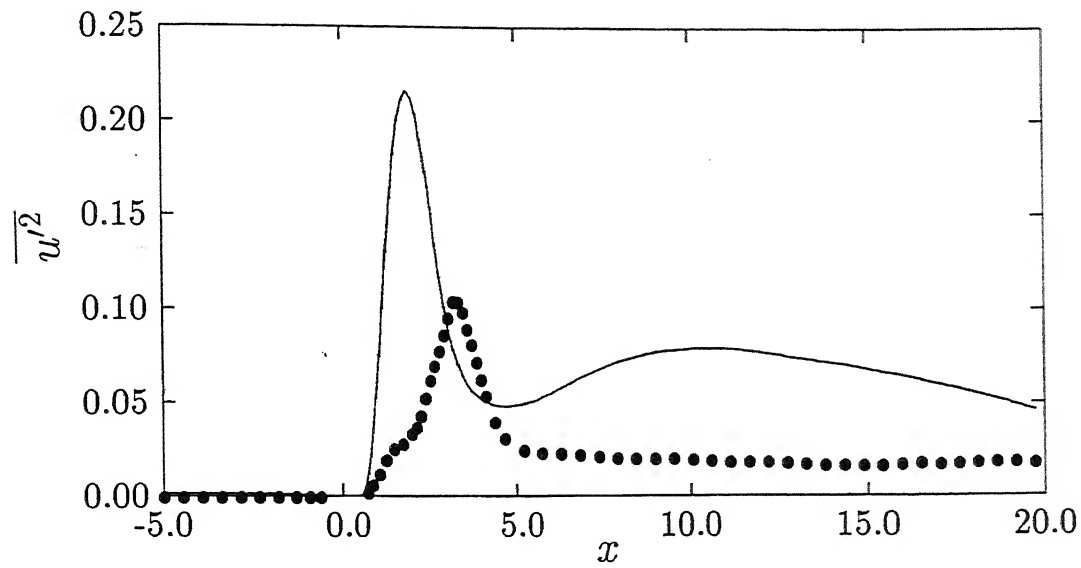
which shows that production attains a maximum value at this point. Similarly it can also be proved that the production of the transverse normal stress is a maximum at the wake

centreline. It can also be shown that the maximum value of the shear stress occurs at the inflexion point.

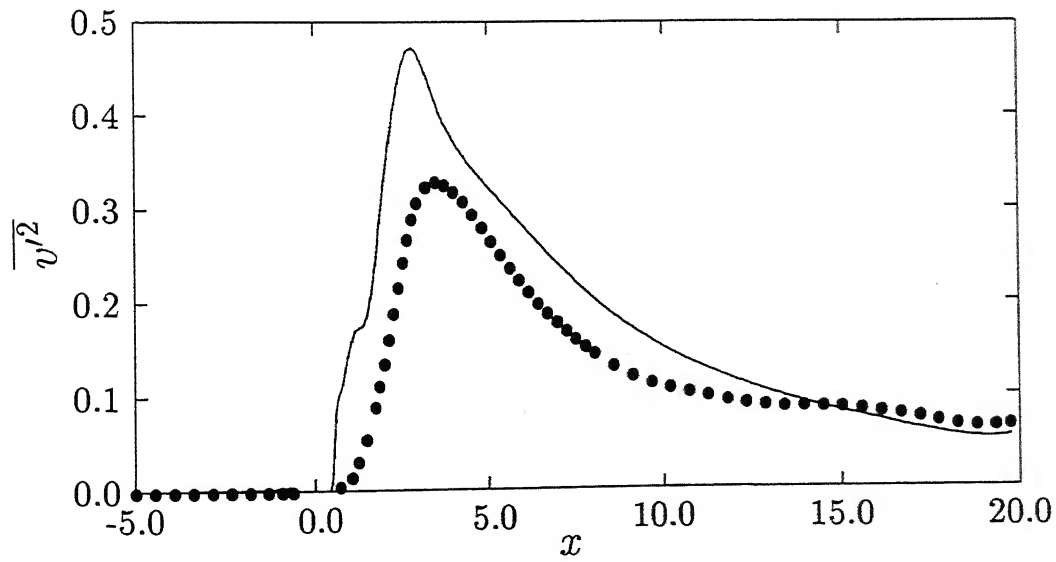
Figure 5.4.9(a) shows the variation of the streamwise normal stress along the wake centreline ($y=0$). The vortex formation length, defined as the distance at which $\overline{u'^2}$ is the highest, differs significantly for the two simulations. The corresponding peak values are also quite different. The vortex formation length (l_{vf}) for the two- and three-dimensional computations with their respective peak magnitudes are $l_{vf}=1.88$ with $\overline{u'^2}=0.216$ and $l_{vf}=3.23$ with $\overline{u'^2}=0.104$ respectively. A similar plot corresponding to the transverse component has been depicted in Figure 5.4.9(b). The downstream locations at which they attain maximum values are also not equal, with differences seen in their respective peak magnitudes. Unlike the streamwise component, $\overline{v'^2}$ shows a slower decay of its magnitude after attaining a peak. The transverse component of velocity fluctuation is associated with the fluid entrainment. Thus entrainment of the fluid inside the wake continues over a larger streamwise direction. The positions and magnitudes of the peak values for the two- and three-dimensional computations are $x=2.82$ with $\overline{v'^2}=0.472$ and $x=3.23$ with $\overline{v'^2}=0.33$ respectively.

The spatial distribution of the fluctuating velocity components shows distinct differences between the two simulations. Figure 5.4.10 shows such a distribution for the streamwise velocity fluctuations. Both simulations show similar qualitative behaviour of symmetric double peaks about the wake centreline. But a closer investigation shows that the two-dimensional simulation (Figure 5.4.10(a)) produces stronger fluctuating field compared to the three-dimensional counterpart ((Figure 5.4.10(b))). The higher fluctuations lead to higher aerodynamic forces on the cylinder. The peaks in the streamwise velocity fluctuation are larger compared to the three-dimensional calculation. This is consistent with the observation of a higher fluctuating velocity in the two-dimensional simulation. The maximum value of the velocity fluctuation in two-dimensions is about two times higher than its three-dimensional counterpart.

Figure 5.4.11(a) depicts the contours of the transverse component of the normal stress for the two-dimensional simulation. The three-dimensional simulation gives a lower peak value at a farther streamwise location (Figure 5.4.11(b)). One salient feature to be noted is that the peak fluctuations are closer to the cylinder in two-dimensions. Figures 5.4.12(a-b) show the spatial distribution of the shear stress for the two simulations. As for streamwise normal stresses the two-dimensional simulation gives peak shear stresses

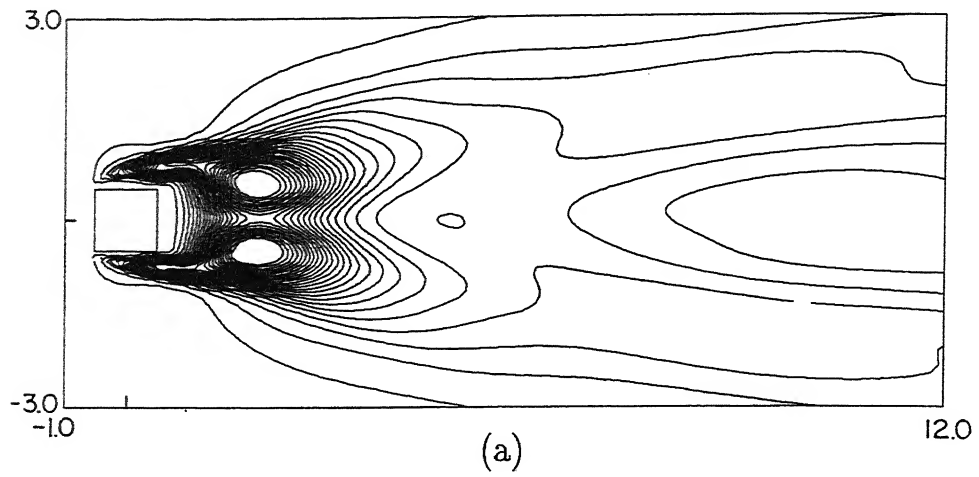


(a)

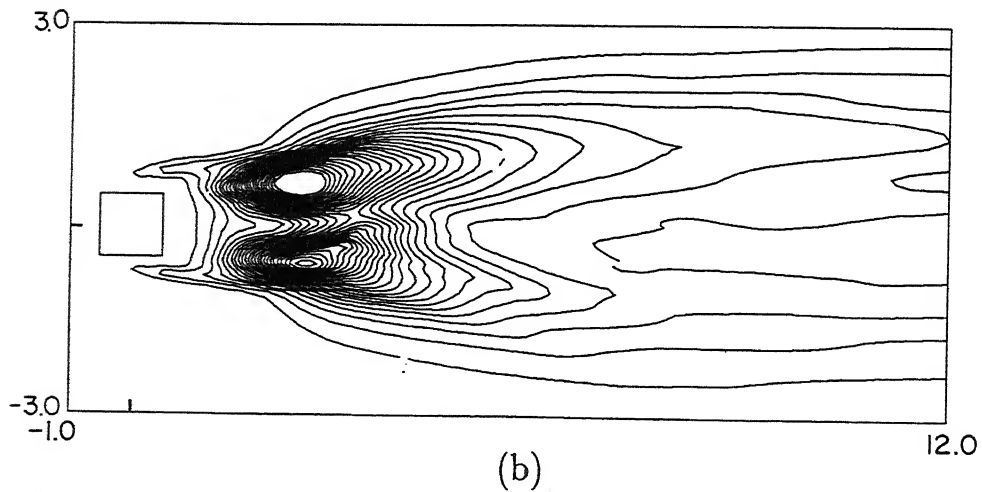


(b)

Figure 5.4.9: Comparison of streamwise variations of velocity fluctuations along the wake centreline: (a) streamwise component and (b) transverse component. (Line: Two-dimensions, Symbol: Three-dimensions)

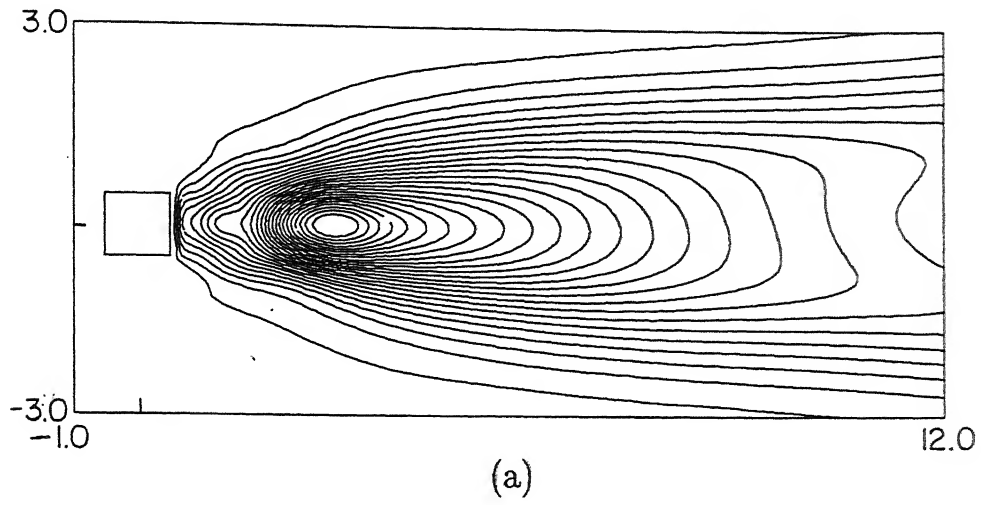


(min, max, increment) \equiv (0.012, 0.3, 0.012)

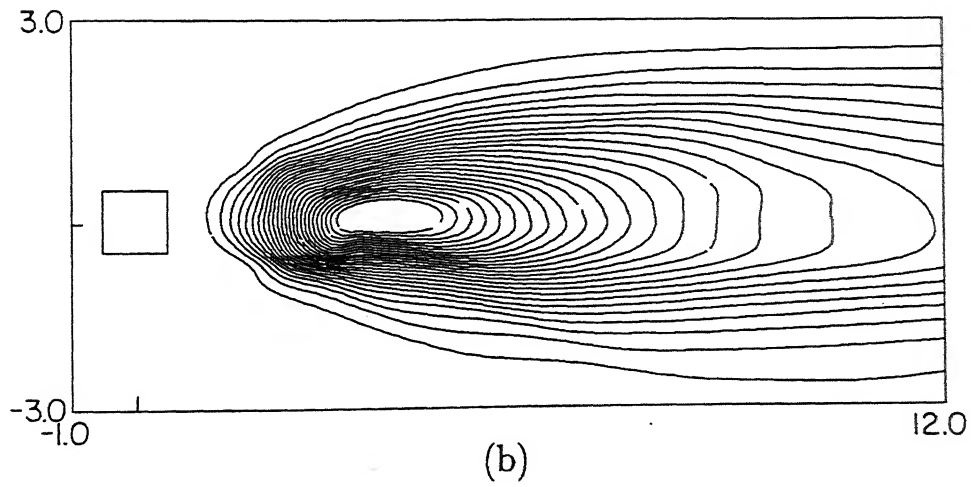


(min, max, increment) \equiv (0.007, 0.175, 0.007)

Figure 5.4.10: Comparison of spatial distribution of streamwise fluctuations $\overline{(u'^2)}$: (a) two-dimensional and (b) three-dimensional simulation.

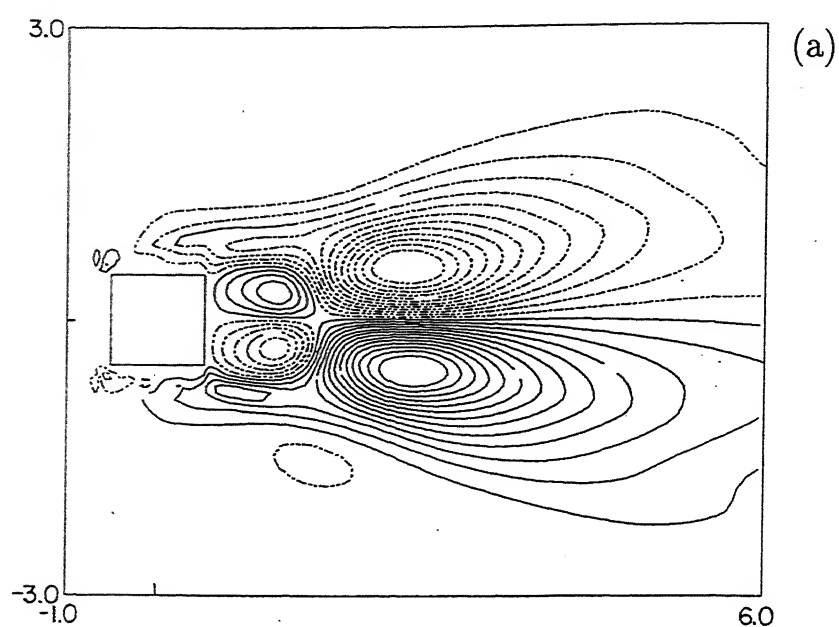


(min, max, increment) \equiv (0.018,0.45,0.018)



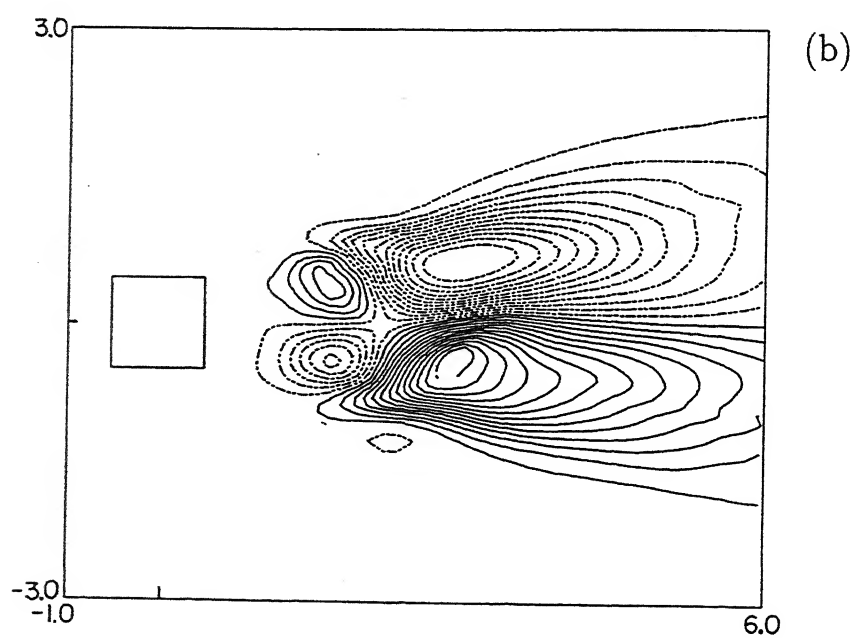
(min, max, increment) \equiv (0.012,0.30,0.012)

Figure 5.4.11: Comparison of spatial distribution of transverse fluctuations ($\overline{v'^2}$): (a) two-dimensional and (b) three-dimensional simulation.



Solid lines: (min, max, increment) $\equiv (0.004, 0.11, 0.009)$

Broken lines: (min, max, increment) $\equiv (-0.100, -0.004, 0.009)$



Solid lines: (min, max, increment) $\equiv (0.004, 0.09, 0.007)$

Broken lines: (min, max, increment) $\equiv (-0.083, -0.004, 0.007)$

Figure 5.4.12: Comparison of spatial distribution of shear stress $(\overline{u'v'})$: (a) two-dimensional and (b) three-dimensional simulation.

very near the cylinder. The three-dimensional simulation does not show this trend. The peak value of $\overline{u'v'}$ is also higher for the two-dimensional simulation. The higher drag coefficient and the fluctuating aerodynamic forces in two-dimensions can be summarized to be due to the following reasons:

1. higher fluctuating components of velocity which affect the base pressure distribution on the cylinder surface.
2. shorter spread of the fluctuating fields near the cylinder which in turn affect the pressure field on the suction side of the cylinder.

5.4.4 Closure

Two- and three-dimensional models of the wake of a square cylinder at a transitional Reynolds number of 250 show significant differences. The differences are mainly due to the higher fluctuations associated with the two-dimensional model. The following conclusions emerge from the comparative study.

1. The fluctuations are higher in the two-dimensional model which lead to higher rms fluctuations of forces, while the mean value is unaffected.
2. The three-dimensional model shows longer shear layer due to the presence of diffusion like terms in the mean vorticity equations.
3. The fluctuations in the three-dimensional model are smaller due to increased diffusion arising from the extra strain rates that couple velocity and vorticity.
4. The higher fluctuating forces in case of the two-dimensional model are attributed to the higher stochastic velocity fluctuations and the higher and closer distribution of shear stresses around the cylinder.
5. The position and magnitude of the peaks are different for the two models. In three-dimensions, the peaks are smaller and are located farther downstream of the cylinder.
6. The fluctuations are the highest at the points of inflexion.

5.5 Influence of Inlet Shear on the Structure of Wake

The flow past a square cylinder can be expected to be sensitive to inflow conditions such as nonuniform upstream velocity, turbulence level and the end conditions. The section is aimed at estimating the influence of upstream shear on the wake structure and the aerodynamic forces.

Two-dimensional numerical simulation of flow past a square cylinder exposed to uniform shear flow has been performed for the geometry shown in Figure 1.3. The above work has been taken up to analyze the forces on the cylinder and the structure of the wake for varying shear strength. The computation has been carried out for a Reynolds number range of 250 to 1500. Two nondimensional parameters which govern the flow around a square cylinder with uniform inlet shear are the Reynolds number, Re and the shear parameter, K . These are defined as

$$Re = \frac{u_{av}B}{\nu} \quad \text{and} \quad K = \frac{GB}{u_{av}}$$

where the uniform shear at the inflow plane is given as

$$u(y) = u_{av} + G(y - 0.5H)$$

Here the transverse velocity gradient on the inflow plane is G , the width of the obstacle is B , the average velocity is u_{av} and H is the transverse dimension of the domain of interest.

The boundary conditions employed for the above investigation are: Top and bottom boundary are modeled as the free-slip condition. Uniform shear with vanishing transverse velocity has been used in the inlet boundary. The convective boundary conditions of the Orlanski type has been employed on the exit plane. No-slip boundary conditions are used for the velocities on the obstacle.

For computation, the flow domain has been divided into number of square cells. A uniform mesh of 402×102 grids has been used. In order to achieve the grid independent solution, computations were performed for a mesh with 642×162 grids. The time-averaged drag coefficient value was seen to differ by less than 2 percent. Finally a mesh size of 402×102 was chosen for all the computations. Computations have been carried out in a

Table 5.5.1: Variation of vortex strength with distance in the downstream behind the obstacle. $Re=500$, $K=0.0$

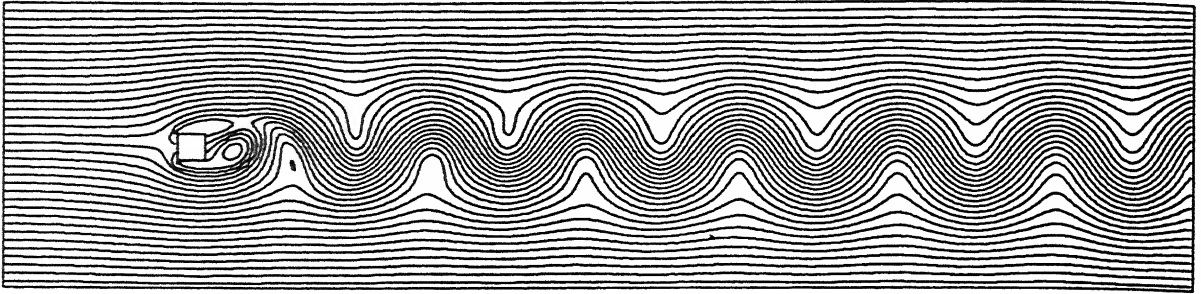
Distance behind the obstacle	$ \omega_z _{\text{peak}}$
0.085	4.80
0.505	3.16
1.015	2.68
1.535	2.30
2.065	2.02

domain of length $L=40$ and transverse width $H=10$. The study has been carried out for a single blockage ratio namely 0.1.

5.5.1 Wake details

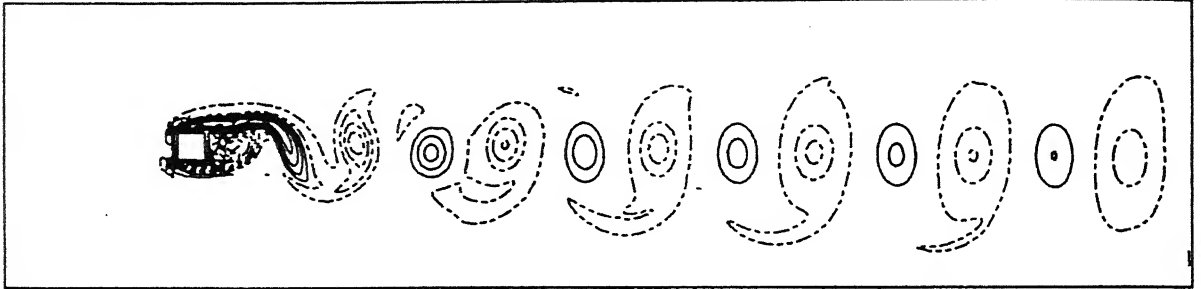
Figure 5.5.1 illustrates the computational results for a Reynolds number of 500 for a square cylinder placed in a uniform flow. A Kármán vortex street is formed behind the cylinder at this moderately high Reynolds number (Figure 5.5.1(a)). In such a situation, the spanwise vortices in the near-wake are convected in the downstream of the cylinder. Figure 5.5.1(b) presents the instantaneous spanwise vorticity at a prescribed time instant. The negative vorticity corresponds to clockwise rotation and is indicated by solid lines, whereas the positive spanwise vorticity corresponds to counterclockwise rotation and is indicated by dashed lines. As expected, it is seen in Figure 5.5.2(b) that the convected vortices are shed in an alternating sequence. The peak value of the counterclockwise vortex core decreases with increasing downstream distances from $|\omega_z|_{\text{peak}}=2.68$ at $x=1.02$ to $|\omega_z|_{\text{peak}}=2.02$ at $x=2.07$ behind the obstacle. An interesting feature of vortex signature is the coincidence of pressure minima with the centre of the vortices at any streamwise location (Figure 5.5.1(c)). The peak value of the vorticity decreases with downstream distance, a trend that can be attributed to vorticity diffusion. Table-5.5.1 shows the variation of peak vorticity with the distance in the downstream behind the obstacle.

Table-5.5.2 shows the variation of mean and rms values of the lift and drag coeffi-



(a)

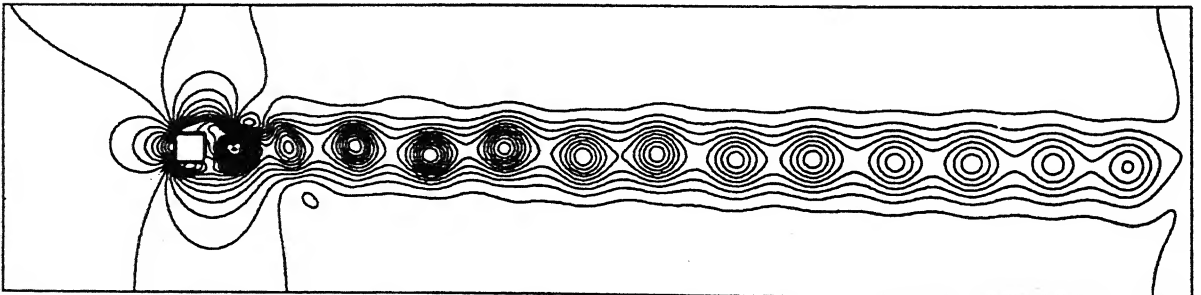
$$(\psi_{\min}, \psi_{\max}, \Delta\psi) \equiv (1.90 \times 10^{-2}, 0.500, 0.014)$$



(b)

$$\text{Broken lines: } (\omega_{\min}, \omega_{\max}, \Delta\omega) \equiv (0.1, 34.2, 1.9)$$

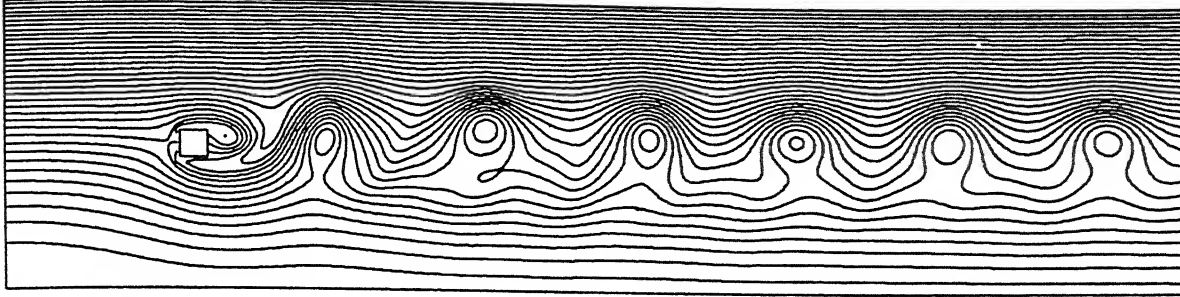
$$\text{Solid line: } (\omega_{\min}, \omega_{\max}, \Delta\omega) \equiv (-30.2, -1.8, 1.9)$$



(c)

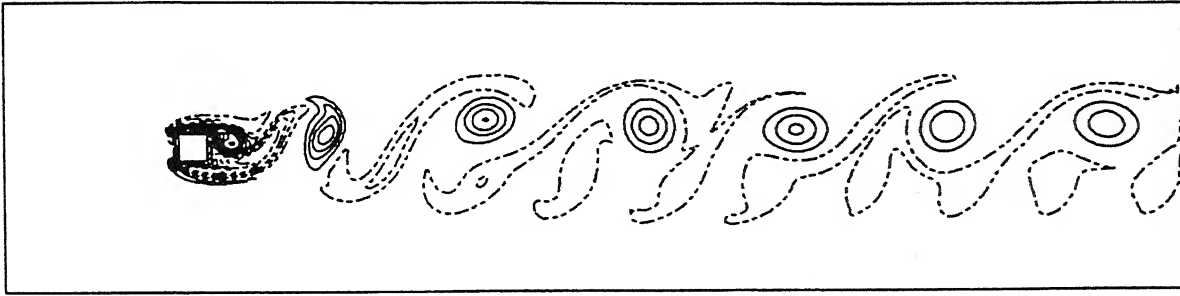
$$(p_{\min}, p_{\max}, \Delta p) \equiv (4.99 \times 10^{-2}, 1.574, 0.054)$$

Figure 5.5.1: Instantaneous (a) streamlines (b) vorticity contours and (c) pressure contours for a Reynolds number of 500 with $K=0.0$



(a)

$$(\psi_{\min}, \psi_{\max}, \Delta\psi) \equiv (1.42 \times 10^{-2}, 0.496, 0.014)$$



(b)

Broken lines: $(\omega_{\min}, \omega_{\max}, \Delta\omega) \equiv (0.1, 28.5, 2.0)$

Solid lines: $(\omega_{\min}, \omega_{\max}, \Delta\omega) \equiv (-40.4, -1.9, 2.0)$

Figure 5.5.2: Instantaneous (a) streamlines and (b) vorticity contours for a Reynolds number of 500 with $K=0.2$

Table 5.5.2: Effect of shear on the Strouhal number, mean and rms values of drag coefficient and rms values of lift coefficient

Reynolds numbers Re	Shear parameters K	Strouhal numbers S	Mean Drag coefficients $\overline{C_D}$	Rms Drag coefficients C'_D	Rms Lift coefficients C'_L
250	0.0	0.187	1.486	0.053	0.398
	0.05	0.186	1.473	0.038	0.382
	0.10	0.185	1.464	0.031	0.381
	0.15	0.182	1.463	0.038	0.400
	0.20	0.180	1.471	0.059	0.438
500	0.0	0.189	1.612	0.116	0.580
	0.05	0.188	1.599	0.092	0.561
	0.10	0.185	1.591	0.072	0.563
	0.15	0.181	1.589	0.065	0.586
	0.20	0.178	1.596	0.081	0.620
750	0.0	0.187	1.714	0.154	0.659
	0.05	0.185	1.703	0.125	0.641
	0.10	0.181	1.697	0.100	0.649
	0.15	0.176	1.698	0.087	0.678
	0.20	0.173	1.704	0.101	0.715
1000	0.0	0.190	1.817	0.165	0.710
	0.05	0.189	1.815	0.146	0.685
	0.10	0.184	1.810	0.116	0.691
	0.15	0.180	1.813	0.099	0.725
	0.20	0.177	1.822	0.112	0.769
1250	0.0	0.191	1.838	0.167	0.741
	0.05	0.189	1.834	0.156	0.723
	0.10	0.187	1.835	0.132	0.714
	0.15	0.181	1.836	0.110	0.754
	0.20	0.178	1.845	0.119	0.803
1500	0.0	0.194	1.848	0.166	0.761
	0.05	0.187	1.846	0.159	0.757
	0.10	0.185	1.845	0.139	0.735
	0.15	0.179	1.846	0.115	0.776
	0.20	0.176	1.856	0.125	0.825

cients and Strouhal number for different Reynolds numbers at different shear parameters. The trends corresponding to $K=0$ are in good agreement with the results of Davis and Moore (1982). In engineering terms, Table-5.5.2 shows that the time-averaged quantities

are not unduly sensitive to the shear parameter. The time-averaged lift was uniformly small over the complete range of parameters studied and has not been included. However, as discussed below, the flow structure shows a strong dependence on inlet shear. Table 5.5.2 shows that the Strouhal number ($=fB/u_{av}$, where f is the frequency) decreases with increasing shear parameter. In the beginning rms values of lift and drag coefficient decrease with increasing shear parameter upto a certain value and then increases with further increase in shear. Similar trends are also seen in case of the time-averaged drag coefficient ($\overline{C_D}$).

The wake structure at Reynolds number of 500 and $K=0.2$ has been depicted in Figures 5.5.2(a-b). Figure 5.5.2(a) is a sketch of the instantaneous streamlines while the instantaneous vorticity contours at the same time level are shown in Figure 5.5.2(b). The most interesting observation is that the counter-clockwise vortices dissipate more rapidly in the presence of shear compared to the clockwise vortices as they travel downstream of the square cylinder. Finally they breakdown into less intense structures. It is to be understood that $K=0.2$ signifies adding up a strong additional vortical motion (clockwise in this study) in the flow field. The present study shows that with a higher shear rate the von Kármán vortex street is broken down. The counterclockwise vortices are blown away obliquely between two consecutive clockwise vortices and mainly clockwise vortices prevail in the far-wake.

The spectra of lift and drag coefficients together with signal traces at $Re=1000$ for various shear parameters are shown in Figure 5.5.3. The spectra have been determined using the FFT algorithm. The effect of shearing is observed in the time evolution of lift coefficient. For increasing value of the shear parameter the time evolution of the lift coefficient gradually tends to show a pure sinusoid. The time evolution of drag coefficient shows the presence of multiple frequencies for all the shear parameters. It is to be noted that (see Figure 5.5.3(a)) one period in the shedding cycle (during which two alternate vortices are shed) is the time between similar adjacent peaks in the lift curve. The instantaneous drag thus oscillates at twice the frequency of the lift. Figure 5.5.3(a) shows the presence of one dominant frequency (Strouhal number around 0.2) with side bands. Otherwise all the lift coefficient spectra show the presence of one dominant frequency which becomes more pronounced with inlet shear. On the other hand the drag coefficient spectra have multiple dominant frequencies. For uniform flow, the drag coefficient spectra show multiple frequencies. For the shearing inlet cases, the drag coefficients continue to

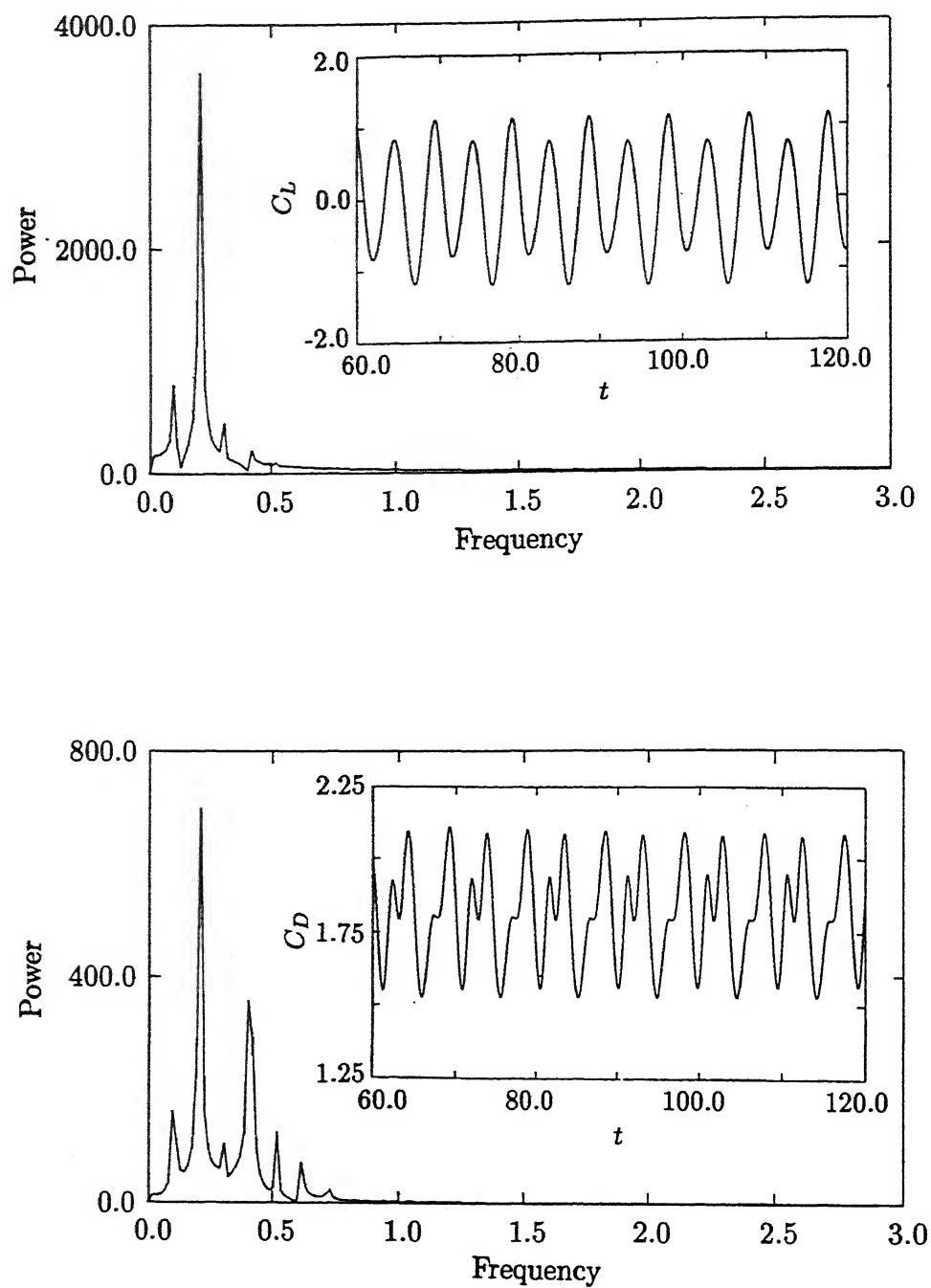


Figure 5.5.3(a): for caption see next page

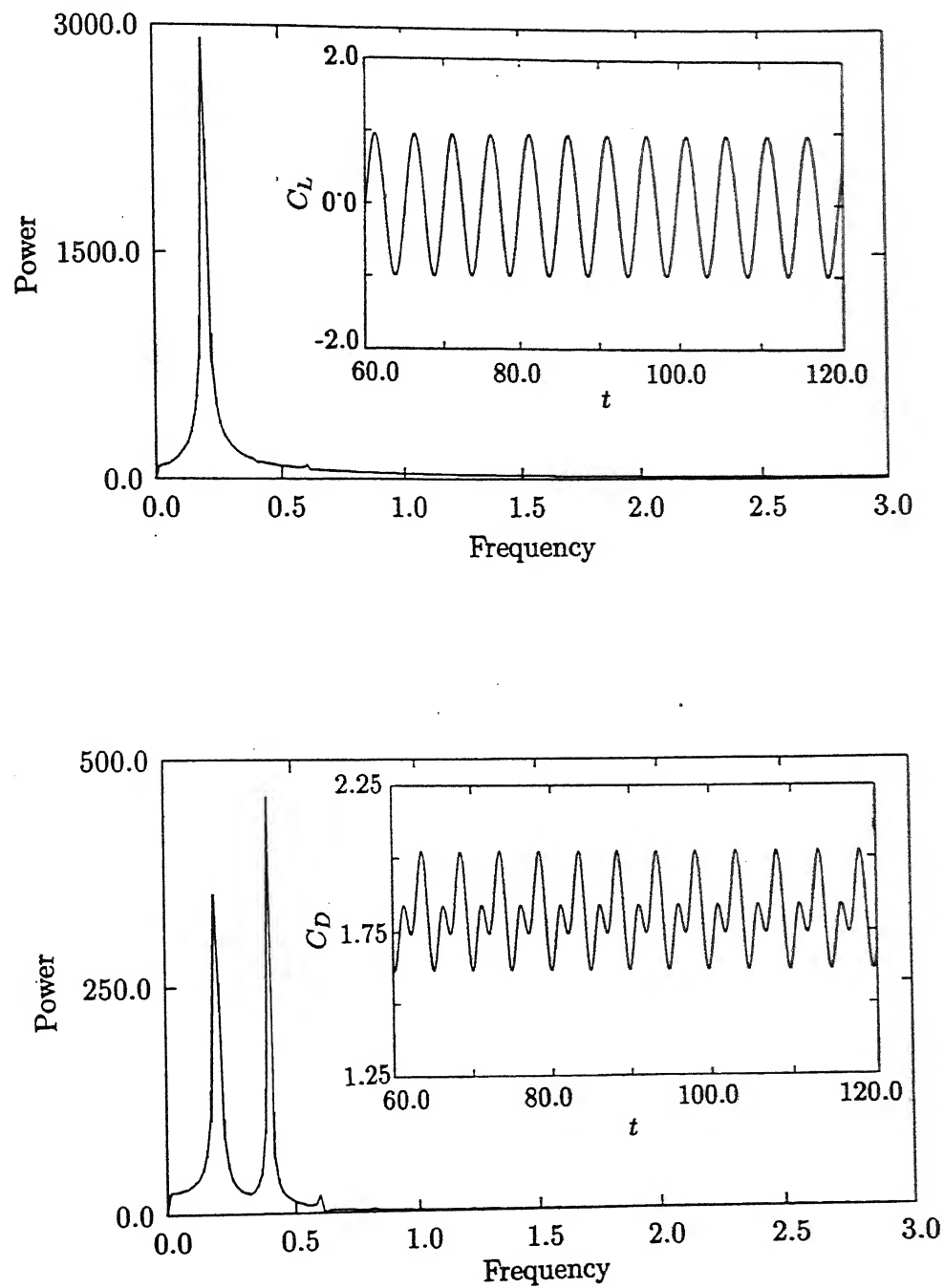


Figure 5.5.3(b): for caption see next page

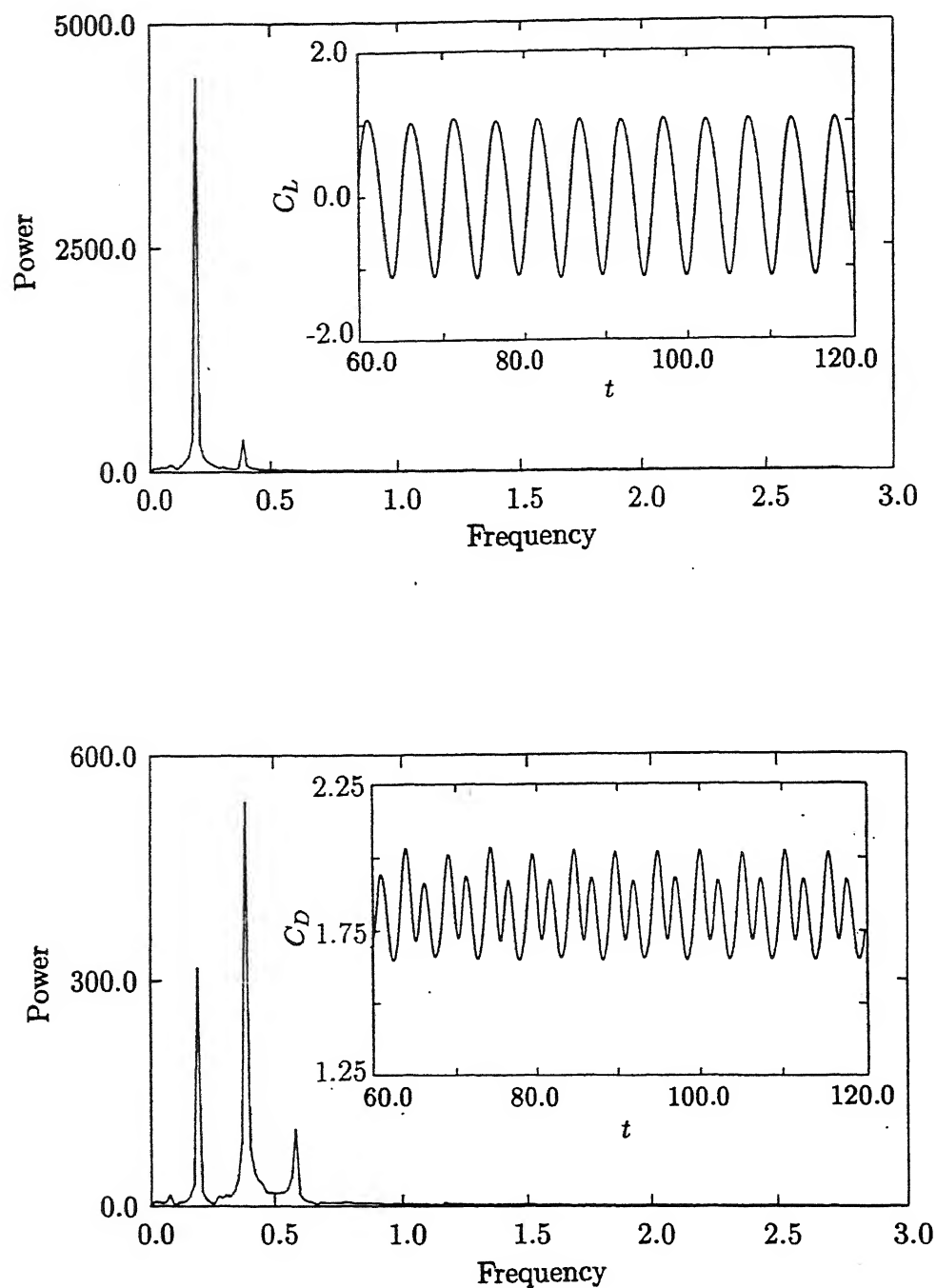


Figure 5.5.3: Power spectra and time series of lift and drag coefficients for a Reynolds number of 1000 with (a) $K=0$ (b) $K=0.1$ and (c) $K=0.2$

have multiple frequencies but the side bands progressively disappear.

5.5.2 Closure

Uniformly sheared flow past a square cylinder has been investigated using the two-dimensional form of the Navier-Stokes equations. The important conclusions to emerge from the study are the following:

1. With increasing inlet shear the time evolution of the lift coefficients gradually tends to show a pure sinusoid and the drag oscillates at twice the frequency of the lift.
2. Strouhal number decreases with the increase in shear parameter. The mean and rms values of the drag coefficient decrease with increase in shear parameter upto a certain value, but increase with further increase in the shear parameter. The rms values of the lift coefficient show a similar behaviour.
3. At higher shear, the von Kármán vortex street breaks down and clockwise vortices mainly prevail in the far-wake.

5.6 Numerical Study of the Partially Enclosed Turbulent Unsteady Wake using RANS

The present and the two following sections evaluate the wake of the square cylinder at high Reynolds numbers. The essential difference between low and high Reynolds numbers is the following: In the former, the flow in the boundary layers around the cylinder is laminar. The wake is laminar as well, though it is subjected to temporal and spatial transitions. The far-wake may however display turbulence like behaviour. At high Reynolds number, the flow is turbulent everywhere, including the boundary layers, shear layers, recirculation region and the near- and far-wakes. Thus, the grid has to be sufficiently small to resolve the fine length and time scales, or alternately a suitable model has to be employed to represent the turbulent phenomena. The present section adopts the second approach to characterize the high Reynolds number wake¹.

The two-dimensional numerical simulation at a high Reynolds number has been carried out in the present section. The performance of three turbulence models of the k - ϵ type have been compared for flow past a square cylinder. The models selected are the original (standard) k - ϵ model (Launder and Spalding, 1974), k - ϵ with Kato-Launder modification for stagnation regions (Kato and Launder, 1993) and the RNG k - ϵ that has been developed with minimal assumptions regarding the nature of flow and geometry (Yakhot *et al.*, 1992)². The configuration considered in the present work is flow past a square cylinder placed centrally inside a channel. The Reynolds number employed is 21400, based on the cylinder width and the average incoming velocity. Under these conditions, the flow everywhere may be taken as fully turbulent. The time-averaged and rms values of the lift and the drag coefficient, vortex recirculation lengths, Strouhal numbers and the time-averaged velocity profiles in the near-wake have been selected as the basis of performance for comparison among the three different models. Where appropriate, the model predictions have been compared with the experiments of Lyn *et al.*, (1995). Subsequently, the three models have been compared in terms of the instantaneous contour plots of the various flow quantities.

¹It is obvious that the wake at high Reynolds number is three-dimensional and should not be solved using a two-dimensional model. However, three-dimensional calculations are very expensive. Therefore, the present section is also an assessment of the two-dimensional model for handling the high Reynolds number complexity.

²For an interpretation of the k - ϵ equations to unsteady periodic flows, see Section 3.3.

The motivation for using the three particular k - ϵ models is the following. The standard k - ϵ model, though the oldest can give surprising good results in complex flows, provided these have predominantly small-scale turbulence structures. It can be considered to be an interpolate of basic experiments from which the model constants have been determined. However, the standard k - ϵ model was developed originally in the context of thin shear layers and contains a variety of assumptions. These include isotropy in the turbulence fluctuations and a well-developed cascade mechanism for transferring energy from the largest to the smallest scales. Despite such limiting assumptions, the standard model has proved to be robust and with minor modifications, it has been capable of predicting low Reynolds number turbulent flows, recirculation zones and relaminarization. An exception was however seen in the prediction of bluff body flows, where turbulence production in the stagnation region was found to be abnormally large. Consequently, vortex shedding was seen to be completely suppressed in certain situations. Two sources of errors in the standard k - ϵ model were traced to (i) inadequate grid resolution in the stagnation region where the boundary-layer thickness is very small and (ii) incorrect modeling of the pressure-strain correlation. The KaLa model taken up for comparison in the present work addresses the second source of error. Here, the production of kinetic energy in the stagnation region is smaller, the eddy viscosity is also smaller compared to the standard k - ϵ model and hence the shed vortices are no longer weak. As against empiricism and intuitive insight of the standard k - ϵ and KaLa models, the RNG k - ϵ is derived rigorously from first principles with very little approximation about the nature of the flow field and the geometry. It has been tested for curvilinear geometries and in those with sudden expansion, but its performance for strongly unsteady flows, with vortex shedding for example, has not been reported. Hence the choice of the RNG k - ϵ as the third model for the present simulation.

The physical problem considered is flow past a cylinder of square cross-section, placed centrally in a channel. A uniform mesh with 386×98 cells has been used. The obstacle surface, and the top and bottom surfaces are treated as no-slip boundaries. At the inlet, the flow enters with a uniform velocity u_{av} and the prescribed turbulence intensity ($I = \sqrt{\frac{u_i'^2}{2}}/u_{av}$) at the inlet is set to 10%. For all the computations, the eddy viscosity is specified as $\langle \nu_t \rangle / \nu = 10$ at the inflow plane (Bosch and Rodi, 1996). The value of the phase-averaged dissipation $\langle \epsilon \rangle$ is specified using the Equations 3.17 or 3.18. The wall function treatment has been used at all the solid boundaries for the standard k - ϵ and the KaLa models. In contrast, no such treatment has been adopted for the RNG k - ϵ model.

The RNG k - ϵ model has been tested on finer grid sizes in order to see the effect of avoiding the wall function treatment. The time-averaged drag coefficients were seen to change by less than 1.5% for the finest grid used. During wall function treatment, the first set of grid points from the wall fell in the range of $10 \leq y^+ \leq 30$. At the outlet, the Orlanski type convective boundary conditions (Orlanski, 1976) has been used.

The time step used for the present simulation for all the three models is 4% of the time period of vortex shedding. Each cycle of vortex shedding took about 100 minutes of CPU time on a DEC-ALPHA machine having a processor speed of 125MHz and 32MB RAM. The time-averaged quantities have been obtained by integrating the instantaneous field over a long period of not less than 40 shedding cycles, but without including the initial transients.

In order to achieve a grid independent solution, computations have been performed for two different meshes with 386×98 and 330×82 grids for all the three models. The time-averaged drag coefficient ($\overline{C_D}$) for the KaLa model on a 386×98 grid was found to be 1.971. On a 330×82 grid the value was 1.935, a difference of less than 2 percent. For the other models the discrepancy in the predicted values of $\overline{C_D}$ for the two different meshes was also seen to be less than 2 percent. Hence all computational results were obtained on the 386×98 grid mesh.

Three turbulence models, namely the standard k - ϵ , Kato-Launder (KaLa) and RNG k - ϵ have been employed in the present work to simulate the flow past a square cylinder placed centrally in a parallel plate channel. The Reynolds number based on the cylinder size was set at 21400. Though the flow becomes three-dimensional at a Reynolds number of 180 (Williamson, 1988b), a two-dimensional simulation has been carried out in the present study. The assumption of two-dimensionality in the simulation can be justified in the following way: Issues such as three dimensionality, oscillations in vortex shedding frequency and modes of wake formation are related to transition of flow in the wake. These cannot be addressed in the context of turbulence models. Instead, these models readily provide information having engineering importance, for example lift and drag coefficients, centreline recovery of velocity and the size of the recirculation zone. These results can be obtained in a meaningful manner in two-dimensional geometries by using the two-dimensional form of the governing equations. The use of k - ϵ family of models has an added benefit. Energy transfer in the third dimension that is neglected in a two-dimensional formulation is partially accounted for by the dissipation function. Hence

Table 5.6.1: Strouhal number and time-averaged drag and coefficients

Turbulence Model	Strouhal Number	$\overline{C_D}$	$\overline{C_L}$	C'_D	C'_L	Recirculation Length
Standard $k-\epsilon$	0.141	1.93	0.002	0.01	0.552	2.22
KaLa	0.145	1.97	-0.004	0.02	0.707	1.92
KaLa (free-slip)	(0.142)	(1.95)	(0.0004)	(0.02)	(0.724)	(1.92)
RNG $k-\epsilon$	0.145	1.85	0.003	0.005	0.356	2.62
Cheng <i>et al.</i> (1992), Expt.	-	1.9-2.1	-	0.2	0.6	-
Lyn <i>et al.</i> (1995), Expt.	0.135	2.05	-	-	-	1.38

certain features of transition are captured by the two-equation models.

5.6.1 Engineering parameters

The geometrical parameters related to the present study are $H=8.0$, $L_a=8.5$, $L=32.0$ and $B/H=0.125$ (Figure 1.3). The pertinent time-averaged parameters of importance in engineering that have been computed using the three different models are listed in Table-5.6.1. The computed results have been compared with the experiments of Cheng *et al.* (1992) and Lyn *et al.* (1995). The experimental data of Lyn *et al.* (1995) has been taken from the website. It is to be noted that the experiments of Lyn *et al.* (1995) were carried out in a water channel using LDV, the square cylinder being practically unconfined. The lift and drag coefficients in the experiments were determined by the wake survey method. In the present numerical calculations, these were obtained by integrating pressure on the surface of the cylinder. Hence some differences between the experiments and numerical

simulation are to be expected. The dominant frequency was determined by tracking the y -component velocity signal just above the centreline of the parallel plates channel. It can be seen from Table-5.6.1 that the Strouhal numbers predicted by three different models are very close. However, all the three models overpredict the Strouhal number with respect to the experimental value of 0.135. Correspondingly, the drag coefficients in the wall-bounded case are smaller than those in the experiments with the unbounded cylinder. This discrepancy can be partly attributed to the finite blockage of the geometry associated with the walls confining the square cylinder in the present simulation. Taking this factor into account, the time-averaged drag coefficient predicted by the standard $k-\epsilon$ and KaLa models agree quite well with each other and with the experiment. In contrast, the rms values of the lift coefficients predicted by different models vary significantly. The rms values of the drag-coefficient for all three cases are uniformly small. Cheng *et al.* (1992) have reported larger rms values of C_D in their experimental study. The corresponding rms values of lift coefficient is reported to be 0.6 and is comparable to the numerical predictions. As expected in geometries having overall symmetry, the time-averaged lift coefficient is predicted to be quite small by all the three models. The rms values of the lift coefficient is smaller in the standard $k-\epsilon$ model compared to KaLa, but that of RNG $k-\epsilon$ is the lowest. This is surprising because there is barely any difference in the shedding frequency among the models.

To check if differences between the numerical predictions and experiments were related to the side wall boundary conditions, calculations were repeated with free-slip conditions. The lift and drag coefficient as well as the Strouhal number for KaLa model with free-slip conditions are reported within brackets in Table-5.6.1. The differences between the two sets of calculations can be seen to be very small.

The following observations can be drawn from the data in Table-5.6.1

- All the three models predict small time-averaged lift and rms drag coefficients.
- They predict nearly equal shedding frequencies and hence the Strouhal number. These values are smaller than that reported in experiments with an unbounded cylinder.
- Differences are however seen among the model predictions for the time-averaged drag and rms lift coefficients. The recirculation length, namely the distance over

which the time-averaged x -component velocity on the rear side of the cylinder is negative, also shows a considerable variation. The effect of the bounding walls is seen to stretch the recirculation zone beyond what is seen in the experiments with an unbounded cylinder. This is understandable because the walls lead to an acceleration of the flow outside the recirculation region and hence a delay in the recovery of the velocity field.

- Among the three models, the predictions of the standard k - ϵ and KaLa are similar and closer to experiments, but those of the RNG k - ϵ are different. Hence as an engineering tool, predictions of the RNG k - ϵ are seen to be less satisfactory.
- Bosch and Rodi (1996) have observed that the standard k - ϵ model is excessively diffusive. Hence shedding is very weak and the vortex shedding frequency is lowered. This has not been borne out in the present work, and the standard k - ϵ is seen to be quite good for predicting the Strouhal number. A possible explanation could be the choice of the numerical scheme, specifically the details of implementation of the boundary conditions, pressure-velocity coupling and the number of grid points.

Figure 5.6.1 shows the evolution of the lift coefficient with time, as predicted by the three models. It is clear from this figure that the RNG k - ϵ model damps down the oscillation the greatest while the KaLa model shows the highest amplitude of oscillation. The dominant frequencies predicted by the three models are very close to each other. Hence the primary effect of differences in the production and dissipation terms in the three models is felt in terms of the amplitude of velocity fluctuations and all related variables. If the lift coefficient is taken as a measure of the vortex strength in the near-wake, one can conclude that the KaLa model predicts the strongest vortex, the RNG k - ϵ the weakest and the standard k - ϵ predicts an intermediate value.

The streamwise variation of the peak vorticity as determined by the three models are presented in Figure 5.6.2(a). The magnitude of the peak vorticity at any location downstream of the cylinder (specifically, beyond the recirculation zone) is the highest for the KaLa model and lowest for the RNG k - ϵ . This trend is consistent with the earlier discussion that pointed out greatest damping in the RNG k - ϵ and the least in the KaLa model. The vorticity decay rates calculated from the peak vortices show that in the near-wake, the vortices decay fastest in the standard k - ϵ and the slowest in the KaLa model. In the far-wake, the decay rates are the highest for KaLa and the lowest for the RNG k - ϵ .

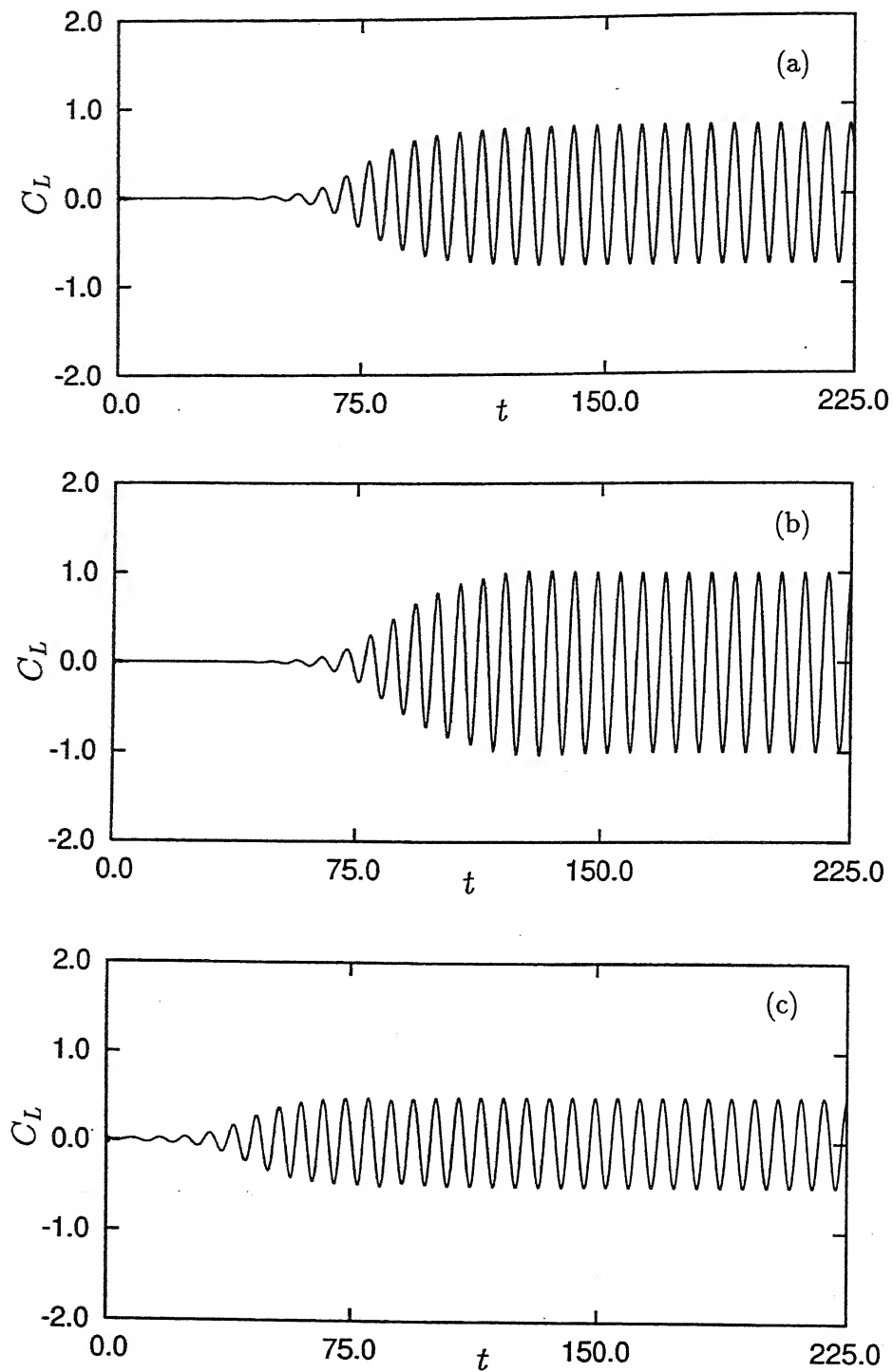


Figure 5.6.1: Time evolution of lift coefficient: (a) standard $k-\epsilon$ (b) KaLa and (c) RNG $k-\epsilon$. The KaLa model shows higher fluctuations as it can handle the stagnation zone properly.

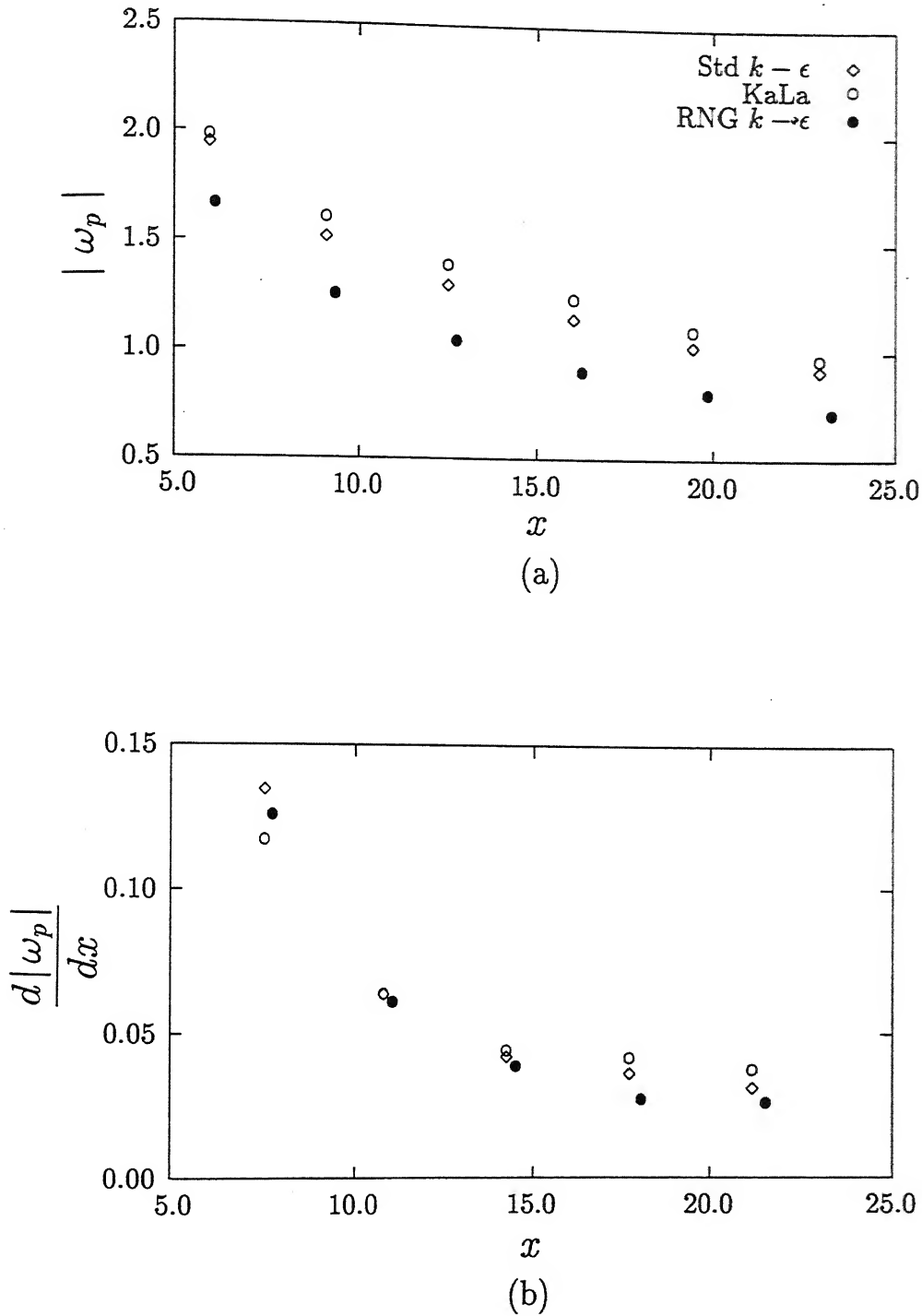


Figure 5.6.2: Streamwise variation of (a) peak vorticity and (b) decay rate of peak vorticity. The RNG $k-\epsilon$ shows lower value of peak vorticity due to its higher damping.

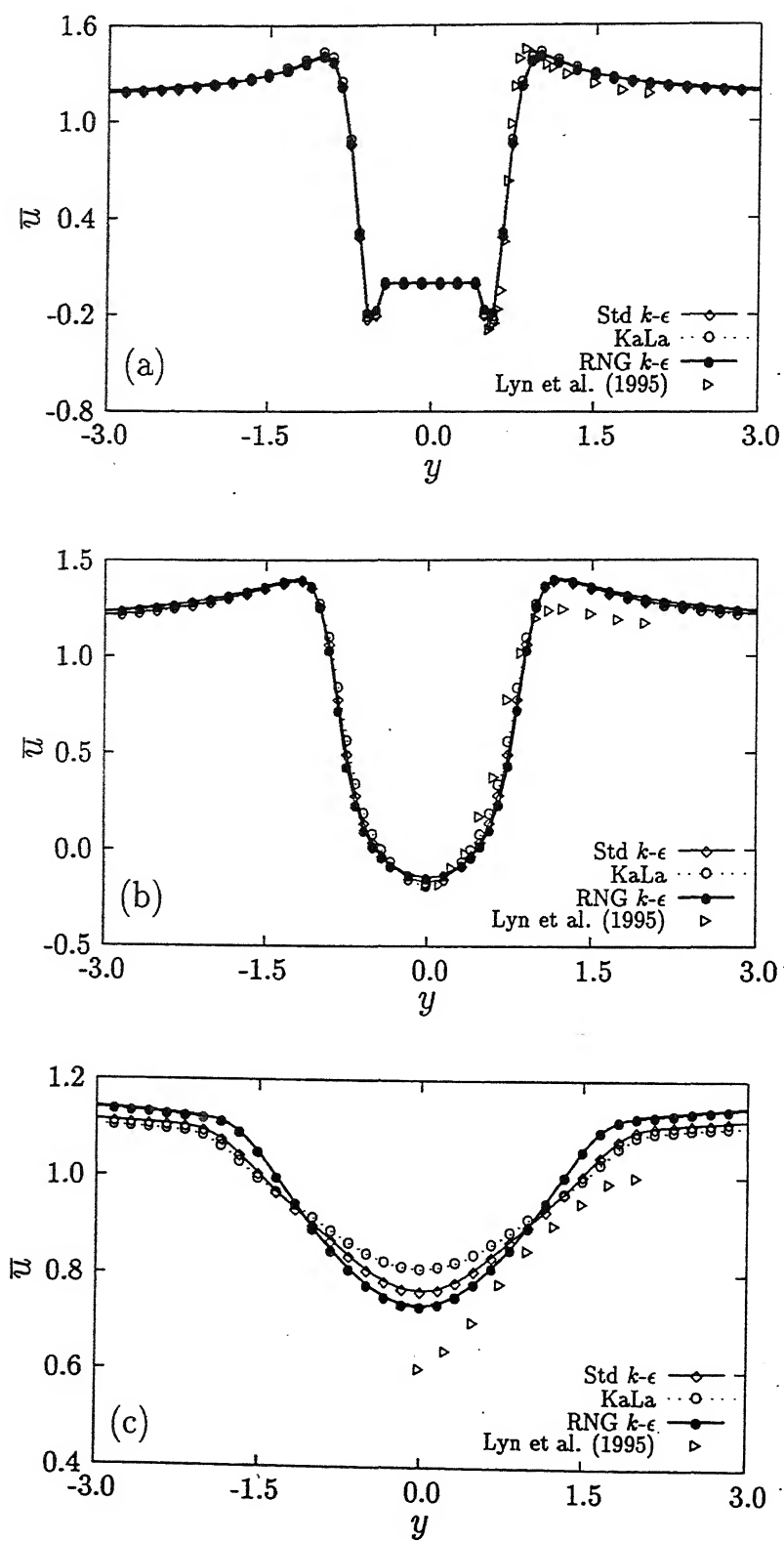


Figure 5.6.3: Time-averaged streamwise velocity profiles at (a) $x=0$ (b) 1.0 and (c) 5.0.

(Figure 5.6.2(b)).

5.6.2 Comparison with experiments

Figure 5.6.3 shows a comparison of the time-averaged streamwise velocity profiles at different downstream locations, namely ($x=0, 1$ and 5) for the three turbulence models. The experimental data of Lyn *et al.* (1995) has also been plotted in this figure. At a location of $x=0$, the comparison is extremely good except very near the obstacle surface. The discrepancy could be due to inadequate positional accuracy in the experiments on one hand and the use of wall functions on the other. At the other two locations, the comparison reveals minor differences. A higher blockage due to the channel walls may also be responsible for the differences between the numerical simulation and experiments. The overall model predictions of the x -component of velocity however are sensibly close.

The numerically obtained time-averaged transverse component of velocity profiles at two different locations ($x=0$ and 5) have been compared with the experiments of Lyn *et al.* (1995) in Figure 5.6.4. At $x=0$, the three models show good agreement with the experiments though the numerical values are higher in regions near the cylinder. Once again, this can be attributed to the finite blockage due to the channel walls in the computation as against the infinite medium in the case of experiments. At $x=5$, the results of the standard $k-\epsilon$ and KaLa models are closer to the experimental measurements. However, those of the RNG $k-\epsilon$ differ significantly.

Figure 5.6.5 shows the time-averaged x -component of velocity variation along the centreline $y=0$. Among the three, the KaLa model displays better agreement with experiments in the immediate downstream of the obstacle. This could be because the KaLa model produces just the right amount of turbulent kinetic energy and helps in retaining the periodic fluctuations. The periodic fluctuations strongly influence the momentum transfer between the instantaneous and time-averaged velocity components in the near-wake. This indirectly affects the centreline recovery of the time-averaged streamwise component of the fluid velocity.

The comparison between the computations and the experiment with regard to the time-averaged kinetic energy variation along the centreline $y=0$ is taken up next (Figure 5.6.6). The kinetic energy plotted in Figure 5.6.6 is that of the total velocity fluctua-

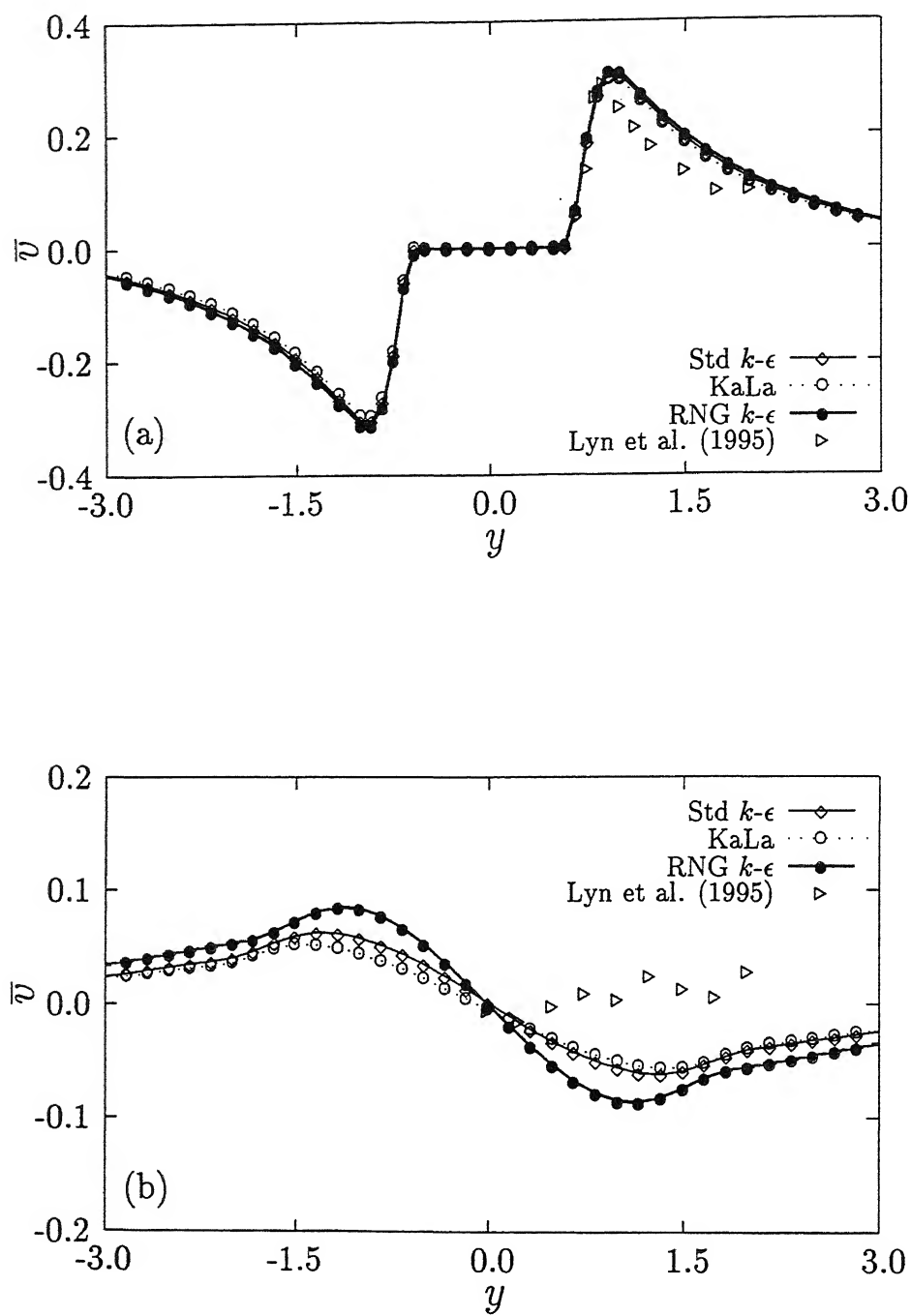


Figure 5.6.4: Time-averaged transverse velocity profiles at (a) $x=0$ and (b) 5.0.

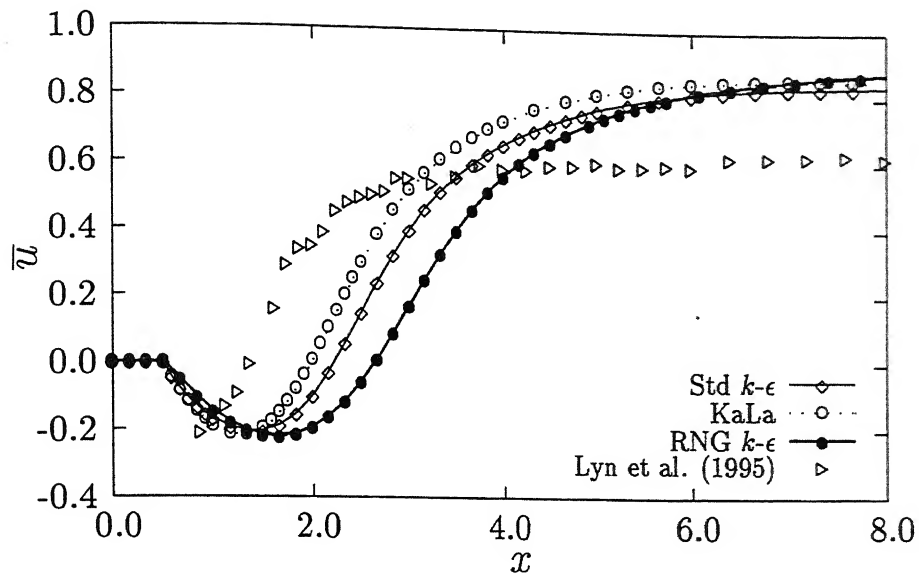


Figure 5.6.5: Time-averaged streamwise velocity recovery along the centreline ($y=0$).

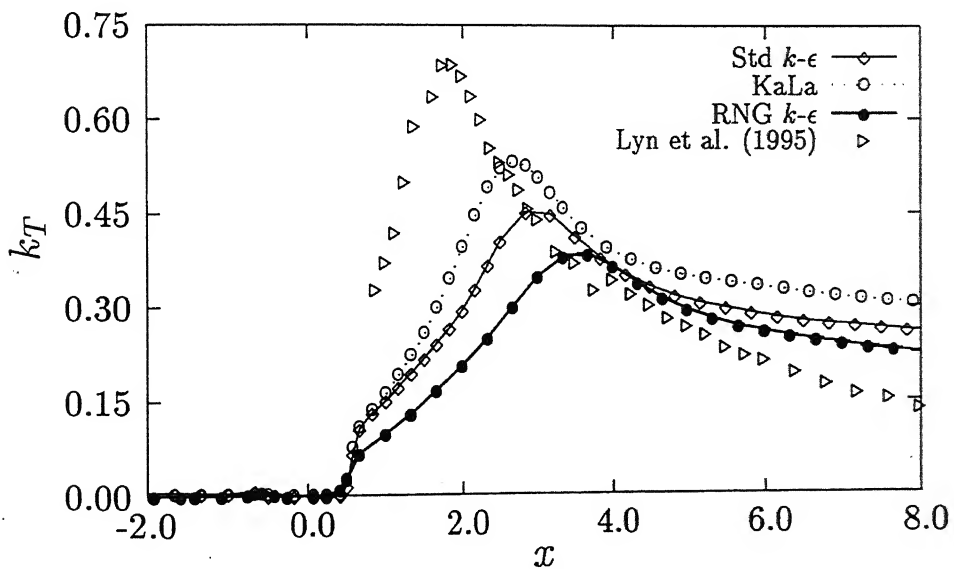


Figure 5.6.6: Streamwise variation of total time-averaged kinetic energy along the centreline ($y=0$).

tion $\hat{u}_i (= \tilde{u}_i + u'_i)$ and is defined for the plane channel flows as Hadid *et al.* (1992)

$$k_T = \frac{3}{4} (\tilde{u}^2 + \tilde{v}^2)$$

using the approximation $\hat{w}^2 = 1/2(\tilde{u}^2 + \tilde{v}^2)$. In experiments, \hat{u} and \hat{v} can be directly measured. In computations one can employ the formula

$$\overline{\hat{u}^2} = \overline{(\tilde{u} + u')^2} = \overline{\tilde{u}^2} + \overline{u'^2} + 2\overline{\tilde{u}u'}$$

Here \tilde{u} can be determined from the computed velocity $\langle u \rangle$ by subtracting \bar{u} , the quantity $\overline{u'^2}$ is associated with kinetic energy k of the k - ϵ model and the third term is limited by the upper bound

$$\overline{\tilde{u}u'} < \sqrt{\overline{\tilde{u}^2}} \sqrt{k}$$

In the present study, the unbiased estimate

$$\overline{\tilde{u}u'} = \frac{1}{2} \sqrt{\overline{\tilde{u}^2} k}$$

has been utilized.

An examination of Figure 5.6.6 shows that the KaLa model predicts the peak value of k_T in good agreement with the experiments. The peak value of k_T due to the RNG k - ϵ model shows the greatest departure. The shift in the location of the peak could be due to the presence of boundary walls in the computations. A similar trend is to be seen in earlier studies as well Hadid *et al.* (1992), but the shift in the present study is seen to be smaller, and hence represents a closer agreement with experiments.

5.6.3 Contours of instantaneous quantities

Figures 5.6.7(a-c) shows a comparison of the instantaneous vorticity contours obtained from the three turbulence models. These have been plotted after matching the phases (strictly, the minimum value of the lift coefficient) of the shed vortices in the numerical simulation of each model. The vortex shedding phenomenon is clearly visible in the three plots and these look qualitatively similar. It may be recalled that the actual flow is three-dimensional. The phenomena such as vortex stretching and tilting would be expected to occur in such flows. The turbulence models provide a crucial link between

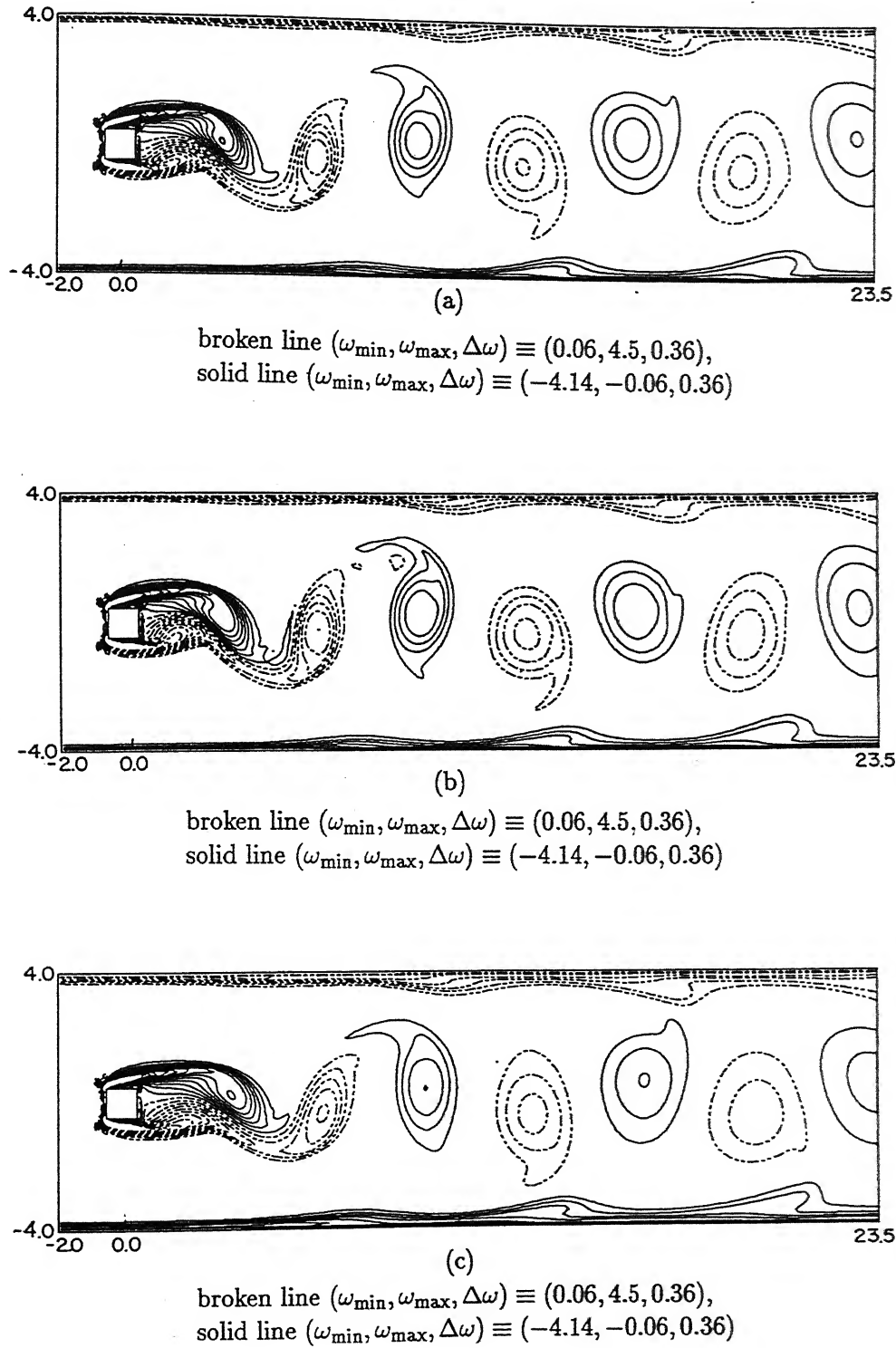


Figure 5.6.7: Instantaneous vorticity contours: (a) standard $k-\epsilon$ (b) KaLa and (c) RNG $k-\epsilon$. The standard $k-\epsilon$ and KaLa models show almost identical contours with respect to contour magnitudes but the RNG $k-\epsilon$ model underestimates the vorticity magnitudes

the two-dimensional paradigm and the observations of shedding in real flows. All the three models reveal two-dimensional flow of non-trivial structure. Figure 5.6.8 depicts the spatial evolution of turbulent kinetic energy at a selected time instant. The contours show that the generation of turbulent kinetic energy is related to the shear in the flow arising from the square cylinder. It is clear that the generation of kinetic energy is greater in regions where the velocity gradients are high, particularly in the near-wake. In the present study, turbulent kinetic energy refers only to that contained in the random velocity components. The kinetic energy is uniformly distributed at the inlet and evolves downstream of the cylinder in a manner that depends on the distribution of shear in the flow. The turbulent kinetic energy grows in magnitude wherever the gradient of the phase-averaged velocity is different from zero. Thus it is vigorous in the near-wake of the cylinder. A comparison of Figures 5.6.7 and 5.6.8 shows that the KaLa model retains a good correlation between the vorticity and kinetic energy fields through the correctly estimated production terms. The correlation is much weaker for the other two models.

The shear layers in the wake of a circular cylinder are structurally different as compared to those of the square cylinder. In the latter, the presence of sharp corners plays a central role in determining their location and thickness. At a low Reynolds number, boundary-layers originating from the corners on the forward face of the square cylinder may reattach over the cylinder surface. Thus wake formation is related to flow separation at the rear corners of the cylinder. At a high Reynolds number, as in the present study, the reattachment referred above does not take place and the wake originates from the corners of the front face of the cylinder. At a very high Reynolds number, the free shear layer formed due to forward corner is distinct from the boundary layer that is seen over the cylinder surface. The free shear layer forms due to the sharp turning of the fluid at a right angle. The net result is that multiple shear zones are formed around the square cylinder, whose total thickness far exceeds that of the boundary-layer. Figures 5.6.8(a-c) show that all the three turbulence models predict shear zones of substantial thickness. All the three models reveal small white patches above and below the cylinder where kinetic energy is not produced (Figure 5.6.7(a-c)). It can be taken to mean that all the three models delineate the outer free shear layer from the inner boundary-layer and thus produce a physically meaningful field.

To take up a quantitative comparison of the three models, consider the range of the quantity (*Production – Dissipation*) in dimensionless form in the kinetic energy equation

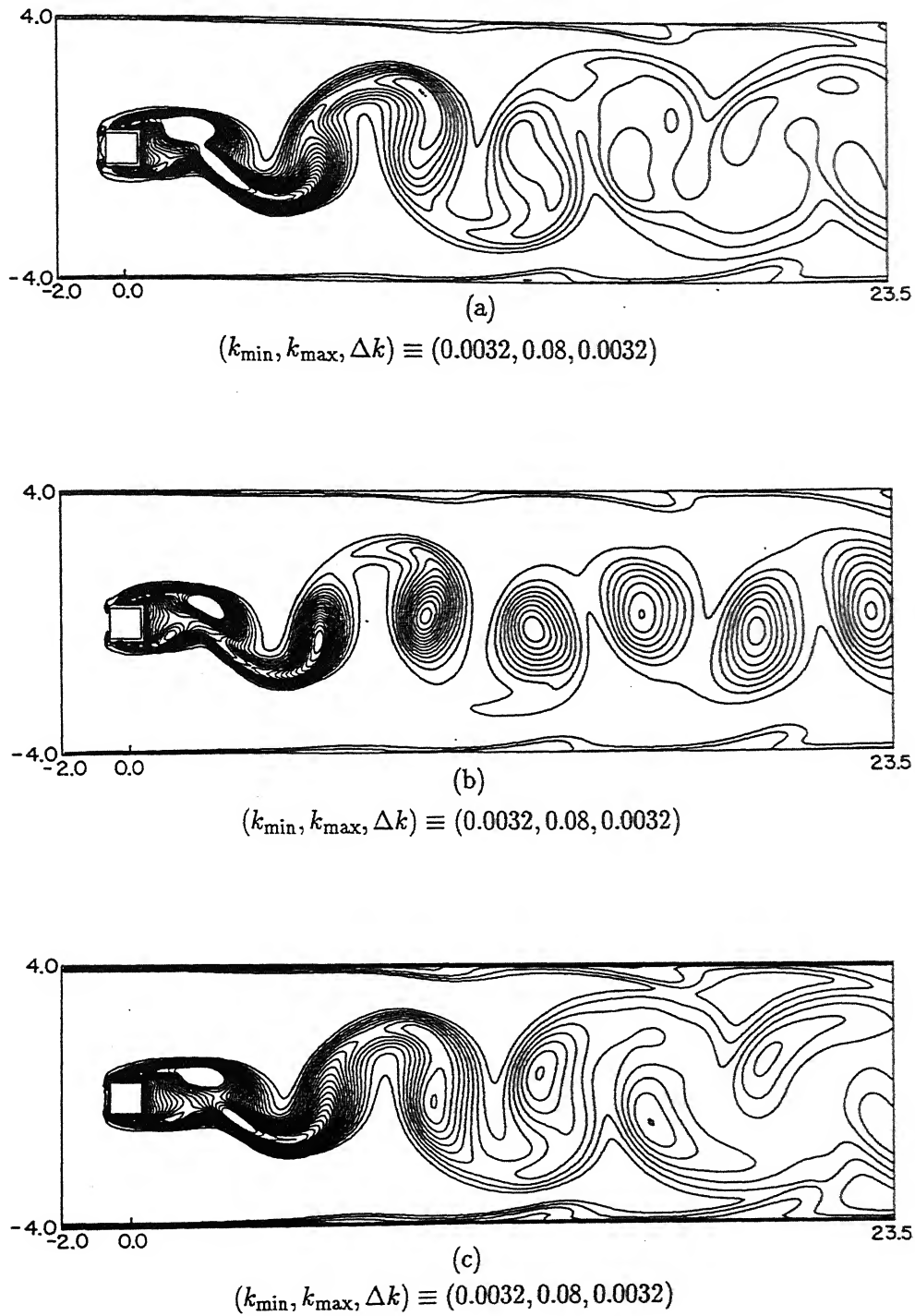


Figure 5.6.8: Instantaneous turbulent kinetic energy contours: (a) standard $k-\epsilon$ (b) KaLa and (c) RNG $k-\epsilon$. KaLa model shows better correlation with the vorticity contours.

due to the three different models. Referring to Equation 3.11, this is $P_k - \langle \epsilon \rangle$. Intuitively, one can associate typical values to this difference with the strength of the vortex generated by the square cylinder. For the standard $k-\epsilon$, the maximum and minimum values in the near-wake are 2.28 and -0.34, for KaLa it is 2.46 and -0.35 and for the RNG $k-\epsilon$, it is 1.18 and -0.67. Clearly, the strongest vortices are associated with the KaLa model, and the weakest with the RNG $k-\epsilon$ model. The minimum values also show that dissipation is over-predicted by the RNG $k-\epsilon$ model. Consider next the magnitude of the turbulent kinetic energy. For the standard $k-\epsilon$ model it is 0.0008 and 0.1160, for KaLa it is 0.0005 and 0.1036 and for RNG $k-\epsilon$ model it is 0.0009 and 0.0953. The standard $k-\epsilon$ model gives rise to a high turbulent kinetic energy near the stagnation zone. The excess of turbulence kinetic energy in such flows culminates in a high turbulent viscosity that is capable of suppressing the leading edge separation. A similar effect is observed for flows past a circular cylinder. Hence the flow field, especially the shear layers are wrongly predicted. The improved prediction of KaLa model in the present context can be attributed to improvement in the modeling of flows with normal straining near the stagnation zone. Specially, the KaLa model lowers turbulence production in the forward stagnation zone and does not damp the velocity fluctuation in the wake. The distribution of $P_k - \epsilon$ as well as k are essentially consistent with the conclusions drawn from Figure 5.6.1.

An interesting feature predicted by all the three models is the wave-like fluid motion at the solid walls of the channel by the vortices shed by the cylinder. As discussed in the context of Table-5.6.1, the walls only marginally influence the vortex shedding process. The shed vortices in turn drive the boundary-layers, thus creating vorticity and kinetic energy at the walls. The sign of vorticity at the two walls are opposite to each other. Hence the reinforcement of vorticity is accomplished by vortices of opposite sense, clockwise for the top wall and counter clockwise for the bottom. The appearance of the wave-like phenomena at the walls will have an impact on the flow development in the far-wake of the cylinder.

The evolution of the instantaneous dissipation predicted by three models is presented in Figure 5.6.9. It can be seen that the dissipation is prominent only in the near-wake. Dissipation is almost uniform in the far-wake where the phase-averaged shear is not as high as in the near-wake. The extent of dissipation is the highest in the RNG $k-\epsilon$ and the lowest in the KaLa model.

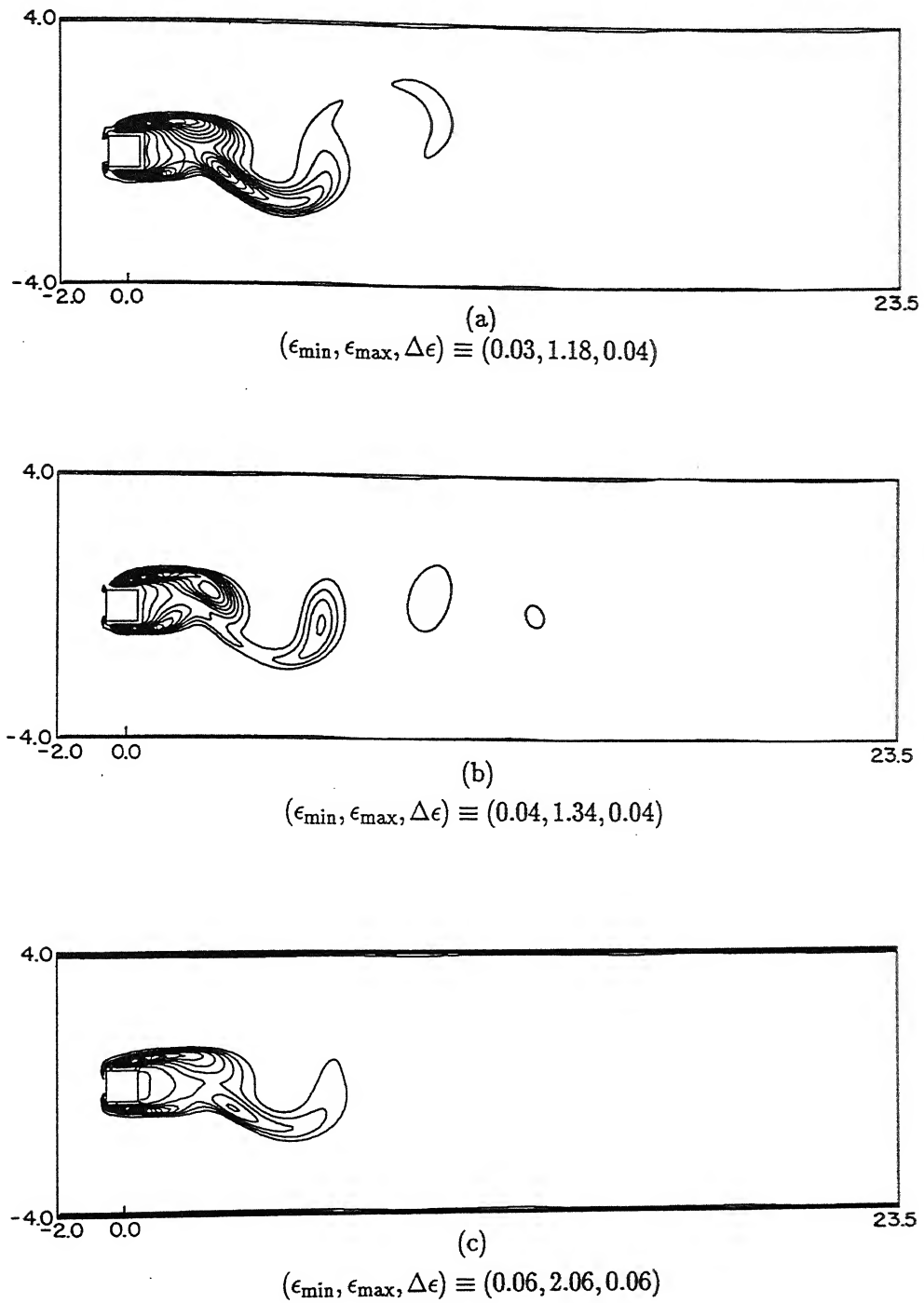


Figure 5.6.9: Instantaneous turbulent dissipation contours: (a) standard $k-\epsilon$ (b) KaLa and (c) RNG $k-\epsilon$.

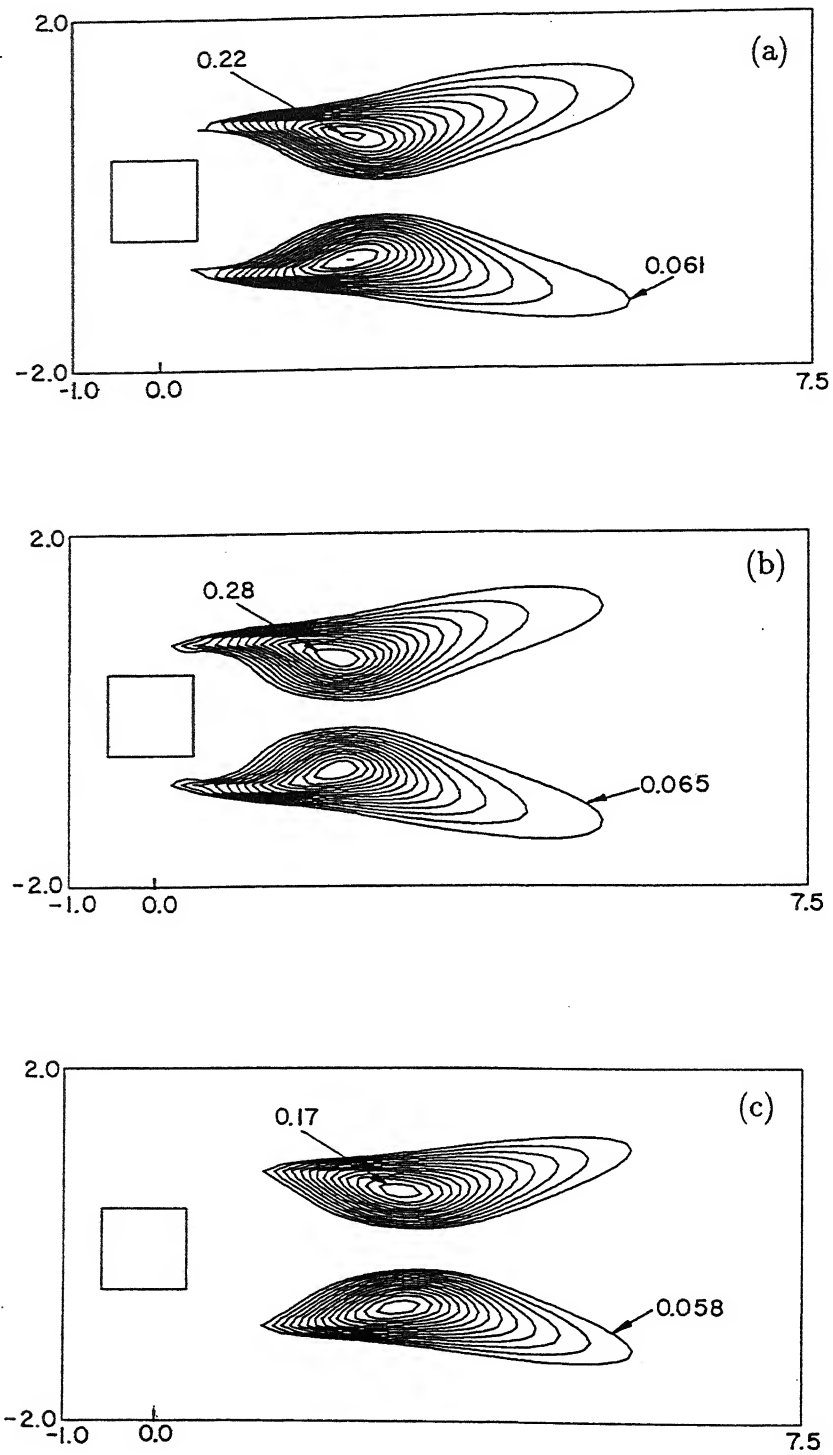


Figure 5.6.10: Contours of the time-averaged streamwise normal stress: (a) standard $k-\epsilon$ (b) KaLa and (c) RNG $k-\epsilon$

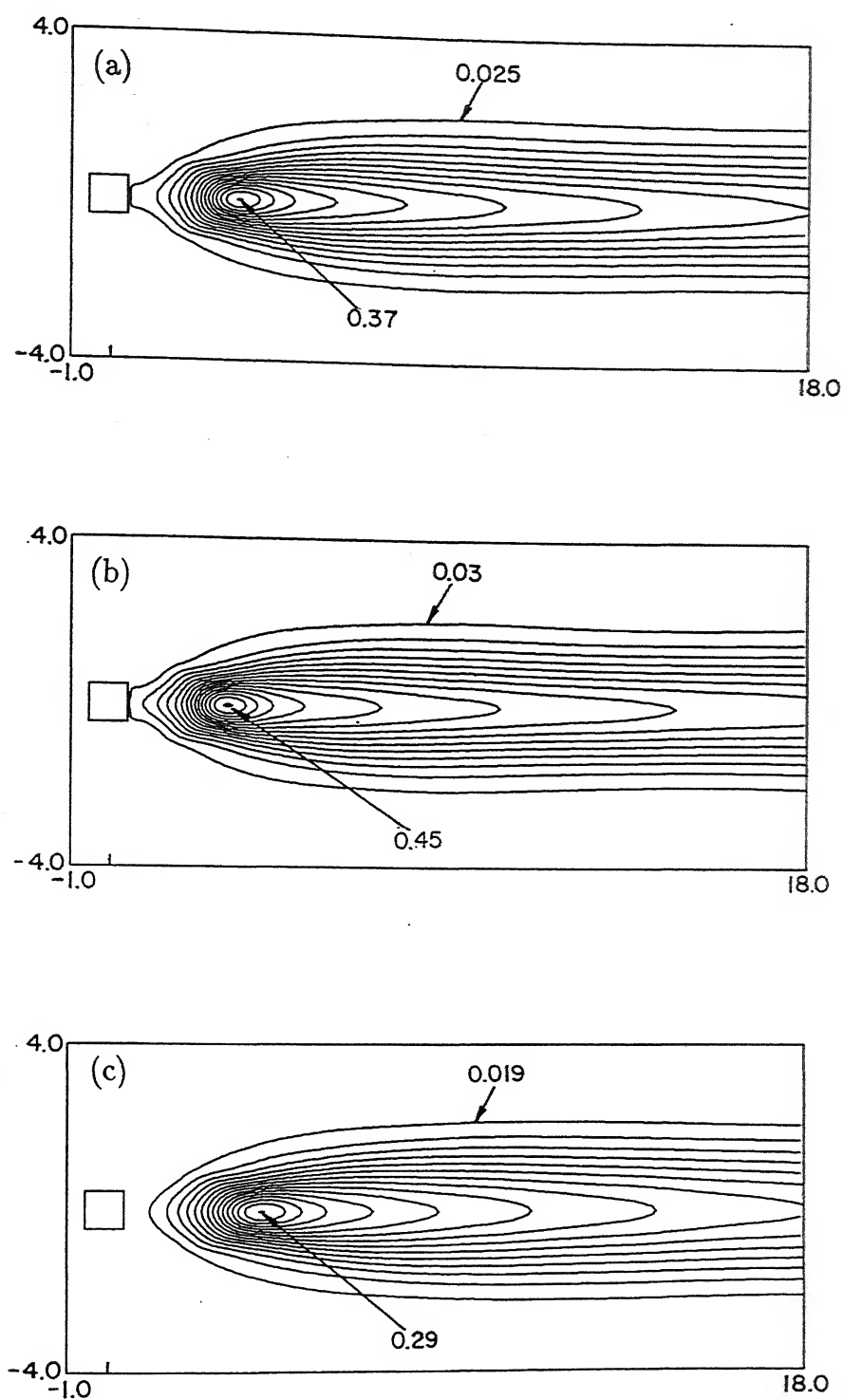


Figure 5.6.11: Contours of the time-averaged transverse normal stress: (a) standard $k-\epsilon$ (b) KaLa and (c) RNG $k-\epsilon$

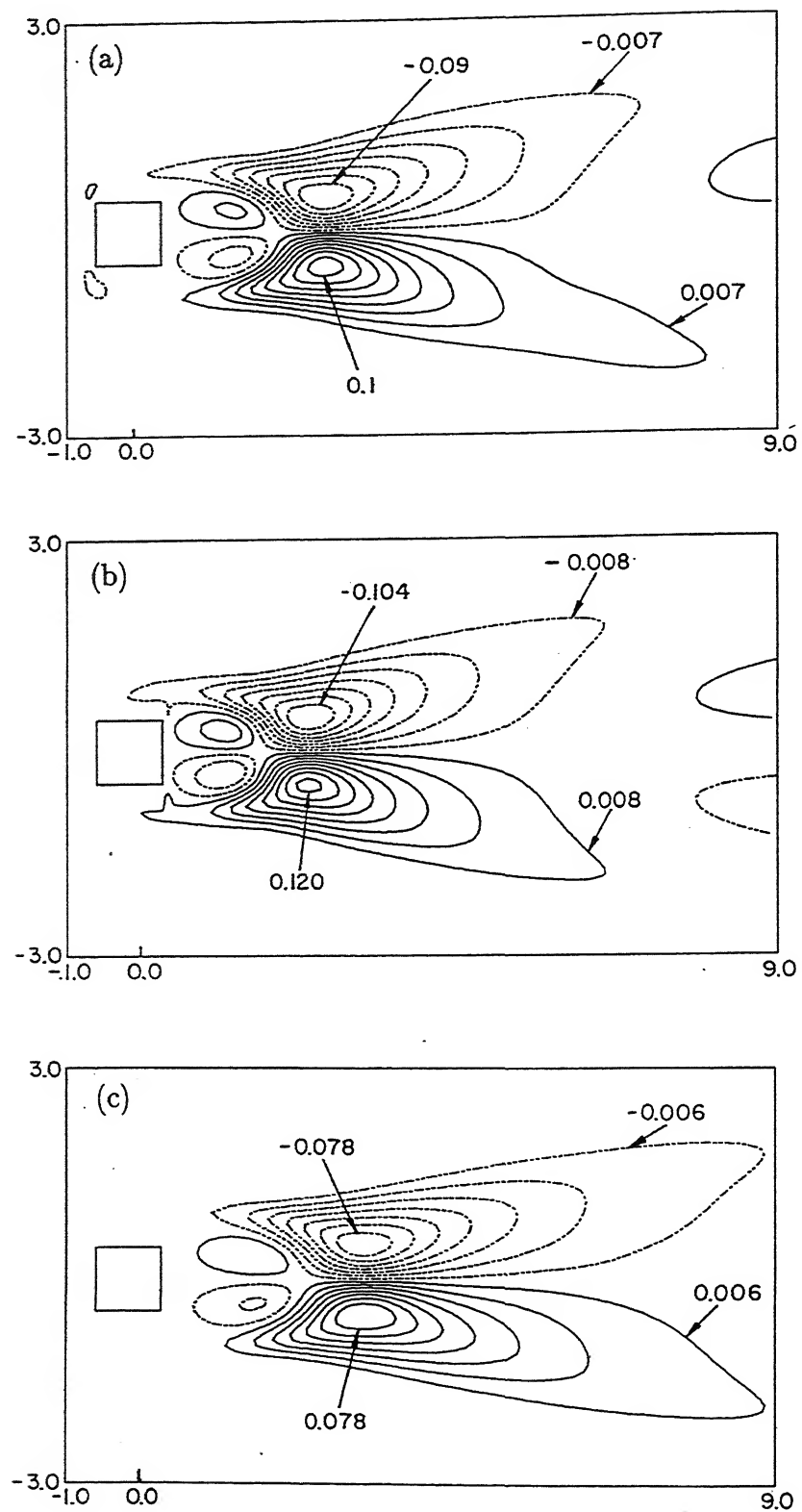


Figure 5.6.12: Contours of the time-averaged shear stress: (a) standard $k-\epsilon$ (b) KaLa and (c) RNG $k-\epsilon$

5.6.4 Contours of time-averaged stresses

The contours of time-averaged streamwise normal stresses ($\overline{u^2}$) associated with the periodic fluctuations are presented in Figure 5.6.10. Each model shows symmetric contours about the wake centerline and predicts double peaks. The peak value of $\overline{u^2}$ calculated from the standard $k-\epsilon$ model is 0.22. The peaks calculated from the KaLa and RNG $k-\epsilon$ models are 0.28 and 0.17 respectively. The distance between the rear end of the cylinder and the location of the maximum of the streamwise normal stress is somewhat greater in the case of RNG $k-\epsilon$ model. The wake width corresponding to streamwise periodic components is greater in the case of the standard $k-\epsilon$ model. The width of the wake envelope due to the RNG $k-\epsilon$ model and the KaLa model are nearly equal.

The transverse normal stresses due to the periodic components of fluctuations contribute positively to the centreline with a single peak for all the models. The location of the maxima follows a trend similar as to the streamwise component. The wake widths of the wake measured using $\overline{v^2}$ are nearly equal for all the models (Figure 5.6.11).

The contours of the quantity \overline{uv} are seen to behave like a shear stress component (Figure 5.6.12). However, as far as the mean flow is concerned this term is dissipative. Hence, the flow of energy is from the mean flow to the turbulence scales but the reverse is not observed. This term has no contribution at the wake centreline. Instead, two peaks of opposite signs on either side of the centreline are to be seen. Thus, the trends for the time-averaged stress contours show similarity with the corresponding patterns in laminar flow.

5.6.5 Closure

Numerical simulation using three turbulence models for the configuration of flow past a square cylinder placed centrally in a channel is reported. The models considered are the standard $k-\epsilon$, KaLa and the RNG $k-\epsilon$. The following conclusion have been drawn in the present work.

1. In terms of engineering parameters such as Strouhal number and lift and drag coefficients, the predictions of the KaLa and the standard $k-\epsilon$ are close to each other, and reasonably close to experiments performed in an unbounded medium. Those of

the RNG k - ϵ are not as close to the experimental values.

2. A detailed comparison in terms of velocity profiles reveals KaLa to have the closest agreement with experiments. This is further reinforced in the centreline profiles of the kinetic energy of the total fluctuations.
3. All the three models show similar instantaneous contours of vorticity. They also reveal interesting vortex-wall interactions, leading to waves moving along each of the walls though with a phase difference.
4. The time-averaged contours of stresses formed from the periodic velocity components are symmetric with double peaks for $\overline{u^2}$, symmetric with a single peak for $\overline{v^2}$ and antisymmetric for \overline{uv} . These trends are identical to what is observed in laminar wakes at a much lower Reynolds number.

5.7 Model-free Computation of High Reynolds Number Turbulent Flow

The results presented in the previous section are based on the k - ϵ model for turbulence. This model has the obvious advantage of not requiring resolution of the velocity and pressure fluctuations and hence the turbulent length and time scales. Clearly the focus of the model is towards extracting the time-averaged and phase-averaged velocity field, turbulence being lumped in the kinetic energy and dissipation variables. The k - ϵ model employed in the present study is two-dimensional.

The k - ϵ approach is not suitable when detailed information is required for the instantaneous three-dimensional velocity and pressure fields. To address this issue, model-free computation of the Navier-Stokes equations has been undertaken in the present work. The computation has been carried out for a Reynolds number of 21400 at which the flow is turbulent in the shear layer, boundary layer and the wake. The computation is model-free in the sense that the governing equations continue to be the original Navier-Stokes equations with no special provision to handle turbulence fluctuations. The spectra of length and time scales are handled by grid refinement on one hand and higher order finite differencing on the other. In this sense, the model-free computation is similar to DNS, except that the algebraic problem is generated not by the spectral method but by finite differences. Using model-free computing, the three-dimensional instantaneous flow field at a relatively high Reynolds number has been characterized in the present study.

The overall geometry considered for computation is essentially similar to the one in Section 5.2. The associated initial and boundary conditions are identical to those considered in Section 5.2. Instead of the hybrid scheme, the advection terms have been discretized using the third order Kuwahara scheme (Kawamura *et al.*, 1986). Second order central differencing has been retained for the diffusive terms. Time marching is accomplished by the second order Adams-Bashforth method. No wall function treatment has been used for any of the runs. To establish grid independence, four different grids of increasing fineness have been considered (Runs 1-4). The results of grid independence study are summarized in Table 5.7.1. The time step used for the first three runs (Run 1, Run 2 and Run 3) is 0.007 and for the last run (Run 4) it is 0.004. The time-averaged flow field is obtained by averaging the flow field over 12-17 cycles.

The flow past a square cylinder has been simulated using higher order spatial as well as temporal discretization at a Reynolds number of 21400. The relevant dimensions related to geometry as shown in Figure 1.3 are $B=1.0$, $L_a=6.0$, $L=20.0$, $H=10.0$ and $A=6.0$. Four grid sizes of progressively increasing fineness have been considered and the grid independence study has been carried out. The summary of grid independence study is presented in Table 5.7.1.

5.7.1 Integral parameters

Table-5.7.1 shows different computations using grids of varying refinement and the corresponding integral parameters, namely the drag and lift coefficients, rms values of the drag and lift coefficients, Strouhal number and the mean recirculation length. The table also shows the experimental data of Lyn *et al.* (1995) and the LES results of Wang *et al.* (1996). It can be seen that the time-averaged drag coefficients obtained by various grids are close. The rms values of the drag coefficient however vary significantly. The time-averaged and the rms values of the drag coefficient are higher in model-free computation compared to the experiments of Table-5.7.1. The rms values of the lift coefficient for the various runs are also higher for the present simulations. The Strouhal numbers for the different grids of the present computation show a small scatter about a value of 0.158 but are higher compared to the experiments and LES results. The possible explanation for the discrepancy between numerical computations and experiments could be (i) the blockage in the present study is considerably higher and (ii) there is inadequate grid points near the obstacle to resolve the steep gradient associated with the near wall flow. The blockage in the present study is 10% whereas the blockages are 7%, 13% and 5% in Lyn *et al.* (1995), Durão *et al.* (1988) and Wang *et al.* (1996) respectively. The higher turbulence level (=8%) in the work of Durão *et al.* (1988) leads to a smaller Strouhal number though it has higher blockage. The mean recirculation length (l_r) computed in the present study is a minimum for Run 3 (=1.12) and maximum (=1.35) for Run 1. These values match well with the range 1.33-1.38 recorded in experiments.

The grid independence study has also been extended to the time-averaged as well as turbulent flow field. Figure 5.7.1(a) shows the comparison of the time-averaged streamwise velocity profile at an axial location $x=1.5$ for the Runs 1, 3 and 4. All the three runs show a similar qualitative trend and the recovery of streamwise velocity in the transverse

Table 5.7.1: Comparison of model-free computations with experiments and LES

Calculations	Grid Sizes	$\overline{C_L}$	C_L'	$\overline{C_D}$	C_D'	S	l_r
Run 1	178×80×22	-0.01	1.54	2.62	0.12	0.158	1.35
Run 2	218×104×22	0.03	1.55	2.59	0.16	0.159	1.17
Run 3	218×104×32	-0.01	1.45	2.58	0.13	0.159	1.12
Run 4	240×130×32	0.03	1.40	2.65	0.13	0.158	1.30
LES							
Wang <i>et al.</i> (1996)		-0.03 - 0.06	1.23 - 1.48	2.07 - 2.67	0.09 - 0.27	0.13 0.13	0.89 - 1.26
Experiments							
Lee (1975)				2.05	0.23		
Cheng <i>et al.</i> (1992)			0.6	1.9-2.1	0.2		
Durão <i>et al.</i> (1988)						0.138	1.33
Lyn <i>et al.</i> (1995)						0.132	1.38

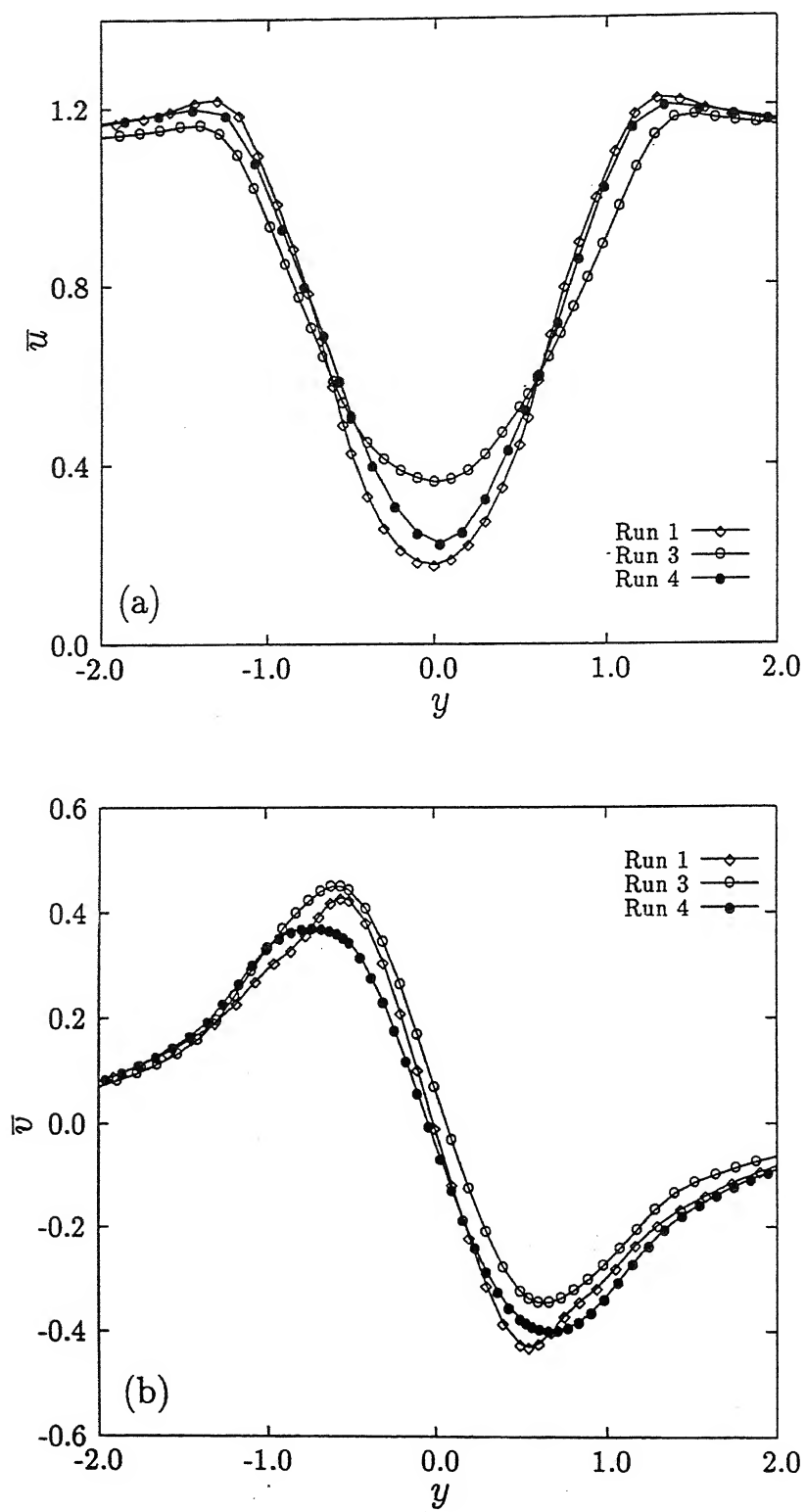


Figure 5.7.1: for caption see next page

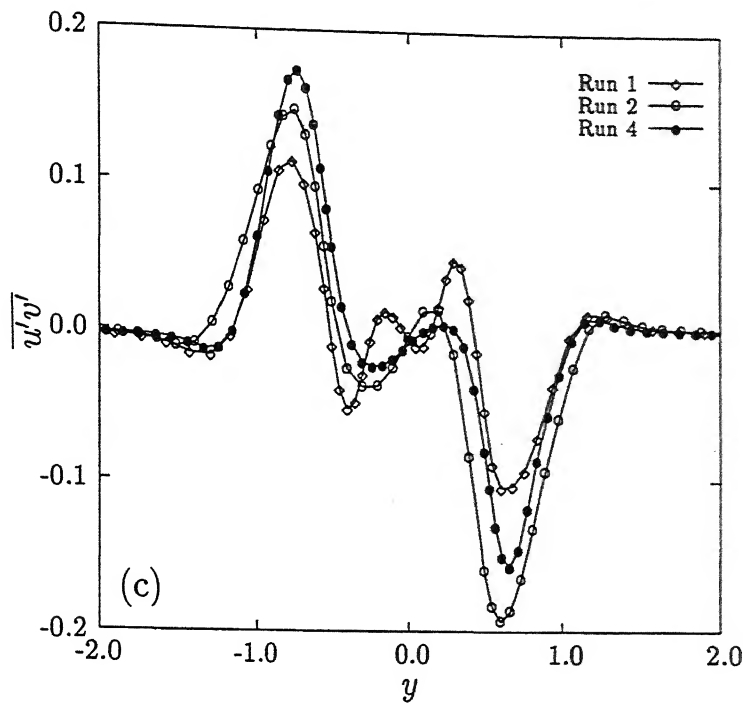


Figure 5.7.1: Time-averaged profiles of (a) streamwise velocity at $x=1.5$ (b) transverse velocity at $x=1.5$ and (c) shear stress at $x=1.0$.

direction. However, the centreline velocity differs for different grid sizes. A possible reason is that in the turbulent mixing zone ($-0.5 < y < 0.5$) the velocity is sensitive to grid size as both production and dissipation are dominant along the wake centreline. The transverse velocity profile is depicted in Figure 5.7.1(b) at a streamwise location $x=1.5$. Runs 1, 3 and 4 show a closer match compared to the streamwise velocity. The entrainment from both sides of the centreline of the wake is related to the centreline recovery of the streamwise velocity. It is clear that larger the entrainment, the higher the recovery rate. Figure 5.7.1(c) compares the turbulent (total) shear stress profiles at a location $x=1.0$ for Runs 1, 2 and 4. Run 1 shows a different variation compared to 2 and 4 in the central zone of the wake *i.e.*, mixing region. Otherwise, all the runs show a qualitative similar trend. Since the flow is shedding dominated, the double-peak antisymmetric variation of the shear stress is to be anticipated. There is no basis, however for additional peaks near the wake centre unless the location falls with the recirculation bubble¹. In Figure 5.7.1(c) it is likely that $x=1$ is such a location. Thus, the multiple peaks close to $y=0$ are justified.

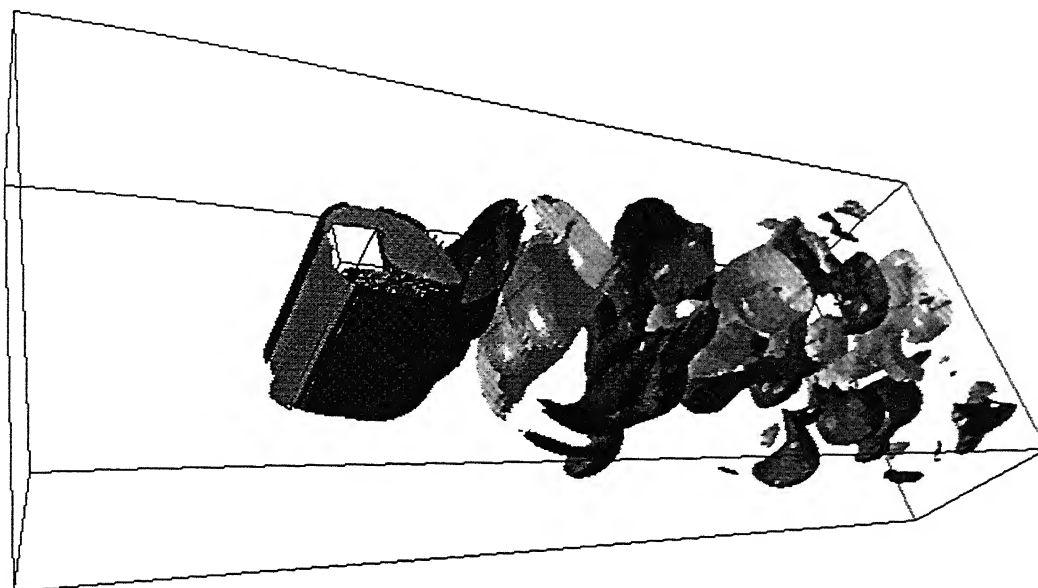
¹In the recirculation bubble, four peaks including the maximum and the minimum are to be expected; outside the number of peaks is 2.

In Runs 1 and 2, the peaks are abnormally large, while Run 4 shows a smooth variation. A shift of the data towards the prediction of Run 4 with grid refinement is also visible.

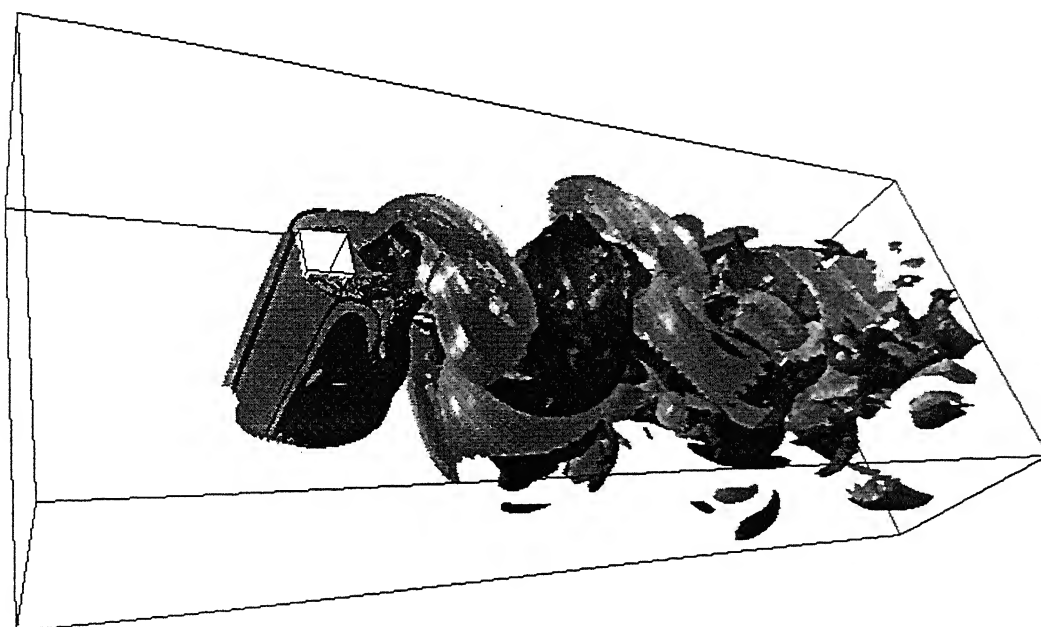
The three-dimensional iso-surfaces of spanwise vorticity ($\omega_z = \pm 0.5$) for two different runs (Run 2 and Run 4) are shown in Figures 5.7.2(a-b). Both the figures show a prominent Kármán vortex street. Run 4 shows an irregular turbulent far-wake compared to Run 2. These phenomena can be explained since the resolved length scale is much smaller in Run 4 owing to a finer grid, the far-wake having the appearance of turbulent flow. Figures 5.7.3(a-b) show the three-dimensional distribution of streamwise secondary vorticity ($\omega_x = \pm 0.5$) for the two runs. The two plots show that there is a similarity between the two distributions but the strength of the secondary vortex is greater in Run 2, owing to the limitation of a partially resolved flow field. Results given below pertain to the finest grid, namely Run 4.

5.7.2 Time-averaged flow field

The time-averaged velocity field is obtained by averaging the flow field over 15-17 cycles. This averaging period was found to be good enough for all the velocity components. In the following discussion, the time-averaged data obtained from model-free computation has been compared with the experiments of Lyn *et al.* (1995) and the LES results of Wang *et al.* (1996). Such a comparison with the experiments was presented in the Section 5.6 for the k - ϵ model. It is worth observing that the experimental data is truly a global time-average. In contrast, the predictions of the k - ϵ model are to be viewed as phase-averages from which the global time-average is to be determined as a second step. The LES results quoted in this section are also global time-averages. The model-free calculations predict the instantaneous flow field comprising of the global average, periodic components and the incoherent turbulent fluctuations. Each of these quantities can be recovered selectively by using suitable techniques. A further point of comparison is the following. The experiments had a low blockage and high upstream turbulence. The LES calculations had low blockage and low aspect ratio and zero upstream turbulence level. In the present study, the blockage and aspect ratios are moderate and zero upstream turbulence level. While LDV measurements suffer from the need for very long averaging signals, particularly in water, LES has potential drawbacks arising from periodicity conditions on the spanwise surfaces and grid restrictions. These factors must be considered while evaluating the three

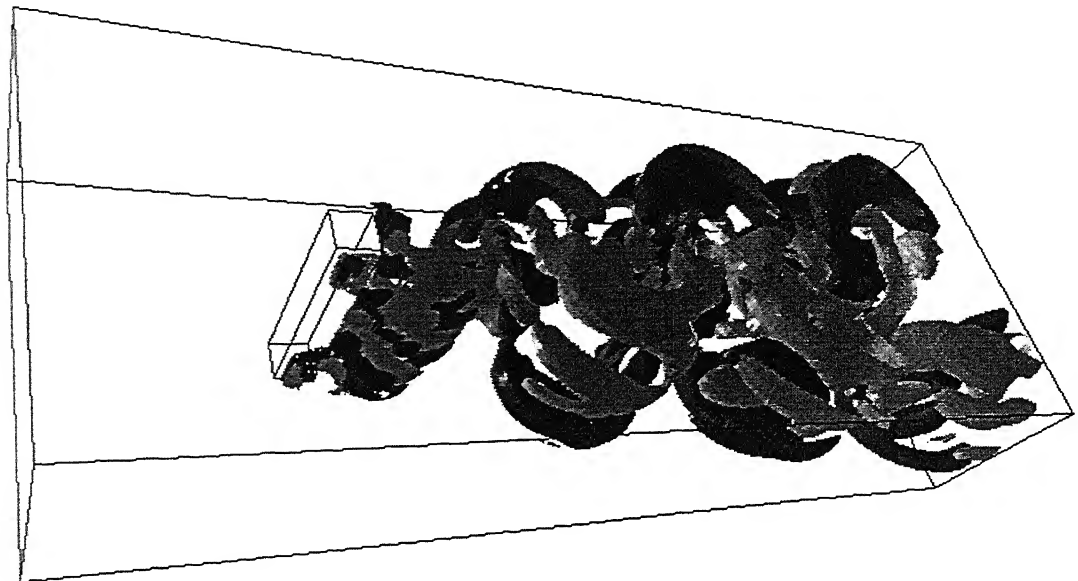


(a)

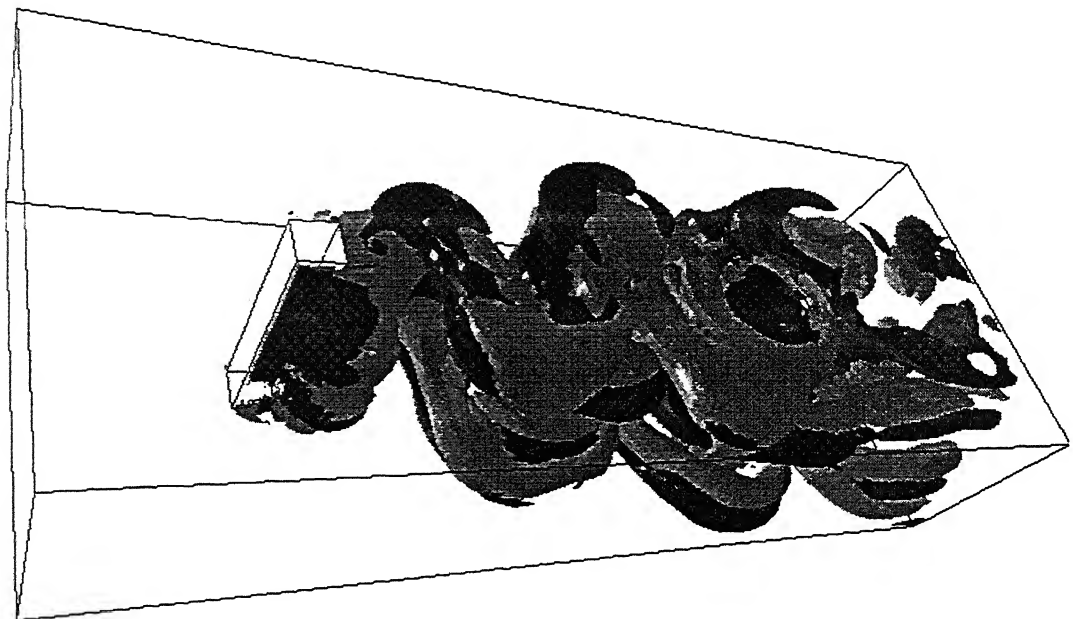


(b)

Figure 5.7.2: Iso-surfaces of spanwise vorticity ($\omega_z = \pm 0.5$): (a) Run 2 and (b) Run 4. The spanwise vorticity in the far-wake for Run 4 shows broken small-scale structures compared to Run 2 where the large-scale coherent structures are seen.



(a)



(b)

Figure 5.7.3: Iso-surfaces of streamwise vorticity ($\omega_x=\pm 0.5$): (a) Run 2 and (b) Run 4. There is no difference between the two figures except the arrangement of the vortices in the spanwise direction.

sets of data.

Figure 5.7.4(a) shows the comparison of the time-averaged streamwise velocity profile at four streamwise locations, namely $x=0.0$, 1.0, 1.5 and 4.0 with the experimental results of Lyn *et al.* (1995) and the LES results of Wang *et al.* (1996). The results at $x=0.0$ reveal good comparison except near the boundary of the obstacle where LES predicts a stronger flow. The present results are seen to be in better agreement with experiments. At $x=1.0$ and 1.5, all the results are close to one another. At $x=4.0$, the results due to present computation are higher compared to the experiments and LES. The reason may be higher blockage in the present study leading to a higher velocity recovery rate. The comparison of the transverse component of the time-averaged velocity has been depicted in Figure 5.7.4(b). The velocity profile at a location $x=1.5$ has higher peaks in the present study, once again to be attributed to the higher blockage. Figure 5.7.4(c) shows the centreline recovery of the streamwise component of velocity for the three approaches. The recovery rate of the present work matches well with the experiments and LES. However, the asymptotic value of the recovered velocity is somewhat higher which oscillates before attaining an asymptotic condition.

5.7.3 Time-averaged turbulence statistics

The turbulence statistics referred here is for the total fluctuations (periodic + random) with respect to the time-averaged field. The comparisons has been made with the finest grid (Run 4). This is important because the energy cascading mechanism and the major scales of the flow need to be captured. The turbulence fluctuations have also been averaged over 15-20 cycles. The profiles of the streamwise normal stress $\overline{u'^2}$ have been depicted in Figures 5.7.5(a) for four different locations, namely $x=0.0$, 1.0, 1.5 and 4.0. At the first three locations, the peak values are overpredicted. However, at the location $x=4.0$ a good overall match is seen. Figure 5.7.5(b) illustrates the transverse normal stress $\overline{v'^2}$ profile at four locations, $x=0.0$, 1.0, 1.5 and 4.0. The fluctuations at the first two locations ($x=0.0$ and 1.0) show excellent agreement with the experiments and the LES results. The other two locations overpredict the fluctuations and give higher peaks compared to the experiments and LES. Higher blockage in the present simulation can lead to higher fluctuations for this component of velocity and is a possible explanation for the discrepancy. The turbulent shear stress $\overline{u'v'}$ profiles for four stations, namely $x=0.0$, 1.0,

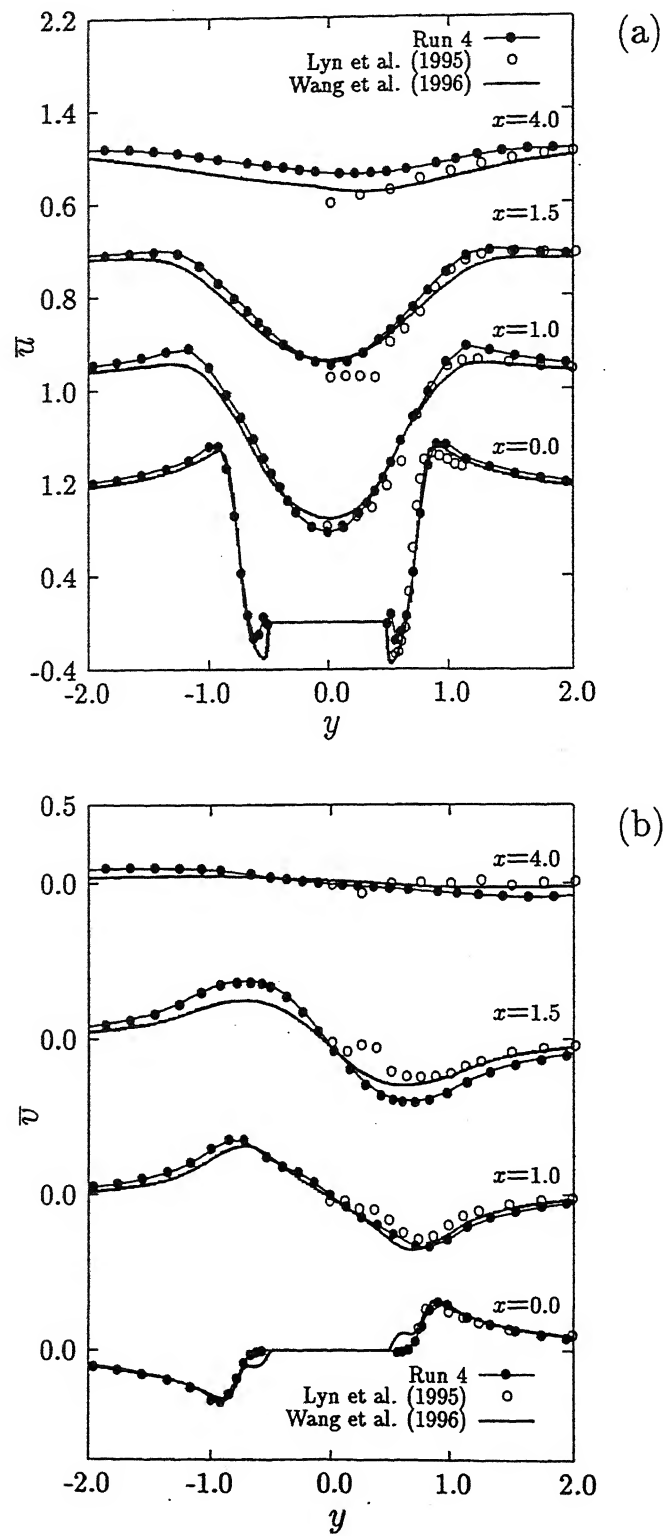


Figure 5.7.4: for caption see next page

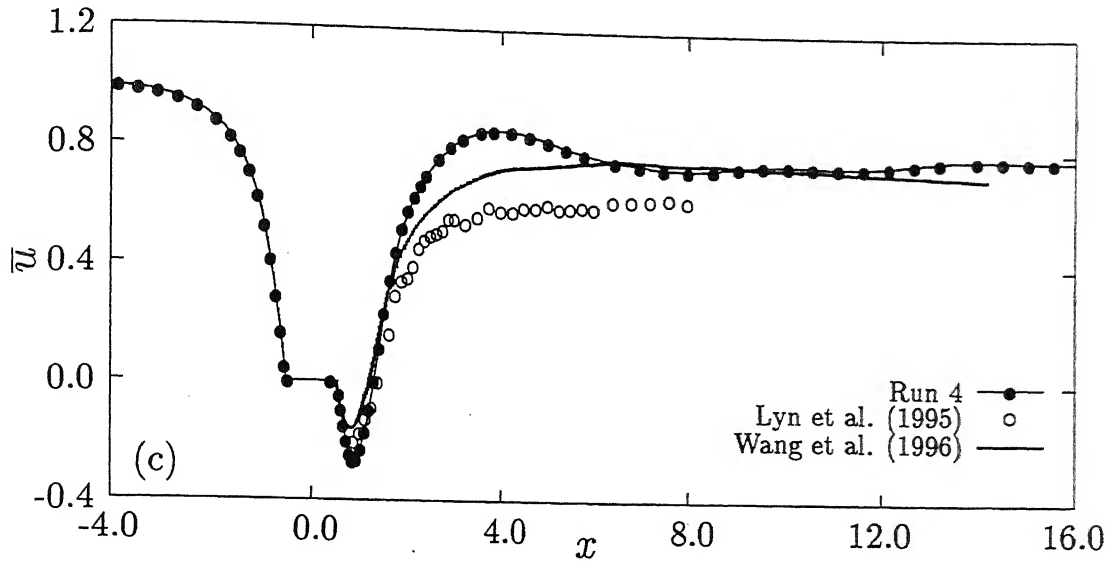


Figure 5.7.4: Comparison of the time-averaged flow: (a) streamwise and (b) transverse velocity at locations $x=0.0$, 1.0 , 1.5 and 4.0 and (c) centreline recovery of streamwise velocity. The time-averaged flow field shows very good match except the centreline recovery of streamwise velocity in (c) which shows a small acceleration before attaining its asymptotic value.

1.5 and 4.0 have been shown in Figures 5.7.5(c). The turbulent shear stress is a quantity that is quite difficult to determine, both in experiments and in computation mainly due to its slow convergence with the length of the signal. This inadequacy has been felt in the present study since data for more than 15-20 cycles could not be handled for the grid sizes considered. The signal lengths considered in experiments as well as LES are reported to be substantially longer. The present results show good agreement with the experiments and LES for x upto 1.5 . At $x=4.0$, there exists considerable mismatch between the model-free computations and the experiments as well as LES. This behaviour can be related to the inadequate number of averaging cycles employed in the present study.

5.7.4 Phase-averaged flow field

Flow past a square cylinder at a high Reynolds number is characterized by the evolution of turbulence in the downstream direction. The coherence of flow is established by vortex shedding, but decreases in the downstream direction. The various components of velocity show different rates at which coherence is lost. Figure 5.7.6(a) shows the sequence of

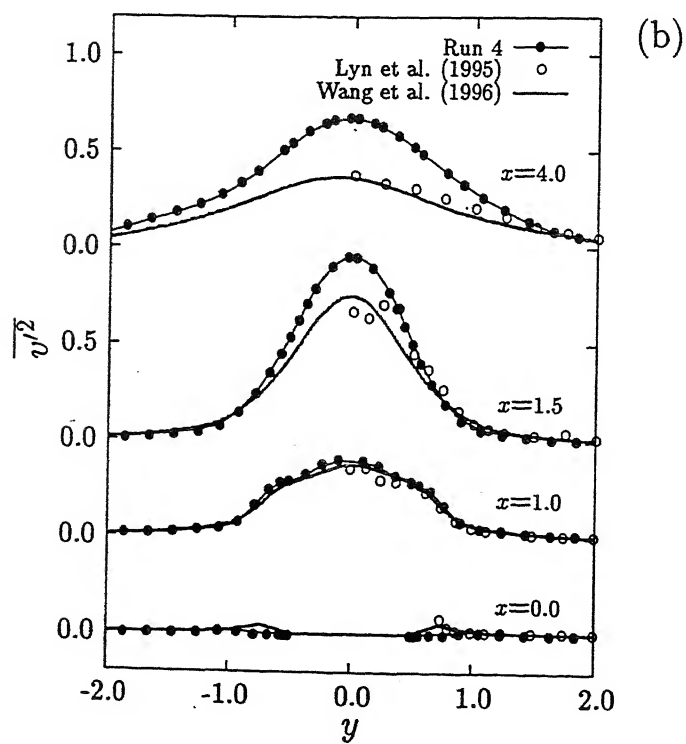
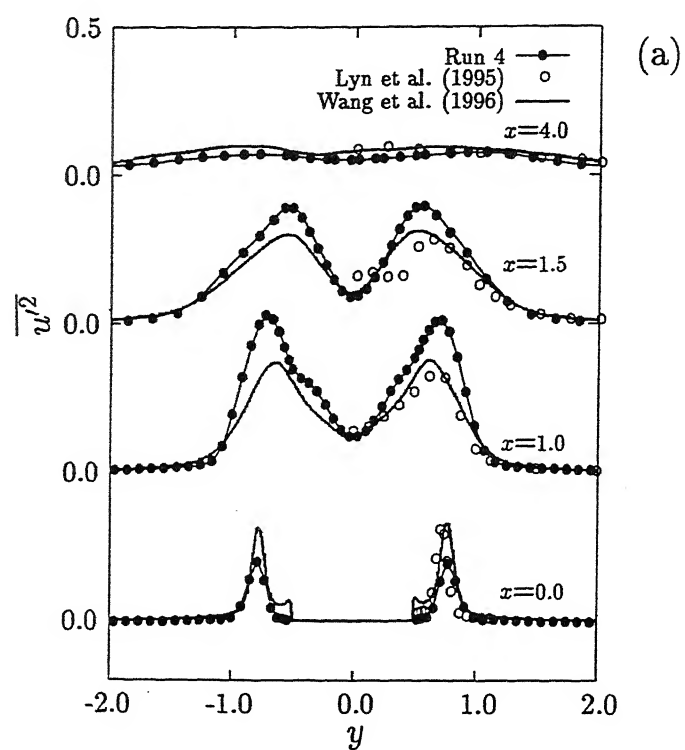


Figure 5.7.5: for caption see next page

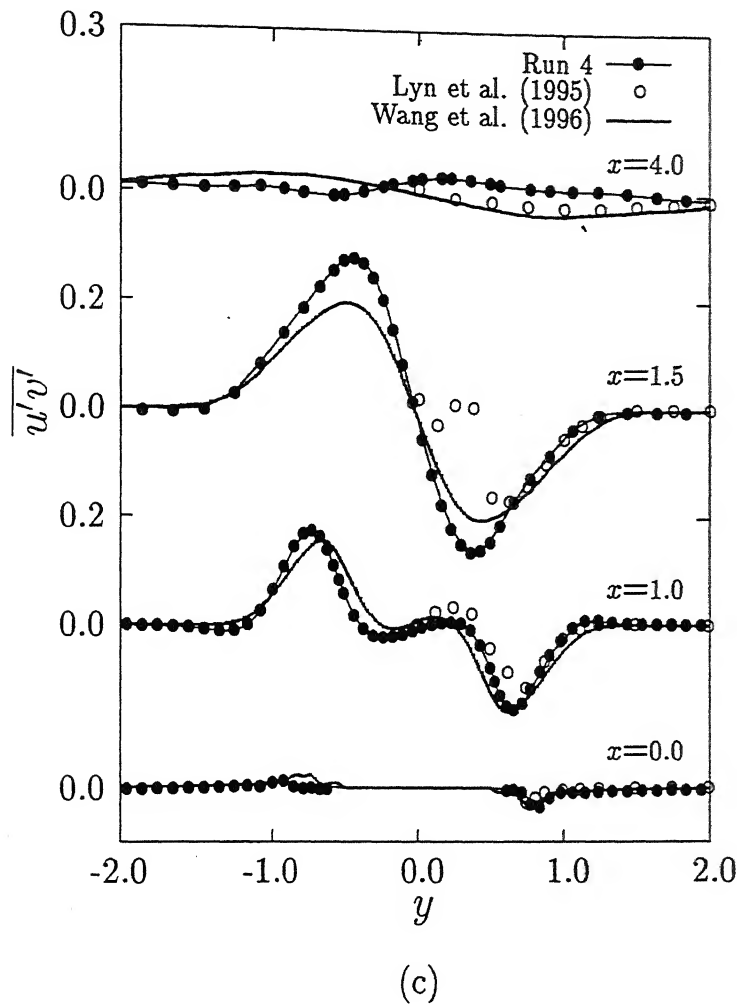


Figure 5.7.5: Comparison of time-averaged fluctuations at locations $x=0.0, 1.0, 1.5$ and 4.0 : (a) streamwise normal stress (b) transverse normal stress and (c) shear stress. The match with the experiments in the base region ($x \leq 1$) is seen to be good whereas the profiles at the spatial locations beyond $x=1.5$ show some differences which may be attributed to the finite blockage in the present computation. The boundary effect on the diverging far-wake causes the fluctuations to grow.

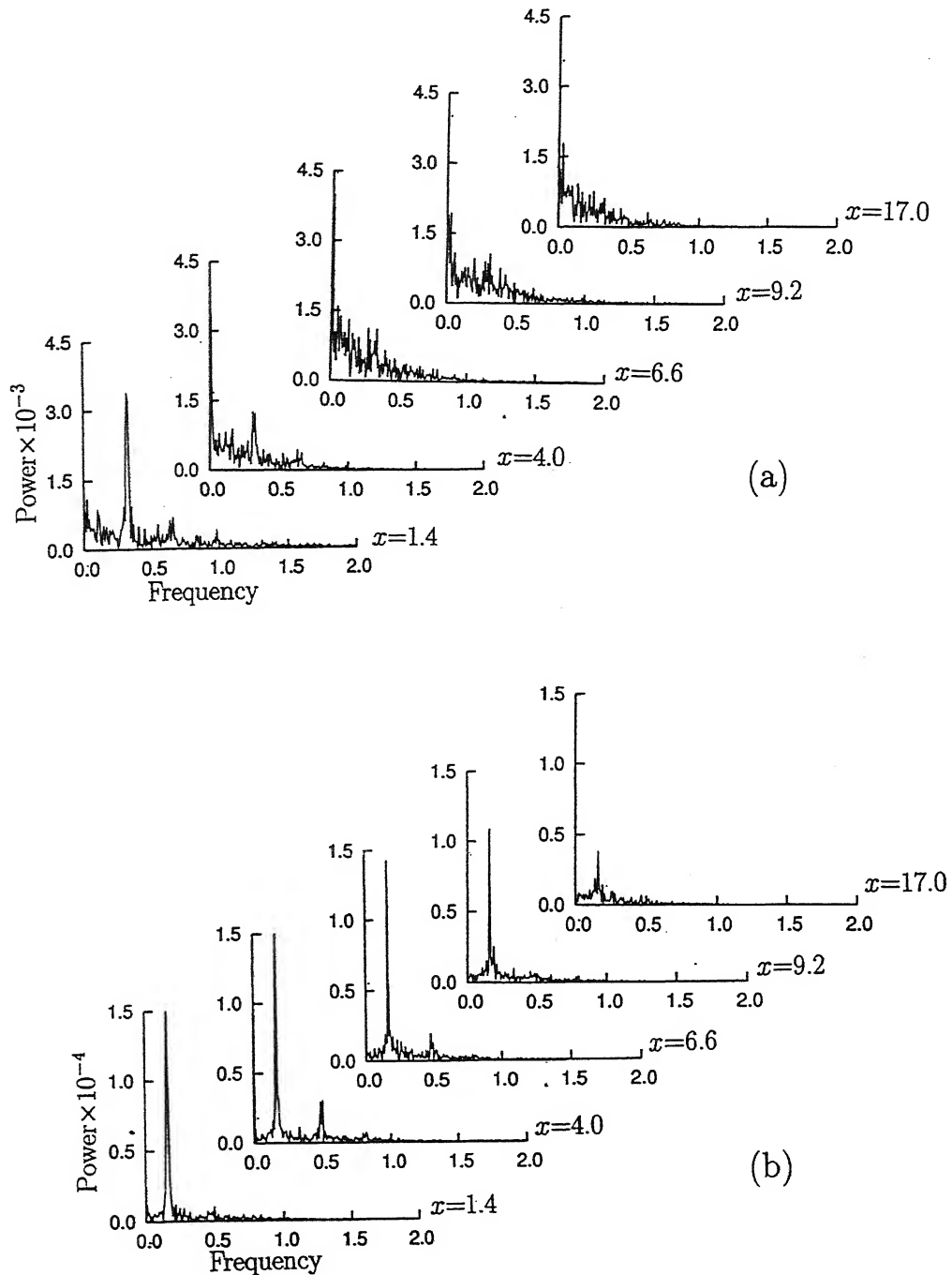


Figure 5.7.6: Spectra at different axial locations: (a) streamwise velocity and (b) transverse velocity. The spectra of u -velocity loses its dominant peak with downstream distances and become broadband signifying the wake becoming developed and turbulent with increasing distance. The spectra of v -velocity show the dominant peak way upto the location $x=17.0$ and reveal that this component of velocity is more coherent than the streamwise component.

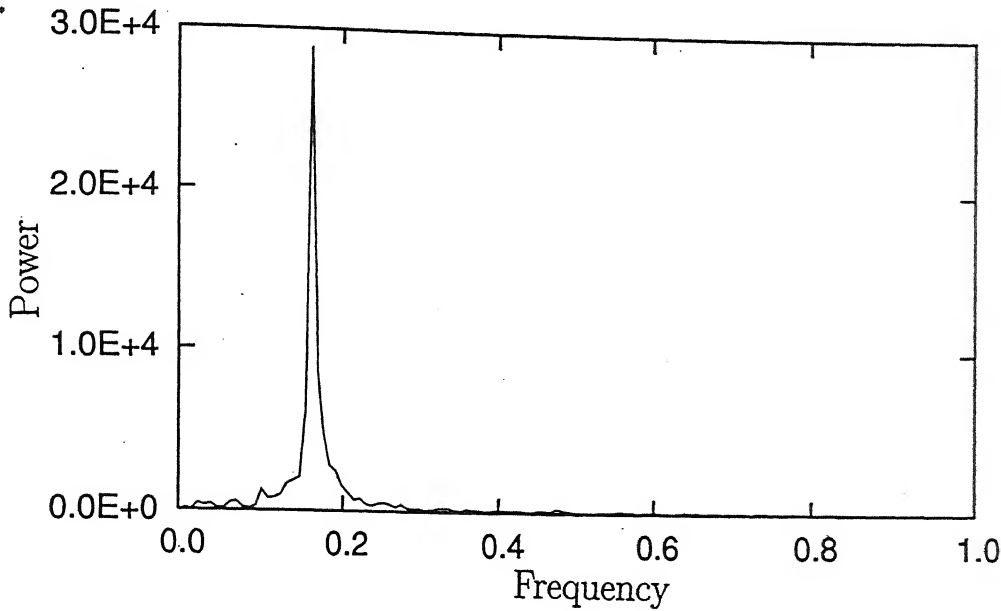


Figure 5.7.7: Spectrum of lift coefficient.

spectra of streamwise velocity at different downstream distances. It is clear that the streamwise velocity even at a location $x=1.41$ is not fully coherent in nature. There are multiple frequencies present at this location although a dominant frequency is seen. The flow field becomes chaotic and fully turbulent beyond $x=4.0$. Therefore, the phase information which is present in the near-wake is lost beyond the intermediate-wake. The spectra of the transverse component of velocity at different x -locations are portrayed in the Figure 5.7.6(b). Unlike the streamwise component, the transverse component of velocity show coherence over a larger distance. Even at a streamwise location of $x=17.0$ the v -spectrum shows a single dominant frequency though other frequencies are also present. Comparing Figures 5.7.6(a) and (b) it can be said that the streamwise component loses the phase information very early compared to the transverse component with increasing downstream distance.

At a high Reynolds number, the three-dimensional random turbulent fluctuations are superimposed on the unsteady periodic motion. The random motion represents small-scales of turbulence and can be simulated by a stochastic model. As discussed in earlier sections, in the wake of a bluff-body flow, the time varying component ϕ (for example, velocity and pressure) may be written as the combination of global mean component $\bar{\phi}$, a periodic component $\tilde{\phi}$ and a random component ϕ'' (Hussain, 1983). In the present

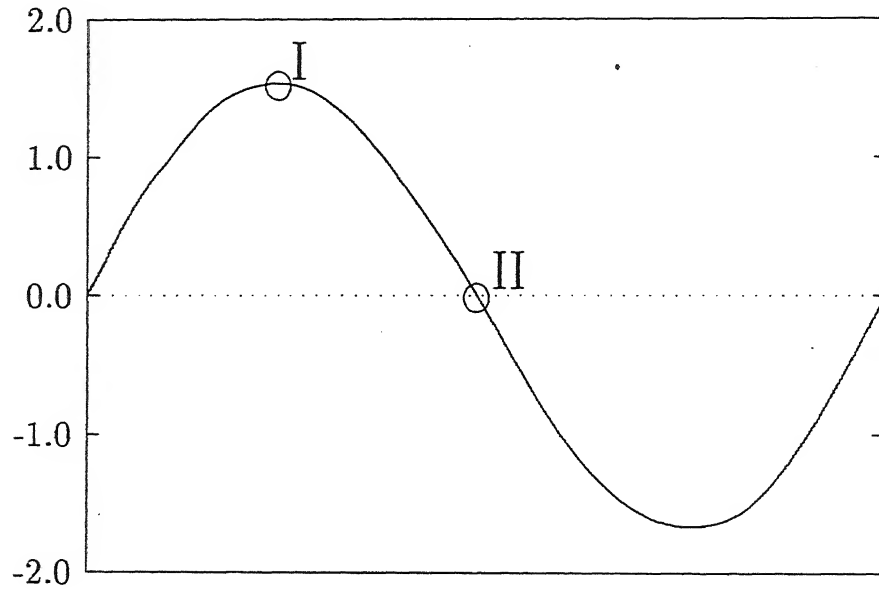


Figure 5.7.8: Two different phases for phase-averaging.

section, the phase-averaging technique has been applied to separate out the coherent ($\tilde{\phi}$) and incoherent (ϕ'') fluctuations downstream of the cylinder. Phase averaging is the method which helps in removing the small-scale universal fluctuations and thus the small-scale structures and retains only the large-scale structures. The large structures are boundary dependent *i.e.*, depend on the geometry of the flow. Phase-averaging in the present work has been carried out over 17 cycles only, in contrast to 1024 cycles in Cantwell and Coles (1983) and 400 cycles in Lyn *et al.* (1995), mainly due to the limitations in the computational resources. The reference signal taken for phase-averaging is that of the lift coefficient. The lift coefficient signal (Figure 5.7.7) appeared to be the most clear compared to others, namely drag coefficient, streamwise and transverse velocities in the near-wake. The spectrum of the lift coefficient resembles the spectrum of the transverse component of velocity in the near-wake. The reason for such a resemblance is that the lift coefficient is governed by the transverse, rather than the streamwise fluctuations.

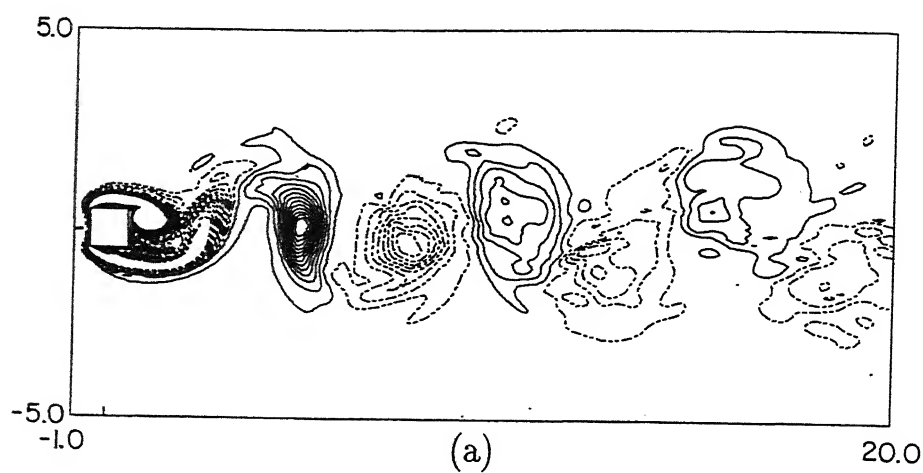
The important factor to be considered while doing phase averaging with reference to any signal is that the reference signal should be clean enough to detect the phases without phase jitter. The reference signal should be able to correlate well with the flow variables at any spatial location. In this respect, the lift coefficient signal has been found to be the most suitable reference for phase-averaging. The phase-averaging technique has been

applied for two different phases as described in Figure 5.7.8. The phase-I corresponds to the maximum in the lift coefficient and the phase-II corresponds to the zero-crossing of the lift coefficient. A note on phase jitter: The vortex shedding frequency is not strictly a constant and shows small fluctuations from cycle to cycle. This is related to the fluctuations in the far-wake and hence is significant at high Reynolds number. The associated physical mechanism is the propagation of pressure information in all directions. The changes in the vortex shedding frequency are higher for a circular cylinder because of the possibility of movement of the points of separation. An immediate consequence of disturbances in the vortex shedding frequency is that lift and the transverse velocity cannot be pure reference signals. The fluctuations in the frequency will in effect corrupt the phase information, resulting in phase jitter. Indeterminacy in the phase naturally causes errors in phase-averaging. These can be partly circumvented by referring to the peaks, valleys and zero crossing of the reference signals rather than the corresponding phase values. This approach has been adopted in the present work¹.

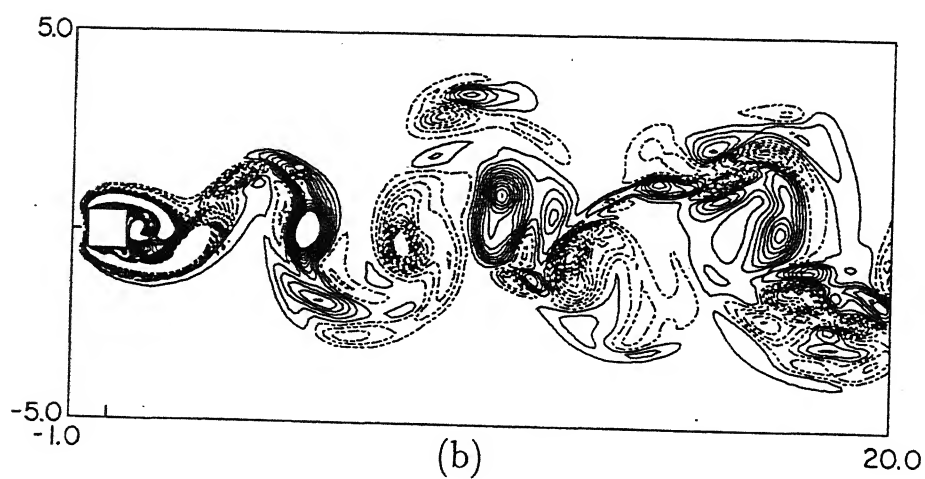
Figure 5.7.9(a) depicts the phase-averaged spanwise vorticity contours for the mid-span ($z=3.0$) at phase-I. It can be seen that the phase-averaged vortices in the far-wake do not show strong coherence as in the near-wake. Figure 5.7.9(b) shows the instantaneous vorticity contours for the plane at the mid-span at phase-I. Though the instantaneous vorticity in the base region shows some similarity to the phase-averaged, the far-wake shows dissimilarity between the two. It is thus evident from Figure 5.7.9(b) that the near-wake is coherent while the far-wake ($x>12$) shows the complex structures of vortex pairing and tearing. At a much higher Reynolds number, the far-wake shows complexity due to the non-linear interactions among different scales generated in the intermediate-wake. Thus, the far-wake shows a wide range of scales analogous to the behaviour of the isotropic turbulence. Figure 5.7.9(c) depicts the phase-averaged pressure contours at a phase-I. The phase-averaged vorticity and pressure are correlated as the pressure minima coincide with the vorticity peaks. Figure 5.7.9(d) shows the phase-averaged spanwise vorticity contours at phase-II. Figure 5.7.9(d) shows similar trend as that of phase-I, the only difference being the streamwise advancement of the flow structures. This advancement is due to phase-II being at a later time than phase-I.

The phase-averaged streamwise normal stresses ($\bar{u}\bar{u}$) at phase-I due to periodic fluc-

¹This technique has a disadvantage: Intermediate values of the ϕ cannot be treated; consequently the global time-average as 'average of all phase-averages', particularly of the periodic and random parts individually cannot be calculated.

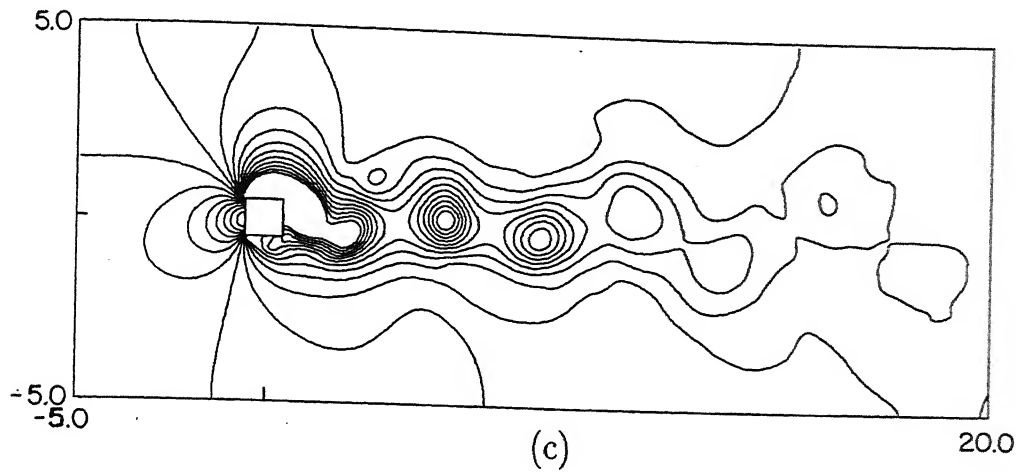


Broken lines: $(\omega_{\min}, \omega_{\max}, \Delta\omega) \equiv (0.12, 3.0, 0.24)$
 Solid lines: $(\omega_{\min}, \omega_{\max}, \Delta\omega) \equiv (-2.76, -0.12, 0.24)$

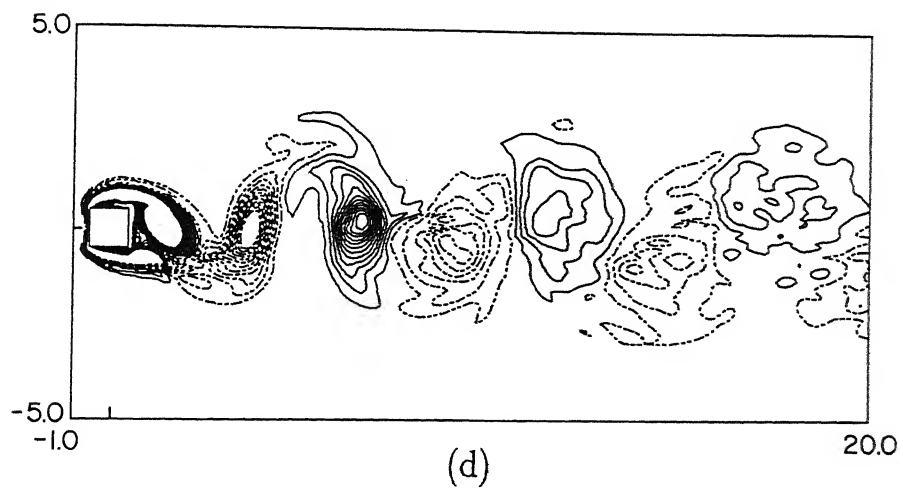


Broken lines: $(\omega_{\min}, \omega_{\max}, \Delta\omega) \equiv (0.12, 3.0, 0.24)$
 Solid lines: $(\omega_{\min}, \omega_{\max}, \Delta\omega) \equiv (-2.76, -0.12, 0.24)$

Figure 5.7.9: for caption see next page



(min, max, increment) \equiv (0.57, 1.9, 0.07)



Broken lines: $(\omega_{\min}, \omega_{\max}, \Delta\omega) \equiv (0.12, 3.0, 0.24)$

Solid lines: $(\omega_{\min}, \omega_{\max}, \Delta\omega) \equiv (-2.76, -0.12, 0.24)$

Figure 5.7.9: Contours of (a) phase-averaged spanwise vorticity (b) instantaneous spanwise vorticity (c) phase-averaged pressure at phase-I and (d) phase-averaged vorticity at phase-II. The phase-averaged field in (a) is more irregular and symmetric in nature compared to its instantaneous field in (b). This is because of the averaging technique which removes most of incoherent fluctuations. The phase-averaged pressure shows good coherence with the phase-averaged spanwise vorticity and proves the correctness of the phase-averaging technique.

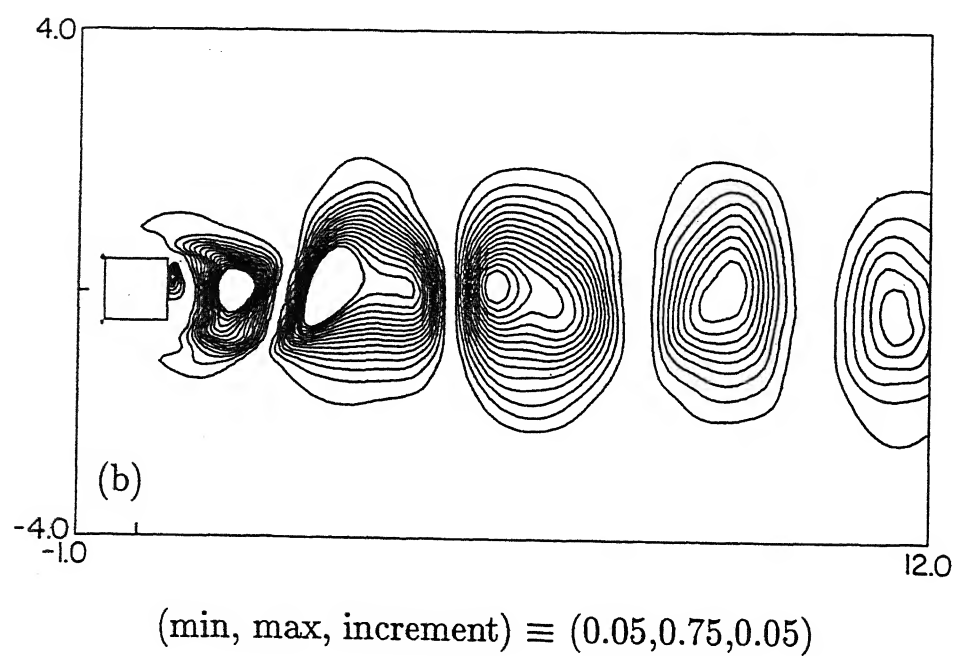
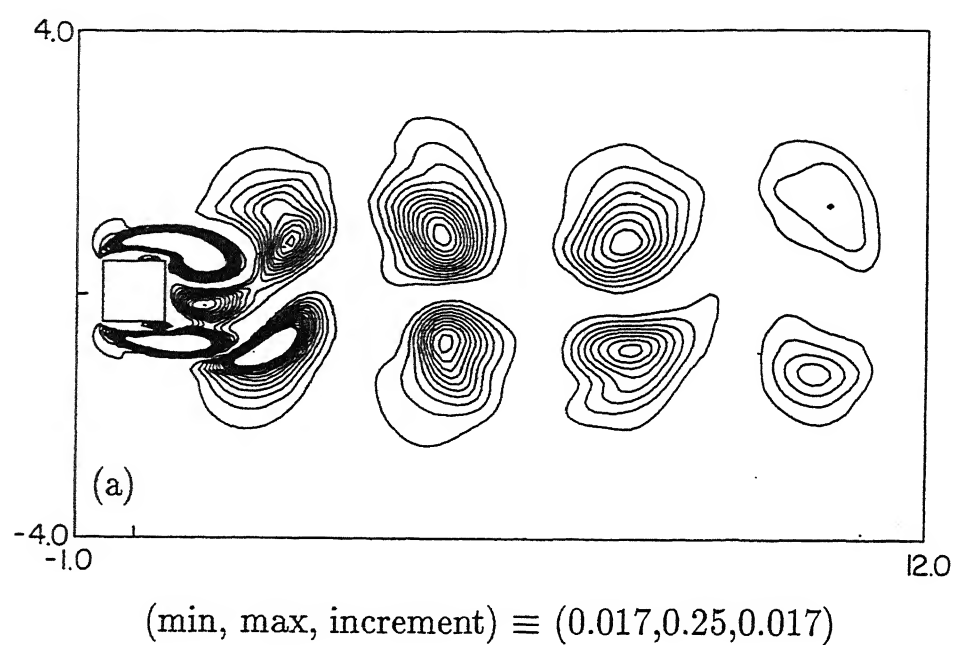
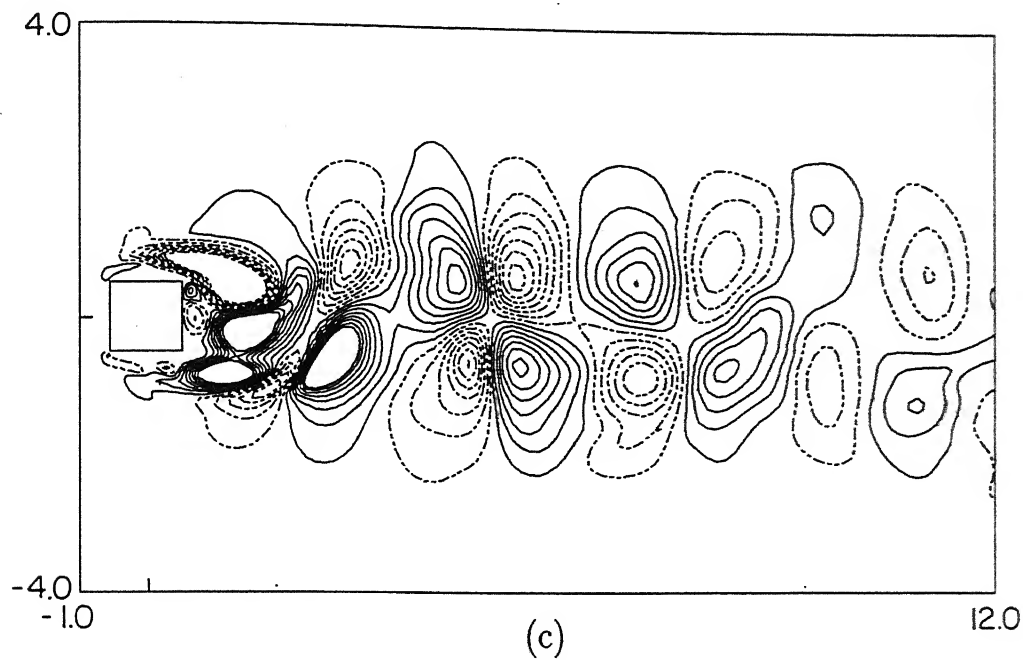


Figure 5.7.10: for caption see next page



Solid lines: (min, max, increment) \equiv (0.013, 0.2, 0.013)

Broken lines: (min, max, increment) \equiv (-0.173, -0.013, 0.013)

Figure 5.7.10: Contours of phase-averaged stresses due to periodic fluctuations at phase-I for the horizontal mid-span ($z=3.0$): (a) streamwise normal stress (b) transverse normal stress and (c) shear stress. These contours look very similar to those for the low Reynolds number ones in Section 5.3. The only difference is seen very near to the wall and these are because of the turbulent boundary layer associated with the high Reynolds number wake.

tuations are presented in Figure 5.7.10(a). The contours of the normal stresses show the local rotation with their peaks above and below of each phase-averaged vortex. The two peaks on each side of the wake centreline correspond to positive and negative values of the periodic component (\tilde{u}) of the fluctuations. Figure 5.7.10(b) shows the transverse normal stresses ($\tilde{v}\tilde{v}$) corresponding to the periodic component of fluctuations. Similar to $\tilde{u}\tilde{u}$, alternating peaks in $\tilde{v}\tilde{v}$ correspond to positive and negative peaks in \tilde{v} . Unlike the streamwise component, the transverse velocity shows a single local rotation about the wake centreline. One important point to be noted is that the local rotation of \tilde{v} is in between two consecutive rows of rotations of \tilde{u} . The maximum of $\tilde{u}\tilde{u}$ corresponds to the minimum of $\tilde{v}\tilde{v}$ and vice versa. Figure 5.7.10(c) shows the spatial variation of shear stresses ($\tilde{u}\tilde{v}$) due to periodic fluctuations. The positive and negative contours are respectively marked by solid and dashed lines. Essentially, two contour shapes are to be demarcated in Figure 5.7.10(c). One is an elongated shape spanning the entire width of the wake and the other is a closed contour on one half of the wake alone. The slope of the elongated contour alternates in sign but is generally has the same magnitude in the flow direction. Many of these features are seen to carry over to the experimental results of Lyn *et al.* (1995), though the magnitude of the dimensionless shear stress increase with Reynolds number. The phase-averaged shear stresses ($\tilde{u}\tilde{v}$) (Figure 5.7.10(c)) are antisymmetric about the wake centreline. These can be explained as being due to the independent influences of a strong and a weak x -momentum fluxes towards and away from the wake centreline respectively. Figure 5.7.10(a) is similar to that reported by Cantwell and Coles (1983) (Figure 5.3.12(b)) for a circular cylinder and Lyn *et al.* (1995) (Figure 5.3.12(c)) for a square cylinder, both at comparable Reynolds number.

It is interesting to note that the wake size defined on the basis of the periodic component is greater than that defined using the time-averaged flow field. This phenomenon can be explained in terms of the greater transport of momentum under unsteady conditions. Figure 5.7.11 shows the phase-averaged three contour plots corresponding to the three Reynolds stresses ($u''u''$, $v''v''$ and $u''v''$) associated with the random components of fluctuations and one contour plot corresponding to the pressure fluctuation at phase-I. Figure 5.7.11(a) shows that the phase-average of the streamwise component is intrinsically noisy. It is evident from Figure 5.7.11(b), that a good correlation exists between the phase-averaged vorticity field (Figure 5.7.9(a)) and the corresponding transverse component of random fluctuation. Both components show that their respective peak values coincide with the peak vorticity or vortex centres. It is interesting to note that the

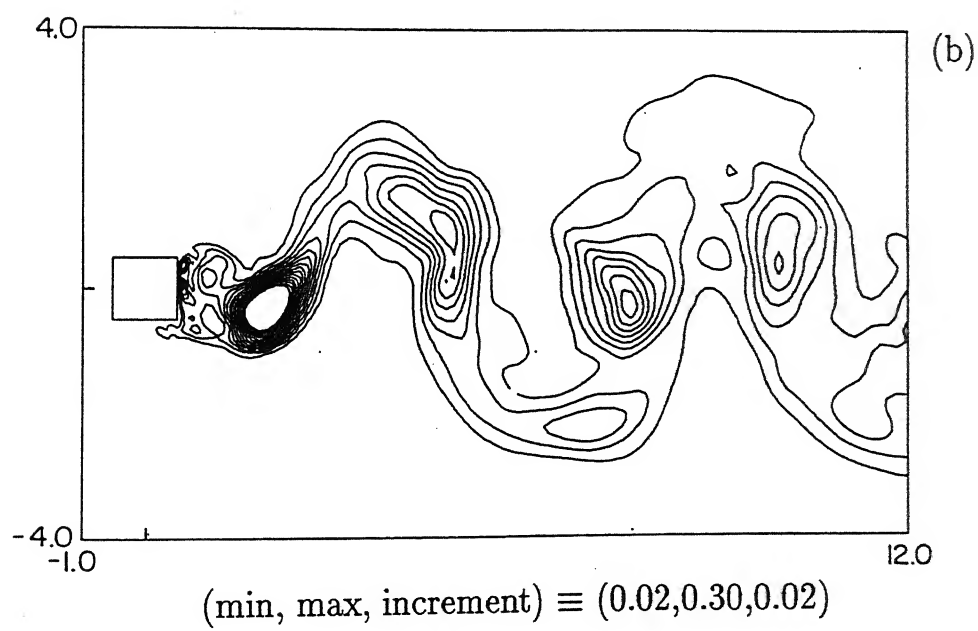
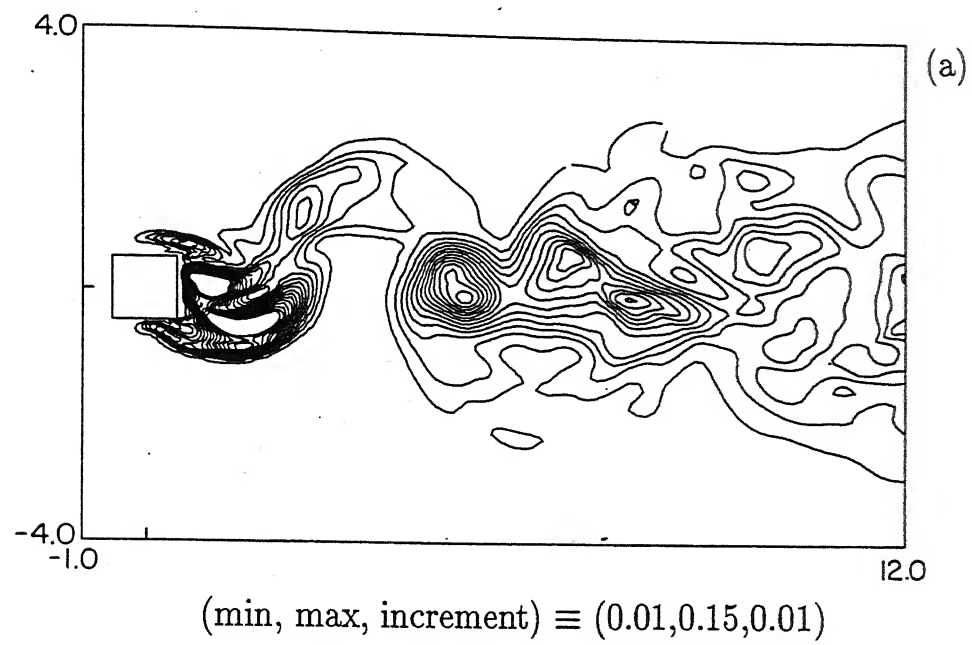


Figure 5.7.11: for caption see next page

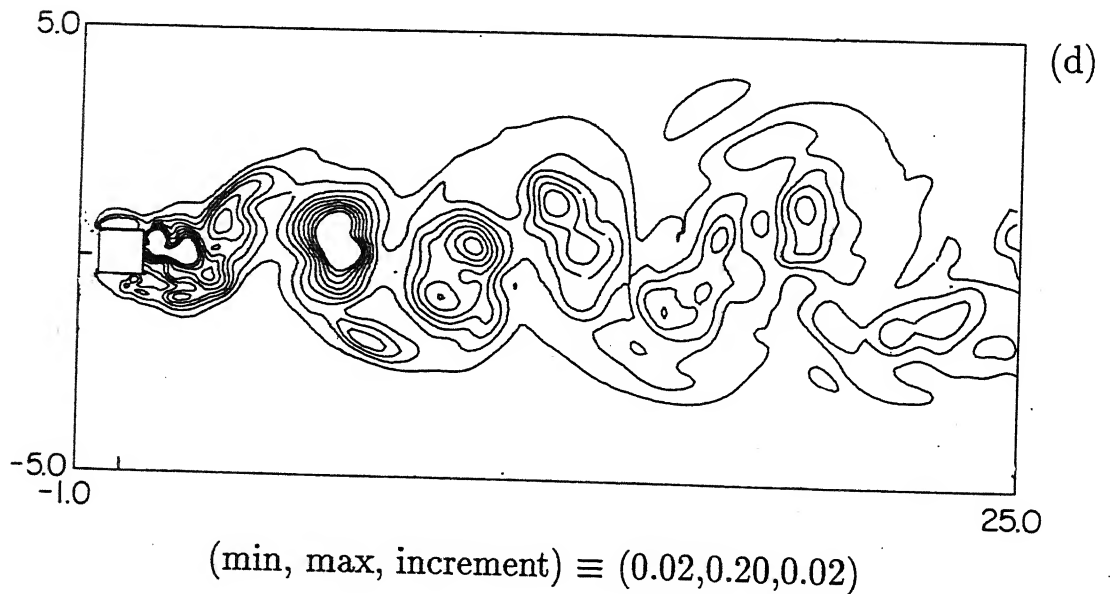
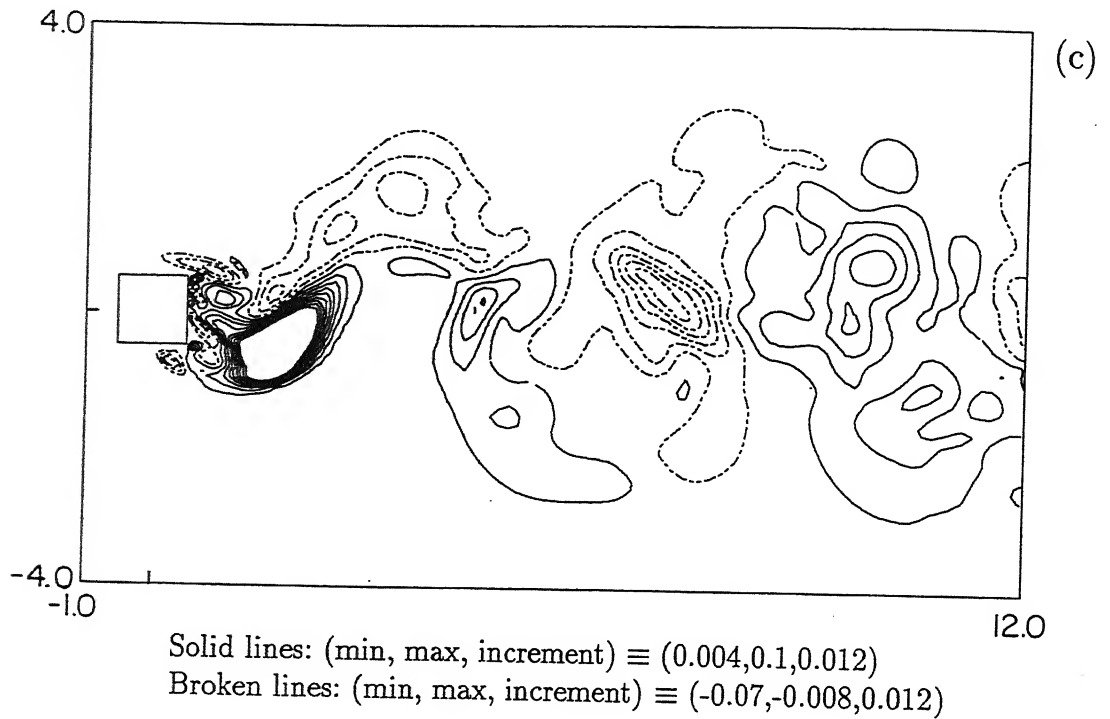


Figure 5.7.11: Contours of phase-averaged (a) streamwise normal stress (b) transverse normal stress (c) shear stress and (d) pressure fluctuations due to random components at phase-I for the horizontal mid-span ($z=3.0$). The transverse normal stress stress shows good coherence compared to the streamwise normal stress and the reason is that the streamwise component more number of frequencies in the far-wake compared to transverse component.

peak values of the two normal stresses of random fluctuations are decorrelated with the peak values of both the normal stresses of periodic components for $x > 2$. The Reynolds shear stress due to the random component has been depicted in Figure 5.7.11(c). Unlike the normal stresses, the shear stress shows alternate arrays of contours. Cantwell and Coles (1983) and Lyn *et al.* (1995) have shown that the peak values of the shear stress due to random fluctuations will occur at the saddle point or very near to it¹. Only the base region shows that the peak of shear stress coincides with the saddle points of the phase-averaged vorticity contours in Figure 5.7.9(a). The streamwise locations $x > 2$ do not show such a correlation. Double peaks can be associated with each sign of the shear stress contours. From Figure 5.7.11(c), it is quite evident that one peak coincides with the saddle while the other coincides with the centre (point of peak vorticity or a closed streamline). The above discussion and figures show that the variations of the random components largely depend on the coherence of the phase-averaged flow. The generation of the random components are higher where there is higher shear in the coherent field. Figure 5.7.11(d) shows contours of the random pressure fluctuations. The centres of the contours coincide with the vorticity centres. Unlike the periodic component it shows peak values at the vortex centres. This means that the random pressure fluctuations are the highest at the vortex centres where the production of kinetic energy takes place. Hence random fluctuations of pressure are correlated with the phase-averaged vorticity contours of Figure 5.7.9(a).

The comparison between the streamwise variation of periodic and random fluctuations have been brought about by comparing their relative maximum magnitudes at phase-I. Since the comparison has been made at a single phase it was not possible to compare only the maximum values of the quantities as the vortices travel downstream over a number of phases within a cycle. But the present comparison also shows the trends which would have been established with a large number of phases in a cycle. Figure 5.7.12(a) is a comparison between the streamwise normal stresses due to periodic ($\bar{u}\bar{u}$) and random ($u''u''$) fluctuations. The region very near the cylinder (within the vortex formation zone) the periodic fluctuations are very high compared to the random fluctuations. But the two values are comparable in the intermediate-wake. The far-wake reveals higher random fluctuations compared to the periodic. Lyn *et al.* (1995) showed that after a dimensionless distance of 2 units, the random component resulted in higher fluctuations compared to the periodic fluctuations. The possible reason for the higher value of the

¹A saddle point is one of zero vorticity or where the intersection of streamlines takes place.

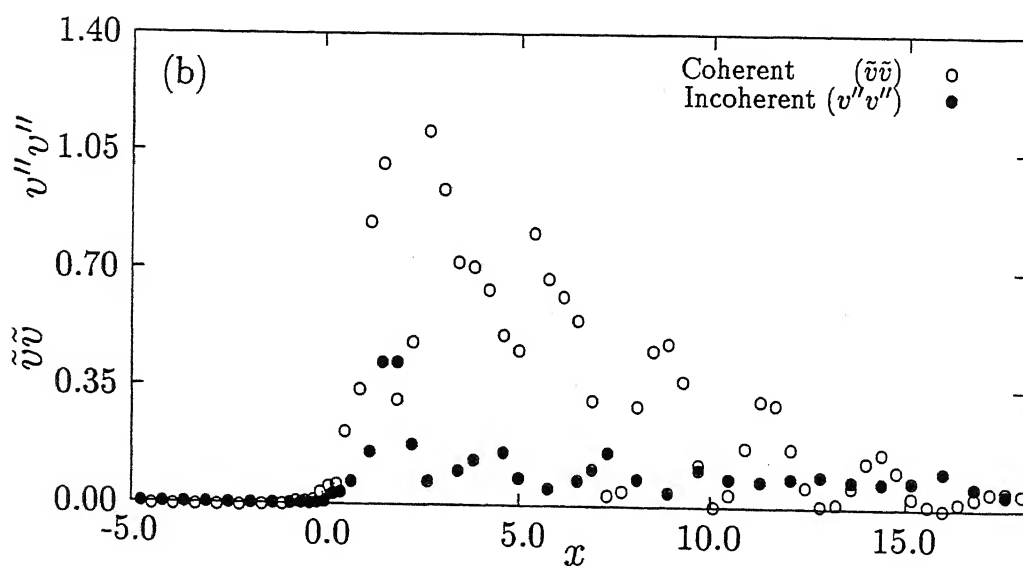
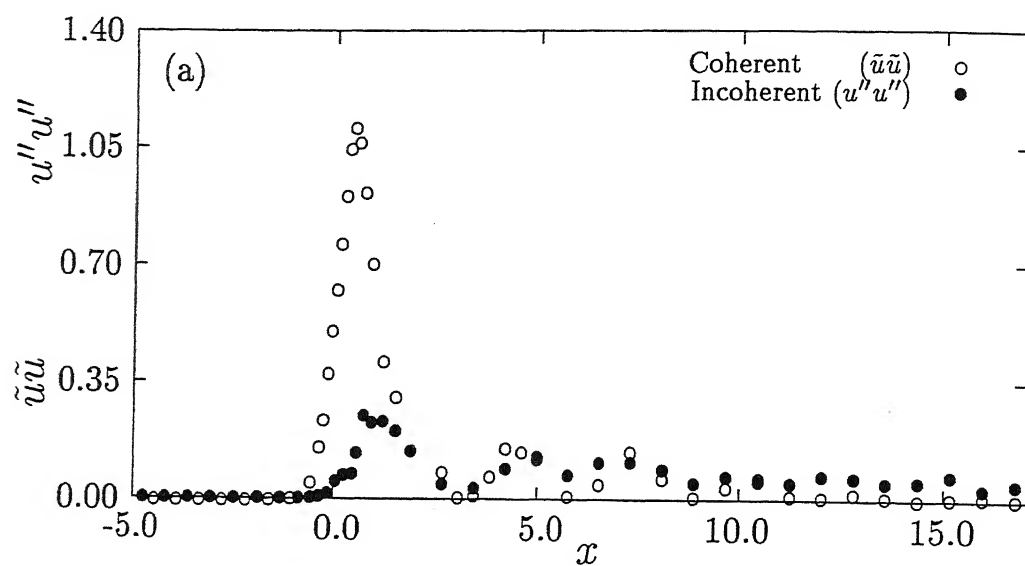


Figure 5.7.12: for caption see next page

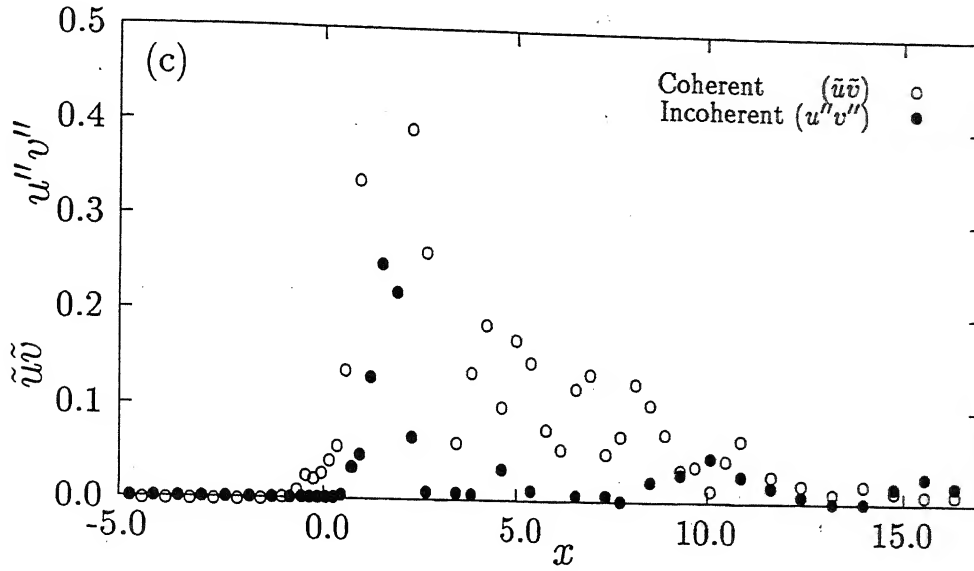


Figure 5.7.12: Comparison of streamwise variation of maximum (a) streamwise normal stress (b) transverse normal stress and (c) shear stress at phase-I. The random component reveals comparable magnitude in the far-wake because only one frequency out of many has been removed in the far-wake by phase-averaging.

random fluctuations in their study is that the inlet turbulence is high in the experiments (as compared to zero in the present study). The streamwise variations of $(\tilde{v}\tilde{v})$ and $(v''v'')$ are shown in Figure 5.7.12(b). The periodic fluctuations are higher upto a distance of $x=14.0$, beyond which both values are of comparable magnitude. A similar behaviour has also been reported by the Lyn *et al.* (1995). Figure 5.7.12(c) shows the distribution of the maximum values of shear stresses due to periodic and random component of fluctuations. The periodic component shows higher values in the near- and intermediate-wake and beyond this distance, both show comparable magnitudes.

The results discussed above show two important trends. One is randomness of the phase-averaged data in the far-wake, and second, the phase-averaged incoherent fluctuations being larger than the coherent motion. The two results emanate from a single physical phenomenon and are hence equivalent. This effect is the following. At high Reynolds number, vortices shed in the near-wake undergo breakup, and establish the cascade mechanism of energy transfer as in the developing turbulent flow. When phase-averaging is carried out using the vortex shedding frequency, the large structures of the near-wake are highlighted. In contrast, the full spectrum is established in the far-wake

and the averaging with respect to single frequency leaves the spectrum intact. Thus, the far-wake continues to remain noisy and shows up large values of the incoherent velocities. The eddy breakup mechanism ensures that the coherent part has become sufficiently small.

5.7.5 Closure

Model-free three-dimensional computations have been carried out at a Reynolds number of 21400 using higher order spatial discretization. The following is the list of important results derived from the study:

1. The time-averaged flow matches well with the existing experiments and LES results.
2. The time-averaged fluctuating field shows a good match in the base region but is overpredicted in the streamwise locations beyond $x=1.0$ due to the higher blockage in the present study.
3. The streamwise velocity loses phase information rapidly in the downstream direction compared to the transverse component.
4. The near-wake shows higher coherence whereas in the far-wake, both coherent and incoherent components are of comparable magnitude.
5. The far-wake shows an irregular structure even in the phase-averaged field because of the elimination of only one out of the many phases present in it.

5.8 Experimental Study at Low and High Reynolds Numbers

In the earlier sections, the wake of the square cylinder has been explored using numerical techniques. The present section is concerned with experiments using a hotwire anemometer. Experiments have been employed in the present work to provide supporting evidence for the overall trends in time-averaged flow quantities and the integral parameters. Since the probe involved is a hotwire, it is to be expected that the reliability of the experiments is higher at higher Reynolds numbers. Consequently, it has not been possible to test the appearance of Modes-A, A* and B and the route to chaos, these being predominantly at low Reynolds numbers.

Experiments at low as well as high Reynolds numbers have been conducted in the present study. The respective experiments were carried out in two different apparatus.

The low Reynolds number experiments have been carried out in the test cell that is schematically shown in Figure 4.1(a). The cross-section of the test cell is 10 cm×5 cm, the test section being 80 cm long. Flow in the apparatus was manually controlled against a voltmeter output, the voltage supplied to the blower being stepped down through two variacs in series. An additional factor responsible for low flow rates was the increased resistance of the test cell created by mesh screens as well as the blocked passage to flow through blower.

With the arrangements given above, a low stable velocity of 0.4 m/s was attainable in the experiments. Further, it was possible to maintain constancy of the average velocity over the range 0.4–4 m/s for the duration of the experiments. The free stream turbulence level in the flow upstream of the cylinder was found to be 0.3%. The inlet velocity was uniform to within $\pm 3\%$ over the 85% of the tunnel cross-section under the most unfavourable conditions. The quality of the inflow was seen to be markedly better for velocities greater than 1.0 m/s. The size of the cylinder used in the low Reynolds number experiments was 5 mm×5 mm and was made of perspex. The cylinder was placed along the shorter length of the test cell thus giving a blockage of only 5%. Two different velocities, namely 0.63 and 1.21 m/s were chosen for experiments, thus resulting in Reynolds numbers of 200 and 390 respectively. The average room temperature during the experiments was at $22^\circ(\pm 2)$ C.

The high Reynolds number experiments of the present work were carried out in an open circuit wind tunnel having a nominal cross-section of 40 cm×40 cm shown in Figure 4.1(b). A 3 m long test section of the wind tunnel was available for experiments. The divergence angle of the test section being 4°, and a fair constancy of pressure was observed. The wind tunnel fan was electronically controlled and stable velocities in the range 5-20 m/s were realizable in the experiments. The speed control was formally rated at $\pm 0.5\%$ but over a 3-hour period, no noticeable change was observed in the approach velocity. Free stream turbulence in the approach flow was damped by an array of mesh screens. In all experiments, turbulence was found to be less than the background noise of the anemometer, being equivalent to 0.01% at an approach velocity of 10 m/s. The inlet velocity profile was uniform to within $\pm 0.5\%$ over 90% of the tunnel cross-section. The square cylinder used was made of perspex, 25 mm×25 mm in cross-section. The use of perspex was advantageous since (i) good quality smooth surfaces were attainable over the entire cylinder and (ii) precise sharpness of the cylinder edges could be maintained. The cylinder length was 40 cm, thus spanning the entire width of the wind tunnel. Upstream velocities of 5.2 and 10.53 m/s were utilized to produce Reynolds numbers of 8700 and 17625 respectively in the experiments. The room temperature during the all experiments was $26^\circ(\pm 2)$ C.

Velocity was measured using a two-channel hotwire anemometer along with an X-wire probe. The X was formed in the vertical plane with the cylinder being placed in a horizontal position. The probe was mounted on a traversing mechanism that facilitated all three orthogonal movements, to a positional accuracy in the most significant direction, namely the vertical being ± 0.1 mm. The commercially available DANTEC anemometer and probes were employed in the present work. The two wires of the probe were calibrated in the wind tunnel itself. Small changes in room temperature ($\pm 1^\circ$ C) have been compensated through the use of a correction formula that assumes a constant heat transfer coefficient. The probe was recalibrated for larger changes in temperature. Both wires were operated at 200° C and their calibration curve were seen to be practically identical. The assumption of equal sensitivity coefficients of the two wires was occasionally employed during data reduction. During calibration, a pitot tube connected to a FURNES CONTROLS 19.99 mm of H₂O digital manometer was utilized. Both DC and rms values of voltages were recorded using 'true' voltmeters supplied by DANTEC. Integration

times of typically 300 seconds were used to obtain for all time-averaged quantities. The cross-correlation between the voltage fluctuations was determined by collecting long time traces through ADVANTEST spectrum analyser, followed by a numerical integration of the product of the two signals (over 10 seconds). The frequency of vortex shedding was measured by the spectrum analyser using the FFT algorithm. The conversion of voltages to velocities was accomplished through an explicit non-real time method developed by Chew and Simpson (1988). This technique has the advantage of determining the mean and the fluctuating components of velocity as well as their cross-correlations with very few assumptions regarding probe parity and turbulence level.

Velocity and velocity fluctuations in the wake of the square cylinder have been measured from a dimensionless distance of 1.5 and beyond. In view of the insensitivity of the hotwire probe to reversed flow, measurements in the recirculation region of the cylinder are questionable. Earlier studies show the size of the recirculation region at high Reynolds numbers to be in the range 1.3-1.4 (Lyn *et al.* (1995); Durão *et al.* (1988)). The recirculation zone has been established in these studies through alternative techniques such as LDV and the flying hotwire. Hence the choice of the first measurement station for the time-averaged velocity as 1.5 can be taken as acceptable to begin with.

In experiments with low as well as high velocities, the velocity fluctuations close to the cylinder can be expected to be large. Under these conditions, the hotwire measurements using the fixed operating points approach (corresponding to mean velocity) are questionable. In the present experiments, the first x -location was at $x=1.5$ and definite positive value of the mean velocity was recorded. Hence on no occasion was the calibration curve utilized close to zero velocity. Secondly, the instantaneous voltage signal of the anemometer was converted to velocity pointwise and time-averages subsequently computed. The difference between this strategy as against the conventional operating point approach was found to be negligible, particularly in the high Reynolds number experiments. This observation also finds support in the work of Swaminathan *et al.* (1986). These authors have shown a turbulence correction factor of 10% at a turbulence intensity of as high as 45% with respect to the mean flow. The corresponding probability of occurrence of reversed flow was found to be less than 1%. The above discussion improves the degree of confidence that can be reposed on the hotwire data.

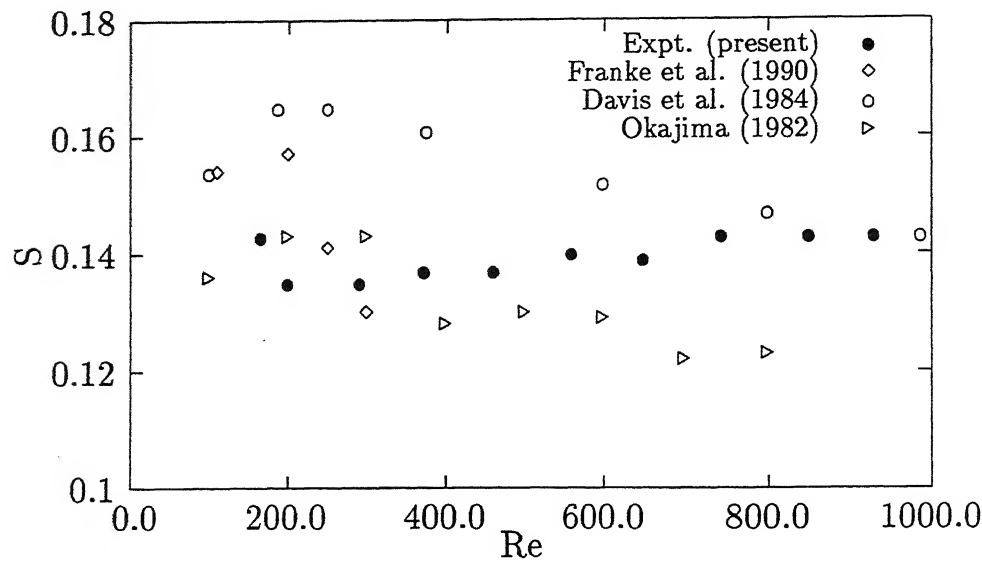


Figure 5.8.1: Comparison of measured Strouhal number with published data.

5.8.1 Low Reynolds number measurements

Figure 5.8.1 depicts the comparison of the measured Strouhal number as a function of Reynolds number with published data. The present results lie between the numerical results of Davis *et al.* (1984) and the experimental results of Okajima (1982) and show a meaningfully good match. The comparison of drag coefficient as a function of Reynolds number is shown in Figure 5.8.2. The measured values follow the pattern shown by the two numerical results. The drag coefficient shows an increasing trend with Reynolds number before it becomes practically asymptotic¹.

The detailed experimental results for two Reynolds numbers (200 and 390) are presented below. The Strouhal numbers corresponding to these Reynolds numbers of 200 and 390 are 0.135 and 0.138 respectively. The time-averaged streamwise component of the velocity at three different locations, namely $x=2.5$, 3.5 and 5.5 are shown in Figure 5.8.3.

¹(1) It was not possible to measure drag below a Reynolds number of 400 by the wake survey method owing to diffusive and wall effects (2) Measured values of drag at low Reynolds numbers have not been reported in the literature.

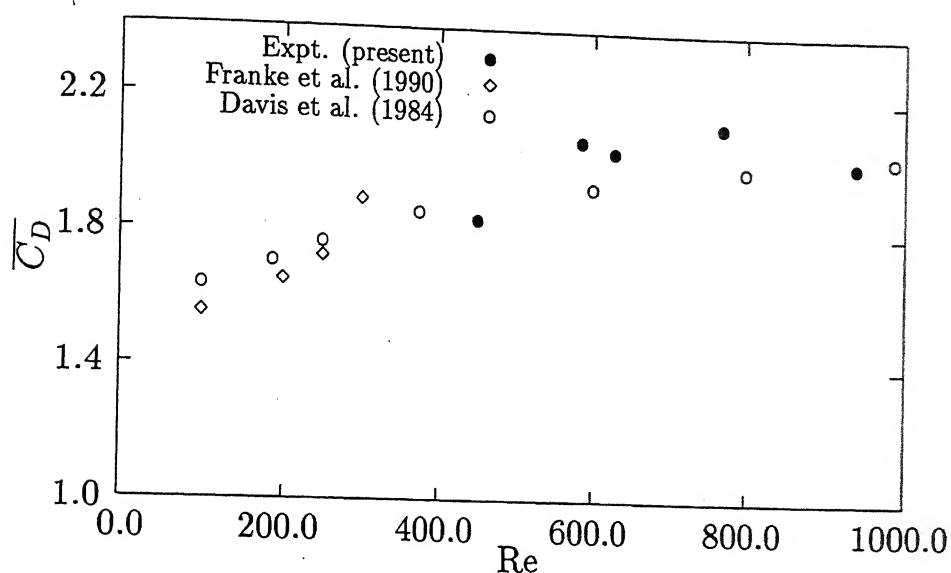


Figure 5.8.2: Comparison of measured drag with published data.

The time-averaged velocity profiles have been compared with the two-dimensional numerical results for a Reynolds number of 200 (Figure 5.8.3(a)). The measured profiles follow the overall trend seen in numerical results. However, the centreline recovery rate of velocity for the experiments is slow compared to the numerical results. The faster recovery rate in numerical results can be attributed to its higher blockage (10%) compared to the measurements (5%) and the essentially three-dimensional nature of the flow even at low Reynolds numbers. Figure 5.8.3(b) depicts the time-averaged streamwise velocity profiles at the above referred locations for a Reynolds number of 390. The profiles show faster recovery of the streamwise velocity compared to a Reynolds number of 200. The velocity profiles at both the Reynolds numbers show good symmetry about the wake centreline, and thus reflect correctness of the experiments as well as the measurement technique.

The time-averaged transverse velocity profiles have been presented in Figure 5.8.4 at the locations $x=2.5$, 3.5 and 5.5. The present experiments showed a small but finite transverse velocity, (around 10% of the average at the lowest velocity studied and smaller at a higher velocity) particularly at the lower Reynolds number. A possible reason could be the presence of the plugs on the top surface, needed to position the probe. Figure 5.8.4(a)

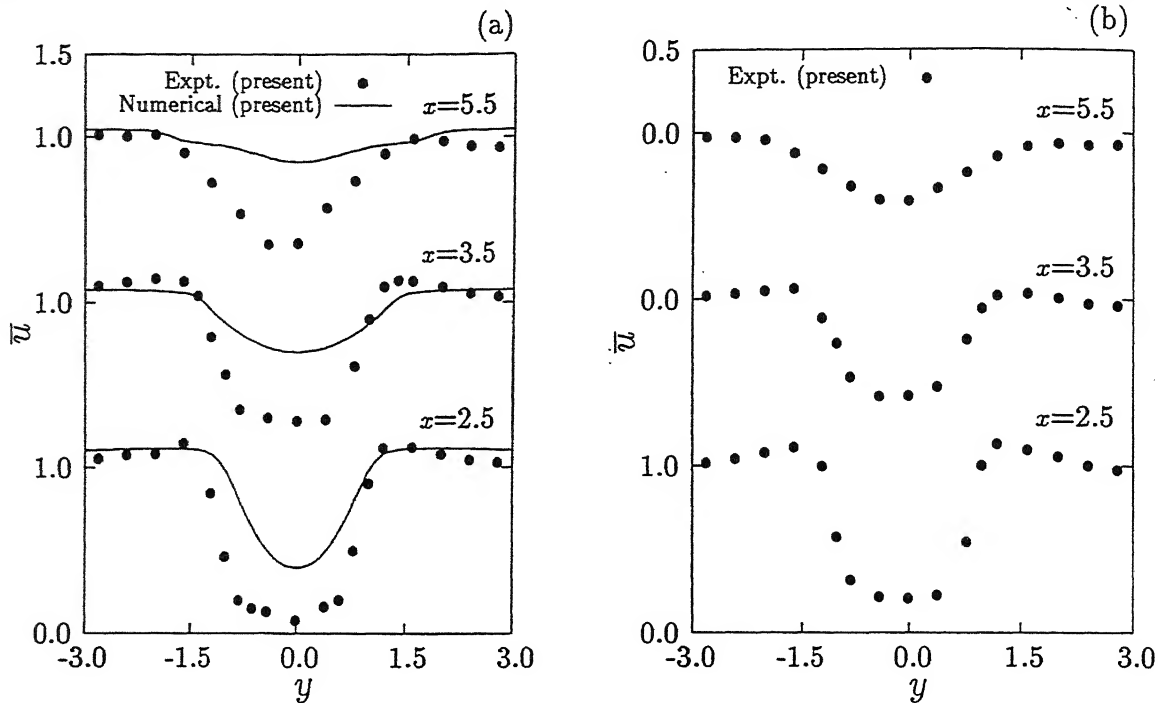


Figure 5.8.3: Measured time-averaged streamwise velocity profiles: (a) $Re=200$ and (b) $Re=390$.

has been drawn after subtracting the nonzero transverse velocity from the measured data. The comparison at a Reynolds number is not satisfactory. The measured profile at $x=5.5$ looks identical in Figure 5.8.4(a) to the numerical profile at $x=3.5$. This observation shows that the measurements differ from the numerical results with respect to the recovery rate. This could be due to the higher blockage in the numerical study. The measured profiles however follow the numerical trends. The time-averaged transverse velocity profiles at a Reynolds number of 390 are shown in Figure 5.8.4(b). The results at this Reynolds number show fewer anomalies as compared to $Re=200$.

The profiles of the time-averaged streamwise fluctuations $(\overline{u'^2})^{1/2}$ at different locations are shown in Figures 5.8.5(a) and (b) at Reynolds numbers of 200 and 390 respectively. The fluctuations are higher in the numerical results when compared to the measured values, once again due to the higher blockage of 10% in the computation. Both profiles show double peaks, and the agreement improves in the downstream direction. It is to be noted that with increasing Reynolds number, the nondimensional streamwise fluctuations also increase. The measured results show that initially the fluctuations are small ($x=2.5$). With increasing distance the fluctuations increase ($x=3.5$) and then decrease at

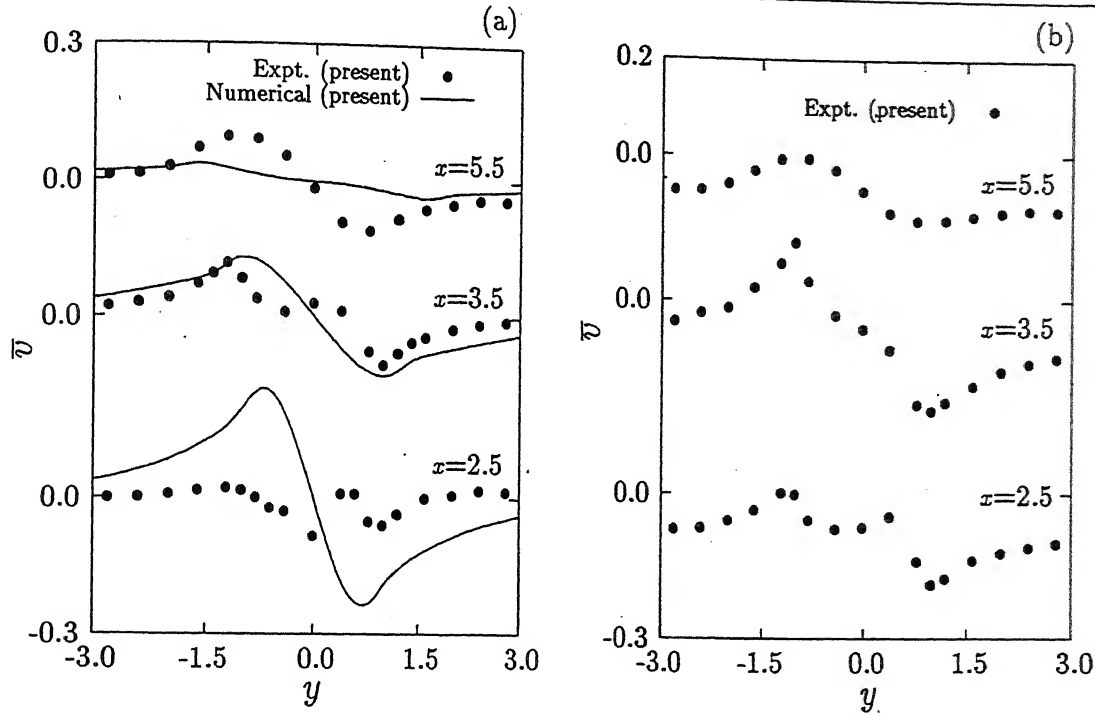


Figure 5.8.4: Measured time-averaged transverse velocity profiles: (a) $Re=200$ and (b) $Re=390$.

the subsequent locations. This behaviour is at variance with the data obtained at higher Reynolds numbers¹.

Figure 5.8.6 shows the shear stress profiles at locations $x=2.5$, 3.5 and 5.5 for Reynolds number of 200 (Figure 5.8.6(a)) and 390 (Figure 5.8.6). The measured results at both Reynolds numbers significantly underestimate the shear stress. Higher values of the shear stresses are seen at the Reynolds number of 390. Experiments clearly bring out an increase in fluctuation levels followed by a drop, with the distance. This is at variance with the two-dimensional numerical prediction, where fluctuations continuously decrease in the downstream direction. The experimental data is better explained from the three-dimensional calculations, Sections 5.2 and 5.4.

¹The experimental data at a Reynolds number of 400 appears less anomalous and projects a definite pattern. The corresponding numerical data in two-dimension was seen to show very large peaks. The three-dimensional calculation could not be continued for sufficiently large number of time steps for averaging to be performed. Hence comparison of the experiments with three-dimensional computation has not been possible.

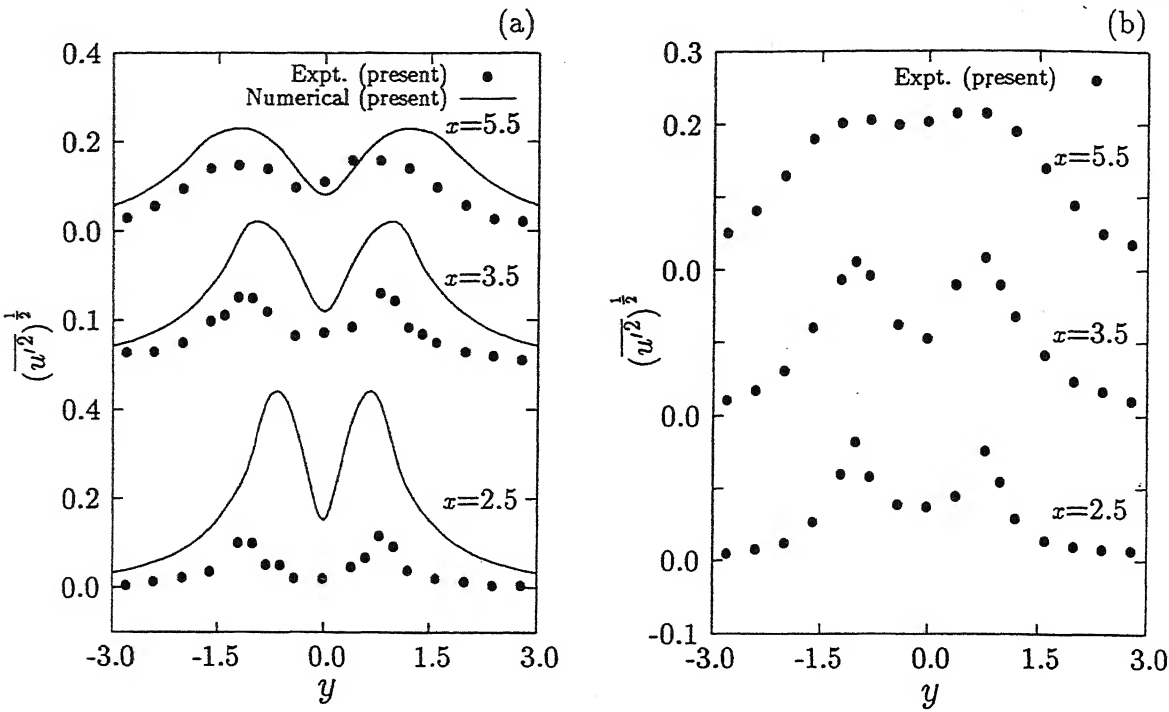


Figure 5.8.5: Measured time-averaged streamwise velocity fluctuations: (a) $Re=200$ and (b) $Re=390$.

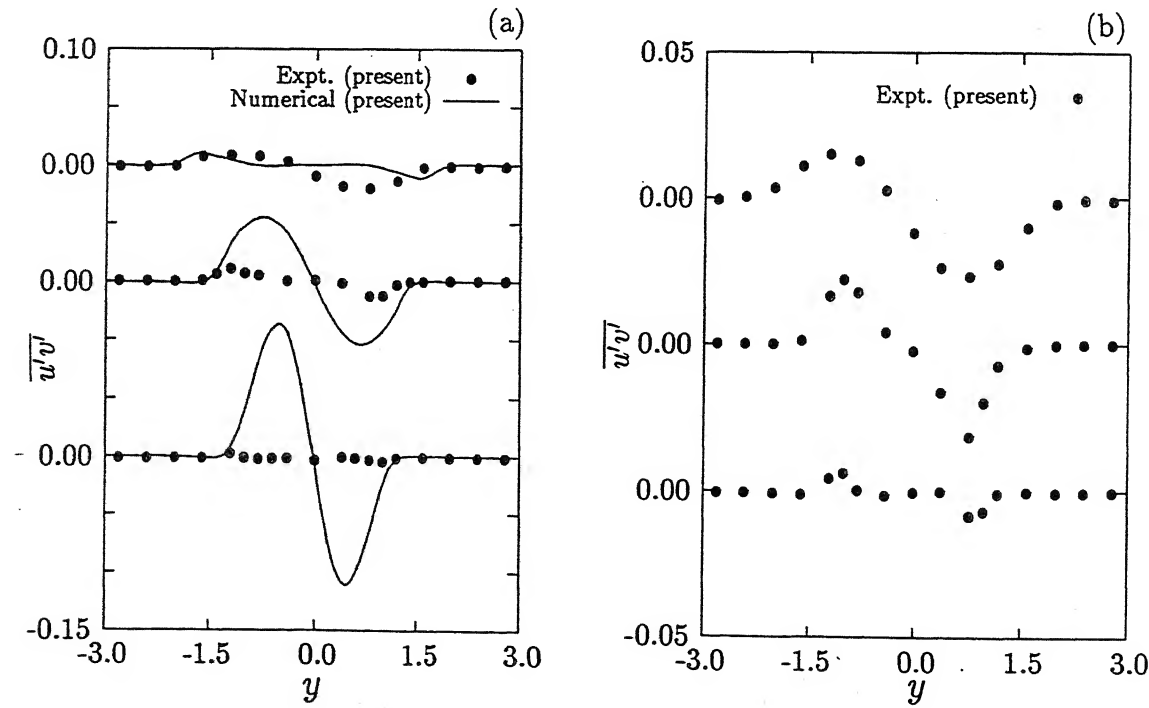


Figure 5.8.6: Measured time-averaged shear stress: (a) $Re=200$ and (b) $Re=390$.

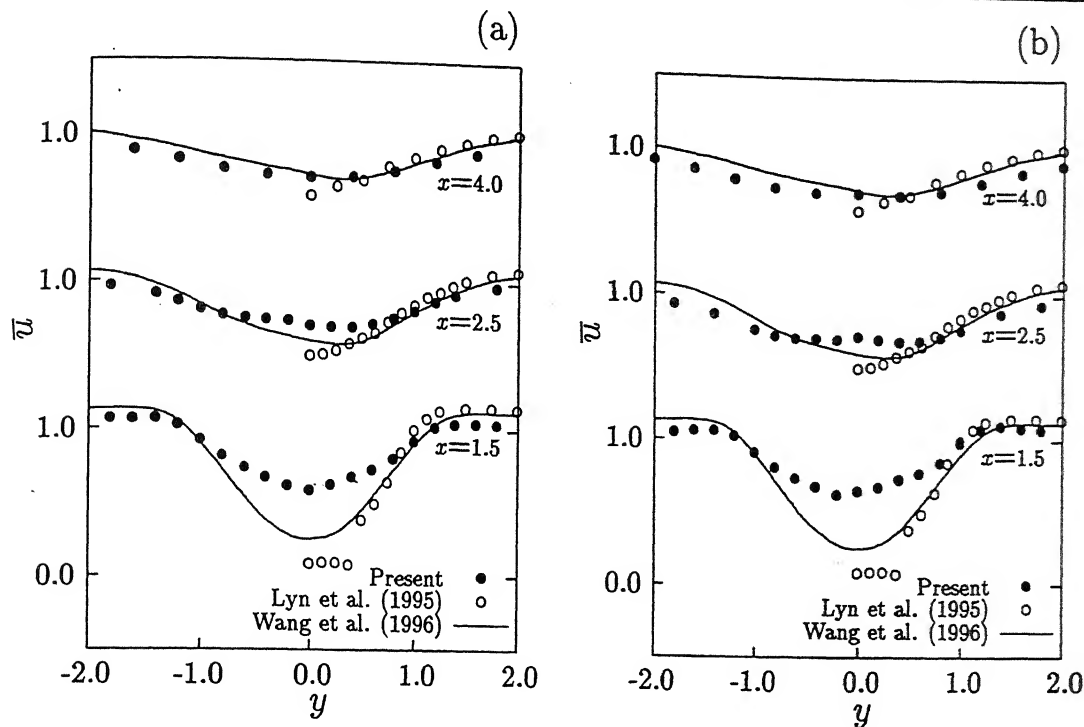


Figure 5.8.7: Comparison of measured time-averaged streamwise velocity profiles: (a) $Re=8700$ and (b) $Re=17625$.

5.8.2 High Reynolds number measurements

Experimental results have been reported in the present study for high Reynolds number flow at $Re=8700$ and 17625 . The blockage ratio based on the wind tunnel height is 6.25% and the length to width ratio of the cylinder is 16. To a first approximation, this represents the cylinder in an infinite medium; to a first approximation, blockage and aspect ratio effect are thus expected to be of secondary importance (West and Apelt, 1982).

The experiments were validated in the following manner. The time-averaged drag acting on the cylinder was determined by the wake survey method. Momentum loss calculation was carried out at the mid-plane of the cylinder at a dimensionless distance of $x=15$. A considerable variation in the static pressure was seen within the wake and so the measurements were directed individually at the total and static pressure. Some variation in the tunnel static over a distance of 15 units was also accommodated for. At Reynolds numbers of 8700 and 17625, the drag coefficients were found to be 2.13 and

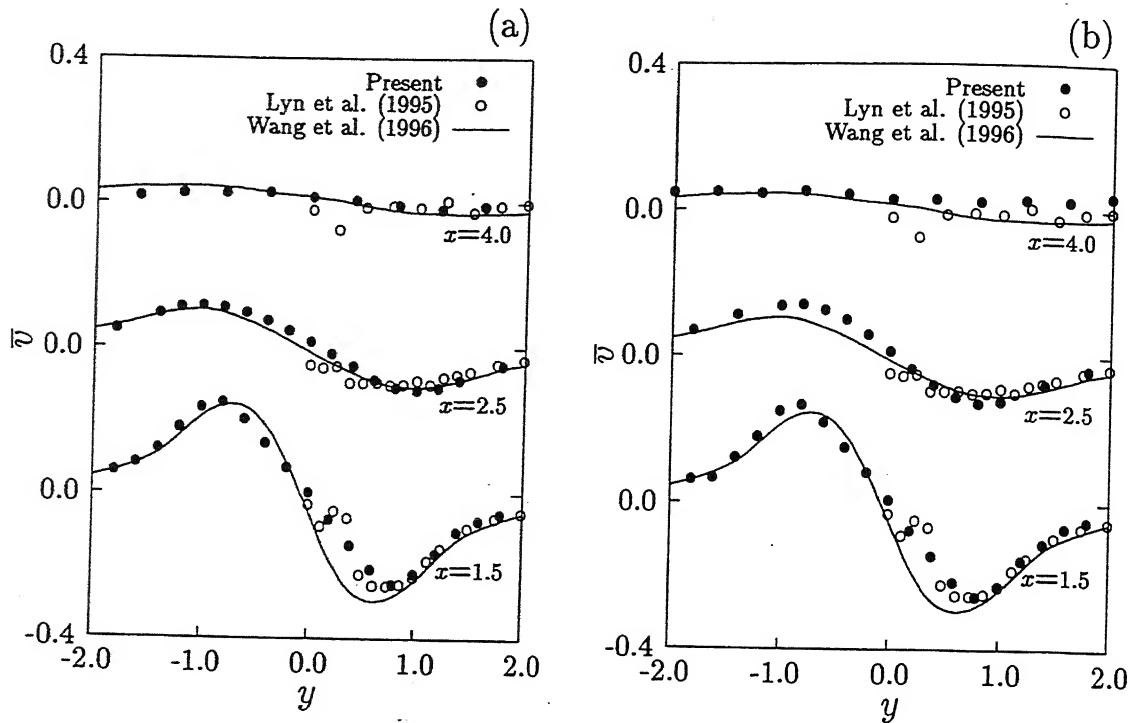


Figure 5.8.8: Comparison of measured time-averaged transverse velocity profiles: (a) $Re=8700$ and (b) $Re=17625$.

2.2 respectively. These values are comparable to the numerical estimate of 2.07-2.67 at a Reynolds number of 21400 by Wang *et al.* (1996). It is also in closer agreement with experiments of Cheng *et al.* (1992) who have presented the drag coefficient to be 2.1.

Based on the vortex shedding frequencies, the respective Strouhal numbers have been found in the present experiments to be 0.144 and 0.142 respectively. These values differ from those reported by Durão *et al.* (1988) as well as Lyn *et al.* (1995) who present the Strouhal number to be 0.138 and 0.132 at Reynolds numbers of 14000 and 21400 respectively. The reasons for this discrepancy is certainly due to high inlet turbulence level of 2-6% in the referred experiments. The numerical simulation of Wang *et al.* (1996) show a Strouhal number of 0.13 at a Reynolds number of 21400.

A detailed comparison of the measured profiles of velocity and velocity fluctuations with LES calculations of Wang *et al.* (1996) is now presented. Time-averaged velocities and velocity fluctuations have been nondimensionalized using u_{av} , the average incoming

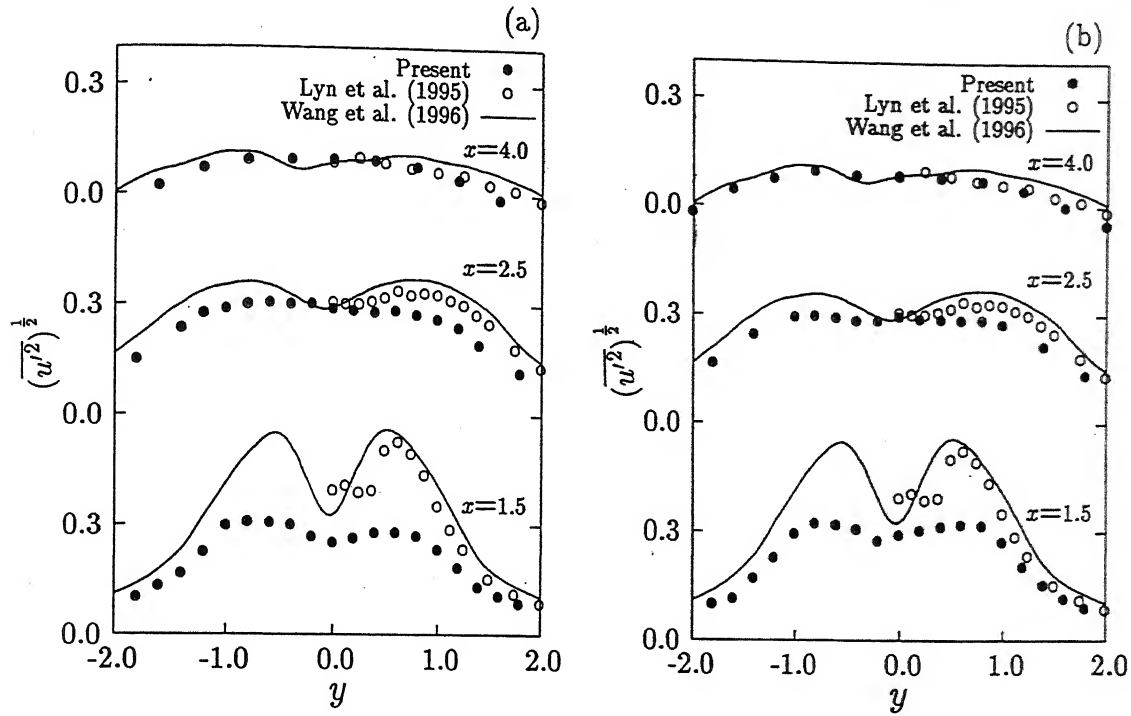


Figure 5.8.9: Comparison of measured time-averaged profiles of streamwise velocity fluctuations: (a) $Re=8700$ and (b) $Re=17625$.

velocity. The turbulent shear stress has been nondimensionalized using u_{av}^2 . The numerical calculations of Wang *et al.* (1996) employ a Reynolds number of 21400 as stated above. Besides, the cylinder length is π , the blockage ratio is 0.05 and periodicity boundary conditions have been applied in the spanwise direction. Hence one cannot expect a total match between numerical calculations and the present hotwire measurements.

Figures 5.8.7(a) and 5.8.7(b) show the time-averaged streamwise velocity profiles at three locations downstream of the cylinder at Reynolds numbers of 8700 and 17625 respectively. The numerical results have been shown on the same graph by solid lines. A remarkable aspect to be noticed in Figure 5.8.7 is the invariance of the dimensionless velocity distribution with respect to both Reynolds numbers. This is also an indication of a low uncertainty level in the high Reynolds number experiments.

Figure 5.8.8 is a comparable plot for the transverse component of velocity. Both figures (Figure 5.8.8(a) and (b)) reveal good symmetry (and antisymmetry) in velocities with respect to the wake axis. The measurement of a negative transverse velocity is a check on the correctness of the data reduction procedure. The agreement between experimental

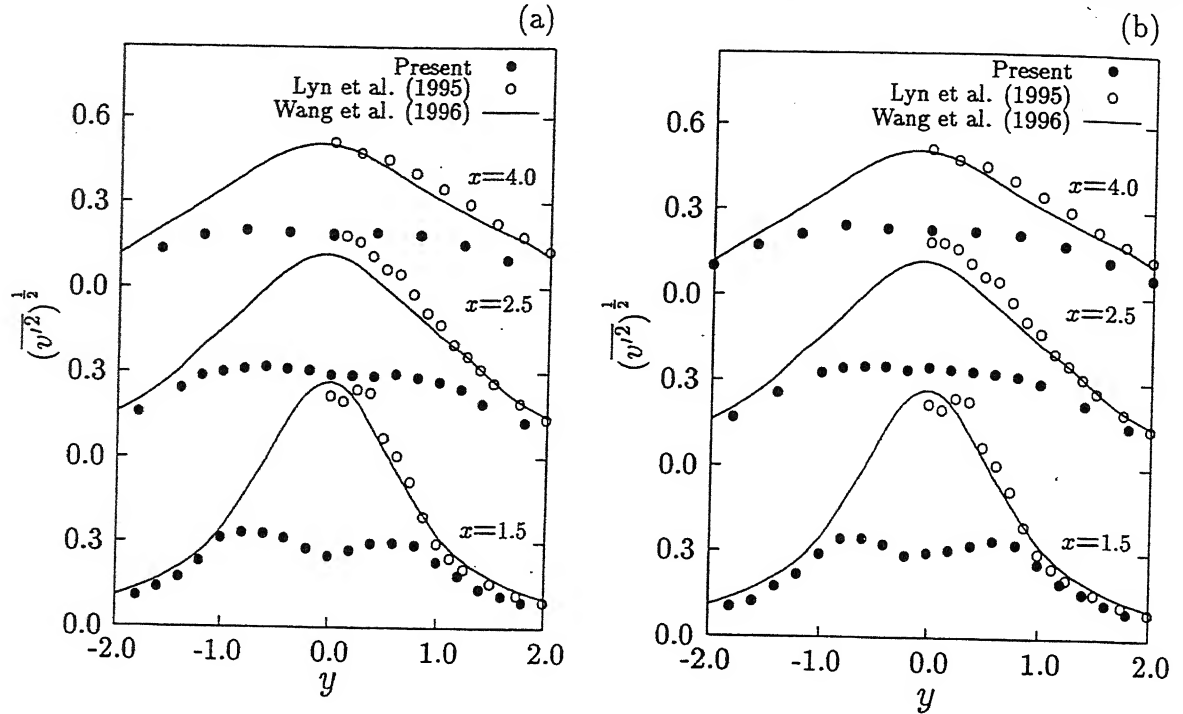


Figure 5.8.10: Comparison of measured time-averaged profiles of transverse velocity fluctuations: (a) $Re=8700$ and (b) $Re=17625$.

and numerical data is uniformly satisfactory.

Figures 5.8.9 and 5.8.10 compare the streamwise $((\overline{u'^2})^{1/2})$ and transverse $((\overline{v'^2})^{1/2})$ velocity fluctuations between experiments and numerical simulation. The agreement here is good in qualitative terms. Significant differences can however been seen at the first measurement station. Both experiments as well as calculations reveal a double-peaked profile in $\overline{u'^2}$ while a single peak is seen in $\overline{v'^2}$ with a maximum occurring along the axis. The differences between experiments and simulations tend to diminish at larger streamwise locations.

Figure 5.8.11 compares the turbulent shear stress between the present experiments and the numerical computation. The comparison is seen to be closer in these figures compared to $\overline{v'^2}$. The change of sign in $\overline{u'v'}$ about the wake centreline is clearly revealed. Once again, the agreement improves in the downstream direction.

The centreline recovery of time-averaged streamwise velocity is shown in Figures 5.8.12(a) and (b) for the Reynolds numbers under discussion. The present mea-

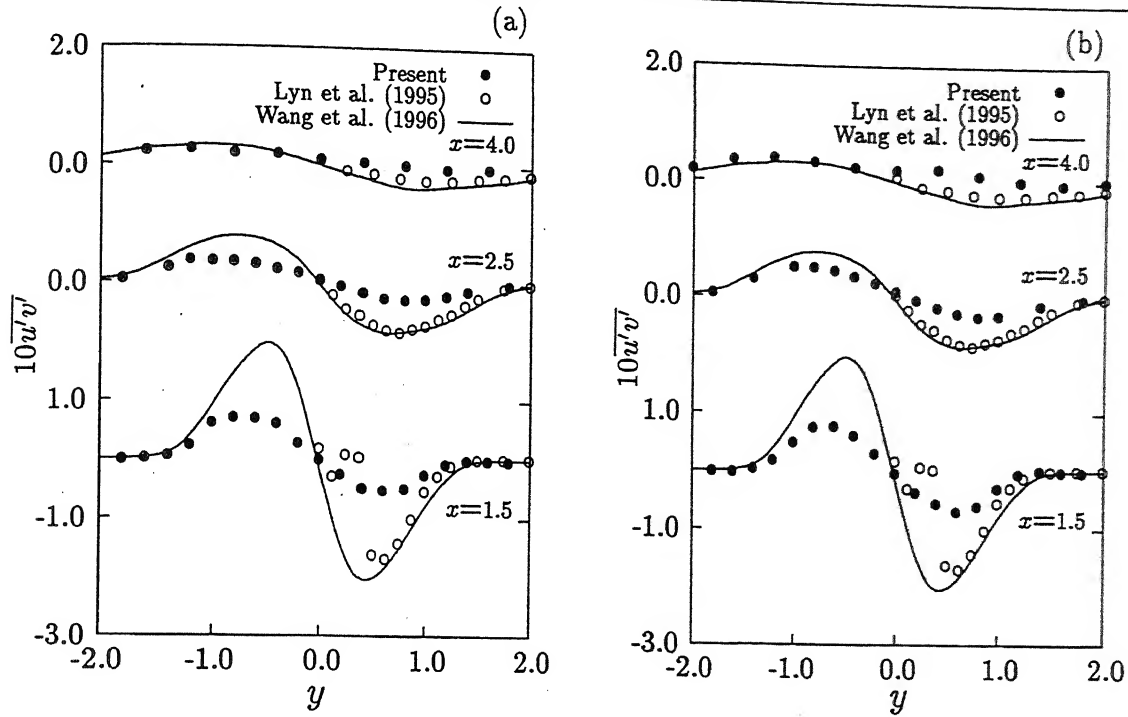


Figure 5.8.11: Comparison of measured time-averaged profiles of turbulent shear stress: (a) $Re=8700$ and (b) $Re=17625$.

measurements show that the recovery is faster compared to the experiments by Lyn *et al.* (1995) and LES results of Wang *et al.* (1996).

In summary, the numerical results match experiments at high Reynolds number when compared in terms of the time-averaged velocities, the streamwise velocity fluctuations and the turbulent shear stress. Numerical predictions of the transverse velocity fluctuations are significantly higher than the measured values. The possible reason for the discrepancy could be the very short spanwise dimensions ($=\pi$) in computations as against a value of 16 used in experiments.

A physical discussion on the results obtained can be conducted in the following manner. The separation of flow over a bluff object causes a pressure drop across its surface, thus leading to a non-zero form drag. Equivalently this is manifested as loss of momentum of the fluid in the wake. Thus the time-averaged streamwise velocity is smaller within the wake compared to its value in the free stream. A minimum in this velocity is attained close to the wake centreline. As seen in Figure 5.8.7 the minimum velocity increases in the downstream direction. Simultaneously there is an increase in the

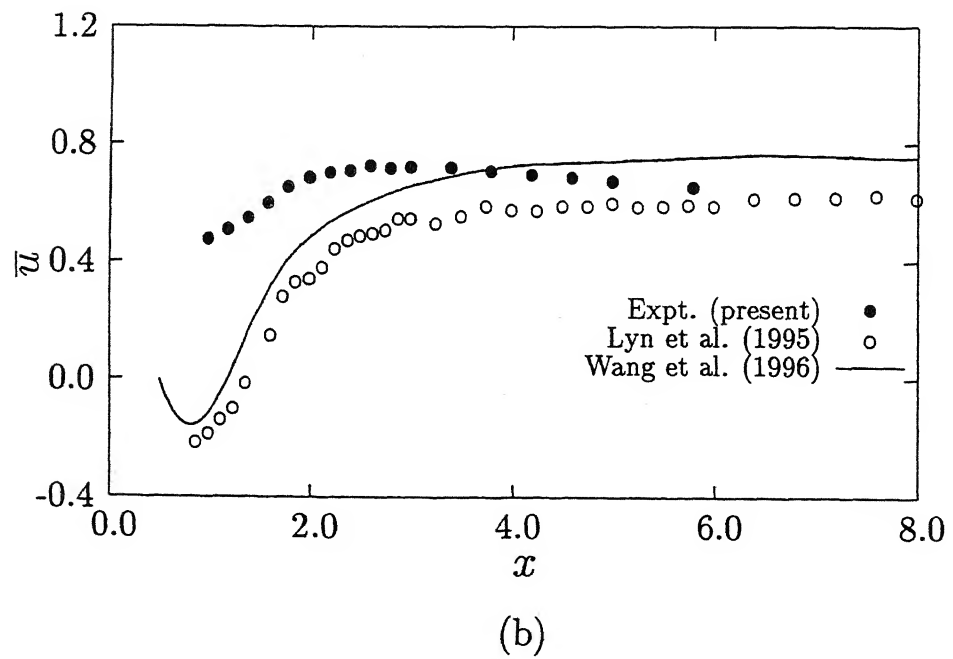
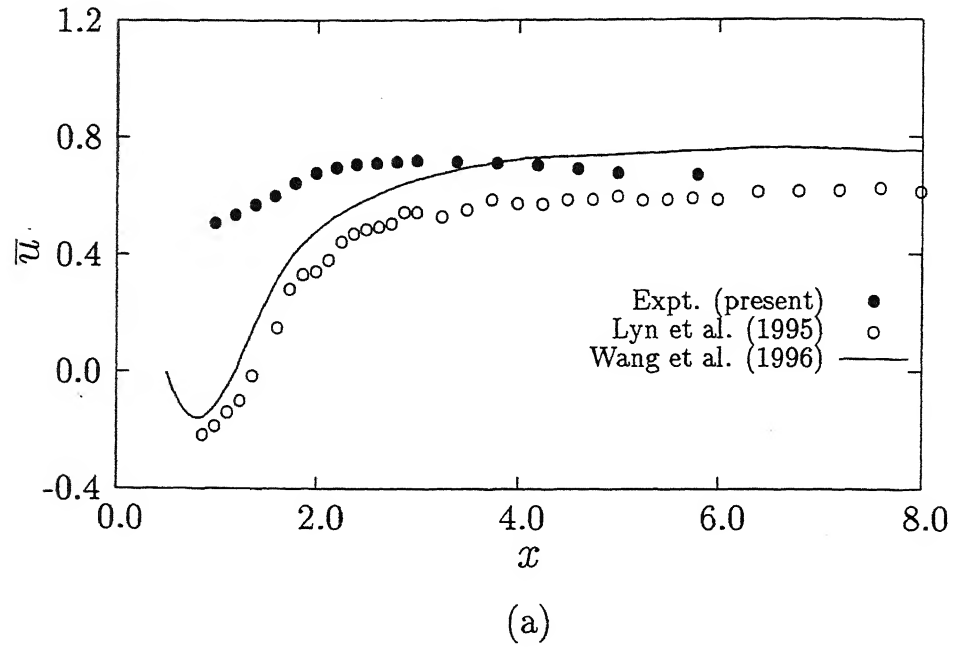


Figure 5.8.12: Comparison of recovery of measured time-averaged streamwise velocity along the wake centreline: (a) $Re=8700$ and (b) $Re=17625$.

wake size. The two processes can happen only when fluid is entrained from the edges of the wake on each side of the centreline. A measure of the entrainment of the fluid can be derived from the transverse velocity profiles in Figure 5.8.8. It can now be seen that entrainment and hence the velocity recovery are both very high for small distances behind the cylinder. Both of them asymptotically reach their respective limits for higher downstream distances.

The variation of the turbulent fluctuations in the wake requires greater elaboration. The mechanism involved is not only dissipation but also the substantial energy transfer from the core to the surrounding fluid. A detailed study of the energetic interactions of periodic fluctuations in the wake is presented in Section 5.3.

5.8.3 Effect of inlet turbulence on the wake

In comparison to the low Reynolds number experiments, the agreement between the experiments and numerical simulation at the high Reynolds number was seen to be substantially better. Yet, there were differences, particularly in the velocity fluctuations and turbulent shear stress. One factor that has not been matched among the published experiments, numerical simulation and the present experiments is the turbulence level in the incoming flow. The present section is concerned with the study of inlet turbulence on the turbulence profiles in the wake.

The effect of inlet turbulence has been studied by placing a circular cylinder centrally at a distance 150 diameters (of the circular cylinder) upstream of the square cylinder. The approximate turbulence level measured just upstream of the square cylinder ($y=-2.0$ to 2.0) was about 3.5%. The measurements at two different streamwise locations, namely $x=1.5$ and 2.5 were conducted at a Reynolds number of 12000. The time-averaged profiles at $x=1.5$ (Figure 5.8.13(a)) show the influence of inlet turbulence on the recovery rate. The increase turbulence level leads to a slow recovery compared to low inlet turbulence. Simultaneously, the measured profiles approach the profiles of Lyn *et al.* (1995). The effect of inlet turbulence on transverse velocity is depicted in Figure 5.8.13(b). The transverse velocity at this location is seen to be insensitive to inlet turbulence. The time-averaged streamwise fluctuations at $x=1.5$ are presented in Figure 5.8.13(c). The figure shows that there is a decrease in fluctuations due to the increase in inlet turbulence. Figure 5.8.14 shows the effect of inlet turbulence at a location $x=2.5$ over one half of the

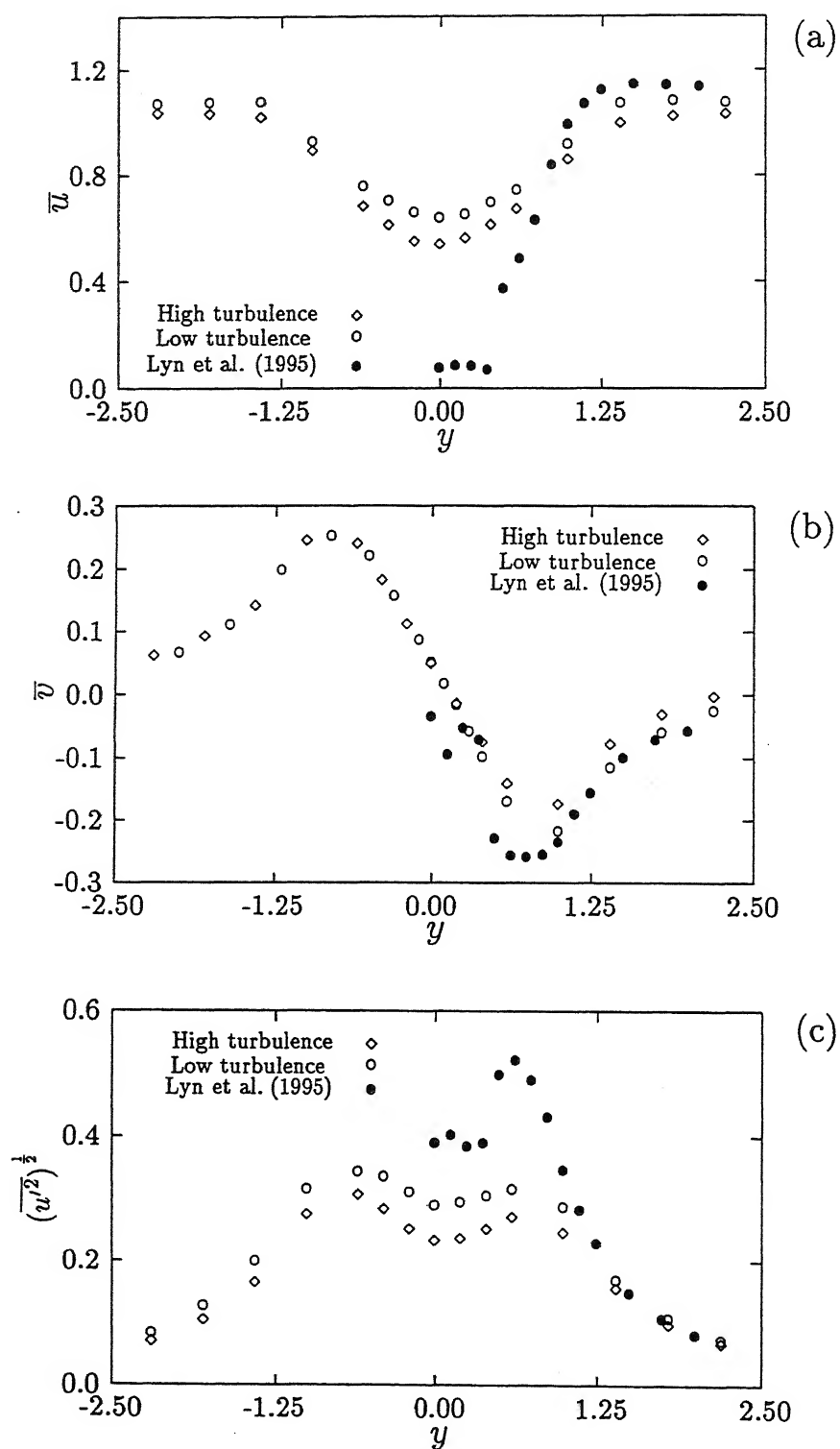


Figure 5.8.13: Effect of upstream turbulence on time-averaged profiles of (a) streamwise velocity (b) transverse velocity and (c) streamwise velocity fluctuations at $x=1.5$ for a Reynolds number of 12000.

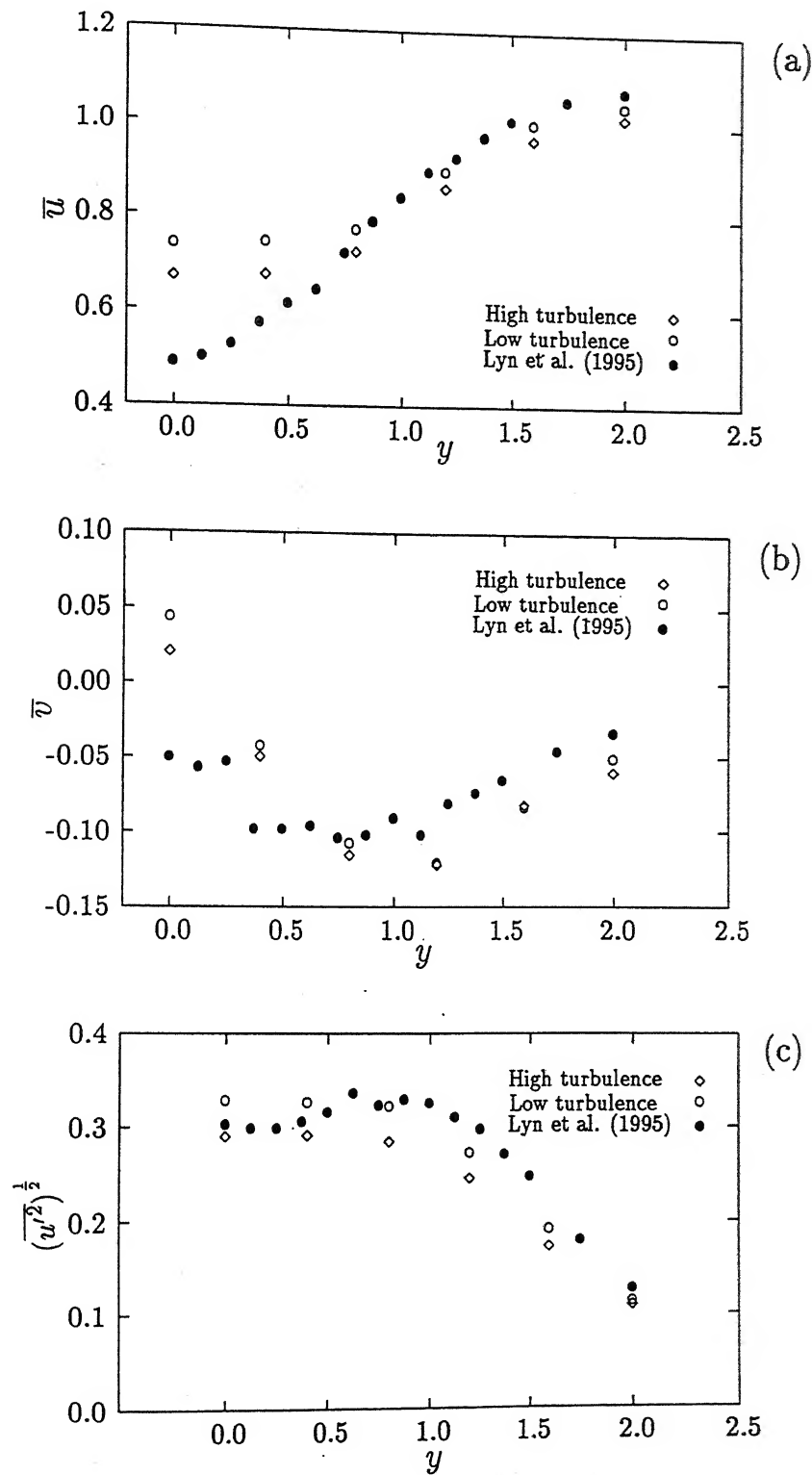


Figure 5.8.14: Effect of upstream turbulence on time-averaged profiles of (a) streamwise velocity (b) transverse velocity and (c) streamwise velocity fluctuations at $x=2.5$ for a Reynolds number of 12000.

wake. The measurements have been carried at this location because of good symmetry found in earlier measurements. The streamwise velocity is influenced to a great extent at this location and approaches the value of Lyn *et al.* (1995). In conclusion, it can be said that an increase in upstream turbulence in the present experiments shows uniformly better comparison with the published measurements for $x=2.5$ (and probably beyond).

The role of upstream turbulence can be explained as follows. External turbulence increases the entrainment of fluid into the free shear layer from the recirculation zone and hence increases their curvature (Huot *et al.*, 1986). When the entrainment becomes very large, the free shear layers eventually reattach to the sides of the obstacle. Consequently separation is reinitiated at the rear edges. The entrainment of the fluid from the freestream to the wake is then slow and the recovery rate is small. Figure 5.8.14(b) shows that the transverse entrainment in the present measurements is marginally higher at a location $x=2.5$ compared to Lyn *et al.* (1995). The higher entrainment in the present experiments with low upstream turbulence is possibly the cause for a higher recovery rate compared to the published results.

5.8.4 Spectra

Since hotwire experiments reveal local pointwise information, it is usually cumbersome to map the flow field in all respect. The power spectra of x - and y -components of velocity determined at selected locations in the wake can shed light instead on the wake dynamics. With these objectives, the u - and v -spectra were recorded both along the centreline ($y=0$) and an offset position ($y=1.0$) at a Reynolds number of 17625. Figure 5.8.15 shows the u -spectra at locations $x=2.5$, 5.0, 10.0 and 30.0 for two y -planes in the cylinder wake. Figure 5.8.16 is a comparable plot for v -spectra. In these figures, the abscissa is the dimensionless frequency, while the ordinate is plotted in consistent units¹.

Figure 5.8.15 clearly brings out a dominant peak at the shedding frequency, particularly when the probe is away from the centreline. The spectra along the centreline do not reveal a clear trend. At $y=0$, the second harmonic is seen to be excited at $x=2.5$, signifying the influence of vortices shed from both halves of the cylinder on the probe. At higher x -locations the u -spectra tend to become broader with a peak developing close to

¹At low Reynolds numbers, the near-wake spectra showed dominant peaks. The far-wake spectra were not recorded owing to the potential influence of the bounding walls.

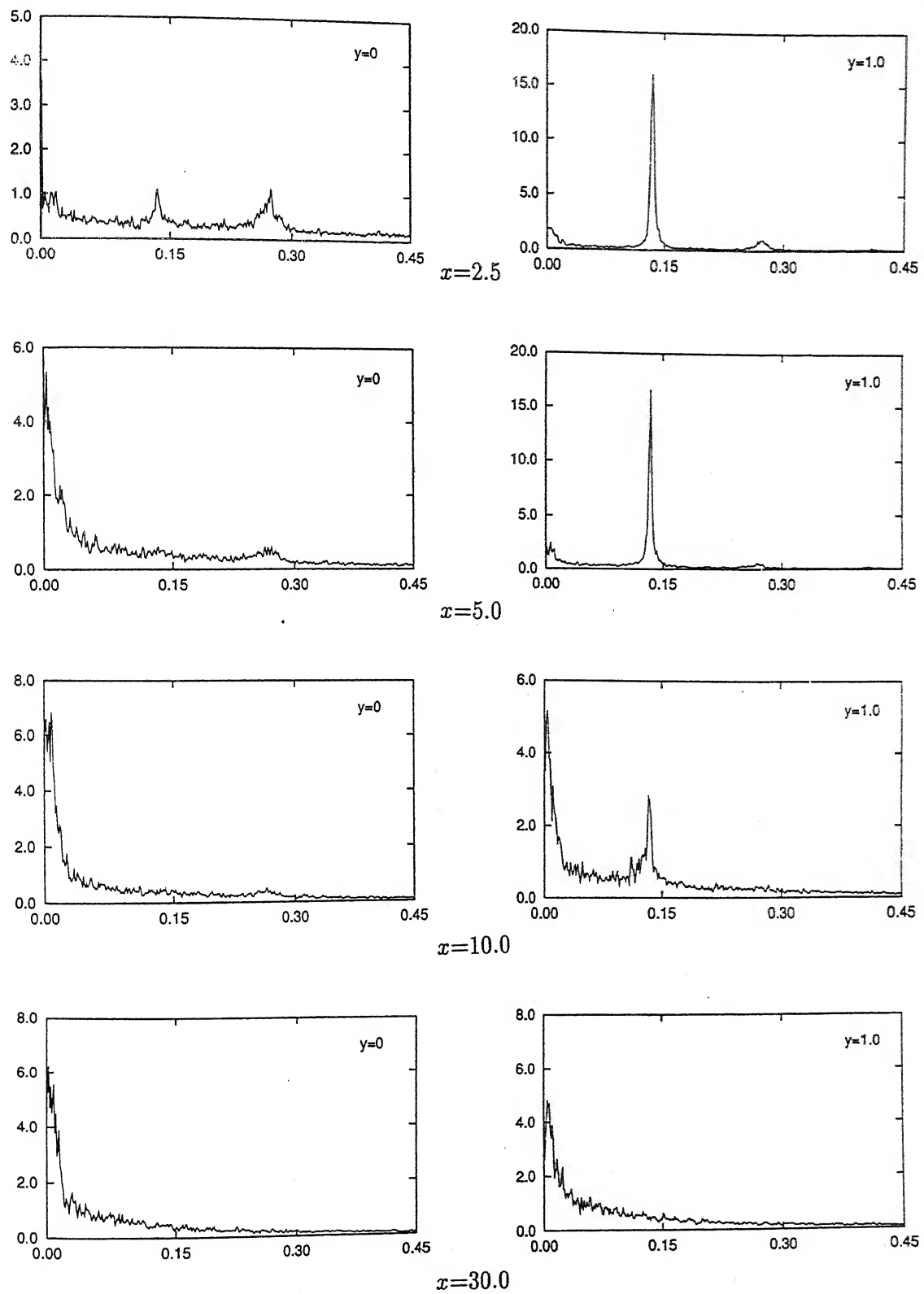


Figure 5.8.15: u -spectra at various streamwise locations plotted against the dimensionless frequency.

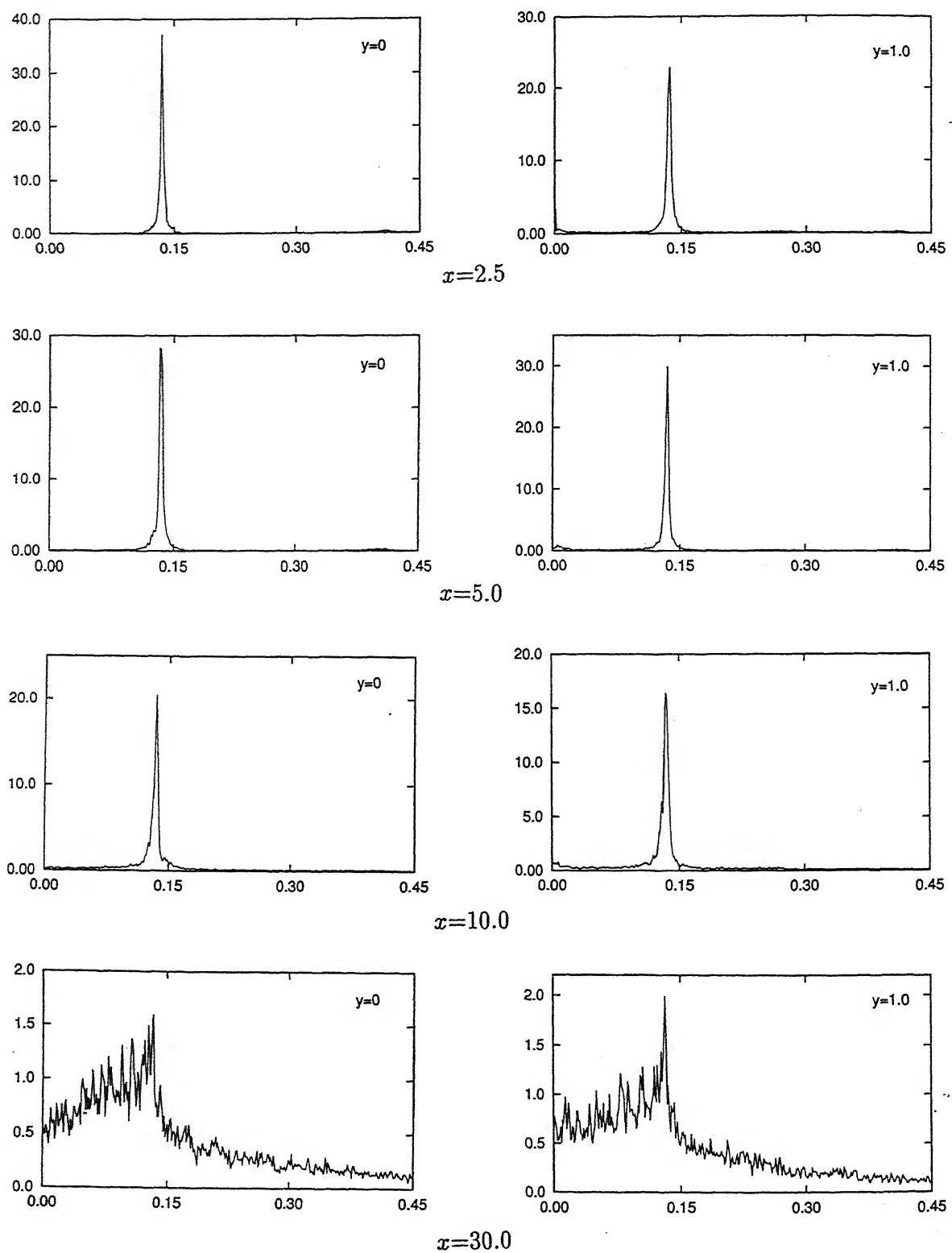


Figure 5.8.16: v -spectra at various streamwise locations plotted against the dimensionless frequency.

the origin. Thus, flow near the centreline is dominated by the time-averaged streamwise velocity with small fluctuations superimposed on it.

The peak in the u -spectra seen at the offset location diminishes in strength as compared to that for the mean flow for x -locations greater than 10.0. At $x=30.0$, a broadband spectrum in u is seen to be established.

In contrast to u -velocity, clean peaks are visible in the v -spectra at $y=0$ as well as at $y=1.0$. The peak is observable all the way upto $x=30.0$, though it is stronger at the offset location. The broadening of the v -spectra at $x=30.0$ indicates the loss of coherence in the flow field and evolution towards a fully developed state.

An interesting result can be discerned by comparing the peak values of u and v -spectra between $x=2.5$ and 5.0 ($y=1.0$). One can see an increase in the peak values in the downstream direction, followed by decay at farther distances. This result is in agreement with the observation of intensification of the vortices in the near-wake, followed by their decay.

The two new results that arise from the spectral plots can be summarized as follows:

1. The appearance of a peak in u -spectra near the origin at $x=2.5$ confirms energy transfer from the mean flow to the streamwise velocity fluctuation very close to the cylinder. The redistribution of kinetic energy between u and v occurs over a much longer length, and is not complete even at $x=30.0$.
2. The initial growth of the spectral peaks followed by a decay indicates a strengthening of the vortices outside the vortex formation length, namely 1.0-1.5. This can occur by the transport of transverse momentum from the core of the wake to the free shear layer.

5.8.5 Closure

Hotwire measurements in the wake of a square cylinder have been reported at low and high Reynolds numbers, namely 200, 390, 8700 and 17625. The following are the major findings of the present low Reynolds number experiments.

1. The integral parameters, namely Strouhal number and drag coefficient show a good comparison with published experimental and the numerical results.
2. The velocity profiles reproduce the qualitative trends of the numerical results. The agreement improves with an increase in the Reynolds number. The discrepancy between the present experiments and numerical results is in the rate of velocity recovery. The difference is possibly due to the higher blockage in the computations compared to experiments.

The high Reynolds number measurements have been compared with recently reported LES calculations. The important conclusions of this part of the study are as follows.

1. The agreement between the measured and simulated data is satisfactory in terms of the time-averaged velocity components, streamwise velocity and the turbulent shear stress. The numerical prediction of transverse velocity fluctuations is substantially higher than the measured values. This discrepancy can be attributed to (1) a small spanwise length in the simulation in comparison to the experiments and (2) a low upstream turbulence level in the present experiments.
2. A fresh set of experiments with a higher turbulence level in the approach flow was seen to improve comparison with the published experimental data.
3. A comparison of experiments at low and high Reynolds numbers reveals the following. In the low Reynolds number regime, the velocity profiles in dimensionless form depend crucially on the Reynolds number itself. In otherwords, the velocity profile is sensitive to the specific choice of Reynolds number. This can be explained in terms of the number of transitions taking place in the range $150 < Re < 600$. In contrast, the flow seen to have attained an asymptotic state and is invariant over $8700 < Re < 17625$.

Chapter 6

Conclusions and Scope for Future Work

6.1 Conclusions

The wake of a square cylinder has been explored numerically as well as through experiments. The flow regime considered for analysis is $40 \leq Re \leq 21400$. The focus of the research is towards understanding the structure of the near-wake. A clear distinction in the wake structure is brought out in the present studies relating to low and high Reynolds numbers. Experiments play a supporting role in validating the computation on one hand and highlighting certain key parameters, on the other. For this reason, the conclusions of the present research can best be appreciated when bracketed into (a) a low Reynolds number study, (b) computations at high Reynolds number and (c) hotwire experiments.

Low Reynolds Number Wake ($Re \leq 800$):

The most prominent observation in this part of the work was the appearance of transitions in the temporal as well as the spatial domains. The temporal analysis showed that the flow underwent transition in the following sequence: Periodic \rightarrow quasi-periodic \rightarrow frequency locking \rightarrow chaotic. The critical Reynolds numbers for each transition respectively was computed to be 45, 218, 325 and 600. Quasi-periodicity and frequency-locking were clearly brought out in terms of spectra, autocorrelation function, time-delay recon-

struction and Poincaré section. When the flow became chaotic, the spectrum was seen to broaden, the autocorrelation function diminished rapidly towards zero, the Poincaré section was space filling and the time-delay reconstruction became completely irregular. The Lyapunov exponent and the fractal dimension of the time series were consistent with the identified transition sequence. For the Lyapunov exponent the numerical values were $0 \rightarrow 0 \rightarrow 0 \rightarrow 0.137$ corresponding to the transition Reynolds numbers. The fractal dimensions were 1.0 and 1.41 at Reynolds numbers of 210 and 600 respectively. The flow at a Reynolds number of 500 was non-chaotic based on the Lyapunov exponent (which was zero) while the Poincaré section had a strange attractor.

The spatial-domain analysis examines the transition to three-dimensionality and the evolution of spatial structures in the flow field. The wake of a square cylinder was found to become three-dimensional at a Reynolds number between 150 and 175. Two different modes of shedding were discerned in the present study at the transitional Reynolds number range of 175 - 250. These could be characterized by the spanwise wavelength of the secondary vortices. At a Reynolds number of 175, the wake structure was seen to be Mode-A and the corresponding wavelength was 3. The wake pattern at a Reynolds number of 250 was Mode-B with a spanwise wavelength range of 1.2-1.4. At a Reynolds number of 175, the wake is seen to have intermittent low frequency fluctuations associated with a large-scale irregularity called vortex dislocation. The wake was seen to undergo a transition in the sequence $2D \rightarrow \text{Mode-A}^* \rightarrow \text{Mode-B}$.

The low Reynolds number instantaneous flow ($Re=100$) was similar to the phase-averaged high Reynolds number flow in terms of the wake structure. The similarities were in terms of vortex decay owing to transverse diffusion of the stress components, instantaneous isovorticity contours, instantaneous stress contours and time-averaged contours of the stress components. The decay rate of circulation downstream of the cylinder was however seen to differ. The kinetic energy budget of the oscillatory components revealed that the convection due to mean motion, the production term and the pressure fluctuations played a vital role for the energy exchange between the mean and the fluctuating motion. Unlike turbulent flow, the dissipation and diffusion terms were uniformly negligible, except in the region of the shear layers.

Two- and three-dimensional calculations of the wake of the square cylinder revealed major differences even at a Reynolds number of 250. The two-dimensional model over-predicted the rms values of the forces on the cylinder and consequently higher shear

stresses. The three-dimensional model showed a higher recirculation length with a longer shear layer. The three-dimensional model predicted lower velocity and pressure fluctuations and led to a faster decay of spanwise vortices. The coherence of the wake structures revealed by the two-dimensional model was greater compared to three-dimensional model.

The wake of a square cylinder was found to be sensitive to the shape of the upstream velocity profile. With increasing inlet shear, the time evolution of the lift coefficient gradually showed a pure sinusoid. Strouhal number decreased with the increase in the shear parameter. The mean and rms values of the drag coefficient decreased with the increase in shear parameter upto a certain value but increased with further increase in the shear parameter. The rms values of the lift coefficient revealed similar behaviour. At higher shear, the von Kármán vortex street was seen to break down and clockwise vortices mainly prevailed in the far-wake.

High Reynolds Number Wake ($Re \geq 8000$):

The predictions of the KaLa and the standard $k-\epsilon$ were close to each other in terms of engineering parameters such as Strouhal number and lift and drag coefficients and reasonably close to experiments performed in an unbounded medium. Those of the RNG $k-\epsilon$ were not as close to the experimental values. KaLa revealed the closest agreement with experiments in terms of time-averaged profiles. This was further reinforced in the centreline profiles of the kinetic energy of the total fluctuations.

The three-dimensional model-free computation of high Reynolds number turbulent flow showed good match with both LES and experiments. The phase-averaged field revealed significant difference when compared with instantaneous field. The near-wake showed that the stresses due to the coherent part of fluctuations were higher than those due to the random part. In the intermediate-wake, the two were of comparable magnitude. The time-averaged flow field revealed good quantitative match with those of LES and LDV experiments.

Hotwire Experiments:

Experiments have been carried out at both low and high Reynolds numbers using an

×-wire hotwire anemometer. Measured drag coefficient and Strouhal number showed good match with published literature over a wide range of Reynolds number. The time-averaged profiles revealed fair comparisons with those of LES and LDV measurements. However, at a streamwise location of $x=1.5$, peculiar discrepancies have been noticed due to its differences in the geometrical factors between theory and experiments. Unexpectedly, the inlet turbulence in the approach flow was seen to play an important role in the wake velocity profiles.

6.2 Scope for Future Work

Admittedly the present work is incomplete in certain respects. Future research on this topic should include the following: (1) Finer grids particularly near the obstacle, (2) Closer comparison between the theory and experiments by reproducing all the experimental conditions, (3) A comparison between free-slip and periodicity conditions in the spanwise direction and (4) Sensitivity of the results to the location of the outflow and side boundaries. An extension of the present research using DNS and LES for high Reynolds number flow is also proposed. From an engineering viewpoint, it would be of interest to study changes in the wake structure (a) when the incoming flow is stratified, (b) the cylinder is heated and (c) when the cylinder is flexible enough to be set into motion.

The wake of a square cylinder is rich in detail and throws up a variety of theoretical issues that need to be examined. Several topics belonging to this category were encountered in the present work. Examples are (1) the relationship between the transitions observed in the time domain versus those in the spatial domain, (2) a proper characterization of chaos as Lagrangian or Eulerian and (3) the resolution of the velocity scales in a model-free calculation on a fixed grid and the possibility of correctly predicting the cascade mechanism and back-scatter at high Reynolds number. While performing the experiments, persistent questions came up in the context of instantaneous reversed velocity in the base region and the role of very large turbulence fluctuations on data analysis. The limitation of a hotwire probe as a tool exclusively for point measurements suggests that non-invasive optical methods be utilized to capture the wake structure.

Wake analysis is a topic of great importance in naval applications, detection of unidentified objects from their wake signatures, for example. A related topic is the sup-

pression of the wake signature to avoid detection. A new phenomenon to be included in this analysis is the compressibility of the fluid. Compressibility can occur during wake signature analysis using acoustic sources and wave propagation in wakes from body-mounted actuators. The square and circular cylinders are excellent bluff body models to understand and develop these ideas. It is proposed that the analysis reported in the present work be extended in this direction.

References

- [1] Amano, R. S. and Goel, P. (1984), A Numerical Study of a Separating and Reattaching Flow by Using Reynolds-Stress Turbulence Closure, *Numerical Heat Transfer*, Vol. 7, pp. 343-357.
- [2] Ayukawa, K., Ochi, J. and Hirao, T., (1993), Effects of Shear Rate on the Flow around a Square Cylinder in a Uniform Shear Flow, *J. Wind Engg. Ind. Aerodyn.*, Vol. 50, pp. 97-106.
- [3] Baker, G. L. and Gollub, J. P., (1996), *Chaotic Dynamics, An Introduction*, Cambridge University Press, USA.
- [4] Bearman, P. W., (1971), Corrections for the Effect of Ambient Temperature Drift on Hotwire Measurements in Incompressible Flow, *DISA Information*, Vol. N.11, pp. 25-30.
- [5] Bearman, P. W. and Trueman, D. M., (1972), An Investigation of the Flow around Rectangular Cylinders, *Aero. Q.*, Vol. 23, pp. 229-237.
- [6] Behr, M., Hastretier, D., Mittal, S. and Tezduyer, (1995), Incompressible Flow Past a Circular Cylinder: Dependence of the computed flow field on the location of the lateral boundaries, *Comput. Meth. Appl. Mech. Eng.*, Vol. 123, pp. 309-316.
- [7] Bergé, P., Pomeau, Y. and Vidal, C., (1986), *Order within Chaos*, Wiley, New York.
- [8] Bosch, G. and Rodi, W., (1996), Simulation of Vortex Shedding Past a Square Cylinder Near a Wall, *Int. J. Heat and Fluid Flow*, Vol. 17, pp. 267-175.
- [9] Bloor, M. S., (1964), The Transition to Turbulence in the Wake of a Circular Cylinder, *J. Fluid Mech.*, Vol. 19, pp. 290-304.

- [10] Braza, M., Chassaing, P. and Ha Minh, H., (1986), Numerical Study and Physical Analysis of the Pressure and Velocity Fields in the Near Wake of a Circular Cylinder, *J. Fluid Mech.*, Vol. 165, pp. 79-130.
- [11] Braza, M., Chassaing, P. and Ha Minh, H., (1990), Prediction of Large-Scale Transition Features in the Wake of a Circular Cylinder, *Phy. Fluids*, Part-A, Vol. 2, pp. 1461-1471.
- [12] Brede, M., Eckelmann, H. and Rockwell, D., (1996), On Secondary Vortices in the Cylinder Wake, *Phys. Fluids*, Vol. 8, pp. 2117-2124.
- [13] Bruun, H. H., (1995), *Hot-wire Anemometry Principles and Signal Analysis*, Oxford University Press, USA.
- [14] Buchave, P. George, W. K. Jr. and Lumley, J. L., (1979), The Measurement of Turbulence with the Laser-Doppler Anemometer, *Annu. Rev. Fluid Mech.*, Vol. 11, pp. 443-503.
- [15] Butler, T. and Wanger, J. H., (1982), An Improved Method for Calibration and Use of a Three Sensor Hotwire Probe in Turbomachinery Flows, *AIAA Paper*, 82-0195.
- [16] Cantwell, B. and Coles, D., (1983), An Experimental Study of Entrainment and Transport in the Turbulent Near Wake of a Circular Cylinder, *J. Fluid Mech.*, Vol. 136, pp. 321-374.
- [17] Canuto, C., Hussaini, M. Y., Quarteroni, A. and Zang, T. A., (1986), *Spectral Methods in Fluid Dynamics*, Springer-Verlag, New York.
- [18] Cheng, C. M., Lu, P. C. and Chen, R. H., (1992), Wind Loads on Square Cylinder in Homogeneous Turbulent Flows, *J. Wind Engg. Ind. Aerodyn.*, Vol. 41, pp. 739-749.
- [19] Chew, Y. T. and Simpson, R. L., (1988), An Explicit Non-real Time Data Reduction Method of Triple Sensors Hot-wire Anemometer in Three-Dimensional Flow, *Trans. ASME, J. Fluids Engg.*, Vol. 110, pp. 110-119.
- [20] Chorin, A. J., (1967), 'A numerical method for solving incompressible viscous flow problems', *J. Comput. Phys.*, Vol. 2, pp 12-26.
- [21] Chua, K., Lisoski, D., Leonard, A. and Roshko, A., (1990), A Numerical and Experimental Investigation of Separated Flow Past an Oscillating Flat Plate, *FED-Vol. 92*,

- International Symposium on Unsteady Fluid Dynamics*, Edited by J. A. Miller and D. P. Telionis, pp. 455-464.
- [22] Collis, D. G. and Williams, J. J., (1959), Two-dimensional Forced Convection from Cylinder at Low Reynolds Numbers, *J. Fluid Mech.*, Vol. 6, pp. 357-384.
- [23] Davies, P. O. A. L. and Fisher, M. J., (1964), Non-isothermal Calibration of Hotwire, *Proc. Roy. Soc. London, Part-A*, Vol. 280, pp. 486-527.
- [24] Davis, R. W. and Moore, E. F., (1982), A Numerical Study of Vortex Shedding from Rectangles, *J. Fluid Mech.*, Vol. 116, pp. 475-506.
- [25] Davis, R. W., Moore, E. F., and Purtell, L. P., (1984), A Numerical-Experimental Study of Confined Flow Around Rectangular Cylinders, *Phys. Fluids*, Vol. 23, pp. 46-59.
- [26] Drazin, P. G. and Reid, W. H., (1984), *Hydrodynamic Stability*, Cambridge University Press, USA.
- [27] Durão D. F. G., Heitor, M. V. and Pereira, J. C. F., (1988), Measurements of Turbulent and Periodic Flows Around a Square Cross-section Cylinder, *Expts. Fluids*, Vol. 6, pp. 298-304.
- [28] Eckmann, J. P., Kamphorst, S. O., Ruelle, D. and Ciliberto, S., (1986), Liapunov Exponents from Time Series, *Phys. Rev.*, Part-A, Vol. 34, pp. 4971-4979.
- [29] Eisenlohr, H. and Eckelmann, H., (1989), Vortex Splitting and its Consequences in the Vortex Street Wake of Cylinders at Low Reynolds Number, *Phys. Fluids*, Part-A, Vol. 1, pp. 189-192.
- [30] Feder, J., (1988), *Fractal*, Plenum Press, New York.
- [31] Feigenbaum, M. J., (1980), The Onset Spectrum of Turbulence, *Phys. Lett.*, Part-A, Vol. 74, pp. 375-378.
- [32] Fletcher, C. A. J., (1988), *Computational Techniques for Fluid Dynamics*, Vol. II, Springer Verlag, New York.
- [33] Franke, R. and Rodi, W., (1993), Calculation of vortex Shedding Past a Square Cylinder with Various Turbulence Models, In *Turbulent Shear Flows 8*, F. Durst *et al.* (eds.), Springer, New York, pp. 189-204.

- [34] Franke, R., Rodi, W. and Schönugh, B., (1990), Numerical Calculation of Laminar Vortex-Shedding Flow Past Cylinders, *J. Wind Engg. Ind. Aerodyn.*, Vol. 35, pp. 237-257.
- [35] Frederickson, P., Kaplan, J. A., Yorke, E. D. and Yorke, J. A., (1983), The Liapunov Dimension of Strange Attractors, *J. Diff. Equat.*, Vol. 49, pp. 185-207.
- [36] George, W. K. and Lumley, J. L., (1973), The Laser-Doppler Velocimeter and Its Application to the Measurement of Turbulence, *J. Fluid Mech.*, Vol. 60, pp. 321-362.
- [37] Gerrard, J. H., (1978), The Wakes of a Cylindrical Bluff Bodies at Low Reynolds Number, *Phil. Trans. R. Soc. Lond.*, Part A, Vol. 288, pp. 351-382.
- [38] Ghosal, S., Lund, T. S., Moin, P. and Akselvoll, K., (1995), A Dynamic Localization Model for Large Eddy Simulation of Turbulent Flows, *J. Fluid Mech.*, Vol. 286, pp. 229-255.
- [39] Goldstein, R. J. and Kreid, D. K., (1967), Measurement of Laminar Flow Development in a Square Duct Using a Laser Doppler Flowmeter, *J. Appl. Mech.*, Vol. 34, pp. 813-817.
- [40] Goldstein, R. J. (Editor), (1997), *Fluid Mechanics Measurements, 2nd Edition*, Hemisphere Publishing Corporation, New York.
- [41] Gollub, J. P. and Benson, S. H., (1980), Many Routes to Turbulent Convection, *J. Fluid Mech.*, Vol. 100, pp. 449-470.
- [42] Gottlieb, D. and Orszag, S. A., (1977), *Numerical Analysis of Spectral Methods: Theory and Applications*, SIAM-CBMS Philadelphia.
- [43] Grassberger, P. and Procaccia, I., (1983), Measuring the Strangeness of Strange Attractors, *Physica D*, Vol. 9, pp. 189-208.
- [44] Guzmán, A. M. and Amon, C. H., (1996), Dynamical Flow Characterization of Transitional and Chaotic Regimes in Converging-diverging Channels, *J. Fluid Mech.*, Vol. 321, pp. 25-57.
- [45] Hadid, A. H., Sindir, M. M. and Issa, R. I., (1992), Numerical Study of Two-Dimensional Vortex Shedding from Rectangular Cylinders, *Compt. Fluid Dyn. J.*, Vol. 2, pp. 207-214.

- [46] Hama, F. R., (1957), Three-Dimensional Vortex Pattern Behind a Circular Cylinder, *J. Aeronaut. Sci.*, Vol. 24, pp. 156-158.
- [47] Hammache, M. and Gharib. M., (1989), A Novel Method to Promote Parallel Shedding in the Wake of Circular Cylinder, *Phys. Fluids*, Part-A, Vol. 1, pp. 1611-1614.
- [48] Hammache, M. and Gharib. M., (1991), An Experimental Study of the Parallel and Oblique Vortex Shedding from Circular Cylinder, *J. Fluid Mech.*, Vol. 232, pp. 567-590.
- [49] Harlow, F. H. and Amsden, A. A., (1970), The SMAC Method : A Numerical Technique for Calculating Incompressible Fluid Flows, Los Alamos Scientific Lab. Rept., LA 4370.
- [50] Harlow, F. H. and Welch, J. E., (1965), Numerical Calculation of Time-Dependent Viscous Incompressible Flow of Fluid with Free Surfaces, *Phys. Fluids*, Vol. 8, pp. 2182-2188.
- [51] Heist, D. K. and Gouldin, F. C., (1997), Turbulent Flow Normal to a Triangular Cylinder, *J. Fluid Mech.*, Vol. 331, pp. 107-125.
- [52] Henderson, R. D., (1996), Nonlinear Dynamics and Pattern Formation in Turbulent Wake Transition, *J. Fluid Mech.*, Vol. 352, pp. 65-112.
- [53] Henderson, R. D. and Barkley, D., (1996), Secondary Instability in the Wake of a Circular Cylinder, *Phys. Fluids*, Vol. 8, pp. 1683-1685.
- [54] Hirt, C. W. and Cook, J. L., (1972), Calculating Three-Dimensional Flows around Structures and Over Rough Terrain, *J. Comput. Phys.*, Vol. 10, pp. 324-340.
- [55] Hinze, J. O., (1987), *Turbulence*, McGraw Hill, USA.
- [56] Hoffman, G. and Benocci, C., (1994), Numerical Simulation of Spatially-Developing Planar Jets, AGARD, CP-551, pp. 26.1-26.6.
- [57] Hollasch, K. and Gebhart, B., (1972), Calibration of Constant Temperature Hot-wire Anemometers at Low Velocities in Water with Variable Fluid Temperature, *Trans. of ASME, Journal of Heat Transfer*, Vol. 94, pp. 17-22.

- [58] Huot, J. P., Rey, C. and Arbey, H., (1986), Experimental Analysis of the Pressure Field Induced on a Square Cylinder by a Turbulent Flow, *J. Fluid Mech.*, Vol. 162, pp. 283-298.
- [59] Hussain, A. K. M. F., (1983), Coherent Structures - Reality and Myth, *Phys. Fluids*, Vol. 26, No. 10, pp. 2816-2850.
- [60] Karniadakis, G. and Triantafyllou, G., (1992), Three-dimensional Dynamics and Transition to Turbulence in the Wake of Bluff Objects, *J. Fluid Mech.*, Vol. 238, pp. 1-30.
- [61] Kato, M. and Launder, B. E., (1993), The Modelling of Turbulent Flow around Stationary and Vibrating Square Cylinders, *Proc. 9th Symposium on Turbulent Shear Flows*, Kyoto, Japan, 10-4.
- [62] Kasagi, N. and Matsunaga, (1995), Three-dimensional Particle-Tracking Velocimetry Measurement of Turbulence Statistics and Energy Budget in a Backward-Facing Step Flow, *Int. J. Heat and Fluid Flow*, Vol. 16, pp. 477-485.
- [63] Kawamura, T., Takami, H. and Kuwahara, K., (1986), Computation of high Reynolds number flow around a Circular Cylinder with Surface Roughness, *Fluid Dynamics Research*, Vol. 1, pp. 145-162.
- [64] Keefe, L., Moin, P. and Kim, J., (1992), The Dimension of Attractors Underlying Periodic Turbulent Poiseuille Flow, *J. Fluid Mech.*, Vol. 242, pp. 1-30.
- [65] Kelkar, K. M. and Patankar, S., (1992), Numerical Prediction of Vortex Shedding behind a Square Cylinder, *Int. J. Numer. Meth. Fluids*, Vol. 14, pp. 327-341.
- [66] Kim, J. and Moin, P., (1985), Application of a Fractional Step Method to Incompressible Navier-Stokes Equations, *J. Comput. Phys.*, Vol 59, pp 308-323.
- [67] Kim, J., Moin, P. and Moser, R., (1987), Turbulent Statistics in Fully Developed Channel Flow at Low Reynolds Number, *J. Fluid Mech.*, Vol. 177, pp. 133-166.
- [68] Kiya, M. and Matsumura, M., (1988), Incoherent Turbulence Structure in the Near Wake of a Normal Plate, *J. Fluid Mech.*, Vol. 190, pp. 343-356.
- [69] Kiya, M., Tamura, H. and Arie, M., (1980), Vortex Shedding from a Circular Cylinder in Moderate-Reynolds-Number Shear Flow, *J. Fluid Mech.*, Vol. 141, pp. 721-735.

- [70] Koch, F. A. and Gartshore, I. S., (1970), Temperature Effects on Hotwire Anemometer Calibration, *Journal of Physics E: Sci. Instruments*, Vol. 5, pp. 58-61.
- [71] Kolar, V., Lyn, D. A. and Rodi, W., (1997), Ensembled-Averaged Measurements in the Turbulent Near Wake of Two Side-by-Side Square Cylinders, *J. Fluid Mech.*, Vol. 346, pp. 201-237.
- [72] König, M., Eisenlohr, H. and Eckelmann, H., (1990), The Fine Structure in the $S - Re$ relationship of the Laminar Wake of a Circular Cylinder, *Phys. Fluids*, Part-A, Vol. 2, p. 1607-1614.
- [73] König, M., Eisenlohr, H. and Eckelmann, H., (1992), Visualisation of the Spanwise Cellular Structure of the Laminar Wake of Wall-Bounded Circular Cylinder, *Phys. Fluids*, Part-A, Vol. 4, pp. 869-872.
- [74] Kwon, S., Sung, H. J. and Hyun, J. M., (1992), Experimental Investigation of Uniform-Shear Flow Past a Circular Cylinder, *Transaction of ASME, J. Fluid Engg.*, Vol. 114, pp. 457-460.
- [75] Launder, B. E. and Spalding, D. B., (1974), The Numerical Computation of Turbulent Flows, *Comput. Meth. Appl. Mech. Eng.*, Vol. 3, pp. 269-289.
- [76] Lee, B. E., (1975), The Effect of Turbulence on the Surface Pressure Field of a Square Prism, *J. Fluid Mech.*, Part-II, Vol. 69, pp. 263-282.
- [77] Lyn, D. A., Einav, S., Rodi, W. and Park J. -H., (1995), A Laser-Doppler Velocimetry Study of Ensemble-Averaged Characteristics of Turbulent Near Wake of a Square Cylinder, *J. Fluid Mech.*, Vol. 304, pp. 285-319.
- [78] Lyn, D. A. and Rodi, W., (1994), The Flapping Shear Layer Formed by Flow Separation from the Forward Corner of a Square Cylinder, *J. Fluid Mech.*, Vol. 267, pp. 353-376.
- [79] Majumdar, D. and Amon, C. H., (1997), Oscillatory Momentum Transport Mechanisms in Transitional Complex Geometry Flows, *Trans. ASME, J. Fluid Engg.*, Vol. 119, pp. 29-35.
- [80] Manneville, P. and Pomeau, Y., (1980), Different ways to Turbulent in Dissipative Dynamical Systems, *Physica D*, Vol. 1, pp. 219-226.

- [81] Miller, G. D. and Williamson, C. H. K., (1994), Control of Three-Dimensional Phase Dynamics in a Cylinder Wake, *Expt. Fluids*, Vol. 18, pp. 26-35.
- [82] Mittal, R. and Balachandar, S., (1995a), Effect of Three-Dimensionality on the Lift and Drag of Nominally Two-Dimensional Cylinders, *Phys. Fluids*, Vol. 7, pp. 1841-1865.
- [83] Mittal, R. and Balachandar, S., (1995b), Generation of Streamwise Vortical Structures in Bluff-Body Wakes, *Phys. Rev. Lett.*, Vol. 75, pp. 1300-1303.
- [84] Moin, P. and Kim, J., (1982), Numerical Investigation of Turbulent Channel Flow, *J. Fluid Mech.*, Vol. 118, pp. 341-377.
- [85] Monkewitz, P. A., Williamson, C. H. K. and Miller, G. D., (1996), Phase Dynamics of Kármán Vortices in Cylinder Wakes, *Phys. Fluids*, Vol. 8, pp. 91-96.
- [86] Mukhopadhyay, A., Biswas, G. and Sundararajan, S., (1992), Numerical Investigation of Confined Wakes Behind a Square Cylinder in a Channel, *Int. J. Numer. Meth. Fluids*, Vol. 14, pp. 1473-1484.
- [87] Mukhopadhyay, A., Biswas, G. and Sundararajan, S., (1993), An Explicit Transient Algorithm for Predicting Incompressible Viscous Flows in Arbitrary Geometry, *Int. J. Numer. Meth. Fluids*, Vol. 17, pp. 975-994.
- [88] Mukutmoni, D. and Yang, K. T., (1993), Rayleigh-Bénard Convection in a Small Aspect Ratio Enclosure: Part II-Bifurcation to Chaos, *J. Heat Transfer, Transactions of the ASME*, Vol. 115, pp. 367-376.
- [89] Najjar, F. M. and Vanka, S. P., (1995), Simulations of the Unsteady Separated Flow Past a Normal Flat Plate, *Int. J. Numer. Meth. Fluids*, Vol. 21, pp. 525-547.
- [90] Nichols, B. D. and Hirt, C. W., (1971), Improved Free Surface Boundary Conditions for Numerical Incompressible Calculations, *J. Comput. Phys.*, Vol. 8, pp. 434-448.
- [91] Nishino, K. and Kasagi, N., (1989), Turbulence Statistics Measurement in a Two-Dimensional Channel Flow Using a Three-Dimensional Particle Tracking Velocimeter, *Proc. 7th Symposium on Turbulent Shear Flows*, Stanford, CA, pp. 22.1.1-22.1.6.
- [92] Noack, B. N. and Eckelmann, H., (1994), A Global Stability Analysis of the Steady and Periodic Cylinder Wake, *J. Fluid Mech.*, Vol. 270, pp. 297-330.

- [93] Okajima, A., (1982), Strouhal Numbers of Rectangular Cylinders, *J. Fluid Mech.*, Vol. 123, pp. 379-398.
- [94] Okajima, A., Ueno, H. and Sakai, H., (1992), Numerical Simulation of Laminar and Turbulent Flows around Rectangular Cylinders, *Int. J. Num. Meth. Fluids*, Vol. 15, pp. 999-1012.
- [95] Ong, L. and Wallace, J., (1996), The Velocity Field of the Turbulent Very Near Wake of a Circular Cylinder, *Expts. Fluids*, Vol. 20, pp. 441-453.
- [96] Orlanski, I., (1976), A Simple Boundary Condition for Unbounded Flows, *J. Compt. Phys.*, Vol. 21, pp. 251-269.
- [97] Perry, A. E., (1982), *Hot-wire Anemometry*, Oxford University Press, USA.
- [98] Perry, A. E., Chong, M. S. and Lim, T. T., (1982), The Vortex-Shedding Progress Behind Two-Dimensional Bluff Bodies, *J. Fluid Mech.*, Vol. 116, pp. 77-90.
- [99] Piomelli, U., (1993), High Reynolds Number Calculation using the Dynamic Subgrid-Scale Stress Model, *Phys. Fluids*, Part-A, Vol. 5, pp. 1484-1490.
- [100] Pulliam, T. H. and Vastano, J. A., (1993), Transition to Chaos in an Open Unforced 2D Flow, *J. Compt. Phys.*, Vol. 105, pp. 133-149.
- [101] Rai, M. M. and Moin, P., (1991), Direct Simulation of Turbulent Flow Using Finite-Difference Schemes, *J. Compt. Phys.*, Vol. 96, pp. 15-53.
- [102] Robichaux, J., Tafti, D. K. and Vanka, S. P., (1992), Large Eddy Simulations of Turbulence on the CM-2, *Numerical Heat Transfer*, Part-B, Vol. 21, pp. 367-388.
- [103] Rodi, W., (1993), On the Simulation of Turbulent Flow Past Bluff Bodies, *J. Wind Engg. Ind. Aerodyn.*, Vol. 46 & 47, pp. 3-19.
- [104] Rodi, W., Ferziger, J. H., Breuer, M. and Pourquie, M., (1997), Status of Large Eddy Simulation: Results of Workshop, *Trans. ASME, J. Fluids Engg.*, Vol. 119, pp. 248-270.
- [105] Rodi, W. and Spalding, D. B., (1970), A Two-Parameter Model of Turbulence and its Applications to Free Jets, *Wärme und Stoffübertragung*, Vol. 3, pp. 85-95.

- [106] Roshko, A., (1954), On the Development of Turbulent Wakes from Vortex Streets, *NACA Rep.* 1191.
- [107] Roshko, A., (1993), Perspectives on Bluff Body Aerodynamics, *J. Wind Engg. Ind. Aerodyn.*, Vol. 49, pp. 79-100.
- [108] Ruelle, D. and Takens, F., (1971), On the Nature of Turbulence, *Commun. Math. Phys.*, Vol. 20, pp. 167-192.
- [109] Schumann, U., (1975), Subgrid Scale Model for Finite Difference Simulation of Turbulent Flows in Plane Channels and Annuli, *J. Comput. Phys.*, Vol. 18, pp. 376-404.
- [110] Subbarao, P. M. V., (1995), Experimental Study of the Effect of Stable Thermal Stratification on a Class of Turbulent Shear Flows, Ph.D Thesis, Department of Mechanical Engineering, IIT Kanpur.
- [111] Suzuki, K. and Suzuki, H., (1994), Instantaneous Structure and Statistical Feature of Unsteady Flow in a Channel Obstructed by a Square Rod, *Int. J. Heat and Fluid Flow*, Vol. 15, No. 6, pp. 426-437.
- [112] Swaminathan, M. K., Rankin, G. W., and Sridhar, K. (1986), Evaluation of the Basic Systems of Equation for Turbulence Measurements using the Monte Carlo Technique, *J. Fluid Mech.*, Vol. 170, pp. 1-19.
- [113] Tafti, D. K. and Vanka, S. P., (1991), A Numerical Study of Flow Separation and Reattachment on a Blunt Plate, *Phys. Fluids*, Part-A, Vol. 3, pp. 1749-1759.
- [114] Takens, F., (1981), Detecting Strange Attractors in Turbulence. In *Dynamical Systems and Turbulence, Warwick, 1980*. Lecture Notes in Mathematics, Vol. 898, p. 336, Springer.
- [115] Tamura, T. and Kuwahara, K., (1990), Numerical Study of Aerodynamic Behaviour of a Square Cylinder, *J. Wind Engg. Ind. Aerodyn.*, Vol. 33, pp. 161-170.
- [116] Tamura, T. Ohta, I, and Kuwahara, K., (1990), On the Reliability of Two-Dimensional Simulation for Unsteady Flows around a Cylinder-Type Structure, *J. Wind Engg. Ind. Aerodyn.*, Vol. 35, pp. 275-298.

- [117] Tennekes, H. and Lumley, J. L., (1983), *A First Course in Turbulence*, MIT Press, USA.
- [118] Towfighi, J. and Rockwell, D., (1994), Flow Structure from an Oscillating Nonuniform Cylinder: Generation of Patterned Vorticity Concentrations, *Phys. Fluids*, Vol. 6, pp. 531-536.
- [119] Townsend, A. A., (1949), The Fully Developed Turbulent Wake of a Circular Cylinder, *Aust. J. Sci. Res.*, Vol. 2, pp. 451-468.
- [120] Vastano, J. A. and Moser, R. D., (1991), Short-time Lyapunov Exponent Analysis and the Transition to Chaos in Taylor-Couette Flow, *J. Fluid Mech.*, Vol. 223, pp. 83-118.
- [121] Vieceili, A. J., (1971), A Computing Method for Incompressible Flows Bounded by Moving Walls, *J. Compt. Phys.*, Vol. 8, pp. 119-143.
- [122] Vittori, G. and Blondeaux, P. (1993), Quasiperiodicity and Phase Locking Route to Chaos in the 2D Oscillatory flow around a Circular Cylinder, *Phys. Fluids*, Part-A, Vol. 5, pp. 1866-1868.
- [123] Wang, G., Choudhuri, P. G., Bhandarkar, M. A. and Vanka, S. P., (1996), Report, Large Eddy Simulations of Bluff Body Wakes on Parallel Computers, CFD 96-03, University of Illinois at Urbana - Champaign, Contract No. - 0014 - 92 - J - 1334 of Office of Naval Research.
- [124] West, G. S. and Apelt, C. J., (1982), The Effect of Tunnel Blockage and Aspect Ratio on the Mean Flow Past a Circular Cylinder with Reynolds Numbers between 10^4 and 10^5 , *J. Fluid Mech.*, Vol. 114, pp. 361-377.
- [125] Williamson, C. H. K., (1988a), Defining a Universal and Continuous Strouhal-Reynolds Number Relationship for the Laminar Vortex Shedding of a Circular Cylinder, *Phys. Fluids*, Vol. 31, pp. 2742-2744.
- [126] Williamson, C. H. K., (1988b), The Existence of Two Stages in the Transition to Three Dimensionality of a Cylinder Wake, *Phys. Fluids*, Vol. 31, pp. 3165-3168.
- [127] Williamson, C. H. K., (1989), Oblique and Parallel Modes of Vortex Shedding in the Wake of a Circular Cylinder at Low Reynolds Numbers, *J. Fluid Mech.*, Vol. 206, pp. 579-627.

- [128] Williamson, C. H. K., (1992), The Natural and Forced Formation of Spot-Like 'Vortex-Dislocations' in the Transition of a Wake, *J. Fluid Mech.*, Vol. 243, pp. 393-441.
- [129] Williamson, C. H. K., (1996a), Mode-A Secondary Instability in Wake Transition, *Phys. Fluids*, Vol. 8, pp. 1680-1682.
- [130] Williamson, C. H. K., (1996b), Three-Dimensional Wake Transition, *J. Fluid Mech.*, Vol. 328, pp. 345-407.
- [131] Williamson, C. H. K., (1996c), Vortex Dynamics in the Cylinder Wake, *Ann. Rev. Fluid Mech.*, Vol. 28, pp. 477-539.
- [132] Williamson, C. H. K. and Roshko, A., (1990), Measurements of Base Pressure in the Wake of a Cylinder at Low Reynolds Numbers, *Z. Flugwiss. Weltraumforsch.* Vol. 14, p.38.
- [133] Wolf, A., Swift, J. B., Swinney, H. L. and Vastano, J. A., (1985), Determining Lyapunov Exponents from a Time Series, *Physica D*, Vol. 16, pp. 285-317.
- [134] Wu, J., Sheridan, J., Welsh, M. C., Hourigan, K. and Thomson, M., (1994), Longitudinal Vortex Structures in a Cylinder Wake, *Phys. Fluids*, Vol. 6, pp. 2883-2885.
- [135] Yakhot, V. and Orszag, A., (1986), Renormalization Group Analysis of Turbulence, *J. Sci. Comput.*, Vol. 1, p. 3-51.
- [136] Yakhot, V., Orszag, S. A., Thangam, S., Gatski, T. B. and Speziale, C. G., (1992), Development of Turbulence Models for Shear Flows by a Double Expansion Technique, *Phys. Fluids A*, Vol. 4, pp. 1510-1520.
- [137] Zhang, H., Fey, U., Noack, U., König, M. and Eckelmann, H., (1995), On the Transition of the Cylinder Wake, *Phys. Fluids*, Vol. 7, pp. 779-794.
- [138] Zhou, Y. and Antonia, R. A., (1993), A Study of Turbulent Vortices in the Near Wake of a Cylinder, *J. Fluid Mech.*, Vol. 253, pp. 643-661.